Civil and Structural Engineering

Numerical Modelling of Turbulent Free Surface Flows over Rough and Porous Beds Using the Smoothed Particle Hydrodynamics Method

Ehsan Kazemi

Department of Civil and Structural Engineering

University of Sheffield

Submitted for the degree of

Doctor of Philosophy

Sheffield 2017

To my parents and Booloot

Acknowledgements

This work was supported by the Research Executive Agency, through the 7th Framework Programme of the European Union, Support for Training and Career Development of Researchers (Marie Curie—FP7-PEOPLE-2012-ITN), which funded the Initial Training Network (ITN) HYTECH 'Hydrodynamic Transport in Ecologically Critical Heterogeneous Interfaces', N.316546.

With my deepest appreciation, I would like to thank my supervisors, Prof. Simon Tait and Dr. Songdong Shao for their great support, valuable guidance, and insightful advice. I would have not been able to accomplish this research without their support and help.

I am grateful to Dr. Katinka Koll for her support during my secondment at TU Braunschweig and providing the data which was used to validate the numerical simulations in Chapter 6. I would also like to thank Prof. Vladimir Nikora and Prof. Dubravka Pokrajac for their constructive comments on this research work and the discussions we had during my secondment at the University of Aberdeen.

I am also indebted to Dr. Andrew Nichols for providing the experimental data for the work in Chapter 3. Without this data, the development of the numerical model would have not been possible. I would also like to thank Prof. Shih-Chun Hsiao, Dr. Yunta Wu and Dr. Qinqin Gui for providing the data used for comparisons in Chapter 5. Additionally, many thanks are given to Dr. Eslam Gabreil for his discussions and helps during the completion of this study.

Finally, Special thanks go to the HYTECH team for all the summer schools, conferences, meetings and discussions during my PhD studies.

Abstract

Understanding turbulent flow structure in open channel flows is an important issue for Civil Engineers who study the transport of water, sediments and contaminants in rivers. In the present study, turbulent flows over rough impermeable and porous beds are studied numerically using the Smoothed Particle Hydrodynamics (SPH) method.

A comprehensive review is carried out on the methods of turbulence modelling and treatment of bed boundary in open channel flows in order to identify the limitations of the existing particle models developed in this area. 2D macroscopic SPH models are developed for simulating turbulent free surface flows over rough impermeable and porous beds under various flow conditions. For the case of impermeable beds, a drag force model is proposed to take the effect of bed roughness into account, while for the case of porous beds, macroscopic governing equations are developed based on the SPH formulation, incorporating the effects of drag and porosity.

To simulate the effect of turbulence on the average flow field, a Macroscopic SPH-mixing-length (MSPH-ML) model is proposed based on the Large Eddy Simulation (LES) concept where the mixing-length approach is applied to estimate the eddy-viscosity rather than employing the standard Smagorinsky model. The difficulty in reproducing steady uniform free surface flow is tackled by introducing novel inflow/outflow techniques for the situations in which the flow quantities are unknown at the inflow and outflow boundaries.

The performance of these models is tested by simulating different engineering problems with an insight developed into turbulence modelling and bed/interface boundary treatment. The accuracy of the models is tested by comparing the predicted quantities such as flow velocity, water surface elevation, and turbulent shear stress with existing experimental data.

The limitations of the models are mainly attributed to the macroscopic representation of the roughness layer and porous bed, difficulty in the determination of the values of the empirical coefficients in the closure terms, and limitations with the use of fine computational resolution. On the other hand, the main strength of the model is describing the complicated processes occuring at the bed using simple and practical computational treatments so that the momentum transfer is estimated accurately. It is shown that if the closure terms in the momentum equation which represent the effect of bed drag and flow turbulence are determined carefully based on the physical conditions of bed and flow, the model is capable of being employed for different civil engineering applications.

Contents

List of Figures

List of Tables

Abbreviations

2D	Two dimensional
3D	Three dimensional
CFL	Courant–Friedrichs–Lewy
DNS	Direct Numerical Simulation
EARSM	Explicit Algebraic Reynolds Stress Model
GLM	Generalized Langevin Model
ISPH	Incompressible Smoothed Particle Hydrodynamics
LES	Large Eddy Simulation
LHS	Left-hand side
MAE	Mean Absolute Error
MPS	Moving Particle Semi-implicit
MSPH-ML	Macroscopic SPH-mixing-length
N-S	Navier-Stokes
PDE	Partial Differential Equation
PIV	Particle Image Velocimetry
RANS	Reynolds-Averaged Navier-Stokes
RHS	Right-hand side
RMSE	Root Mean Square Error
SGS	Sub-Grid-Scale
SPH	Smoothed Particle Hydrodynamics

SPHAM	SPH-Averaged Macroscopic
SPS	Sub-Particle-Scale
VAFANS	Volume-Averaged and Favre-Averaged Navier-Stokes
VANS	Volume-Averaged Navier-Stokes
WCSPH	Weakly Compressible Smoothed Particle Hydrodynamics
WG	Wave gauge

Nomenclature

Units are written based on 2D formulations.

$\mathbf{A}_a$	Drag-induced shear term in the momentum equation at the position of particle a	m/s^2
A_d	Cross-sectional area (in the calculation of drag force)	m
A_τ	Planar area parallel to the bed (in the calculation of drag force)	m^2
$A_{\alpha\beta}$	$\alpha-\beta$ interfaces	m
A_Ω	Surface of the averaging volume Ω	m
c_0	Speed of sound	m/s
c_1	Empirical coefficient in Ergun's equation (viscous drag)	-
c_2	Empirical coefficient in Ergun's equation (form drag)	-
C_d	Drag coefficient	-
C_F	Dimensionless form-drag coefficient	-
C_r	Inertia coefficient	-
C_s	Smagorinsky constant	-
d_s	Mean diameter of solid particles	m
$\mathbf{F}$	Forchheimer tensor	-
$\mathbf{F}_d$	Drag force	N

F_o	Outflow boundary relaxing factor	-
F_{vd}	van Driest damping function	-
$\mathbf{g}$	Gravitational acceleration vector	m/s^2
G	Weighting function associated with the averaging volume Ω	1/m^2
H	Water depth	m
H_0	Initial (still) water depth	m
H_w	Wave height	m
H_t^{in}	Height of porous inflow region	m
H_{ow}	Height of outlet imaginary wall	m
h_Υ	Smoothing length associated with the kernel function W	m
h_Ω	Smoothing length associated with the weighting function G	m
$\mathbf{I}$	Unit tensor	-
$\mathbf{K}$	Intrinsic permeability tensor	m^2
k_s	Nikuradse roughness size	m
k_s^+	Equivalent roughness size	-
k_t	SGS (or SPS) turbulent kinetic energy	m^2/s^2
L	Length of numerical channel	m
L_ψ	Microscopic characteristic length (pore scale) of an arbitrary quantity ψ	m
$L_{\langle\psi\rangle^\alpha}$	Macroscopic characteristic length scale of an arbitrary quantity ψ	m
l_0	Initial particle spacing in free flow (clear water) region	m
l_c	Background mesh spacing	m

L_d	A characteristic length of the solid matrix (in a porous medium)	m
$L_{d,i}$	A characteristic length of the solid matrix at an interfacial boundary (in a porous medium)	m
l_m	Mixing-length	m
l_{mb}	Constant mixing-length value inside a porous bed	m
l_{mc}	Value of the mixing-length at the roughness crest	m
m	Particle mass	kg
N	Number of dimensions (= 2 in the present study)	-
$\mathbf{n}_\Omega$	Unit normal vector associated with A_Ω	-
$\mathbf{n}_{\alpha\beta}$	Unit normal vector pointing from α -phase to β -phase	-
$\mathbf{O}_a$	Outflow extra pressure gradient term at the position of particle a	m/s^2
P	Pressure	kg/s^2
q_0^{in}	Inflow discharge per unit width of the channel	m^2/s
Q_{armour}	Armouring discharge	m^3/s
$\mathbf{r}$	Position vector of the centroid of an averaging volume	m
$\mathbf{r}'$	Position vector of other points than the centroid of an averaging volume	m
r_Υ	Support of the kernel function W (radius of the averaging volume Υ)	m
r_Ω	Support of the weighting function G (radius of the averaging volume Ω)	m
R_d	Thickness of the roughness layer (effective roughness height) in the numerical model	m

Re_{ERG}	Ergun Reynolds Number	-
Re_{p}	Pore-based Reynolds Number	-
Re_{τ}	Friction Reynolds Number	-
$\mathbf{S}$	Strain tensor	1/s
$\lvert\mathbf{S}\rvert$	Local strain rate	1/s
S_0	Channel bed slope	-
S_G	Total stroke of a piston wavemaker	m
t	Time	s
T_p	Duration of a piston wavemaker motion	s
$\mathbf{u}$	Velocity vector	m/s
u	Component of velocity vector $\mathbf{u}$	m/s
$\overline{u}$	Component of time-averaged velocity	m/s
u'	Fluctuation associated with component of time-averaged velocity $\overline{u}$	m/s
$\langle u \rangle$	Component of spatial-averaged velocity	m/s
$\tilde{u}$	Spatial deviation associated with component of spatial-averaged velocity $\langle u \rangle$	m/s
$\mathbf{u}_D$	Seepage (discharge) velocity vector	m/s
$\mathbf{u}^i$	Intrinsic (measured) velocity vector	m/s
$\mathbf{u}^s$	Superficial velocity vector ($\equiv$ discharge velocity vector $\mathbf{u}_D$)	m/s
u^*	Shear velocity	m/s
U_0	Initial streamwise velocity	m/s

$\mathbf{u}_{\alpha\beta}$	Velocity vector at $\alpha-\beta$ interfaces	m/s
Vol_{in}	Volume flows inside the computational domain at the inlet boundary	m^2
Vol_{out}	Volume flows out of the computational domain at the outlet boundary	m^2
W	SPH kernel function associated with the averaging volume Υ	$1/ m^2$
W_d	Shape function (in the calculation of drag force)	-
x	Horizontal (streamwise) coordinate	m
X_1^{tr}	Beginning (left side) of the porous inflow transition zone	m
X_2^{tr}	End (right side) of the porous inflow transition zone	m
X_1^s	Beginning (left side) of the numerical measuring zone	m
X_2^s	Middle section of the numerical measuring zone	m
X_3^s	End (right side) of the numerical measuring zone	m
X_p	Displacement of a piston wavemaker	m
z	Vertical (depth-wise) coordinate	m
z_0	Reference level of the mixing-length profile	m
z_b	Bottom wall level	m
z_c	Top level (crest) of the roughness layer	m
z_t	Low level (trough) of the roughness layer	m
z_m	$z_t+\Delta_m$ (Δ_m = volume of melted roughness materials per unit bottom area)	m
z_{ws}	Water surface level	m
z_w	Vertical distance from the bottom wall	m

$\langle \psi \rangle$	Volumetric (spatial) average of an arbitrary quantity ψ over an averaging volume	units of ψ
$\langle \psi \rangle^{\Omega}$	Volumetric average of an arbitrary quantity ψ over the averaging volume Ω	units of ψ
$\langle \psi \rangle^{\alpha}$	Intrinsic average of an arbitrary quantity ψ with respect to phase α within an averaging volume	units of ψ
$\tilde{\psi}$	Spatial Deviation from a volumetric average quantity $\langle \psi \rangle$, $\langle \psi \rangle^{\Omega}$	units of ψ
γ	Porous media distribution function	-
γ_c	Value of the distribution function at the grid point c	-
δ_{ij}	Kronecker delta function with respect to (i, j) coordinates	-
δ_w	Shear boundary layer thickness	m
$\delta_{\alpha\beta}$	Dirac distribution associated with the $\alpha - \beta$ interfaces	-
δ_{Ω}	Dirac distribution associated with A_{Ω}	-
Δ	Eddy length scale (filter width)	m
Δt	Time increment size	s
Δ_s	Thickness of the roughness layer in the physical model	m
ΔV	Volume of particle	m^2
ΔV_c	Volume of the mesh element associated with the grid point c	m^2
η	A small number (here, $0.1h_r$) used to prevent singularity	m
η_w	Water surface elevation	m
κ	von-Karman constant	-
μ	Dynamic viscosity coefficient	kg/(m.s)
μ_{eff}	Effective viscosity in Brinkman's equation	kg/(m.s)

ν_0	Kinematic viscosity coefficient	m^2/s
ν_t	Turbulent eddy-viscosity	m^2/s
Π	Coles parameter	-
ρ	Density	kg/m^2
ρ_0	Reference density	kg/m^2
ρ_a^{app}	Apparent density of particle a	kg/m^2
$\boldsymbol{\tau}_d$	Form drag-induced shear stress	N/m^2
τ_0	Magnitude of turbulent shear stress at the bed (= $\rho g H S_0$)	kg/s^2
$\tau_{\exp}$	Reynolds Stress derived from experimental velocity data	kg/s^2
$\boldsymbol{\tau}_e$	Unresolved part of turbulent shear stress	kg/s^2
$\boldsymbol{\tau}_r$	Part of turbulent shear stress resolved by computational discretisation (particle motion)	kg/s^2
$\boldsymbol{\tau}_t$	Total turbulent shear stress	kg/s^2
$\boldsymbol{\tau}_{SGS}$	SGS stress tensor	kg/s^2
$\boldsymbol{\tau}_{SPS}$	SPS stress tensor	kg/s^2
$\boldsymbol{\tau}_l$	MSPH-ML stress tensor	kg/s^2
Υ	An averaging volume (associated with the kernel function W)	-
ϕ	Porosity	-
ϕ_a	Porosity at the position of particle a	-
ϕ_0	Mean value of porosity of a porous medium	-
ϕ_0^{in}	Porosity of porous inflow region	-
Ω	An averaging volume (associated with the weighting function G)	-

Chapter 1 Aim and Objectives

1.1 Aim of the research

Natural river flows are turbulent and river beds are mostly permeable composed of particles with a wide range of sizes, shapes and configurations. Water penetrates into the bed so that a part of flow occurs beneath the bed surface, although it is significantly weaker than the main flow above the bed. The transfer of momentum at the bed can strongly affect the condition of the overlying flow as well as entrainment and deposition of fine sediments at the bed. Hence, understanding flow mechanisms and momentum exchange at the bed is vital for engineers who study transport of water, sediment and contaminants in rivers. Numerical modelling is a complement to experimental studies of such processes in rivers. When the experimental set-up is difficult and expensive, a numerical model with an acceptable accuracy can be used to simulate the transport phenomena and estimate transport properties especially those which are not easily measured in the laboratory.

The present study aims to investigate turbulent flows over rough impermeable and permeable beds using the most advanced particle based numerical modelling approaches with a focus on turbulence modelling and treatment of the bed boundary. The ultimate goal is providing a simple and appropriate mathematical representation of the complicated processes occur at the bed so that the momentum transfer will be estimated accurately.

1.2 Background

In most of the recent particle models developed for open channel flows, the effect of turbulence has been disregarded, or incorporated in the models without detailed investigation of their accuracy (e.g. in Shakibaeinia and Jin 2011; Federico et al. 2012; Fu and Jin 2013). The treatment of rough impermeable bed boundaries has been mainly based on numerical adjustments (e.g. in Lopez et al. 2010; Fu and Jin 2013) where the momentum reduction at the bed was not related to the physical properties of the bed.

Recently, the Smooth Particle Hydrodynamic (SPH) method has been also used in macroscopic simulation of flow in domains composed of free flow and porous regions (e.g. Akbari and Namin, 2013, Gui et al., 2015, and Ren et al., 2016). Although the desirable approach is solving the equations at the microscopic (pore) level, it requires a three-dimensional (3D) representation of the domain with an extremely fine resolution (Direct Numerical Simulation, DNS) which is almost impossible in the present capacity of particle methods and computational power of most computers.

Some characteristics of the SPH method which make it useful for simulating fluid flow are that the water surface is tracked without using additional techniques and the error associated with numerical diffusion is less than grid-based methods due to its Lagrangian nature. Moreover, in the simulation of fluid flow thorough porous media, discrete elements (particles) carry mass and momentum while they move through different regions, though changes in the volume and momentum of particles when they move from a region to another should be carefully addressed.

Although some efforts have been devoted to the treatment of the interfacial boundary between porous media and free flows in particle models (Akbari and Namin 2013, Gui et al. 2015, and Ren et al. 2016), rather less attention has been paid to a deep investigation of these issues. Often, numerical adjustments and calibrations have been proposed for the averaging process at the interface rather than rigorous mathematical justifications, and the accuracy of the models in predicting turbulent

quantities have not been carefully assessed. Furthermore, the application of SPH in turbulent open channel flows over porous beds with high velocity gradients and turbulent shear stresses at the interface has not been investigated yet.

1.3 Objectives

In the present study, turbulent free surface flows over rough impermeable and permeable beds are studied at a macroscopic scale with a focus on the treatment of interfacial boundary between free flow and the bed. The weakly Compressible SPH (WCSPH) method is employed to develop models in two-dimensional (2D), while the frictional effect of solid bed skeleton and the effect of turbulence on the average flow field are incorporated by appropriate drag and turbulence closure terms in the momentum equations. The objectives for the study are to

- Develop a model based on the SPH method for depth-limited turbulent open channel flows over impermeable rough boundaries with focusing on turbulence modelling and rough boundary treatment. Propose an inflow/outflow boundary technique which produces steady uniform flow conditions. Simulate several cases with different flow conditions, and to validate the developed model using existing experimental data.
- Extend the model for turbulent flows over porous beds with an insight into the interfacial boundary layer between free flow and porous media. Test the model by solving several cases of flow interaction with porous media and to validate the accuracy of the model using existing experimental data.
- Apply the new model for flow over natural porous sediment beds with high velocity gradients at the interfacial boundary and to validate it with existing experimental data.

1.4 Potential future use of the results

If the model is validated for different flow conditions and scales, it could be used to simulate a known range of engineering applications of turbulent flow over impermeable beds, and over/within porous beds. The model will provide a macroscopic description of flow field with simplification of the complicated turbulence mechanism at the bed in order to provide a solution to the practical cases with satisfactory results. Where the model estimates the shear stresses accurately especially at the interface, it could be integrated with a sediment transport model in order to estimate entrainment and deposition of fine particles, thereby predicting sediment transport in turbulent river flows over impermeable/permeable beds.

Chapter 2 Background and Literature Review

Natural river beds are mostly porous consisting of solid particles with a wide range of sizes of a few tenths of a millimetre (fine sand) to several tens of millimetres (gravel). Water penetrates into the bed where flow properties depend on the porous structure of the solid particle matrix. In the last few decades, a great amount of research has been dedicated to numerical modelling of such phenomena, whilst the complicated processes that occur at the channel bed have been treated differently. The two important issues which should be dealt with carefully are the modelling of flow turbulence and the treatment of the bed boundary. In this chapter, focusing on these two issues, the background of turbulent channel flows over impermeable and permeable beds is discussed and then a review is completed on the particle models developed in this area.

In Sections 2.1 and 2.2, turbulence modelling and treatment of the bed in channel flows will be discussed. In Section 2.3, the SPH method will be introduced and the particle models developed for simulation of turbulent channel flow over rough beds as well as the SPH models developed for flow interaction with porous media will be reviewed. Finally in Section 2.4, a summary will be provided with highlighting the required improvements for the present problem.

2.1 Turbulence modelling in open channel flow

It is believed that the Navier-Stokes (N-S) equations describe all motions of fluid flow including turbulent ones. Equation (2.1) shows the N-S equations in the Eulerian form. If one solves these equations at a microscopic scale for an extremely fine computational mesh, i.e. if the size of averaging is too small as all scales of flow is resolved by the mesh, then there will be no need to incorporate any additional closures for turbulence effects. This is known as DNS.

$$\frac{\partial(\rho\mathbf{u})}{\partial t}+\nabla\cdot(\rho\mathbf{u}\mathbf{u})=-\nabla P+\rho\mathbf{g}+\mu\nabla^2\mathbf{u} \tag{2.1}$$

where ρ, $\mathbf{u}$ and P are the microscopic density, velocity vector and pressure, respectively. $\mathbf{g}$ is the gravitational acceleration vector and μ is the dynamic viscosity coefficient.

Although DNS has the advantage of identifying all turbulent vortices through the use of the high resolution of the computational discretisation, there are disadvantages with this method such as its huge computational cost which limits the applicability of the method for practical engineering problems. Hence, the N-S equations are usually solved at a coarse (spatial or temporal) discretisation while the effect of turbulence is incorporated into the equations by extra stress terms. Depending on how these equations are averaged over time or space, there are two different frameworks for dealing with turbulence: Reynolds-Averaged Navier-Stokes (RANS) models, and Large Eddy Simulation (LES) models.

2.1.1 RANS models

Decomposing the instantaneous velocity component u as

$$u=\bar{u}+u' \tag{2.2}$$

where $\overline{u}$ is the time-averaged (Reynolds-averaged) velocity and u' is the associated fluctuation, and applying it into Equation (2.1), leads to the following RANS equation which is presented for an incompressible flow in tensor notation.

$$\rho\frac{\partial\overline{u}_i}{\partial t}+\rho\frac{\partial}{\partial x_j}\left(\overline{u}_i\overline{u}_j\right)=-\frac{\partial P}{\partial x_i}+\rho g_i+\mu\frac{\partial}{\partial x_j}\left(\frac{\partial\overline{u}_i}{\partial x_j}+\frac{\partial\overline{u}_j}{\partial x_i}\right)-\frac{\partial}{\partial x_j}\left(\rho\overline{u_i'u_j'}\right) \tag{2.3}$$

where i and j denotes the coordinates of orthogonal directions. This equation is now represented in terms of (time-) averaged values as well as an additional term $\partial\left(\rho\overline{u_i'u_j'}\right)\big/\partial x_j$ in which $\rho\overline{u_i'u_j'}$ is known as the Reynolds Stress representing the effect of turbulence on the time-averaged flow field.

There are three types of approaches to estimate the Reynolds Stress term thereby providing a treatment of the turbulence in RANS modelling, namely, linear eddy-viscosity models, non-linear eddy-viscosity models, and Reynolds Stress transport models. Linear eddy-viscosity models (hereafter, eddy-viscosity models) which are of interest in the present study, are the most common models applied in approximating Reynolds Stress term. These models work based on the Boussinesq relationship which relates the stress term to average flow quantities as follows.

$$\overline{u_i'u_j'}=-\nu_t\left(\frac{\partial\overline{u}_i}{\partial x_j}+\frac{\partial\overline{u}_j}{\partial x_i}\right) \tag{2.4}$$

where ν_t is the turbulent eddy-viscosity. These eddy-viscosity models are classified in terms of the number of Partial Differential Equations (PDEs) solved in addition to the RANS equations, as zero-, one-, and two-equation models.

The mixing-length model is the most well-known zero-equation model in which the turbulent eddy-viscosity ν_t is defined as a function of mean strain rate based on Prandtl's theory using a turbulent characteristic length called mixing-length l_m. The

following equation shows the relationship for l_m in a 2D open channel case where $\overline{u}$ is the component of the time average velocity in the streamwise direction and z denotes the depth-wise coordinate.

$$\nu_t = l_m{}^2 \frac{\partial \overline{u}}{\partial z} \tag{2.5}$$

According to the Prandtl's assumption, the mixing-length l_m was defined as

$$l_m = \kappa z_w \tag{2.6}$$

where κ is von-Karman constant and z_w is vertical distance from the wall, based on the fact that the eddy size is restricted by the wall so that it decreases linearly to zero at the wall level.

Later, following laboratory measurements, some modifications have been made to Prandtl's assumption (Equation 2.6). For instance, van Driest (1956) modified Prandtl's equation and proposed the following formula for the mixing-length.

$$l_m = \begin{cases} \kappa z_w \left[1 - exp\left(-\dfrac{z_w{}^+}{A^+}\right)\right] & \dfrac{z_w}{\delta_w} \le \dfrac{\kappa_0}{\kappa} \\ \kappa_0 \delta_w & \dfrac{z_w}{\delta_w} \le \dfrac{\kappa_0}{\kappa} \end{cases} \tag{2.7}$$

where δ_w is the boundary layer thickness; $\kappa_0 = 0.09$; $A^+ = 26$; and $z_w{}^+ = z_w u^* / \nu$ in which u^* is the shear velocity. $F_{vd} = \left[1 - exp\left(-z_w{}^+ / A^+\right)\right]$ is a damping function added by van Driest to reduce the contribution of turbulent shear stress near the wall. Another mixing-length formula was proposed by Michel et al. (1969) as

$$l_m^+ = \frac{0.085\delta_w u^*}{\nu} tanh\left(\frac{\kappa z_w}{0.085\delta_w}\right) \tag{2.8}$$

which was later used by some researchers e.g. Krogstad (1989) in combination with van Driest damping function to develop mixing-length models for turbulent boundary layer over rough surfaces.

The above-mentioned formulas were basically proposed for mixing-length distribution within shear boundary layer above the bed. Nezu and Rodi (1986), and Nezu and Nakagawa (1993) proposed Equation (2.9) for the distribution of mixing-length through the channel depth according to their measurements in turbulent open channel flows. According to this equation, the mixing-length declines to zero at the water surface. Nezu and Rodi (1986) stated that the decrease is because of the restriction of the turbulent eddies size by the water surface, though their data do not show such a decline consistently. In fact, there is uncertainty in defining the behaviour of mixing-length near the water surface due to the lack of reliable velocity data close to the free surface.

$$\frac{l_m}{H} = \kappa\sqrt{1-\xi}\left[\frac{1}{\xi} + \pi\ \Pi\ sin\left(\pi\xi\right)\right]^{-1} F_{vd}\left(\xi\right) \tag{2.9}$$

In this equation, H is water depth, ξ is equal to z_w / H, $F_{vd}\left(\xi\right)$ is van Driest's damping function in the near-wall region, and Π is Coles parameter. Coles (1956) introduced the addition of an empirical wake function to the velocity log law in order to describe the deviation of velocity from the log law in the outer region. Coleman (1981) also confirmed that this deviation should not be dealt with by adjusting the integration constant (B_r in Equation 3.20) and/or the von-Karman constant κ, but rather by including a wake function to the log law.

The main advantage of the mixing-length method is that it is simple to be implemented while good predictions are achieved for strongly 2D turbulent free surface flows where the mixing-length distribution is available. However, this model lacks universality and does not include flow history effects on turbulence. Other types of eddy-viscosity models are one-equation and two-equation models such as Spalart-Almaras and $k-\varepsilon$, respectively. In the former, a simple PDE equation is solved for

turbulent eddy-viscosity containing production and dissipation of ν_t . In the latter, two extra equations are solved, one for turbulent kinetic energy and one for turbulent dissipation. The wider range of flow conditions which can be modelled by the $k-\varepsilon$ model, compared to the mixing-length and Spalart-Almaras models, has made the $k-\varepsilon$ model more common in RANS turbulence modelling.

In the $k-\varepsilon$ model, wall functions are often used for the determination of the turbulent boundary layer by assuming a logarithmic distribution of time-averaged flow velocity near the wall surface. In this approach, the near-wall viscous sub-layer is neglected since it is assumed to not have the major effect on the flow structure in turbulent conditions, thus the first computational grid point from the wall is located in the logarithmic layer. Utilizing wall functions is practical and has produced accurate results in modelling open channel flow over smooth and small-scale rough beds (Nicholas and Smith 1999, Hsu et al. 1998, Zeng and Li 2012). However, this approach becomes invalid when the velocity distribution does not follow a logarithmic relationship near the wall, for instance, in case of existence of large-scale roughness elements such as in the natural shallow river flows over rough gravel beds. According to Nikora et al. (2001), the near-bed layer in flow over a hydraulically rough bed can be divided into the form-induced sub-layer, where the flow is influenced by the individual roughness elements, and the interfacial sub-layer, which occupies the flow region between the roughness crest and trough. Nikora et al. (2004) further suggested that flow velocity distribution in the interfacial sub-layer can be either constant, exponential or linear based on roughness geometry, flow conditions, and relative submergence. Another major inadequacy of using wall functions was also addressed by Nicholas (2001), in that the shear stress could not be reproduced accurately by a wall functions because of the difficulty with mesh resolution near the bed boundary.

2.1.2 LES models

In LES, usually a decomposition similar to Reynolds decomposition (Equation 2.2), but in space, is employed and the equations are averaged spatially. The spatial decomposition is written as

$$u = \langle u \rangle + \tilde{u} \tag{2.10}$$

where $\langle u \rangle$ is the spatial average of the velocity component u, and $\tilde{u}$ is its spatial deviation from the point velocity u. The spatial-averaged N-S equation of an incompressible flow is represented in the tensor notation as follows.

$$\rho \frac{\partial \langle u \rangle_i}{\partial t} + \rho \frac{\partial}{\partial x_j}\left(\langle u \rangle_i \langle u \rangle_j \right) = -\frac{\partial P}{\partial x_i} + \rho g_i + \mu \frac{\partial}{\partial x_j}\left(\frac{\partial \langle u \rangle_i}{\partial x_j} + \frac{\partial \langle u \rangle_j}{\partial x_i} \right) - \frac{\partial \tau_{ij}}{\partial x_j} \tag{2.11}$$

where

$$\tau_{ij} = \rho\left(\left\langle \langle u \rangle_i \langle u \rangle_j \right\rangle - \langle u \rangle_i \langle u \rangle_j + \left\langle \tilde{u}_i \langle u \rangle_j \right\rangle + \left\langle \langle u \rangle_i \tilde{u}_j \right\rangle + \left\langle \tilde{u}_i \tilde{u}_j \right\rangle \right) \tag{2.12}$$

is the ij component of the LES Sub-Grid-Scale (SGS) stress tensor. τ_{ij} is composed of three parts:

$$\begin{aligned} L_{ij} &= \rho\left(\left\langle \langle u \rangle_i \langle u \rangle_j \right\rangle - \langle u \rangle_i \langle u \rangle_j \right) \\ C_{ij} &= \rho\left(\left\langle \tilde{u}_i \langle u \rangle_j \right\rangle + \left\langle \langle u \rangle_i \tilde{u}_j \right\rangle \right) \\ R_{ij} &= \rho \left\langle \tilde{u}_i \tilde{u}_j \right\rangle \end{aligned} \tag{2.13}$$

where L_{ij} and C_{ij} are called the Leonard Stress and cross stress, respectively, and the third term R_{ij} is known as Reynolds Stress since it is analogous to the Reynolds Stress tensor $\rho\overline{u_i' u_j'}$ in RANS equations.

In LES, turbulent length scales larger than the discretisation size are resolved by the computational grid, while the smaller ones need to be modelled. Therefore, appropriate closure models need to be applied to estimate the extra stress term, i.e. the SGS stress tensor. The most well-known sub-grid-scale models for LES are the standard Smagorinsky model, dynamic models, and mixed models.

The standard Smagorinsky model, which was proposed by Smagorinsky (1963) and Deardorff (1970), is based on the Boussinesq hypothesis in estimating the SGS stress as follows

$$\frac{\tau_{ij}}{\rho} = -2\nu_t S_{ij} + \frac{2}{3} k_t \delta_{ij} \tag{2.14}$$

where i and j are coordinate components, τ_{ij} is the component of the SGS stress tensor $\boldsymbol{\tau}_{SGS}$, ν_t is the turbulent eddy-viscosity, S_{ij} is the component of the strain tensor $\mathbf{S}$ calculated by Equation (2.15), k_t is the SGS turbulent kinetic energy (Equation 2.16) and δ_{ij} is the Kronecker delta function.

$$S_{ij} = \frac{1}{2}\left(\frac{\partial u_i}{\partial x_j} + \frac{\partial u_j}{\partial x_i} \right) \tag{2.15}$$

$$k_t = \nu_t \left(\frac{\partial u_i}{\partial x_i} + \frac{\partial u_j}{\partial x_j} \right) \tag{2.16}$$

In these equations, x is the component of the position vector and u is the component of the average velocity vector $\mathbf{u}$. To estimate the eddy-viscosity ν_t, the Smagorinsky model (1963) is often employed in SPH simulations, as follows

$$\nu_t = \left(C_s \Delta\right)^2 \left|\mathbf{S}\right| \tag{2.17}$$

Where C_s is the Smagorinsky constant, Δ is the eddy length scale (filter width), and $\left|\mathbf{S}\right|$ is the local strain rate which is equal to $\left|\mathbf{S}\right| = \sqrt{\mathbf{S}:\mathbf{S}^T}$. It is noted that C_s is usually

taken to be between 0.1 and 0.15, and Δ is assumed to be equal to the computational spacing size.

The standard Smagorinsky model is the oldest and simplest LES-SGS model, which has been widely used due to its simplicity and effectiveness. Although it is a valuable tool for engineering applications (Rogallo and Moin 1984), the model produces spurious dissipation which damps the growth of small perturbations and thus restrains the transition to turbulence (Piomelli and Zang 1991).

In the dynamic model which was initially proposed by Germano et al. (1991), a modification has been introduced to the standard Smagorinsky model, so that the Smagorinsky constant is determined as a function of both space and time by applying a second filtering operation into the equations. In the mixed models, a combination of a dissipative eddy-viscosity model such as the standard Smagorinsky model, and a scale similarity model, usually by applying a second filtering operation, is used to estimate the extra shear stress tensor. Details of such combinations of models are given in Sagaut (2001).

2.2 Treatment of bed boundary in open channel flow

In treating the natural bed boundary in open channel flow simulations, an important issue is that whether it is possible to introduce the bed interface as a fixed boundary condition in the model, or is it essential to simulate the flow in the porous bed deposit too. When the bed is impermeable or flow inside the bed is negligible, the modellers treat the bed boundary as a zero-velocity boundary condition. However, the effect of bed friction and turbulence on the mean velocity field, as well as the level at which the velocity becomes zero should be adequately addressed, particularly when the bed is rough. In the case that flow inside the bed is significant and the momentum exchange at the interface boundary is not negligible, the flow inside the porous bed also needs to be simulated. In the following Sections 2.2.1 and 2.2.2, a comprehensive review is carried out on the treatment of bed boundary in both cases, i.e. i) turbulent

channel flow over impermeable rough beds, and ii) turbulent channel flow over porous beds, respectively.

2.2.1 Rough and impermeable bed

According to classic hydraulics studies such as Nikuradse (1933), Clauser (1954), Rotta (1962) and Perry et al. (1969), the slope of the time-averaged streamwise velocity profile in a semi-logarithmic scale has the same value for both smooth and rough walls (von-Karman constant, κ), but with a vertical shift in the case of a hydraulically rough boundary. A great amount of research has been carried out in the last decades to relate the shift in the velocity profile to the size of physical boundary roughness; and also to find the location at which the time-averaged velocity becomes zero near the wall. Nikuradse (1933) carried out experiments on uniform sand grains and showed that the shift (ΔU^+) is a function of equivalent roughness height $k_s^+ = k_s u^* / \nu$ only (u^* is the shear velocity and k_s is the height of sand grain). In these experiments, the vertical coordinate was measured from some distance below the top of sand grains. Later, Clauser (1954) showed that the shift is also related to the roughness type. Generally speaking, there has been no agreement on the zero position of the vertical coordinate and the level of zero-velocity plane.

Due to the importance of the subject, after Nikuradse (1933), many researchers have carried out numerous experimental and numerical studies to understand the complex interaction of turbulent flows with the bed and also to parameterize the effects of bed roughness on the mean flow field. In the numerical studies, the effect of wall roughness on the flow is modelled usually by modifying the turbulence model near the wall boundary or by applying extra models to take the effect of roughness into account. In the following paragraphs, a review is carried out on some of those studies.

Van Driest modified his mixing-length formula (Equation 2.7) which was originally derived for smooth walls. According to this modification, the damping function F_{vd} was reduced based on the assumption that the effect of turbulent mixing is higher

near a rough wall than a smooth wall. Sivykh (1984) pointed out that the maximum of the modified van Driest damping function is one, while it could be even higher for the cases where the roughness effect is high. Accordingly, he modified van Driest formula for such cases. Rotta (1962) introduced a different modification to the formula of van Driest by introducing a shift in the wall coordinate, considering that the shear stress increases near the wall so that the velocity decreases. Some other studies have also been carried out on turbulent boundary layer near rough walls based on the mixing-length model for sand grain roughness (Granville 1985, Granville 1988, Krogstad 1991). In these studies, either a damping function was applied into the mixing-length formula or a shift was introduced in the velocity profile, in order to account for the effect of roughness.

Although eddy-viscosity models, such as mixing-length and $k-\varepsilon$, have been applied for a wide range of flow conditions, sometimes they are insufficient to adequately address the shear boundary layer near the walls composed of discrete elements with large-scale roughness. Hence, the drag force concept has been applied as an alternative approach for such cases.

Generally, in drag-based models, a drag term is added to the N-S equations. However, different formulations and empirical factors have been used in different models. Christoph and Pletcher (1983) and Taylor et al. (1985) added a form-drag term to the momentum equation to account for the bed roughness effect. The former modified the mixing-length model to include the effect of roughness while the latter applied the standard smooth-wall mixing-length formula of van Driest (Equation 2.7). Taylor et al. (1985) argued that since the effect of bed roughness is explicitly accounted for by adding the drag term into the momentum equation, the eddy-viscosity (mixing-length) model does not need to be modified for the effect of bed roughness. According to Patel (1998), the advantage of these drag force models was that they could reflect the effect of rough walls based on the shape and geometry of the roughness elements, rather than only a single representative length scale such as k_s^+. Wiberg and Smith (1991) carried out a theoretical study for the velocity distributions

in steep streams over coarse gravel beds by partitioning the total shear stress into two components: a purely fluid component which is the stress generated between fluid parcels, and a form-induced stress part of which is the result of drag force acting on the bed grains. Accordingly, an eddy-viscosity model was used for the fluid stress component, and an additional drag-induced stress term was added to the momentum equation, as presented in the following equation, to represent the effect of roughness elements.

$$\tau_d = \frac{F_d}{A_\tau} \tag{2.18}$$

where

$$F_d = \frac{1}{2}\rho C_d A_d u^2 \tag{2.19}$$

F_d is the drag force in the streamwise direction and u is the streamwise velocity. Besides, A_τ is the planar area parallel to the bed, affected by one roughness element perpendicular to the bed plane, A_d is the cross-sectional area of the element, and C_d is the drag coefficient.

Follow-on applications of the drag force models include Miyake et al. (1999), who developed a DNS model for simulating turbulent flow in a rough wall channel and used a drag-based formulation to consider the effect of sand grains on the flow. Cui et al. (2003) developed a computationally efficient LES model, where the bed roughness was decomposed into the resolved and subgrid-scale components. The geometric features of the resolved roughness were determined through LES without using any empirical treatment, but the subgrid-scale roughness was modelled by a random drag force distribution. Moreover, Nicholas (2005) developed a drag force model to parameterize the roughness of gravel-bed rivers by using a stochastic model for fluvial process. Carney et al. (2006) treated the bed roughness layer as a porous region and constructed their model on FLUENT with a $k-\varepsilon$ turbulence closure, in which a sink term was added to the momentum equation to account for the influence of bed

roughness defined by a drag force equation with a constant drag coefficient. On the other hand, Rameshwaran et al. (2011) used the drag force concept to model the influence of bed roughness but they solved double-averaged (in time and space) N-S equations which included the drag term, form-induced momentum flux and blockage (porosity) effect resulting from the spatial averaging procedure. Zeng and Li (2012) also solved the double-averaged N-S equations for depth-limited flows over gravel-bed channels for cases of small-scale and large-scale roughness elements. They used the wall function approach for the small-scale roughness and applied a drag based model to the large-scale roughness since the wall function did not perform well in the latter case. Finally, in Busse and Sandham (2012), the drag force term was added to the N-S equations to account for the additional pressure drag-induced by the roughness elements and it contained two parameters, i.e. roughness height and roughness factor that the latter was related to the roughness density and a shape function.

2.2.2 Porous bed

In Section 2.2.1, the models developed for treating impermeable rough bed boundaries in turbulent free surface flows were reviewed. However, in most river engineering cases, the channel bed is porous composed of sands and gravels so that flow can penetrate and move also inside the bed. In such conditions, the momentum transfer at the interfacial boundary between porous media and the adjacent turbulent flow plays an important role in the formation of the flow structure and has a significant effect on the possible transport, entrainment and deposition of solid particles by the flow such as fine sediments. Hence, many research studies have been devoted to the understanding of fluid flow through porous media and the complex processes that occur at the interfacial boundary.

There are two general approaches in the mathematical modelling of flow through porous media, i.e. the microscopic and macroscopic approaches. In the microscopic representation of the media, the fluid-solid interfaces are modelled as rigid

boundaries, while in the macroscopic approach, the media is represented as a single-phase continuum and the frictional effects of the solid matrix on the macroscopic field are incorporated as drag terms in the governing equations. In the microscopic modelling, all geometrical characteristics of the media as well as all scales of flow are resolved (DNS). Hence, it is ideal, but often impractical due to the limitations with the computational power and cost. Therefore, macroscopic approach has been more attractive to the researchers for decades for studying fluid flow through porous media.

In 1856, Henry Darcy performed experiments on unidirectional flow in a uniform sand column and proposed Darcy's law as the following relationship.

$$\mathbf{u}_D = -\frac{\mathbf{K}}{\mu}\nabla P \tag{2.20}$$

where $\mathbf{u}_D$ is the seepage (discharge) velocity, $\mathbf{K}$ is the intrinsic permeability tensor and ∇P is the intrinsic (measured) pressure gradient in the sand column. It is notable that $\mathbf{u}_D$ is equivalent to the superficial (volume average) velocity which is equal to $\phi\mathbf{u}^i$ where $\mathbf{u}^i$ is the intrinsic (measured) velocity and ϕ is the porosity of the media. Later, Forchheimer (1901) observed that when the flow velocity increases, the inertial effects become dominant. Then he included an inertial term, representing the kinetic energy, to the Dracy's equation and proposed the following relationship for flow through porous media.

$$\nabla P = -\frac{\mu}{\mathbf{K}}\mathbf{u}_D - \frac{C_F}{\sqrt{\mathbf{K}}}\rho\mathbf{u}_D\left|\mathbf{u}_D\right| \tag{2.21}$$

where C_F is a dimensionless form-drag coefficient. In fact, the linear (Darcy) term represents the viscous effects while the nonlinear Forchheimer term represents the form-drag effects. Ergun (1952) also proposed an empirical equation for drag effects with a form similar to Equation (2.21). Although it was derived specifically for flow through packed beds of spheres, it has been widely used in many engineering applications.

In the case of existence of a free flow adjacent to the porous media, Darcy's equation (2.20) does not match with the N-S equations of free flow (Equation 2.1) at the interface boundary due to the second derivative term of viscosity in the N-S equation. Binkman (1947) added another term to Darcy's equation as the following which resolved this issue.

$$\nabla P = -\frac{\mu}{\mathbf{K}}\mathbf{u}_D - \mu_{eff}\nabla^2\mathbf{u}_D \tag{2.22}$$

where μ_{eff} in the Brinkman's term is known as the effective viscosity which is approximately equal to the fluid viscosity.

Later, a combination of Equations (2.20), (2.21) and (2.22) was considered as Darcy-Brinkman-Forchheimer flow model which was also obtained by local volume averaging of the N-S equations in some studies. For example, Vafai and Tien (1981) obtained the following equation for the macroscopic equation of momentum considering a 2D steady, isotropic, incompressible, homogeneous flow through a porous medium.

$$\rho\left(\mathbf{u}_D \cdot \nabla\right)\mathbf{u}_D = -\nabla P + \mu_{eff}\nabla^2\mathbf{u}_D - \frac{\mu}{\mathbf{K}}\mathbf{u}_D - \frac{C_F}{\sqrt{\mathbf{K}}}\rho\mathbf{u}_D\left|\mathbf{u}_D\right| \tag{2.23}$$

It is notable that the local volume averaging method for deriving the macroscopic governing equations of fluid flow through porous media was previously proposed by Slattery (1967), Whitaker (1969) and Gray and Lee (1977). Later, Whitaker (1996) applied the method of volume averaging to the N-S equations and obtained the Darcy's law with the Forchheimer correction for homogeneous porous media. They provided the Volume-Averaged N-S (VANS) equations in which the following term was added to the momentum equation as the drag effects of the solid matrix.

$$\mathbf{A}_s = -\frac{\mu}{\mathbf{K}}\left(\mathbf{I} - \mathbf{F}\right)\mathbf{u}^s \tag{2.24}$$

$\mathbf{A}_s$ is equivalent to the last two terms on the right-hand side of Equation (2.23); and $\mathbf{u}^s$ is the superficial velocity which is equivalent to the discharge velocity $\mathbf{u}_D$ in that

Equation. Besides, $\mathbf{K}$, $\mathbf{I}$ and $\mathbf{F}$ are the permeability, unit, and Forchheimer tensors, respectively.

VANS equations have been used in a large number of studies to macroscopically simulate flow through porous media in various engineering applications. However, in the presence of an adjacent turbulent flow, treatment of the interfacial boundary between porous media and free flow has always been a challenging task. There have been two different types of treatments in the literature for this purpose. I) in many studies, flow inside porous media is disregarded; or simulated separately while matching conditions of velocity and shear stress are applied at the interfacial boundary. The matching conditions apply either continuous flow quantities or a discrete step change in the streamwise flow quantities at the interface boundary. II) A set of governing equations is solved in a unified domain including both porous and free flow (clear water) regions while the difference between the two regions is characterised by porosity, permeability and drag stress terms in the equations.

Beavers and Joseph (1967) was one of the first studies where a discrete step change in the boundary condition was proposed for treating the interface. They studied a Poiseuille flow over a naturally permeable block and assumed that the velocity changes rapidly from a slip velocity at the interface to the Darcy velocity within the block. Accordingly, they related the tangential shear stress at the interface to the difference between the interface slip velocity and the Darcy velocity using an empirical coefficient which depends on the parameters of the porous surface. Ochoa-Tapia and Whitaker (1995a) also proposed a stress jump condition at the interface in which an excess stress appears in the formulation of the boundary conditions with an adjustable coefficient. Hahn et al. (2002) used an extended version of Beavers and Joseph (1967) boundary condition in their DNS of turbulent channel flow bounded by permeable walls. At the interface, they imposed a slip velocity condition at streamwise and spanwise directions and a zero-velocity condition at the wall-normal direction. Huang et al. (2003) separately solved unsteady 2D N-S equations for free flow and N-S type equations including drag terms for flow through porous media to

simulate the interaction between a solitary wave and a submerged porous breakwater. At the interface boundary, following Deresiewicz and Skalak (1963), they applied the matching conditions which represent the continuity of the velocities as well as the continuity of the normal and the tangential stresses.

From the physical point of view, the interface should be addressed as a boundary layer over which the flow quantities transfer smoothly (i.e. defining free flow and porous media in a unified domain) rather than by matching up the equations at a single interface line. Hence, the latter has been more attractive among researchers in recent years. Breugem and Boersma (2005) carried out two DNS simulations for turbulent flow over and within a Cartesian grid of cubes by solving the N-S equations in a unified computational domain. In one, an immersed boundary method was employed to impose the no-slip and no-penetration conditions on the surface of cubes (i.e. the cube surfaces were simulated as rigid boundaries), while in the other one, the porous media (grid of cubes) was simulated as a continuum based on the VANS equations of Whitaker (1996). They stated that the continuum approach requires less computational power although it needs closures for drag force and turbulent stresses. In the continuum DNS, the same equations were solved for both porous and free flow regions with a continuous variable-porosity formulation at the interface. Breugem and Boersma (2005) concluded that the direct simulation is not always possible with present-day computer facilities, while the continuum approach can provide reliable result if the drag closure model is carefully selected.

All of the studies reviewed have been developed based on grid-based methods, such as Finite Difference or Finite Volume Methods, where a fixed grid system is used in the Eulerian framework. Recently, Lagrangian particle methods such as SPH have shown promising capacities in simulating turbulent free surface flows. Some of the applications in this area (which are of interest in the present study) will be reviewed in the following section.

2.3 Particle based methods for simulating turbulent channel flow

SPH is a Lagrangian particle method that was initially proposed by Lucy (1977) and Gingold and Monaghan (1977) to solve astrophysical problems. Since then due to its capacity in simulating fluid flows, it has been widely used in this area. In SPH, the following integral representation is used for approximating a quantity like A at the position $\mathbf{r}$.

$$A(\mathbf{r}) = \int_{\Upsilon} A(\mathbf{r}')W(\mathbf{r}-\mathbf{r}', h_{\Upsilon})d\mathbf{r}' \tag{2.25}$$

where Υ denotes the averaging volume, $\mathbf{r}'$ is the position vector of other points than the centroid $\mathbf{r}$, $W(\mathbf{r}-\mathbf{r}', h_{\Upsilon})$ is the weighting (kernel) function, and h_{Υ} is its associated smoothing length (see Figure 2-1). Besides, the derivative of A is approximated as the following

$$\nabla A(\mathbf{r}) = \int_{\Upsilon} A(\mathbf{r}')\nabla W(\mathbf{r}-\mathbf{r}', h_{\Upsilon})d\mathbf{r}' \tag{2.26}$$

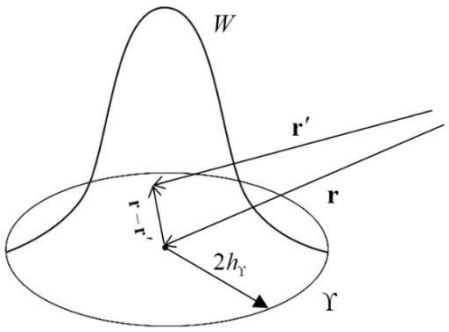

Figure 2-1 Averaging volume Υ and weighting function W.

Equations (2.25) and (2.26) are written in the following form, respectively, after discretising the computational domain.

$$A\left(\mathbf{r}_a\right)=\sum_b A\left(\mathbf{r}_b\right)W\left(\mathbf{r}_a-\mathbf{r}_b,h_\Upsilon\right)\Delta V_b \tag{2.27}$$

$$\nabla A\left(\mathbf{r}_a\right)=\sum_b \nabla A\left(\mathbf{r}_b\right)W\left(\mathbf{r}_a-\mathbf{r}_b,h_\Upsilon\right)\Delta V_b \tag{2.28}$$

where indices a and b denote the particle at the centroid where the quantities are calculated for and its neighbouring particles, respectively. ΔV is the volume of particles which is defined as m/ρ in which m and ρ denote particle mass and volumetric density, respectively.

Particle methods like SPH have several advantages for simulating free surface flows, although just a small number of studies have been carried out in this area. Due to its Lagrangian nature, SPH is capable of dealing with large deformations of free surface boundaries, simulating complex solid boundaries appropriately, and simulating fluid flow with no numerical diffusion. Specifically, for the present applications of turbulent flow over porous beds, it has the advantage of treating the interface between porous media and free flow as a continuous boundary as the computational domain including both porous and free flow regions is discretised by moving particles which carry mass and momentum while moving from one region to another. This capacity makes the simulation of complex interfacial boundaries easy and effective. However, this area of research is still new and there have been no comprehensive SPH model developed for simulating turbulent flow over porous beds.

In the following Sections 2.3.1 and 2.3.2, respectively, the turbulence modelling and impermeable boundary treatment in existing particle-based models will be reviewed. Then, since there has been no particle model developed specifically for turbulent open channel flows over porous beds, the SPH models developed for free surface flow interaction with porous media (which are mostly in the area of coastal engineering) will be reviewed in Section 2.3.3.

2.3.1 Turbulence modelling in particle models

Although some attempts have been made in recent years to model turbulence in particle methods, this issue is still challenging since all well-known turbulence models have been originally developed and tested for the grid-based methods. One of the earliest attempts to model turbulence in particle methods was made by Gotoh et al. (2001) where a Sub-Particle-Scale (SPS) model was introduced and applied with Moving Particle Semi-implicit (MPS) method to simulate a turbulent jet. SPS is the particle version of the LES-SGS model of Smagorinsky (1963) which was discussed in Section 2.1.2. Later, two other approaches were proposed and tested by Violeau et al. (2002) for modelling flow turbulence in SPH based on the eddy-viscosity assumption and the Generalized Langevin Model (GLM). These models were used to simulate a turbulent Poiseuille flow in a pipe. Violeau and Issa (2007) also investigated the application of some turbulence models with the SPH method for simulation of some complex free surface flows. In their study, a $k-\varepsilon$ model, an Explicit Algebraic Reynolds Stress Model (EARSM), and a 3D LES model were developed to simulate the collapse of a column of water. According to their study, the LES-SPS model requires more computational costs compared the traditional RANS turbulence closures. Lopez et al. (2010) simulated hydraulic jumps with different Froude numbers (Fr) using the SPH method and achieved good agreement between numerical and experimental results for the cases with low Fr number by using the standard SPH formulations without any turbulence treatment, while they had to employ a variable artificial viscosity formulation in order to achieve desirable accuracy for flows with Fr > 5. The standard SPS model was also used by some researchers for turbulence modelling in particle methods, including but not limited to Sahebari et al. (2011), Fu and Jin (2013), and Chern and Syamsuri (2013), in which the Smagorinsky constant was set to 0.12 to 0.15. But, De Padova et al. (2013) used a mixing-length approach with SPH for simulating 3D hydraulic jumps in a large channel. Firstly, they solved a 2D uniform open channel flow over a wall boundary with roughness $k_s = 0.02H$ (H = water depth) to validate the turbulence model. Then hydraulic jumps were simulated by the

model and the computed water surface profiles were compared with those obtained from a $k-\varepsilon$ model.

Recently, some detailed investigations of turbulence modelling of wall-bounded flows using SPH were made by Mayrhofer et al. (2013, 2015). Mayrhofer et al. (2013) treated the noises coming from the SPH discretization by introducing an additional volume diffusion term into the equation of continuity. This term was estimated using an eddy-viscosity model with the mixing-length approach. More recently, Mayrhofer et al. (2015) developed DNS as well as LES of 3D wall-bounded turbulent channel flows based on the SPH method and revealed interesting findings. They firstly performed a 3D quasi-DNS where good match was achieved with the reference data except for some near-wall oscillations. Then a LES of a free surface channel flow with friction Re Number (Re_τ) of 1000 was carried out with the unified semi-analytical wall boundary condition and an eddy-viscosity model with the Smagorinsky constant C_s = 0.065. In contrast to the DNS, the LES result was poor with regard to the streamwise velocity and fluctuations. They attributed the failure to the SPH collocated discretization effect on the velocity-pressure interactions and concluded that LES of free surface channel flows with SPH is still impossible due the problems inherent in the standard SPH discretisation. It is notable that to reproduce the shear boundary layer near the wall in their LES, Mayrhofer et al. (2015) employed a wall function based on Reichardt's law. However, no information was provided regarding the characteristics of the wall boundary such as the surface roughness.

Another SPH turbulence model that should be mentioned here is the model proposed by Monaghan (2011) which was based on a Lagrangian scheme similar to that used for the Lagrangian averaged N–S (LANS) turbulence model, but with a different smoothed velocity. This model was later used to simulate 2D turbulence driven by a moving cylinder by Monaghan (2017).

2.3.2 Treatment of rough bed boundary in particle models

In simulating turbulent open channel flows, an adequate treatment of the bed boundary is as important as the inclusion of an appropriate turbulence model. However, the effect of bed roughness has not been taken into consideration in most of the developed particle models. In the studies of Sahebari et al. (2011), Shakibaeinia and Jin (2011), Federico et al. (2012) and De Padova et al. (2013), the treatment of the channel bed has not been explicitly included in their models. On the other hand, in some other MPS and SPH studies, this issue has just been tentatively addressed. Violeau et al. (2002) and Violeau and Issa (2007) impose logarithmic velocity distributions near the wall by applying wall functions. Lopez et al. (2010) employed Lennard-Jones repulsive forces to prevent the fluid particles from penetrating into the wall and this produced a numerical resistance representing the roughness effect. Chern and Syamsuri (2013) defined smooth, triangular, trapezoidal and sinusoidal bed boundaries by lines of particles to simulate the effect of corrugated bed on the characteristics of hydraulic jumps. They used a repulsive force similar to Lopez et al. (2010) in that the wall particles exert a force on the fluid particles to represent the resistance of the rough bed. In the study of Fu and Jin (2013), several layers of ghost particles were set beyond the boundary line and artificial velocities were assigned to those particles in the opposite direction of the flow to account for the bed roughness in their MPS model. The model presented a simple method to reflect the roughness effect by imposing a numerical adjustment of velocity at the bed, but this was not based on sound physical understanding.

2.3.3 Flow interaction with porous media by SPH

A small number of studies have been devoted to the application of SPH in simulating flow interaction with porous media. Here, some of them which are mostly developed in the area of coastal engineering are reviewed.

Shao (2010) developed an Incompressible SPH (ISPH) model following the macroscopic equations presented in Huang et al. (2003) for wave interactions with porous media. He separated the computational domain into porous and free flow regions and imposed the matching conditions (proposed by Huang et al. 2003) of velocity and normal and tangential stresses at the interface boundary line. This method is difficult to use (Gui et al. 2015) and not physically sound. Furthermore, the turbulence effect as well as the effect of the volume occupied by the solid particles was disregarded in the governing equations. In other words, only two extra resistance terms were added to the N-S equation where the laminar and turbulent resistance coefficients were in the same form as that proposed by Sollit and Cross (1972) and to determine the permeability and nonlinear resistance coefficient, empirical formulas were used following Huang et al. (2008).

In their ISPH model for simulating fluid flow through porous media, Akbari and Namin (2013) used the local VANS equations proposed by Vafai and Tien (1981) with considering inertia coefficient C_r as presented by Sakakiyama and Kajima (1992) and van Gent (1995). In contrast to Shao (2010), they solved a unified set of governing equations at a single computational domain by introducing a transitional layer at the interface where a gradual porosity was imposed. This process was applied using a background mesh where the porosity at the position of SPH particles was calculated by averaging the reference porosity of the neighbouring mesh points over an interpolating area using the SPH interpolation method. The interpolation was performed by using a smoothing length h_{Υ} in the range of the mean porous grain diameter. Therefore, the thickness of the transitional layer over which porosity is variable was 4 times the solid particle diameter. The model was tested by solving 3 cases of wave interaction with porous structures where the results of water surface elevation were compared to the experimental data. The effect of turbulence was ignored; no presentation/validation was performed with regard to the velocity distribution; and no investigation was carried out on the behaviour of flow quantities at the interface.

Gui et al. (2015) applied the transitional layer approach of Akbari and Namin (2013) in order to improve the model of Shao (2010). However, their model still had the same limitations as in Shao (2010). Neither Akbari and Namin (2013) nor Gui et al. (2015) incorporated turbulence closures in their models. Akbari (2014) modified the model of Akbari and Namin (2013) by applying the standard SPS turbulence model (with $C_s = 0.1$) into their ISPH model for simulating wave interaction with multi-layered porous structures. The estimated water surface profiles were presented in comparison with the experimental data, while no validation was considered for the velocity and turbulent quantities.

To simulate wave interaction with porous structures, Ren et al. (2014) employed the spatially averaged N-S equations as in Liu et al. (1999) except that the porous resistance terms were of the form proposed by Sollitt and Cross (1972). They applied a transitional layer at the interfacial boundary between free flow and porous media which was divided into two equal parts by a boundary line, i.e. the fluid part and the porous part. Then at each time step, in each part of the transitional layer, the velocity was calculated using only neighbouring particles of the same type, ignoring the particles of the other type. Finally, the calculated velocity was interpolated over a kernel area for each particle using all its neighbouring particles. The SPS model with $C_s = 0.1$ was applied for turbulence only in the free flow region, while the effect of turbulence in the porous region was ignored. In spite of the enforcement of continuity of the velocity across the transitional layer by the velocity interpolation treatment, a large discontinuity was observed in the turbulent quantities at the interface. Besides, the thickness of the transitional layer was set to one smoothing length, i.e. it was related only to the computational resolution rather than the conditions of flow or porous media skeleton near the interface. Two test cases of interaction of water waves with porous structures were simulated and water surface profiles were validated by experimental data. Some preliminary results of pressure distribution, velocity vectors and flow vorticity were presented with no further validation.

Afterwards, Ren et al. (2016) used the Volume-Averaged and Favre-Averaged N-S (VAFANS) equations along with the SPS turbulence closure model (with $C_s = 0.1$) to describe the flow both inside and outside the porous media. The empirical coefficients for the drag terms were determined through Du Plessis (1994) equation. Regarding the interfacial boundary treatment, they applied a transitional interface layer similar to Akbari and Namin (2013) with the difference that the thickness of the layer was set to the mean diameter of the porous solid particles. Two test cases of wave interaction with porous media were simulated and the water surface elevation was compared to the experimental data. Some preliminary results of velocity vectors and turbulent eddy-viscosity were presented with no experimental validation. The change of flow quantities at the interface was not investigated too.

In their recent studies, Pahar and Dhar (2016, 2017a and 2017b) developed ISPH and MPS models to simulate interaction of flow with porous media. Porous media interface conditions were implicitly implemented by using discharge (Darcy) velocity in the governing equations and introducing porosity into Pressure Poisson Equation. They successfully simulated sevral hydraulic cases and validated their model with regards to free surface profiles of dame break flow through a porous dam. No validation on velocity and turbulence fields was presented and some artificial treatments were introduced e.g. no turbulence effect was computed inside the porous media and therefore the viscosity of the pure fluid region and effective viscosity of porous media was simply averaged to diminish the discontinuity of viscosity at the interfacial boundary (Pahar and Dhar 2016); and non-constant smoothing length (which represents the spatial averaging support size) was used due to the change of porosity (Pahar and Dhar 2017b).

2.4 Summary

In this chapter, a review was completed on the numerical modelling of turbulent open channel flows with focus on the turbulence modelling and the treatment of rough

impermeable and porous bed boundaries. In Section 2.1, the background of turbulence in open channel flows was briefly discussed and then in Sections 2.1.1 and 2.1.2, two types of turbulence models (RANS and LES, respectively) were investigated following a review on some grid-based numerical models in each section. Bed boundary treatments in open channel flows was discussed in Section 2.2, where background on flow over rough impermeable and porous beds was presented respectively in Sections 2.2.1 and 2.2.2 following review of some grid-based models. Finally, in Section 2.3, the SPH method was introduced and a review was carried out in Sections 2.3.1, 2.3.2, and 2.3.3, respectively, on the turbulence modelling, treatment of rough impermeable boundaries, and flow interaction with porous media using particles methods.

2.4.1 Required improvements for the turbulence modelling

In some of the existing SPH models developed for open channel flows, the effect of turbulence was disregarded and in some of them it was incorporated into the momentum equation by the SPS model with the standard Smagorinsky coefficient. Unfortunately, in most of the studies, no detailed results of turbulent quantities were presented. Only, in the study of Mayrhofer et al. (2015), the application of SPS for LES of turbulent channel flows was investigated in detail with some results of velocity fluctuations being provided. They discussed that a reduced momentum transfer was simulated due to the incorrect reproduction of velocity-pressure interactions inherent in the standard SPH discretization. This issue should be more serious when the bed is rough. In such a case, either the roughness layer is modelled using wall functions or as a macroscopic boundary layer using drag models, the near-boundary dispersion which is a result of flow blockage by solid elements, is disregarded. In order to provide an accurate representation of the complex processes occur near a rough/porous bed, a microscopic representation of flow (with DNS) is ideal in order to resolve all scales of flow. However, due to the limitation regarding the computational costs, LES is usually used with a macroscopic representation of rough/porous layer. In this case, it

is essential to improve the existing turbulence modelling approach to accurately reproduce the balance in the flow momentum with regard to the turbulent effects, especially in the present highly-sheared flow problems.

Although the standard SPS-Smagorinsky model has been widely applied with the SPH method in simulating various engineering problems such as those in coastal engineering or hydraulics, in the present work it will be shown that this model provides poor results in 2D macroscopic LES of fully-turbulent channel flows over rough beds. Accordingly, it will be modified as to correctly estimate the transfer of momentum throughout the flow depth (Chapter 3).

2.4.2 Required improvements for the treatment of the rough impermeable bed

As reviewed in Section 2.3.2, in most of mesh-free particle models developed for open channel flows, the effect of bed roughness has not been explicitly taken into account or has been modelled based on numerical adjustments. Bed boundary is usually the main source of turbulence production in open channel flows. The roughness reduces velocity near the bed; velocity gradient increases accordingly; and the turbulent shear stress transfer this effect to the upper flow layers. According to the review in Section 2.2.1, the drag force method coupled with a suitable turbulence model has been shown to be an appropriate way of modelling the roughness effect in grid-based methods for impermeable rough boundaries (Wiberg and Smith 1991, Nicholas 2005, Zeng and Li 2012). Therefore, a similar technique will be applied in Chapter 3 with SPH in macroscopic modelling of roughness effect in turbulent open channel flows over impermeable rough beds.

2.4.3 Required improvements for the treatment of the porous bed

SPH has shown promising capacity in macroscopically dealing with flow interaction with porous media. However, the SPH models developed in this area have had some

limitations. According to the review in Section 2.3.3, these limitations can be considered as follows: i) In most of those studies, the interface boundary layer has been simulated based on numerical calibrations rather than rigorous mathematical justifications (e.g. Ren et al. 2014, and Pahar and Dhar 2016); and no investigation has been performed on the behaviour of flow quantities at this layer (e.g. Akbari and Namin 2013, and Ren et al. 2016); ii) The turbulence effect is disregarded, or included by the SPS model with no further validation (e.g. Shao 2010, Akbari and Namin 2013, and Gui et al. 2015); and iii) Most of the existing SPH studies are in the area of coastal engineering (wave interaction with porous structures), mostly providing the results of water surface elevation, while there have been no application in turbulent open channel flows over/within porous beds, especially for the situation of high velocity gradients at the interface. Being motivated by these points, in the present work, firstly the macroscopic governing equations for flow interaction with porous media will be developed based on the principles of the SPH method in order to find the limitations and constraints, illuminate the range of applicability of the equations, and provide effective solutions for practical situations (Chapter 4). Then, the developed model will be tested by different applications with regard to the estimated water surface profiles and velocity distributions (Chapter 5), and more importantly, it will be applied for simulation of highly-sheared free surface channel flows over and within natural porous beds and validated by experimental data (Chapter 6).

Chapter 3 Modelling Turbulent Open Channel Flow over Rough Impermeable Beds

In many cases of turbulent river flows, the channel bed could be considered as an impermeable boundary. Examples of this situation are when the bed is naturally impermeable, or the flow inside the bed is weak and there is no (or a very small) flow penetration into the bed (highly consolidated sediment and a rock bed channel). In these cases, an appropriate boundary condition could represent the complicated processes occur at the bed. However, the frictional effect of the bed as well as the turbulence behaviour should be addressed adequately, particularly when the bed is rough.

In this chapter, a 2D SPH model will be developed for simulating turbulent open channel flow over rough beds. The model will be tested based on a set of experimental data of turbulent flow over a sloping bed consisting of a thin layer of spherical particles placed on an impermeable channel bed. In Sections 3.1, 3.2 and 3.3, respectively, the mathematical development, applications, and some concluding remarks will be provided.

3.1 Numerical modelling scheme

The physical problem under consideration is turbulent open channel flow over rough bed boundaries. Steady uniform flow is considered, and the bed roughness elements are assumed to be uniformly distributed. Conservation equations of mass and

momentum are considered as the governing equations. The numerical solution scheme is based on LES for taking the effect of turbulence into account; and is developed at the macroscopic scale in dealing with the bed roughness effect. The WCSPH method is used to discretise and solve the equations in 2D. In the following sections, governing equations, discretisation of the equations by WCSPH method, time implementation scheme, and boundary conditions of the problem are presented.

3.1.1 Governing equations

The governing equations for the present problem are the spatially averaged equations of continuity and momentum in 2D in their Lagrangian form. Two closure terms are added to the momentum equation representing the effects of turbulence and form-drag induced stresses on the average flow field.

$$\frac{D\rho}{Dt} = -\rho \nabla \cdot \mathbf{u} \tag{3.1}$$

$$\frac{D\mathbf{u}}{Dt} = -\frac{1}{\rho}\nabla P + \mathbf{g} + \nu_0 \nabla^2 \mathbf{u} + \frac{1}{\rho}\nabla \cdot \boldsymbol{\tau}_e + \frac{1}{\rho}\boldsymbol{\tau}_d \tag{3.2}$$

where $\mathbf{u}$ is average flow velocity; ρ is fluid density; P is average pressure; $\mathbf{g}$ is the gravitational acceleration; ν_0 is the kinematic viscosity coefficient; t is time; $\boldsymbol{\tau}_e$ is the unresolved part of turbulent shear stress that should be modelled; and $\boldsymbol{\tau}_d$ is form drag-induced shear stress which is imposed only on the particles in the roughness layer near the bed. The last two terms are approximated by the following closure models.

3.1.1.1 Drag closure

The ideal way of simulating flow over a rough surface is to use DNS with very high computational resolution in order to both resolve all turbulent eddies as well as the geometry of the rough bed as solid boundaries. However, DNS is not practical due to

its high cost of computation. Therefore, the LES is used for turbulence together with a macroscopic representation of flow in the roughness layer near the bed. For this purpose, the form drag-induced shear stress term $\boldsymbol{\tau}_d / \rho$ is added to the momentum Equation (3.2) for the fluid particles locating in the roughness layer. The determination of the roughness layer will be discussed in Section 3.1.4.2. $\boldsymbol{\tau}_d$ is calculated by

$$\boldsymbol{\tau}_d = \frac{\mathbf{F}_d}{A_\tau} \tag{3.3}$$

where

$$\mathbf{F}_d = -\frac{1}{2} C_d W_d \rho A_d \mathbf{u} |\mathbf{u}| \tag{3.4}$$

is the drag force exerted on a fluid particle from the rough bed and A_τ is the bed-parallel, planar area affected by the fluid particle. In Equation (3.4), A_d is the cross-sectional area, C_d is the drag coefficient and W_d is a shape function representing the effect of geometry of the bed roughness which is a non-dimensional quantity holding values between 0 and 1. In fact, it brings the effect of solid material density into the equation. The quantifications of these parameters will be presented in Section 3.1.4.2.

3.1.1.2 Turbulence closure

As mentioned above, LES is considered in this study for dealing with the effect of turbulence on the average flow field. In LES, the eddies larger than the computational discretisation size are resolved while the effect of the smaller ones is modelled. In other words, a part of turbulence is resolved by the numerical discretisation while the missing part is estimated by an appropriate closure model and incorporated to the momentum equation. Hence, the total turbulent shear stress ($\boldsymbol{\tau}_t$) can be defined as the sum of the resolved ($\boldsymbol{\tau}_r$) and unresolved ($\boldsymbol{\tau}_e$) parts, as the following.

$$\boldsymbol{\tau}_t = \boldsymbol{\tau}_r + \boldsymbol{\tau}_e \tag{3.5}$$

The SPS model proposed by Gotoh et al. (2001) is usually used with SPH for estimating $\boldsymbol{\tau}_e$. It is the particle version of the LES-SGS-Smagorinsky model introduced in Section 2.1.2. Equation (2.14) is applied to calculate $\boldsymbol{\tau}_e$ from the average flow field where τ_{ij} is the component of the modelled shear stress tensor, and ν_t is estimated by Equation (2.17). In the present simulations, the SPS model of Gotoh et al. (2001) is employed but with a modification in the estimation of the eddy-viscosity ν_t.

Although, Equation (2.17) has been widely used with SPH in coastal engineering applications for estimating the turbulent eddy-viscosity, its applicability in open channel flows with SPH has not been investigated comprehensively, except in the study of Mayrhofer et al. (2015) where a semi-DNS as well as a LES of turbulent open channel flow were investigated. The LES was based on the SPS-Smagorinsky model with $C_s = 0.065$ which failed to reproduce the correct turbulent statistics. They attributed the failure to the velocity-pressure interactions of vortices which is inherent in the standard SPH discretization; and concluded that 'should the pressure gradient not be calculated sufficiently accurately, then a reduced momentum transfer takes place'.

This issue could be even more serious in the present study where the flow dispersion at the bed is ignored due to the macroscopic modelling of the roughness layer. In other words, the Standard Smagorinnsky model may not perform well for 'highly rough surfaces' as it has not been designed for such condition. It is assumed that due to the macroscopic modelling of the roughness layer near the bed, no particle-scale vortices (or very weak ones) will be produced in the 'average flow field' as the bed elements (spheres here) do not exist in the model. Observations show that in the absence of the geometry of the roughness elements as solid boundaries, fluid particles move in nearly strainght lines. Therefore, it is assumed that the part of flow turbulence resolved by the particle motion ($\boldsymbol{\tau}_r$) is negligible compared to the unresolved part, i.e. $\boldsymbol{\tau}_r << \boldsymbol{\tau}_e$. It means,

$$\boldsymbol{\tau}_t \approx \boldsymbol{\tau}_e \equiv \boldsymbol{\tau}_l \tag{3.6}$$

where $\boldsymbol{\tau}_l$ is the turbulent shear stress that should be modelled/estimated. This assumption will be tested in Section 3.2.6.

According to Equation (3.6), the total effect of flow turbulence should be modelled, similar to the RANS modelling. Therefore, instead of using the standard Smagorinsky model with a C_s being around 0.15, the application of a standard mixing-length model is explored here to estimate the turbulent eddy-viscosity in the present SPH scheme. Accordingly, the eddy-viscosity is written as the following.

$$\nu_t = l_m{}^2 \left|\mathrm{S}\right| \tag{3.7}$$

To estimate the mixing-length, Nezu and Rodi (1986) formula (Equation 2.9) is employed with the values of 0.41, zero, and 1.0 for κ, Π and F respectively, so that this equation is simplified to the following equation for estimating the mixing-length. This relationship was also used by Violeau and Issa (2007) in simulating turbulent open channel flows using the SPH method.

$$l_m = \kappa z_w \sqrt{1 - z_w / H} \tag{3.8}$$

It is notable that turbulence is 3D in nature. However, in the present study, uniform flows are simulated where the flow is dominated mainly by the streamwise shear stress and vertical momentum exchange. In other words, the influence of flow in the lateral direction is much smaller than the streamwise flow so that it is reasonable for it to be neglected in the present simulations. Generally speaking, in 2D uniform open channel flows where the macroscopic flow is dominant only in the streamwise direction, the local strain rate $\left|\mathbf{S}\right|$ is approximately equivalent to $\partial u/\partial z$ as other velocity gradients such as $\partial u/\partial x$, $\partial w/\partial x$ and $\partial w/\partial z$ are significantly smaller. x and z denote the streamwise and vertical coordinates respectively; and u and w are the streamwise and vertical velocity components, respectively. In such a case, Equation (3.7) would be equivalent to Equation (2.5) (Prandtl's theory).

3.1.2 Discretization of the equations by SPH

The WCSPH method is applied to discretise the governing equations. Making use of Equations (2.27) and (2.28), the governing equations (3.1) and (3.2) are discretized as follows.

$$\frac{D\rho_a}{Dt} = \rho_a \sum_b \frac{m_b}{\rho_b} \mathbf{u}_{ab} \cdot \nabla_a W_{ab} \tag{3.9}$$

$$\begin{aligned} \frac{D\mathbf{u}_a}{Dt} = &-\sum_b m_b \left(\frac{P_a}{\rho_a{}^2} + \frac{P_b}{\rho_b{}^2} \right) \nabla_a W_{ab} + \mathbf{g} + \sum_b m_b \frac{4\nu_0}{(\rho_a + \rho_b)} \frac{\mathbf{r}_{ab} \cdot \nabla_a W_{ab}}{|\mathbf{r}_{ab}|^2 + \eta^2} \mathbf{u}_{ab} \\ &+ \sum_b m_b \left(\frac{\boldsymbol{\tau}_{la}}{\rho_a{}^2} + \frac{\boldsymbol{\tau}_{lb}}{\rho_b{}^2} \right) \cdot \nabla_a W_{ab} + \frac{1}{\rho_a} (\boldsymbol{\tau}_d)_a \end{aligned} \tag{3.10}$$

where $\mathbf{u}_{ab} = \mathbf{u}_a - \mathbf{u}_b$; $\mathbf{r}_{ab} = \mathbf{r}_a - \mathbf{r}_b$; $\nabla_a W_{ab}$ is the gradient of the kernel function between particles a and b with respect to the position of particle a; and η is a small number (here, $0.1h_{\Upsilon}$) used to prevent singularity. Meanwhile, $\boldsymbol{\tau}_l$ and $\boldsymbol{\tau}_d$ are the MSPH-ML and form-drag induced shear stresses estimated by the approaches introduced in Sections 3.1.1.1 and 3.1.1.2, respectively. In the WCSPH method, the following equation of state is employed to explicitly calculate particle pressure from the change in its density.

$$P = c_0{}^2 (\rho - \rho_0) \tag{3.11}$$

where c_0 is the speed of sound and ρ_0 is the reference density. The assumption is that the flow is compressible in order to be able to use the equation of state for pressure, but the compressibility is restricted to 1%. For this purpose, c_0 is usually set to about 10 times of the velocity of the bulk flow. Meanwhile, a Shepherd density filter is applied at every 30 computational time steps to minimise numerical noise in the pressure field.

3.1.3 Time implementation

To solve the equations in time, the predictor-corrector scheme (Monaghan, 1989) is applied. In this method, firstly density, velocity and position of particles are predicted at a mid-time step ($t+\Delta t/2$) using the values at time (t) as the following.

$$\begin{aligned}\rho^{(t+\Delta t/2)} &= \rho^{(t)} + \frac{\Delta t}{2} D_{mass}^{(t)} \\ u^{(t+\Delta t/2)} &= u^{(t)} + \frac{\Delta t}{2} D_{moment}^{(t)} \\ r^{(t+\Delta t/2)} &= r^{(t)} + \frac{\Delta t}{2} u^{(t)}\end{aligned} \tag{3.12}$$

where Δt is the time increment size; $\rho^{(t)}$, $u^{(t)}$ and $r^{(t)}$ are density and components of velocity and position vectors, respectively, at time *t*; $\rho^{(t+\Delta t/2)}$, $u^{(t+\Delta t/2)}$ and $r^{(t+\Delta t/2)}$ are those quantities at mid-time step; and $D_{mass}^{(t)}$ and $D_{moment}^{(t)}$ are the right-hand side of continuity and momentum equations (Equations 3.9 and 3.10, respectively). Then, particle pressure at the mid-time is calculated based on $\rho^{(t+\Delta t/2)}$ using Equation (3.11).

In the correction step, the quantities are updated as follows.

$$\begin{aligned}\rho^{(t+\Delta t/2)} &= \rho^{(t)} + \frac{\Delta t}{2} D_{mass}^{(t+\Delta t/2)} \\ u^{(t+\Delta t/2)} &= u^{(t)} + \frac{\Delta t}{2} D_{moment}^{(t+\Delta t/2)} \\ r^{(t+\Delta t/2)} &= r^{(t)} + \frac{\Delta t}{2} u^{(t+\Delta t/2)}\end{aligned} \tag{3.13}$$

where $D_{mass}^{(t+\Delta t/2)}$ and $D_{moment}^{(t+\Delta t/2)}$ denote the right-hand side of the equations of mass and momentum, respectively, at the mid-time $t+\Delta t/2$. Finally, the quantities at time $t+\Delta t$ are calculated as the following.

$$\begin{aligned}\rho^{(t+\Delta t)} &= 2\rho^{(t+\Delta t/2)} - \rho^{(t)} \\ u^{(t+\Delta t)} &= 2u^{(t+\Delta t/2)} - u^{(t)} \\ r^{(t+\Delta t)} &= 2r^{(t+\Delta t/2)} - r^{(t)}\end{aligned} \tag{3.14}$$

Besides, pressure at time $t+\Delta t$ is calculated by the equation of state (3.11).

The size of computational time step is selected according to the Courant–Friedrichs–Lewy (CFL) condition corresponding to a CFL number of 0.15 as the following.

$$\Delta t \le 0.15\frac{h_{\Upsilon}}{c_0} \tag{3.15}$$

Furthermore, a Link List technique is applied for efficient searching over particles in order to optimize the numerical scheme in terms of CPU time.

3.1.4 Computational domain and boundary conditions

The 2D computational domain with the boundaries of free surface, rough bed and inflow/outflow is shown in Figure 3-1 and the discretised computational domain is depicted in Figure 3-2. In WCSPH method, the free surface boundary is tracked with no special treatment. The treatment of the two other boundary conditions are presented in the following Sections 3.1.4.1 and 3.1.4.2, while more details on the computational domain and its discretisation are presented in Section 3.2.1.

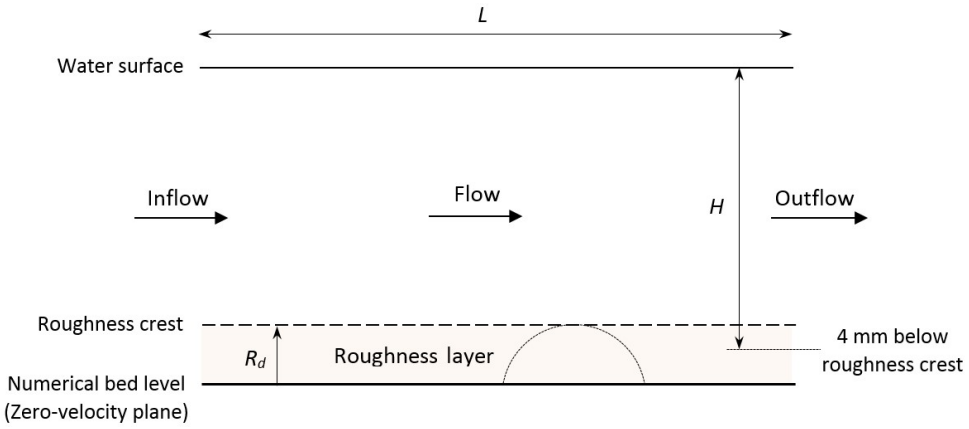

Figure 3-1 2D computational domain and boundaries.

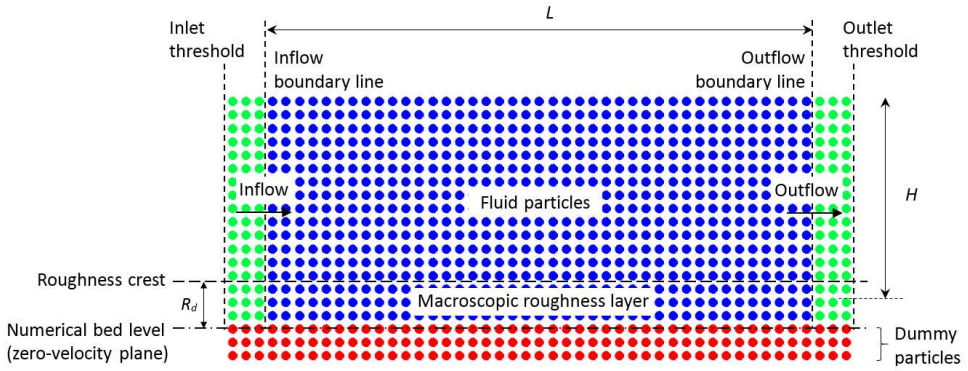

Figure 3-2 Discretised computational domain and boundary conditions.

3.1.4.1 Inflow and outflow boundaries

Some recent works on the modelling of inflow/outflow boundary conditions in SPH include Federico et al. (2012), Aristodemo et al. (2015), and Tan et al. (2015), where various open channel flow cases were simulated over smooth beds. In the present work, a similar approach has been introduced with modifications on the determination of flow quantities at these boundaries. In contrast to the former studies where a prescribed fixed velocity distribution (such as an analytical profile) were used at the inlet, in the present simulations velocity of inflow/outflow particles are determined based on the velocity of fluid particles inside the domain so that the flow is evolved naturally and the desired uniform steady condition is obtained without any prescription at the boundaries. The proposed technique is suitable for problems in which velocity distributions at the inlet and outlet are unknown and/or applying a certain velocity at the inlet to reproduce a certain discharge needs a long distance to get uniform. In other words, uniform condition can be achieved in a quite short distance.

The following equation mathematically represents the conditions which should be satisfied at the inflow/outflow boundaries, i.e. the gradients of velocity and pressure in the streamwise direction x should be zero at the boundary line in order to achieve the uniform flow condition within the domain.

$$\frac{\partial u}{\partial x} = 0, \qquad \frac{\partial P}{\partial x} = 0. \tag{3.16}$$

Firstly, as seen in Figure 3-2, several layers of particles (green) are located beyond the inflow/outflow boundary lines to cover the truncated kernel area of the inner-fluid particles (blue) near the boundary. The governing equations (3.9) and (3.10) are not solved at these particles, but their properties (e.g. velocity and density) are determined through an averaging process as follows. An averaging node is defined for each inflow particle at the same elevation *z* but inside the fluid domain, with a distance of $0.5l_0$ from the boundary line as shown in Figure 3-3 (a), where l_0 is the SPH initial particle spacing. Then velocity and density of the fluid particles are averaged at that node using a kernel function over an averaging area (Figure 3-3 b) and set as the velocity and density of the corresponding inflow particle. Therefore, the gradient of velocity and density at the boundary line becomes zero so that the zero-pressure gradient is also satisfied according to Equation (3.11). When an inflow particle passes the boundary line and enters the inner-fluid area, it switches into a fluid particle (blue particle) and the governing equations are solved at it in the next time step. At the same time, an inflow particle is generated with the same quantities at the inlet threshold at the same elevation (Figure 3-3 a). Through this process, the inflow region bounded by the inlet threshold and inflow boundary line (Figure 3-3 a) acts as a particle generator with uniform flow condition. In the present simulations, the same kernel function and smoothing length of the fluid particles are used for the averaging process at the nodes. The novelty of the proposed inflow boundary treatment is that the uniform flow is evolved based on the flow condition inside the domain where the equations are solved, i.e. based on the conditions of the channel (such as slope and frictional effects of the bed), so the model can be applied to a wider range of hydraulic applications in which the inflow information is unknown.

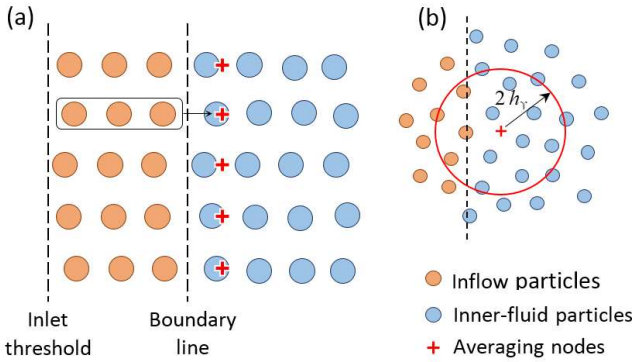

Figure 3-3 Inflow boundary treatment.

Uniform conditions should also be preserved at the outflow boundary in order to keep the uniformity of the flow in the channel. Hence, the same technique applied at the inflow could also be used for the outflow region. However, a slightly different treatment is employed at the outflow to decrease the computational time. When the fluid particle passes the outflow boundary line it changes into an outflow particle and the governing equations are not solved on the particle anymore, but its properties are kept unchanged while it moves through the outflow region. This treatment is similar to the technique proposed by Federico et al. (2012), in which the properties of outflow particles are 'frozen'. Finally, the outflow particles which pass the outlet threshold are removed from the computational domain (See Figure 3-2).

3.1.4.2 Treatment of rough bed boundary

The effect of bed roughness on the flow is modelled macroscopically by defining a layer near the bed over which a drag force is applied on fluid particles. The extent of this layer as well as the drag force should be determined. In the present simulations, the upper extent of the macroscopic roughness layer is taken to be the crest of roughness elements and the lower bound is defined at zero-velocity plane which is at a certain distance below the roughness crest (see Figure 3-1). A solid wall (also called numerical bed level in Figure 3-2) is set at the zero-velocity plane and the drag-induced stress term $\boldsymbol{\tau}_d / \rho$ is computed only for the fluid particles located between

the numerical bed level and the roughness crest, i.e. within the macroscopic roughness layer (Figure 3-2). The distance between these two levels is named thickness of roughness layer or effective roughness height (R_d). It is assumed that R_d is variable for different flow conditions based on the assumption that the effect of bed roughness on the flow field differs for different flow conditions.

At the numerical bed level, several layers of dummy particles (red particles in Figure 3-2) are placed in order to address the truncated kernel of the fluid particles near the boundary. The velocity of the dummy particles are not determined through the solution of the momentum equation, i.e. they are fixed in space, but they hold enough pressure to avoid fluid particles penetrating into the boundary. Note that the numerical bed level corresponds to the upper layer of dummy particles as depicted in Figure 3-2. The pressures of dummy particles are determined by equation of state (3.11) after their density variations are computed through the solution of the continuity equation (3.9). Hence, adequate pressure is applied on the dummy particles to prevent the fluid particles penetrating the wall boundary.

Determination of drag force at the bed is depicted in Figure 3-4 where a section normal to the streamwise direction is considered. As seen, the roughness layer is from the crest of spheres to the numerical bed level. It is assumed that when a fluid particle a is located within the macroscopic roughness layer, it experiences a drag-induced shear stress from the roughness element. In fact, the drag force is exerted on a fluid fragment with width d_s and height l_0 (*ABCD* in Figure 3-4), where d_s is the diameter of the sphere and l_0 is the SPH particle spacing. Therefore, the cross-sectional area A_d and the bed-parallel planar area A_τ are assumed to be equal to the particle size l_0 and $d_s l_0$, respectively. Besides, W_d is a function (called shape function here) defined by the following equation as the area of that part of the water fragment located within the sphere ($A'B'C'D'$ in Figure 3-4) divided by the total area of the fragment (*ABCD* = $d_s l_0$). This function accounts for the shape (density) of the roughness elements which are spheres in the present study.

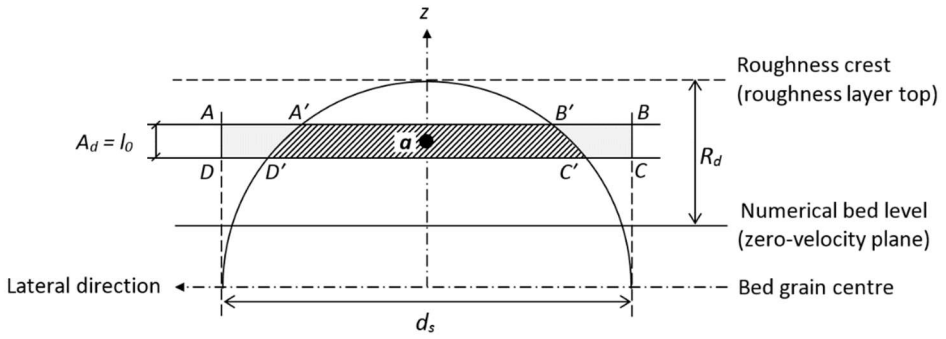

Figure 3-4 Bed drag model.

$$W_d = \frac{A_{A'B'C'D'}}{A_{ABCD}} \tag{3.17}$$

For the drag coefficient C_d in Equation (3.4), the value of 1.0 is taken. This value is chosen following the original work of Gotoh and Sakai (1999) where values between 1.0 and 1.5 were introduced for particle modelling of porous flows using the MPS method. Schmeeckle et al. (2007) found the value of 0.76 for the drag coefficient in the experiments of turbulent open channel flow over fixed spheres. They also measured the drag force in turbulent flows over cubes and natural particles and found that the drag coefficient was significantly higher than that used to model the bed load motion. Considering the product of $C_d W_d$ as the total drag coefficient in the proposed drag force model (Equation 3.4), and assuming half of the bed grain to be the thickness of the roughness layer (i.e. $R_d = 0.5 d_s$) and C_d = 1.0, the average value of $C_d W_d$ for the particles inside the roughness layer would be equal to 0.785, which is close to the value found by Schmeeckle et al. (2007) for spherical particles. It is noted that the roughness effect is modelled at a macroscopic scale, i.e. the surface of spheres shown in Figure 3-4 are not modelled as rigid boundaries in the numerical simulations. Fluid particles can penetrate inside the roughness layer but feel its influence.

3.2 Model applications and results analysis

3.2.1 Model setup and calibration

Uniform turbulent open channel flows over a sloping rough bed are simulated by a 2D WCSPH model and accuracy of the model is validated by an existing set of experimental data measured by Particle Image Velocimetry (PIV) in a laboratory flume (Nichols, 2013). The flume bed consists of uniform sized spheres packed in a hexagonal pattern with a diameter d_s of 24 mm.

The computational domain is a rectangular with a length of $L = 4H$, where H is the water depth. To address the effect of bed roughness and to assess the accuracy of the drag force model, 12 test cases with 3 different bed slopes (0.002, 0.003 and 0.004) and various water depths ranging from 40 to 100 mm are simulated. The choice of different water depths and bed slopes for simulations is based on the fact that the effect of bottom roughness on the flow depends not only on the absolute roughness size but also on the flow conditions. Details of the test cases are summarised in Table 3-1. According to the table, Fr Number is below 1.0 for all the 12 test cases. It means all of them are in the sub-critical flow condition. Besides, the particle spacing is set to l_0 = 2 mm to ensure that there are at least 20 layers of particles in the depth-wise direction for the shallowest test case (i.e. H = 40 mm). The smoothing length h_Υ is set to $1.2 l_0$ since this value has been widely employed in many SPH simulations. Besides, the cubic spline kernel function (Monaghan and Lattanzio, 1985) is chosen for the simulations (see Equation 5.4). Three layers of fixed dummy particles are used for the bottom wall and three layers of moving particles are used for the inflow as well as outflow regions to satisfy the full kernel area of the inner-fluid particles near the boundary lines (Figure 3-2). The number of layers of particles at the boundaries depends on the support of the kernel function $2h_\Upsilon$ (Figure 2-1). Since in the present

study h_{Υ} is set to 1.2 l_0 , support of the kernel function is equal to 2.4 l_0 . Accordingly, three layers of particles are used at the inflow, outflow, and bottom wall boundaries.

Table 3-1 The test cases and associated computational parameters (the first four letters in the test ID denote the bed slope and the last three letters denote the water depth).

Test No.	Test ID	S_0	H (m)	u^* (m/s)	Fr	Re	Calibration / Validation
1	S004H40	0.004	40	0.0396	0.433	10843	'C'
2	S004H50	0.004	50	0.0443	0.430	15067	'V'
3	S004H70	0.004	70	0.0524	0.564	32703	'V'
4	S004H90	0.004	90	0.0594	0.559	47301	'V'
5	S004H100	0.004	100	0.0626	0.603	59698	'C'
6	S003H50	0.003	50	0.0384	0.332	11615	'C'
7	S003H60	0.003	60	0.0420	0.424	19516	'V'
8	S003H70	0.003	70	0.0454	0.481	27926	'C'
9	S003H80	0.003	80	0.0485	0.453	32089	'V'
10	S002H60	0.002	60	0.0343	0.261	12022	'C'
11	S002H70	0.002	70	0.0371	0.339	19671	'V'
12	S002H80	0.002	80	0.0396	0.435	30794	'C'

To restrict the compressibility of flow, the speed of sound c_0 is usually chosen to be at least 10 times the maximum flow velocity (Monaghan 2005). In the present simulations, c_0 is set equal to 16 m/s for all test cases. The highest velocity in the present experiments is about 0.7 m/s (the maximum velocity in test case S004H100). Therefore, the local density fluctuation (compressibility) will be less than about 0.2% in all simulations according to Equation (10.2) of Monaghan (2005). Besides, ρ_0 is taken as 1000 kg/m^2 which is the density of water.

As mentioned in the previous section, the thickness of the roughness layer (R_d) is assumed to be variable. This parameter varies depending on the flow conditions thus

needs calibration. Hence, six of the test cases (S004H40, S004H100, S003H50, S003H70, S002H60 and S002H80) are used for model calibration in terms of R_d and the other six cases (i.e. S004H50, S004H70, S004H90, S003H60, S003H80 and S002H70) are employed for model validation. The calibration tests are selected to cover at least 2 cases of each bed slope and most of the depths range from 40 to 100 mm. Calibration and validation tests are indicated by letters 'C' and 'V' respectively, in Table 3-1.

The calibration process is as follows. Firstly, for each calibration test case, several R_d values are applied and the Mean Absolute Error (MAE) between the experimental and numerical velocity distributions are computed by Equation (3.18), where A and B denote the experimental and numerical velocities, n is the number of points on the velocity profile in the depth-wise direction at which the velocity is computed, and k is the numerator of the points. Then, that value of R_d which corresponds to the minimum MAE is selected as the roughness layer thickness for that test case. After finding the best R_d with the smallest MAE for all the calibration test cases, the relative roughness height R_d/H is plotted versus flow depth H (Figure 3-5) and a power function is used to fit a curve to the points as illustrated in Figure 3-5.

For validating tests, similar procedure is adopted as different values of R_d are used in the simulations and the one with the minimum MAE is selected and plotted on the same graph to check if it follows the fitted curve. Figure 3-5 shows that the R_d/H values of the validation test cases have nearly the same relation with the flow depth. Further evidence of the model validation will be demonstrated in the next section where the estimated and measured velocity and shear stress profiles are compared.

$$\mathrm{MAE} = \frac{1}{n}\sum_{k=1}^{n}\left|A_k - B_k\right| \tag{3.18}$$

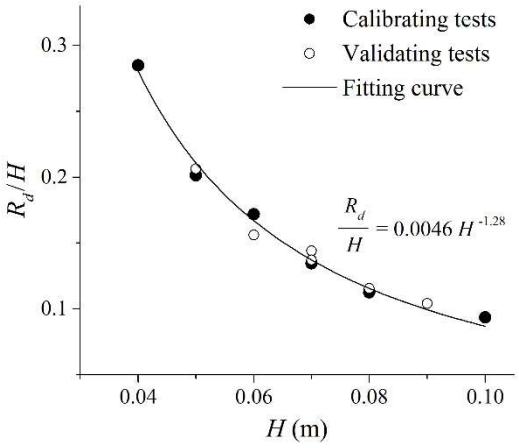

Figure 3-5 Calibration and validation of the model in terms of the thickness of the roughness layer vs. the water depth.

3.2.2 Flow uniformity and steadiness

The uniformity and steadiness of flow is investigated by presenting the results of streamwise velocity and pressure for test case S004H50. The instantaneous streamwise velocity at t = 70 s, instantaneous pressure at t = 70 s, time-averaged velocity, and time-averaged pressure contours are presented in Figure 3-6 (a) to (d), respectively. For time-averaging, the SPH-estimated quantities are averaged over a regular fixed mesh with spacing of l_0 over a period of 20 seconds from t = 70 s to 90 s. The figure shows the capability of the adopted inflow/outflow technique in producing the desirable uniform flow condition. To further investigate this issue, the time-averaged streamwise velocity of three different sections at x = 0.25L, 0.50L, and 0.75L are plotted in Figure 3-7 (a). It is found that maximum difference between the depth-averaged values of these profiles is about 0.5%. Besides, the space-averaged streamwise velocity is plotted for three different times (t = 35, 50 and 65 s) in Figure 3-7 (b). The depth-averaged value of these profiles has a maximum of 1.96%. The small change in the streamwise velocity profile over time also demonstrates the flow steadiness.

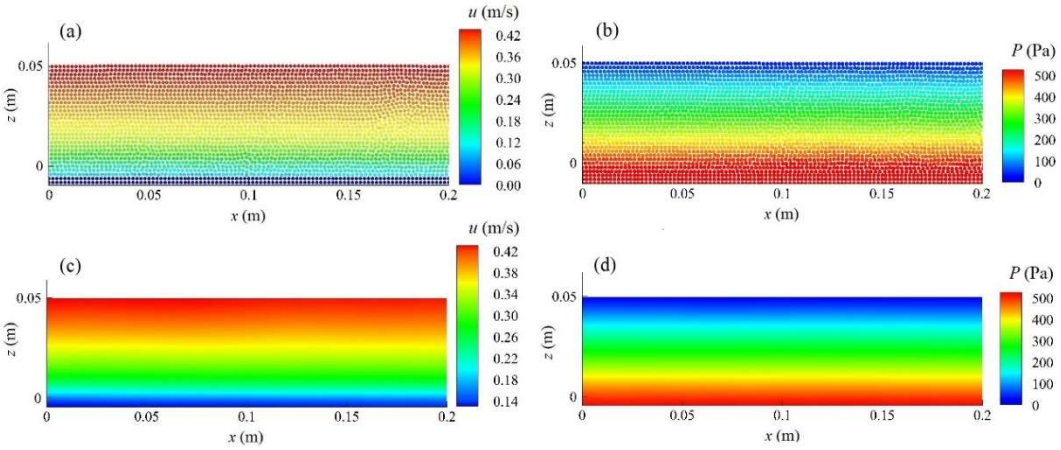

Figure 3-6 Uniformity of the flow for test case S004H50; (a) instantaneous velopcity; (b) instantaneous pressure; (c) time-averaged velocity; and (d) time-averaged pressure.

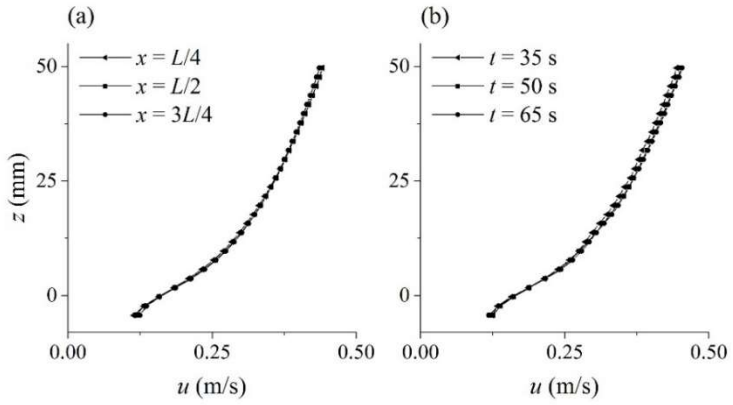

Figure 3-7 (a) time-averaged velocity in three different sections; and (b) space-averaged velocity in three different times, for test case S004H50.

In the present simulations, the time when the steady state is achieved is different for different test cases. However, to determine a threshold, it is confirmed that it takes around 20-30 seconds to reach the steady condition for all the 12 test cases. In fact, the initial velocity of particles (including inner-fluid and inflow/outflow particles) is set to a constant value larger than zero in order to reach the steady state quicker. The criterion used to define if the flow reaches the steady state is that if the differences of the depth-averaged value of the space-averaged velocities at the mid-section of

the channel (x = 0.5L) at different times become less than 2.0%, then the flow is regarded as being steady.

A part of the flow momentum is removed by the shear stress term at the bed and the turbulence model helps in transferring this effect to the upper layers of the flow. As a result, the unbalanced momentum transfer occurs during the first 20-30 seconds and then the flow gradually reaches the steady state condition while the time-averaged quantities such as velocity and shear stress remain unchanged.

Using the proposed inflow/outflow technique, the flow quantities at the inlet boundary are considered to be unknown rather than being prescribed. In fact, the flow is naturally generated based on the hydraulic conditions of the channel such as the roughness and slope of the bed.

The satisfaction of volume conservation at the inlet and outlet boundaries is checked by calculating the volume flows inside the computational domain at the inlet boundary (Vol_{in}) as well as the volume flows out at the outlet boundary (Vol_{out}) at every second of simulation from the initial time to t = 90 s. The maximum difference between Vol_{in} and Vol_{out} has been found to be less than 0.5% at every one second in all simulations. This demonstrates that the volume conservation at the inflow and outflow boundaries is satisfied in all the present simulations. Here, this comparison is shown for one test case (S004H50) from t = 60 s to t = 66 s. The volume of fluid enters the domain at the inlet (Vol_{in}) and the volume leave the domain at the outlet (Vol_{out}) every second are calculated by summing up the volume of each particle passes the inlet and outlet boundaries, respectively, by the following equations.

$$Vol_{in} = \sum_{i} \frac{m_i}{\rho_i} \;; \qquad Vol_{out} = \sum_{o} \frac{m_o}{\rho_o} \tag{3.19}$$

where i and o denote the inlet and outlet boundaries, respectively, between time intervals t and t + 1 s. The calculated values of Vol_{in} and Vol_{out} are presented in Figure

3-8 which shows the maximum relative difference between Vol_{in} and Vol_{out} ($\left|Vol_{out} - Vol_{in}\right| / Vol_{in}$) is less than 0.5 % for every second.

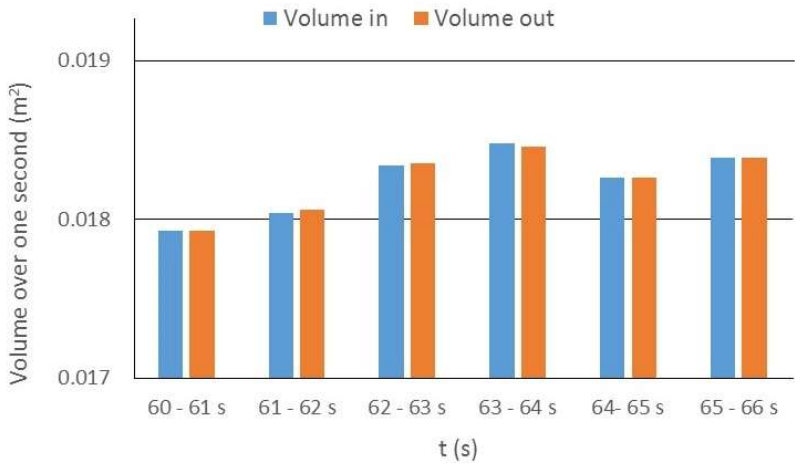

Figure 3-8 Volume entering and leaving the domain at the inlet and outlet boundaries at every second between *t* = 60 s and *t* = 66 s for the test case S004H50.

As mentioned above, a constant initial streamwise velocity larger than zero is usually used to help the simulation reach a steady state quicker. Here, Vol_{in} and Vol_{out} for the case S004H50 with using different values of the initial velocity (U_0 = 0.05, 0.20, 0.40, and 0.70 m/s) over 90 seconds is calculated and presented in Figure 3-9. As can be seen, the difference between Vol_{in} and Vol_{out} is very small (less than 0.5 %) for any initial velocity U_0. The figure also shows the achievement of the steady state condition as the Volume per second (m^2) becomes constant after about 20-30 seconds depending on the initial velocity U_0. When larger U_0 is used, the steady state is achieved quicker. The experimental flow discharge for this case (S004H50) is $Q_{\exp}$ = 0.00825 m^3/s and the flume width is 0.459 m. Dividing $Q_{\exp}$ with the flume width gives the value of $q_{\exp}$ = 0.0018 m^2/s which is correctly estimated by the model (the constant value of the volume per second in the steady state condition in Figure 3-9).

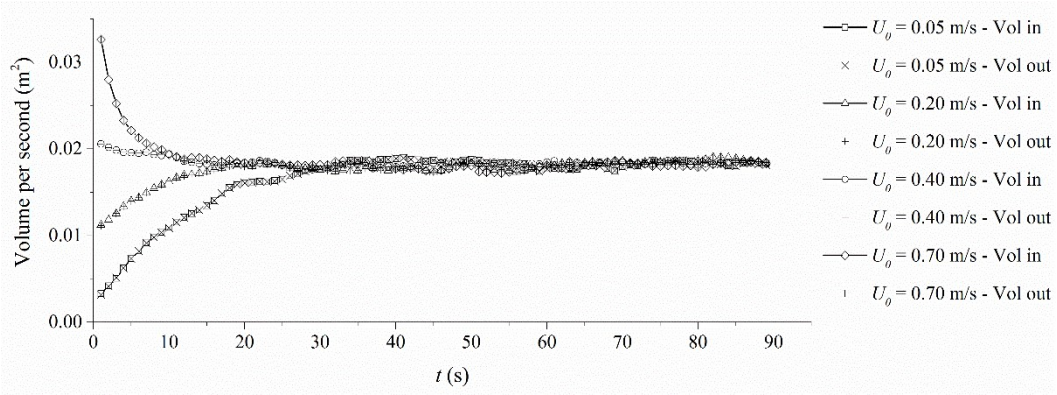

Figure 3-9 Volume entering and leaving the domain at the inlet and outlet boundaries at every second between *t* = 0 s and *t* = 90 s for the test case S004H50 with using different values for the initial streamwise velocity.

3.2.3 Analysis of velocity profiles

Figure 3-10 compares the estimated time-averaged streamwise velocity profiles of all the 12 test cases with the experimental data as well as the analytical profiles obtained by the following equation.

$$\frac{u}{u_*} = \frac{1}{\kappa}\ln\left(\frac{z_w}{k_s}\right) + B_r \tag{3.20}$$

Where k_s is Nikuradse roughness size, z_w is the vertical distance from bed, and B_r is a constant which is equal to 8.5 for the case of rough bed. It is notable that the log law may not be valid in the present cases due to the shallow depth and rough bed. However, the analytical distributions are just used for comparison with the numerical profiles to investigate that if the model is capable of predicting the logarithmic distribution above the roughness layer. Table 3-2 summarises the values of R_d employed to achieve the results presented here as well as MAE of velocity distributions.

In order to assess the performance of the model in the estimation of velocity distribution over the flow depth, the MAE is computed at three different parts, i.e. lower 20%, middle 60% and upper 20% of the depth. The purpose of this is to

investigate the hypothesis that the bottom layer (bottom 20%) is considered as the logarithmic layer while the upper layers could be split up differently (Nichols, 2013). Figure 3-11 represents the result of velocity MAE for all test cases.

Figure 3-12 shows the distribution of velocity gradient ($\partial u/\partial z$) for all the 12 test cases, as this quantity is also of interest in the present study. Besides, the MAE of these profiles are computed and represented Table 3-2; and their distributions in the lower 20%, middle 60% and upper 20% of the depth are illustrated in Figure 3-13.

Table 3-2 Relative roughness height and MAE of velocity and its gradient for all the test cases.

Test No.	Test ID	$\frac{R_d}{H}$	MAE of u (m/s)	MAE of $\partial u/\partial z$ (1/s)
1	S004H40	0.285	0.0052	0.77
2	S004H50	0.206	0.0060	1.17
3	S004H70	0.144	0.0100	1.27
4	S004H90	0.104	0.0100	0.77
5	S004H100	0.094	0.0179	1.25
6	S003H50	0.202	0.0047	1.40
7	S003H60	0.156	0.0063	1.39
8	S003H70	0.135	0.0078	0.67
9	S003H80	0.116	0.0080	1.11
10	S002H60	0.172	0.0052	1.05
11	S002H70	0.137	0.0061	0.81
12	S002H80	0.113	0.0061	0.82

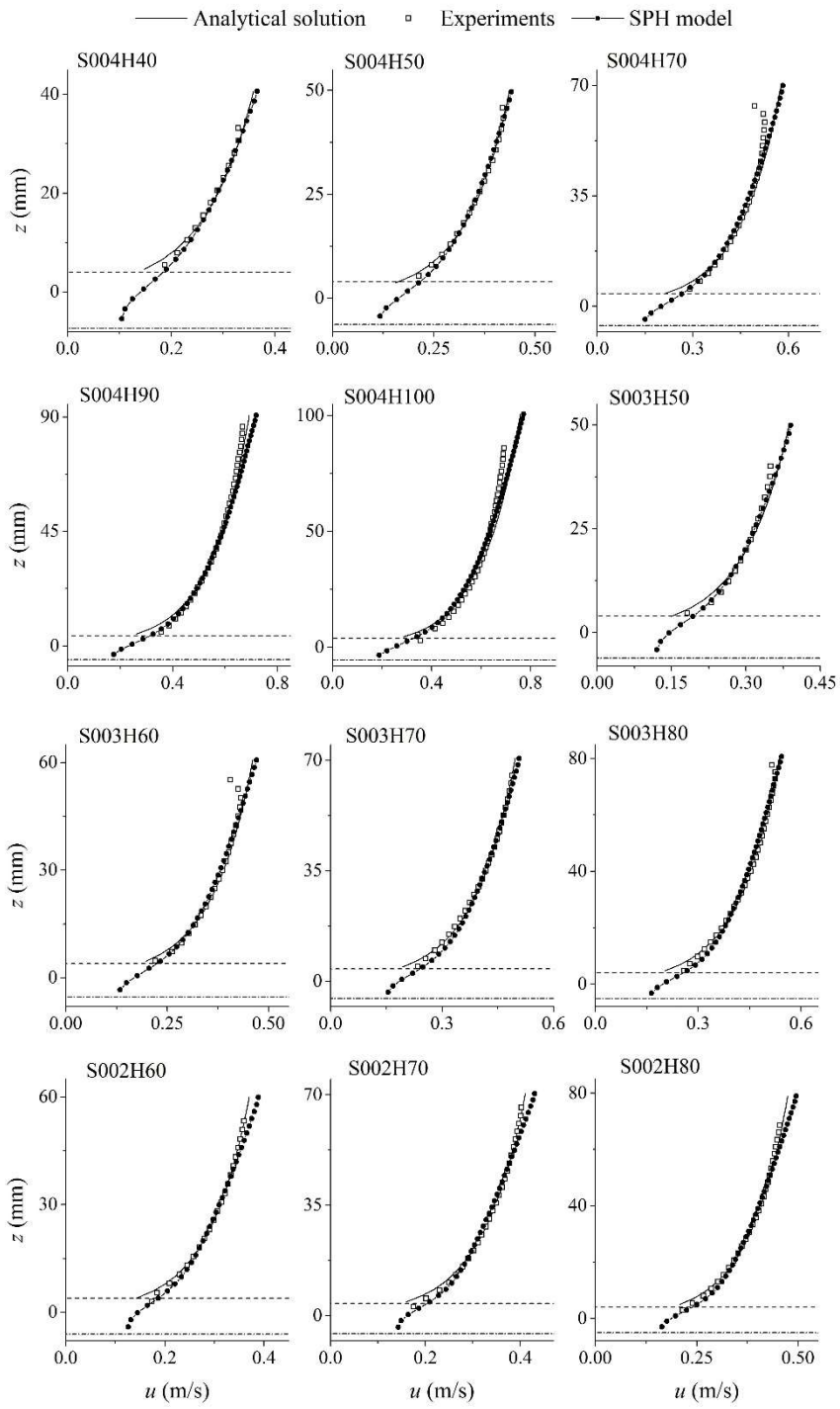

Figure 3-10 Distribution of the time-averaged streamwise velocity over depth. Dash-dotted and dashed lines show the level of the numerical bed and the crest of the roughness layer, respectively.

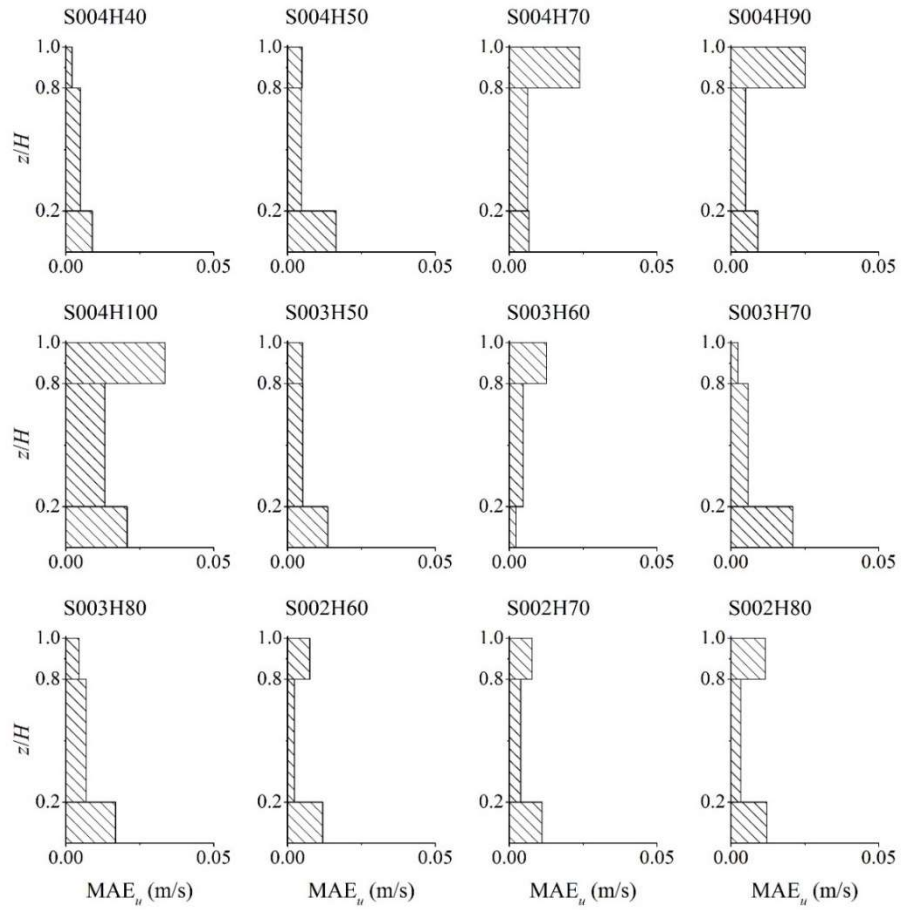

Figure 3-11 MAE of the streamwise velocity in the lower 20%, middle 60% and upper 20% of the depth

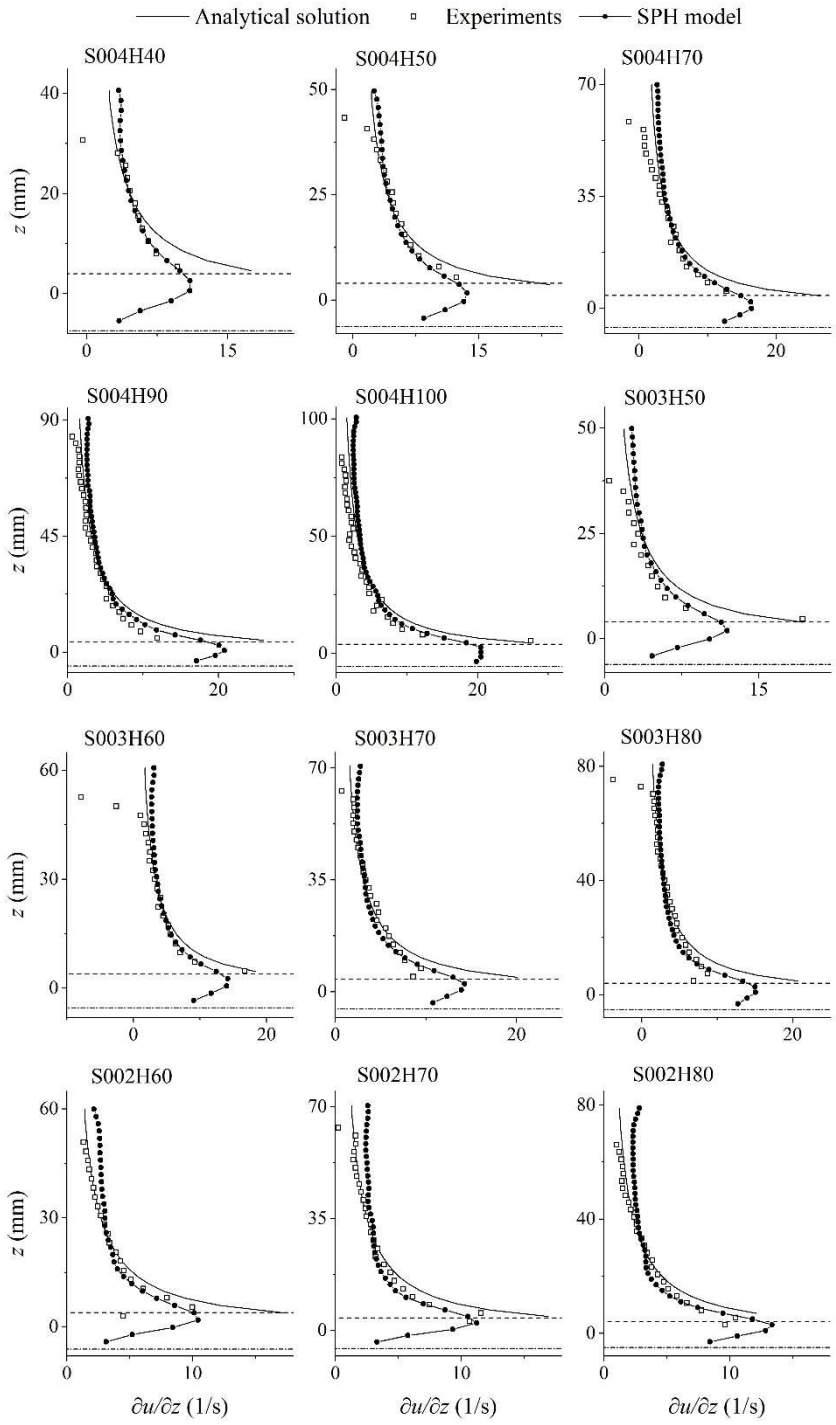

Figure 3-12 Distribution of the gradient of the time-averaged streamwise velocity over depth. Dash-dotted and dashed lines show the level of the numerical bed and the crest of the roughness layer, respectively.

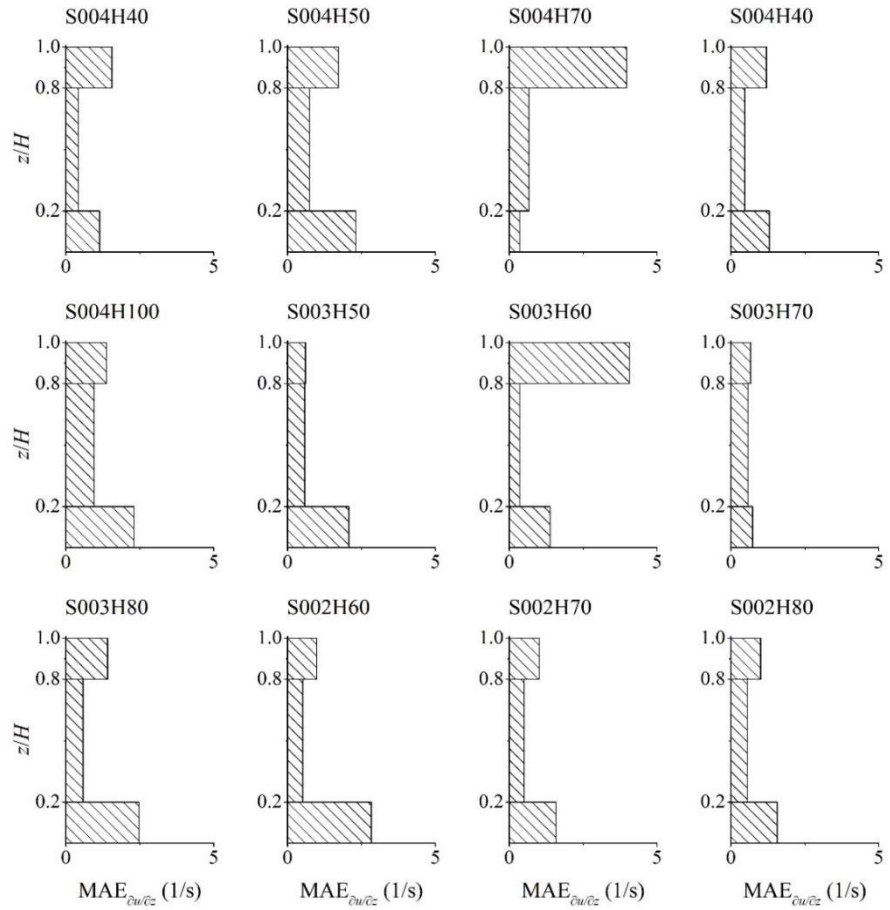

Figure 3-13 MAE of the streamwise velocity gradient in the lower 20%, middle 60% and upper 20% of the depth.

Figure 3-11 demonstrates that as the depth increases, the upper 20% MAE of the velocity profile increases in most cases, and as the bed slope decreases, the MAE of the near-bed velocity generally increases. In most cases, the middle part of the depth has the lowest MAE for velocity and its gradient. Figure 3-13 shows that in the lower 20 % of the depth, the velocity gradient MAE is usually larger, except in some cases such as S004H70 and S003H60, where large errors are seen in the upper part of the depth. In some cases, the slope of experimental velocity profile declines to zero or even negative values just below the surface, while in the numerical results, a non-zero, but small positive value is seen in the velocity gradient profiles (Figure 3-12). This difference could be due to the fact that the experimental flow contains secondary

circulations which cause non-zero shear stress at the water surface while such behaviour is disregarded in the present 2D model. On the other hand, in the mixing-length distribution calculated by Nezu and Rodi (1986) formula, the mixing-length declines to zero at the water surface based on the assumption that the size of turbulent eddies is significantly restricted by the free surface. Such a decrease in the mixing-length may result in a non-zero velocity gradient near the surface.

Comparing the near-bed velocity gradient distribution in the numerical, experimental and analytical profiles reveals that the difference between the numerical and experimental profiles are less than those between the analytical and experimental ones. This is attributed to the use of the proposed drag force model, i.e. relating the near-bed velocity to the shear from the roughness elements rather than assuming a logarithmic distribution in the shear boundary.

3.2.4 Analysis of roughness height

In Section 3.2.1 it was shown that the ratio of R_d (corresponding to the minimum MAE) to the water depth, has a relationship with the depth based on the power function presented in Figure 3-5. This figure illustrates the relative roughness height (R_d/H) should be smaller for higher depths. It is noted that in the present study, the size of roughness elements (spheres) is fixed for all tests. Therefore, the magnitude of the parameter R_d/H decreases with a reduction in the ratio of roughness size to water depth (d_s/H). The reason of selecting test cases with constant bed roughness configuration, is to investigate the roughness effect under different flow conditions.

The relationship between the relative roughness height (R_d/H) and the shear velocity u^* is also explored here, based on the fact that the flow condition is determined not only by the water depth but also by the slope of the channel. The result is presented in Figure 3-14 (a) where different curves are fitted to different bed slope values. The curves are nearly equally-spaced with a vertical shift downwards as

the bed slope decreases. This figure demonstrates that for higher shear velocity, the numerical relative roughness height is milder for all bed slopes.

In Figure 3-14 (b), R_d/S_0H of all test cases are plotted versus u^*, just in order to provide a single relationship between the relative roughness height and the flow condition. It is notable that the same type of fitting function, i.e. power function, is used. This figure also illustrates that as flow becomes more sheared (larger u^*), smaller relative roughness heights are required to simulate the experimental condition. In other words, as the ratio of bed roughness to water depth (d_s/H) becomes smaller, i.e. when the flow is deeper, a lower effect is reproduced at the bed by the proposed drag force model. However, the magnitude of the drag-induced shear stress could be larger for the cases with higher u^* since the near-bed flow velocity is higher for thoses cases (see Figure 3-15).

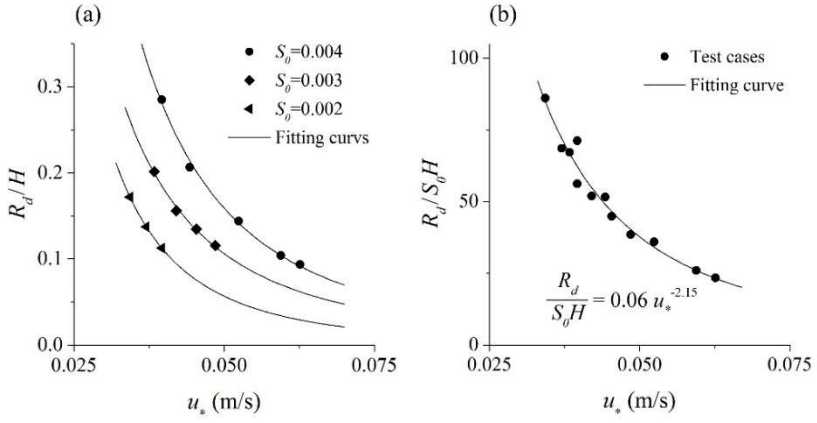

Figure 3-14 Relative roughness height versus flow shear velocity: (a) relationship between R_d/H and u^* for different bed slopes, (b) relationship between R_d/S_0H and u^* for all tests.

3.2.5 Analysis of form-drag and turbulent shear stress

Figure 3-15 represents the streamwise drag-induced shear term ($\boldsymbol{\tau}_d/\rho$) distribution in the roughness layer for all the test cases. As expected, when Re Number or u^* are higher, the average $\boldsymbol{\tau}_d/\rho$ is larger. In other words, where the bed slope is steeper

and/or the flow depth is deeper, the drag-induced shear stress term is larger because of higher velocities. In most test cases, $\boldsymbol{\tau}_d / \rho$ increases with vertical coordinate to some distance above the numerical bed level (bottom wall) and then declines to the roughness crest in spite of velocity increase. This decrease can be attributed to the shape function W_d which decreases sharply below the roughness crest (see Equation 3.17 and Figure 3-4).

In the present simulations, the streamwise velocity is dominant while the macroscopic (average) vertical velocity contribution to the drag-induced shear stress is insignificant. It has been found that in the numerical tests, the scale of the time-averaged vertical velocity in the roughness layer is less than 0.5% of the time-averaged streamwise velocity, while it is about 1.0% to 2.0% in the experiments. The underestimation of the vertical velocity could be attributed to the fact that in the present 2D macroscopic simulations, the physical dispersion in the vertical direction which is the result of flow obstruction by the solid particles at the bed has been disregarded due to the macroscopic discretisation of the computational domain and governing equations.

In order to show the effect of roughness on the velocity under different flow depths, the SPH velocity distributions are plotted separately for different bed slopes in Figure 3-16. As can be seen for each bed slope, as the flow is deeper, the velocity is higher. This effect is simulated by the use of variable R_d in the model.

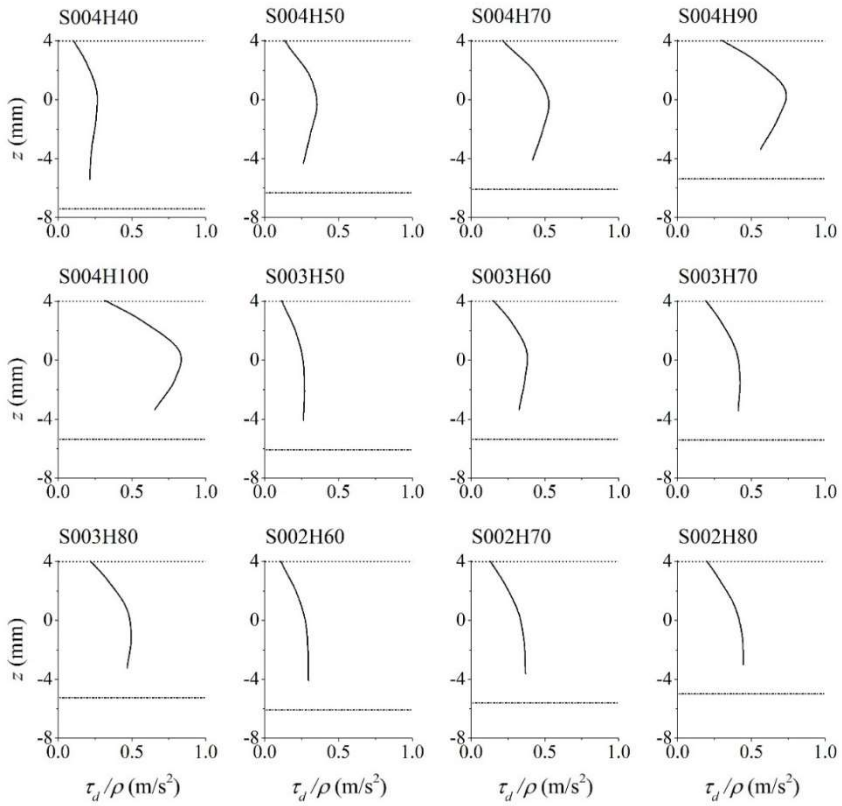

Figure 3-15 Drag-induced shear term distribution in the roughness layer (solid line). Dash-dotted and dotted lines show the level of numerical bed and the crest of the roughness layer, respectively.

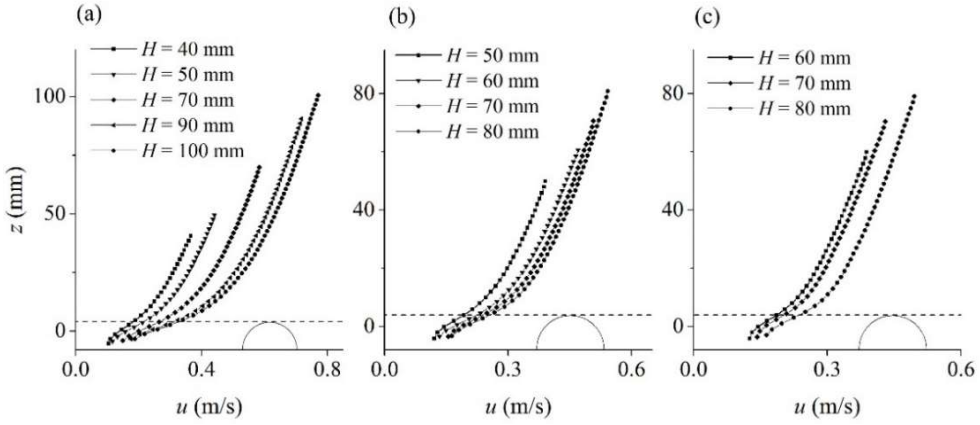

Figure 3-16 Time-averaged streamwise velocity distribution of the test cases with channel slopes (a) 0.004, (b) 0.003, and (c) 0.002. The dashed lines show the level of the roughness crest and the solid half-circles schematically depict the roughness element.

Using a variable roughness height R_d in the model not only affects the computed drag-induced shear stress, but also has an influence on the magnitude and distribution of the near-bed turbulent shear stress. In the present simulations, the numerical bed level is considered to be the zero-reference datum for the mixing-length distribution. This issue is illustrated in Figure 3-17 where the mixing-length l_m distribution is represented for two cases with different thicknesses of the roughness layer, i.e. $R_{d,1}$ and $R_{d,2}$, while $R_{d,2} > R_{d,1}$. When R_d is larger, the estimated eddy-viscosity is higher, and accordingly the shear stress will be higher too. This causes the drag at the bed produces a more significant impact on the upper layers of the flow. Generally speaking, any changes of R_d may have an effect on both the drag-induced and the turbulence shear stress computed by the model. It is also noted that as the velocity gradient is at a maximum near the crest of the roughness layer, a small change in the mixing-length magnitude at this level may have a considerable effect on the estimated eddy-viscosity.

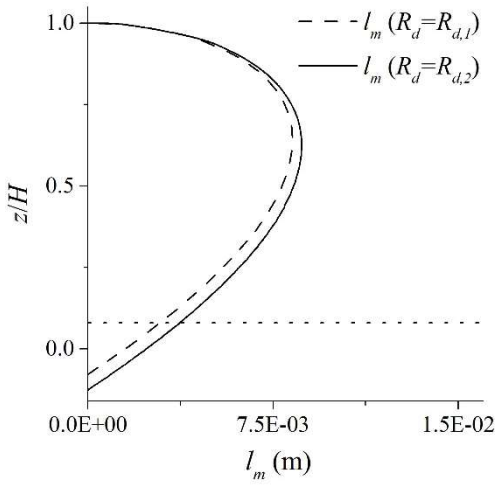

Figure 3-17 Mixing-length profile for 2 cases with the same depth (*H* = 50 mm) and different thicknesses of the roughness layer ($R_{d,2} > R_{d,1}$). The zero reference of the mixing-length is on the numerical bed level and the dotted line shows the crest of the roughness layer.

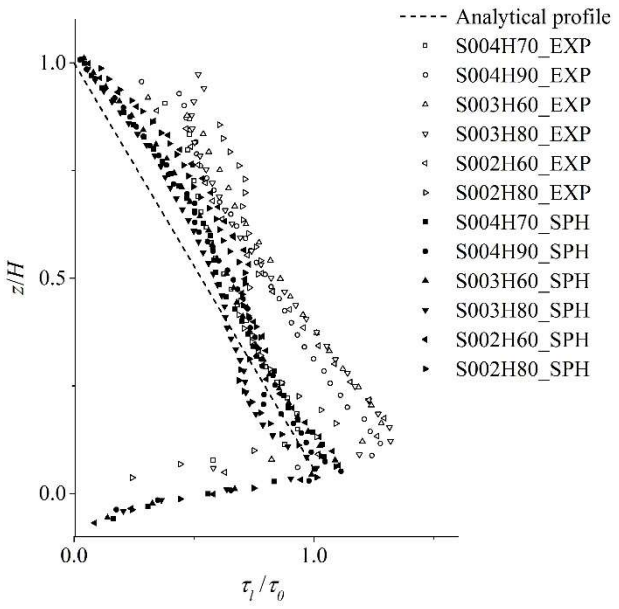

Figure 3-18 Distributions of the normalized turbulent shear stress with depth.

Figure 3-18 represents the time-averaged shear stress profiles of 6 test cases (shown in Table 3-1) estimated by the MSPH-ML model in comparison with the measured data, as well as the analytical distributions calculated by the following equation.

$$\tau = \tau_0 \left(1 - \frac{z}{H} \right) \tag{3.21}$$

where τ_0 is the magnitude of the turbulent shear stress at the bed which is estimated as $\rho g H S_0$. In this figure, the horizontal and vertical axes are normalized by τ_0 and H, respectively. As seen, the experimental profiles exceed the analytical shear stresses by about 20 - 30%. On the other hand, the underestimation of the measured shear stress by the numerical model could be attributed to the underestimation of the mixing-length l_m distribution. As mentioned earlier, in the present model, mixing-length zero reference datum is defined at the numerical bed level (Figure 3-17) since the bottom wall locates at this level and there are no fluid particles below it. For example, for test case S004H50, R_d is set equal to $0.43 d_s$, i.e. the numerical bed level is at $0.43 d_s$ below the roughness crest. According to the present mixing-length

definition (Figure 3-17), l_m becomes zero at this level. However, in the experimental test, the mixing-length might be non-zero at $0.43d_s$ below the roughness crest. For example, it might have some small value below that level to the bottom of the bed spheres. As there is no velocity data available below the roughness crest in the present experiments, no investigation is possible on the distribution of the mixing-length within the roughness layer. Therefore, Nezu and Rodi (1986) formula has been applied with a datum at the numerical bed level since the impermeable wall is set at this level in the present numerical simulations. It should also be noted that the dimensional differences between the numerical and experimental studies could also have some small effects, since in the present 2D model the effect of flow in the lateral direction is neglected though it is very small. Nonetheless, the dimensional differences as well as the probable difference between the numerical and experimental mixing-length profiles should not be too high as the shear stress underestimation does not exceed 20% for all the tests.

3.2.6 Validity of the turbulence model

In the development of the turbulence model is Section 3.1.1.2, it was assumed that the part of turbulence resolved by the computational discretisation is much smaller than the expected total turbulence effect due to the macroscopic modelling of the roughness layer near the bed. Therefore, it was assumed that the total turbulent shear stress should be modelled (Equation 3.6). The MSPH-ML model was proposed for the present problem in order to estimate the turbulent shear stress.

Here, the simulations of two test cases (S004H50 and S003H70) are repeated by applying the SPS-Smagorinsky model with C_s = 0.15 in order to compare its results with the MSPH-ML model. Moreover, the part of shear stress which is resolved by the computational resolution (particle motion) itself is also computed for both cases of using the SPS-Smagorinsky and the present MSPH-ML models and compared to the shear stresses estimated by these models.

In order to compute the resolved shear stress ($\boldsymbol{\tau}_r$), firstly, the velocity estimated by the model u_i is spatially averaged using cubic Spline kernel function (Equation 5.4) with a smoothing length of $1.2\,l_0$ and accordingly, the velocity deviation $\tilde{u_i}$ is calculated as the following.

$$\tilde{u_i} = u_i - \langle u \rangle_i \tag{3.22}$$

where i denotes the i^{th} coordinate component; $\langle\ \rangle$ denotes the spatial averaging operator (cubic Spline), $\langle u \rangle_i$ is the spatially averaged velocity; and $\tilde{u_i}$ is the deviation of the SPH-estimated velocity u_i from $\langle u \rangle_i$. Then, the ij component of the resolved shear stress ($\boldsymbol{\tau}_r$) is computed as the following,

$$\frac{\tau_{r,ij}}{\rho} = \langle \tilde{u_i} \tilde{u_j} \rangle \tag{3.23}$$

Now, using this equation, the xz component of the resolved shear stress is calculated and compared to the shear stresses estimated by the SPS-Smagorinsky model as well as the proposed MSPH-ML model for two test cases S004H50 and S003H70. The results of the MSPH-ML model are presented in Figure 3-19 (a) and Figure 3-20 (a), and the results of the SPS-Smagorinsky model are presented in Figure 3-19 (b) and Figure 3-20 (b), respectively, for those test cases.

Subplots (a-1) and (b-1) represent the turbulent stress $\boldsymbol{\tau}_r$ resolved by the computational discretisation / particle motion; (a-2) and (b-2) show the estimated (modelled) shear stresses by the models ($\boldsymbol{\tau}_l$ and $\boldsymbol{\tau}_{SPS}$, respectively); (a-3) and (b-3) presents resolved, modelled, and total stresses together for comparison; and (a-4) and (b-4) represent the computed velocity distributions in the logarithmic scale in comparison with the experimental data. These figures reveal two important points. Firstly, according to subplots (a-1), (a-2) and (a-3), the part of turbulent stress resolved by the particle motion $\boldsymbol{\tau}_r$ is negligible compared to the estimated part by the MSPH-ML model ($\boldsymbol{\tau}_l$). In other words, $\boldsymbol{\tau}_t \approx \boldsymbol{\tau}_l$. Therefore, the assumption made in Section

3.1.1.2 that the total effect of flow turbulence should be modelled (Equation 3.6) is valid in the present macroscopic simulations. Secondly, according to subplot (b-2), the Smagorinsky model with C_s = 0.15 is unable to estimate the required amount of turbulent shear stress. Therefore, the balance in the momentum is not reproduced correctly and the velocity is highly overestimated (subplot b-4). It is noted that the resolved shear stress $\boldsymbol{\tau}_r$ in the case of using the SPS-Smagorinsky model (subplot b-1) is higher than that in the MSPH-ML model. It is because the velocity gradient is higher in this case since the velocity is significantly overestimated by this model. In fact, as the momentum balance is not adequately produced, the flow discharge is highly overestimated due to the velocity averaging process at the inflow boundary condition for inflow particles (Section 3.1.4.1). In Chapter 6, where a different inflow boundary technique is applied, it will be shown that when the discharge is fixed, the shear stress $\boldsymbol{\tau}_r$ resolved by both models are in the same order. In the case of fixed discharges, $\boldsymbol{\tau}_{SPS}$ is also expected to be lower than here due to the same reason.

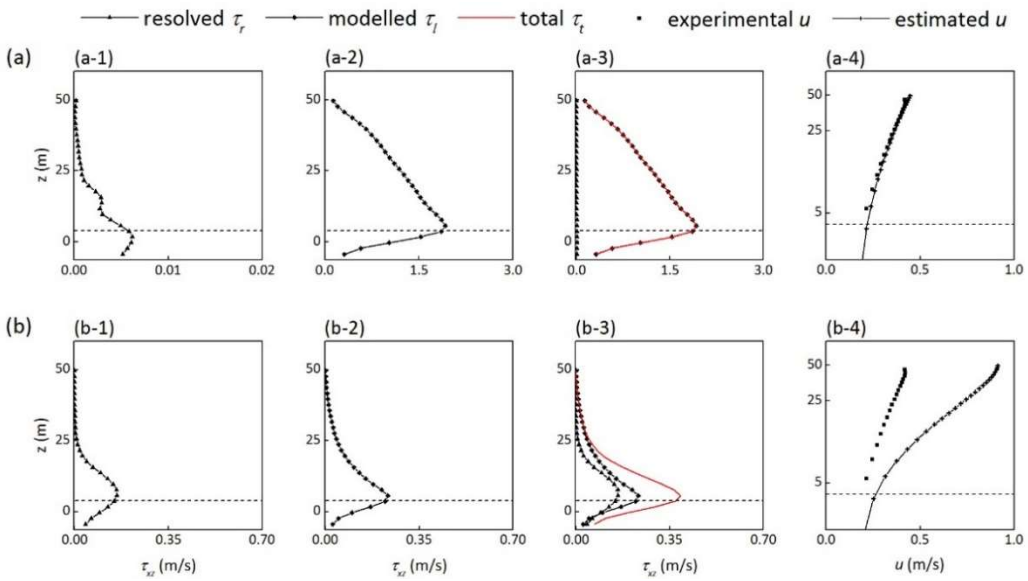

Figure 3-19 Application of (a) the present MSPH-ML model and (b) the SPS-Smagorinsky model with C_s = 0.15, for the test case S004H50.

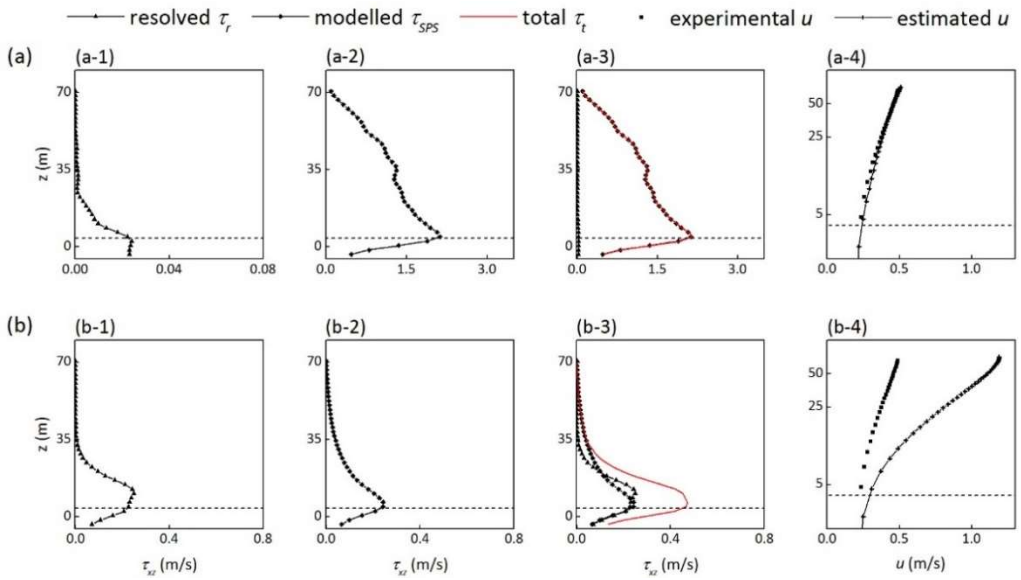

Figure 3-20 Application of (a) the present MSPH-ML model and (b) the SPS-Smagorinsky model with C_s = 0.15, for the test case S003H70.

3.3 Summary

In this chapter, the 2D equations of mass and momentum were discretised using the WCSPH method while two extra stress terms were added to the momentum equation to account for the effects of bed roughness and turbulence. It was shown that, the standard SPS-Smagorinsky model with a fixed C_s around 0.15 is unable to reproduce the correct mechanisms of momentum transfer in uniform open channel flows over rough boundaries. It was also concluded that the part of shear stress resolved by the computational discretisation is very small. Therefore, the MSPH-ML model was proposed for calculation of the turbulent eddy-viscosity. To estimate the extra drag-induced shear term, a drag force model was introduced where a shape function was used to simulate the geometry effect of the roughness elements into the equation. Meanwhile, a new inflow/outflow boundary technique was proposed and demonstrated to generate steady and uniform flow condition within the computational channel without the need of using prescribed velocities at the inlet.

Twelve test cases of different bed slopes and water depths were simulated to investigate the effect of bed roughness under various flow conditions. A roughness layer was defined near the bed boundary where a form-induced drag shear stress is applied on the fluid particles. The thickness of this layer (R_d) was assumed to be variable flow-dependent, such as being related to the flow depth *H* and the shear velocity on bed u^*. Good agreement was observed between the velocity and shear stress results of the model and the experimental and analytical profiles. This shows that the drag force model was successful in addressing the effect of bed roughness, and that the proposed MSPH-ML turbulence model correctly translated this effect to the flow upper layers.

According to the macroscopic representation of the computational domain and the governing equations in the roughness layer, the physical dispersion in the vertical direction is disregarded. Thus, in the simulations, the momentum removal at the bed is dominated mainly by average shear driven in the streamwise direction. However, the effect of this momentum reduction is transferred vertically by the turbulence model. The estimated streamwise velocity and shear stress profiles suggested that this assumption has not caused substantial errors for the 12 flow test cases and the macro flow behaviours have been well reproduced. This is due to the fact that the proposed modification to the turbulence model resulted in reproducing a correct transfer of shear from the roughness layer to the upper flow. To the author's best knowledge, the work presented in this chapter is the most comprehensive SPH work carried out in the simulation of turbulent free surface channel flows over rough beds combined with detailed experimental validation.

Whether the non-accuracy of the SPH-LES in turbulent channel flows over rough beds is related to inaccurate estimation of velocity-pressure interactions (as addressed by Mayrhofer et al., 2015) or to the macroscopic modelling of the roughness layer, the proposed MSPH-ML approach showed to be able to resolve this difficulty when the eddy-viscosity being realistically parameterised. This issue will be investigated in more

detail in Chapter 6. It is also noted that, the distribution of the mixing-length needs to be available to be able to estimate the eddy-viscosity using the present MSPH-ML model. This restricts the applicability of the MSPH–ML model to problems where there is no knowledge of the mixing-length distribution.

The bed in river flows cannot be always treated as a single impermeable boundary condition, particularly when the thickness of the porous bed is comparable to the water depth and/or the turbulent flow has a considerable penetration into the bed. In such a case, the flow within the porous bed also needs to be simulated. In the present model, although the frictional effect of roughness elements was included in the momentum equation, the effect of volume occupied by solid particles was disregarded so that the continuity of mass was not exactly preserved within the roughness layer. In other words, the effect of porosity was ignored in this layer. However, since the thickness of the roughness layer in the present cases was small compared to the water depth, this effect should not have produced considerable errors.

The aim of the next three chapters is to extend the model to be capable of dealing with both flow above and beneath porous beds and finally apply it to a turbulent channel flow over and within natural porous beds with high velocity gradients at the interface.

Chapter 4 Modelling Flow Interaction with Porous Media at a Macroscopic Scale: I) Mathematical Development

In Chapter 3, turbulent channel flow over rough impermeable beds was studied by developing a macroscopic 2D SPH model. As the ultimate goal of the present study is to develop a model for flow over porous beds, in this chapter, the required governing equations for SPH to investigate flow behaviour at the interfacial boundary between free flow and porous media will be developed. In the existing SPH models for flow interaction with porous media which were reviewed in Chapter 2, the governing equations and closure models are often borrowed from grid-based studies, so that usually some simple averaging numerical treatments have been applied with no rigorous justification. Therefore, the aim of the present chapter is to investigate, in depth, the mathematical derivation of the macroscopic equations of flow interaction with porous media with an insight into the treatment of the interfacial boundary. The developed equations then will be applied to solve some problems in Chapter 5 and finally to simulate turbulent open channel flows over natural porous beds in Chapter 6.

The structure of the present chapter is as follows. In Section 4.1, microscopic governing equations will be presented, and the spatial averaging method will be introduced. Then in Section 4.2, the averaging method will be used to derive the

macroscopic governing equations in terms of intrinsic averages of fluid properties. The derivation will be carried out by constructing the convolution product of microscopic equations using a weighting function G. It will be based on the procedure adopted by Quintard and Whitaker (1994), but with addition of the inertial forces and the effects of the turbulence. Besides, the equations will be presented in the Lagrangian form. The detailed mathematical derivation is presented in Appendix B in order to identify the assumptions and constraints required to arrive at the final form of the macroscopic equations. In Section 4.3, the derived equations will be discretised based on the SPH particle approximation scheme in a symmetric form. In this section, firstly the equations are averaged once again using the convolution product of the macroscopic equations, but with a different weighting function W. This will lead to a distinction between the determination of porosity from the microscopic field and the solution of the averaged equations for the macroscopic flow field. The determination of porosity and the treatment of interfacial boundaries in practical situations will be discussed in Section 4.4 and a summary will be provided in Section 4.5.

4.1 Spatial averaging method

The physical process under consideration is a single-phase flow in a rigid porous media at a macroscopic scale. A system is considered comprising of a fluid phase α and a rigid solid phase β as depicted in Figure 4-1. In order to derive the macroscopic governing equations, an appropriate spatial averaging method should be applied to the microscopic equations at a local averaging volume. The goal of the present section is introducing the particle spatial averaging theorem based on the SPH method which will be used in Section 4.2 to derive the macroscopic governing equations for fluid flow through porous media.

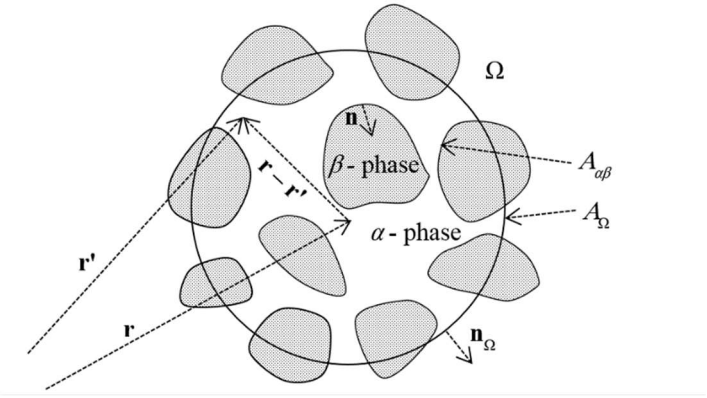

Figure 4-1 Averaging volume Ω comprised of *α*- and *β*- phases.

The full form of the compressible version of microscopic conservation equations of mass and momentum is considered as the governing equations at the pore level while the Lagrangian form of the macroscopic equations for the case of an incompressible flow will be derived as the macroscopic governing equations in the present study. The WCSPH method will be then employed in Section 4.3 to discretise the equations. The equations of conservation of mass and momentum at the pore level are written in the Eulerian form as the following,

$$\gamma \frac{\partial \rho}{\partial t} + \gamma \nabla \cdot \left(\rho \mathbf{u} \right) = 0 \tag{4.1}$$

$$\gamma \frac{\partial \left(\rho \mathbf{u} \right)}{\partial t} + \gamma \nabla \cdot \left(\rho \mathbf{u} \mathbf{u} \right) = -\gamma \nabla P + \gamma \rho \mathbf{g} + \gamma \mu \nabla^2 \mathbf{u} \tag{4.2}$$

where ρ , $\mathbf{u}$ and P are density, velocity and pressure, respectively, at the pore level. $\mathbf{g}$ is gravitational acceleration, μ is dynamic viscosity coefficient, and γ is a distribution function associated with the α -phase (which averaged equations will be developed for). Following Grey and Lee (1977), the distribution function is set to one for the α -phase, and zero for any other phases (here β -phase) as given in Equation (4.3). This means any property like ψ and its temporal and spatial derivatives are respectively, ψ , $\partial \psi / \partial t$ and $\nabla \psi$ in the *α*-phase, and are zero in the β -phase. In

other words, γ is multiplied to both sides of the microscopic equations in order to emphasize the fact that the equations are considered only at the α-phase.

$$\gamma = \begin{cases} 1, & \text{in the } \alpha - \text{phase} \\ 0, & \text{in the } \beta - \text{phase} \end{cases} \tag{4.3}$$

An averaging volume Ω is defined as to be representative of the whole system at time *t*. It may contain both fluid and solid materials which are denoted by α and β respectively in Figure 4-1. It is assumed that the solid phase is fixed in time and space.

The SPH local volumetric average of a quantity ψ over the averaging volume Ω is given in Equation (4.4). The averaging is associated with the centroid of the volume while integration over Ω is performed by using a weighting function $G\left(\mathbf{r}-\mathbf{r}', h_\Omega\right)$, in terms of the relative position vector $\mathbf{r}-\mathbf{r}'$ and a smoothing length h_Ω. As shown in Figure 4-1, $\mathbf{r}$ is the position vector of the centroid of the volume, and $\mathbf{r}'$ is the position vector of the points other than the centroid.

$$\text{Local volumetric average: } \left\langle \psi \right\rangle^{\Omega} = \int_{\Omega} G\left(\mathbf{r}-\mathbf{r}', h_\Omega\right)\gamma\left(\mathbf{r}'\right)\psi\left(\mathbf{r}'\right) d\mathbf{r}' = G*\left(\gamma\psi\right) \tag{4.4}$$

This equation represents the macroscopic description of ψ as the integration is implemented at all points in the averaging volume Ω over which the value is ψ when $\mathbf{r}'$ points in the α-phase and is zero when $\mathbf{r}'$ points in the β-phase. $\left\langle \ \right\rangle^{\Omega}$ is the volumetric averaging operator and $G*\left(\gamma\psi\right)$ denotes the convolution product of $\gamma\psi$ using the weighting function G. It is common to use cellular average operator for the local volumetric average in the derivation of the macroscopic equations. However, the aim of the present section is to derive those equations based on the weighted average form presented in Equation (4.4) which is consistent with the SPH formulation. Quintard and Whitaker (1994) used the weighted average form to derive the Stokes equations and stated that the weighting function should satisfy the following conditions.

$$G\left(\mathbf{r}-\mathbf{r}',h_\Omega\right)\in C^\infty \tag{4.5}$$

$$G\left(\mathbf{r}-\mathbf{r}',h_\Omega\right)=0 \qquad for\left|\mathbf{r}-\mathbf{r}'\right|>2h_\Omega \tag{4.6}$$

$$\int_\Omega G\left(\mathbf{r}-\mathbf{r}',h_\Omega\right)d\mathbf{r}'=1 \tag{4.7}$$

Additionally, in this study, the weighting function has the following symmetry conditions.

$$\begin{aligned} G\left(\mathbf{r}-\mathbf{r}',h_\Omega\right)&=G\left(\mathbf{r}'-\mathbf{r},h_\Omega\right)\\ \nabla G\left(\mathbf{r}-\mathbf{r}',h_\Omega\right)&=-\nabla G\left(\mathbf{r}'-\mathbf{r},h_\Omega\right)\end{aligned} \tag{4.8}$$

The conditions (4.6) and (4.7) are known as compact and normalisation conditions. It is noted that any weighting function that satisfies the conditions presented in Equations (4.5) to (4.8) can be used. However, in this study, efforts are concentrated on using standard SPH kernel functions.

Whitaker (1969) introduced two important length constraints for the size of averaging volume which are presented here as the constraints of the support of the weighting function as follows.

$$r_\Omega >> L_\psi \tag{4.9}$$

$$r_\Omega << L_{\langle\psi\rangle^\alpha} \tag{4.10}$$

where L_ψ is some microscopic characteristic length (pore scale) over which significant variations in the quantity ψ take place; $L_{\langle\psi\rangle^\alpha}$ is the characteristic length scale over which significant variations in the average of the quantity ψ take place; and r_Ω is the support of the weighting function (radius of the averaging volume Ω which is equal to $2h_\Omega$ if one uses a standard SPH kernel function). It is noted that the constraint in Equation (4.10) is defined in terms of the intrinsic average $\langle\psi\rangle^\alpha$. Whitaker (1969) defined these two constraints 'intuitively' to ensure that the averaging volume is 'large enough' to contain all the essential geometrical characteristics of the porous

medium under consideration; and 'small enough' so that the size of the averaging volume is negligible compared to the macroscopic region.

Here, through imposing the constraint in Equation (4.10), it will be possible to find the relationship between the volumetric and intrinsic averages. Decomposing the quantity ψ as (Grey, 1975)

$$\psi = \langle \psi \rangle^{\alpha} + \tilde{\psi}^{\alpha} \tag{4.11}$$

where $\langle \psi \rangle^{\alpha}$ and $\tilde{\psi}^{\alpha}$ are the intrinsic average of ψ and its spatial deviation, respectively, and substituting it in Equation (4.4) yields

$$\langle \psi \rangle^{\Omega} = \int_{\Omega} G\left(\mathbf{r}-\mathbf{r}', h_{\Omega}\right) \gamma\left(\mathbf{r}'\right) \langle \psi \rangle^{\alpha}\Big|_{\mathbf{r}'} \, d\mathbf{r}' + \int_{\Omega} G\left(\mathbf{r}-\mathbf{r}', h_{\Omega}\right) \gamma\left(\mathbf{r}'\right) \tilde{\psi}^{\alpha}\Big|_{\mathbf{r}'} \, d\mathbf{r}' \tag{4.12}$$

Making use of Taylor series expansion it is possible to show that

$$\langle \psi \rangle^{\alpha}\Big|_{\mathbf{r}'} = \langle \psi \rangle^{\alpha}\Big|_{\mathbf{r}} + \left(\mathbf{r}'-\mathbf{r}\right) \cdot \nabla \langle \psi \rangle^{\alpha}\Big|_{\mathbf{r}} + \frac{1}{2}\left(\mathbf{r}'-\mathbf{r}\right)^{2} \cdot \nabla^{2} \langle \psi \rangle^{\alpha}\Big|_{\mathbf{r}} + \ldots \tag{4.13}$$

Substituting this into Equation (4.12) and noting that $\langle \psi \rangle^{\alpha}$ and its derivatives are constant with respect to the integration process if they are evaluated at the centroid $\mathbf{r}$, gives

$$\begin{aligned} \langle \psi \rangle^{\Omega} = {} & \langle \psi \rangle^{\alpha}\Big|_{\mathbf{r}} \int_{\Omega} G\left(\mathbf{r}-\mathbf{r}', h_{\Omega}\right) \gamma\left(\mathbf{r}'\right) d\mathbf{r}' \\ & + \nabla \langle \psi \rangle^{\alpha}\Big|_{\mathbf{r}} \cdot \int_{\Omega} G\left(\mathbf{r}-\mathbf{r}', h_{\Omega}\right) \gamma\left(\mathbf{r}'\right) \left(\mathbf{r}'-\mathbf{r}\right) d\mathbf{r}' \\ & + \frac{1}{2} \nabla^{2} \langle \psi \rangle^{\alpha}\Big|_{\mathbf{r}} \cdot \int_{\Omega} G\left(\mathbf{r}-\mathbf{r}', h_{\Omega}\right) \gamma\left(\mathbf{r}'\right) \left(\mathbf{r}'-\mathbf{r}\right)^{2} d\mathbf{r}' \\ & + \ldots \\ & + \int_{\Omega} G\left(\mathbf{r}-\mathbf{r}', h_{\Omega}\right) \gamma\left(\mathbf{r}'\right) \tilde{\psi}^{\alpha}\Big|_{\mathbf{r}'} \, d\mathbf{r}' \end{aligned} \tag{4.14}$$

The terms containing derivatives will be evaluated as the following.

$$\begin{cases} \nabla\langle\psi\rangle^{\alpha} = \mathrm{O}\left(\dfrac{\langle\psi\rangle^{\alpha}}{L_{\langle\psi\rangle^{\alpha}}}\right) \\ \dfrac{1}{2}\nabla^{2}\langle\psi\rangle^{\alpha} = \mathrm{O}\left(\dfrac{1}{2}\dfrac{\langle\psi\rangle^{\alpha}}{L_{\langle\psi\rangle^{\alpha}}^{\,2}}\right) \\ \vdots \\ \dfrac{1}{n!}\nabla^{n}\langle\psi\rangle^{\alpha} = \mathrm{O}\left(\dfrac{1}{n!}\dfrac{\langle\psi\rangle^{\alpha}}{L_{\langle\psi\rangle^{\alpha}}^{\,n}}\right) \\ \vdots \end{cases} \tag{4.15}$$

$$\begin{cases} \int_{\Omega} G\left(\mathbf{r}-\mathbf{r}',h_{\Omega}\right)\gamma\left(\mathbf{r}'\right)\left(\mathbf{r}'-\mathbf{r}\right)d\mathbf{r}' = \mathrm{O}\left(r_{\Omega}\right) \\ \int_{\Omega} G\left(\mathbf{r}-\mathbf{r}',h_{\Omega}\right)\gamma\left(\mathbf{r}'\right)\left(\mathbf{r}'-\mathbf{r}\right)^{2}d\mathbf{r}' = \mathrm{O}\left(r_{\Omega}^{\,2}\right) \\ \vdots \\ \int_{\Omega} G\left(\mathbf{r}-\mathbf{r}',h_{\Omega}\right)\gamma\left(\mathbf{r}'\right)\left(\mathbf{r}'-\mathbf{r}\right)^{n}d\mathbf{r}' = \mathrm{O}\left(r_{\Omega}^{\,n}\right) \\ \vdots \end{cases} \tag{4.16}$$

Therefore

$$\begin{cases} \nabla\langle\psi\rangle^{\alpha}\int_{\Omega} G\left(\mathbf{r}-\mathbf{r}',h_{\Omega}\right)\gamma\left(\mathbf{r}'\right)\left(\mathbf{r}'-\mathbf{r}\right)d\mathbf{r}' \approx \mathrm{O}\left[\dfrac{r_{\Omega}}{L_{\langle\psi\rangle^{\alpha}}}\langle\psi\rangle^{\alpha}\right] \\ \dfrac{1}{2}\nabla^{2}\langle\psi\rangle^{\alpha}\int_{\Omega} G\left(\mathbf{r}-\mathbf{r}',h_{\Omega}\right)\gamma\left(\mathbf{r}'\right)\left(\mathbf{r}'-\mathbf{r}\right)^{2}d\mathbf{r}' \approx \mathrm{O}\left[\left(\dfrac{r_{\Omega}}{L_{\langle\psi\rangle^{\alpha}}}\right)^{2}\langle\psi\rangle^{\alpha}\right] \\ \vdots \\ \dfrac{1}{n!}\nabla^{n}\langle\psi\rangle^{\alpha}\int_{\Omega} G\left(\mathbf{r}-\mathbf{r}',h_{\Omega}\right)\gamma\left(\mathbf{r}'\right)\left(\mathbf{r}'-\mathbf{r}\right)^{n}d\mathbf{r}' \approx \mathrm{O}\left[\dfrac{1}{n!}\left(\dfrac{r_{\Omega}}{L_{\langle\psi\rangle^{\alpha}}}\right)^{n}\langle\psi\rangle^{\alpha}\right] \\ \vdots \end{cases} \tag{4.17}$$

Now by imposing the restriction in Equation (4.10), all those terms will be negligible, and Equation (4.14) reduces to

$$\langle\psi\rangle^{\Omega} = \langle\psi\rangle^{\alpha} \int_{\Omega} G(\mathbf{r}-\mathbf{r}', h_{\Omega})\,\gamma(\mathbf{r}')\,d\mathbf{r}' + \int_{\Omega} G(\mathbf{r}-\mathbf{r}', h_{\Omega})\,\gamma(\mathbf{r}')\,\tilde{\psi}^{\alpha}\,d\mathbf{r}' \tag{4.18}$$

It is also assumed that the second term on the right-hand side of the equation which represents the volumetric average of spatial deviations from the intrinsic average at the centroid of the averaging volume is negligible compared to the first term (a*ssumption #1*), i.e.

$$\int_{\Omega} G(\mathbf{r}-\mathbf{r}', h_{\Omega})\,\gamma(\mathbf{r}')\,\tilde{\psi}^{\alpha}\,d\mathbf{r}' \approx 0 \tag{4.19}$$

Therefore, Equation (4.18) comes into the following form

$$\langle\psi\rangle^{\Omega} = \langle\psi\rangle^{\alpha} \int_{\Omega} G(\mathbf{r}-\mathbf{r}', h_{\Omega})\,\gamma(\mathbf{r}')\,d\mathbf{r}' \tag{4.20}$$

which represents the key relationship between the volumetric and intrinsic averages. This equation can be written in the following convolution product form.

$$G * (\gamma\psi) = \langle\psi\rangle^{\alpha} (G * \gamma) \tag{4.21}$$

If one defines the porosity corresponding to the averaging volume Ω as

$$\phi = \int_{\Omega} G(\mathbf{r}-\mathbf{r}', h_{\Omega})\,\gamma(\mathbf{r}')\,d\mathbf{r}' = G * \gamma \tag{4.22}$$

then Equation (4.20) represents the classic relationship between the superficial and intrinsic averages (which was based on 'cellular averaging') as follows.

$$\langle\psi\rangle^{\Omega} = \phi\langle\psi\rangle^{\alpha} \tag{4.23}$$

In order to derive the macroscopic equations, there is a need to relate the average of derivatives of a quantity to the average of that quantity. Slattery (1967) and later Whitaker (1969) introduced the spatial averaging theorem by which a relationship was established between the volumetric average of the derivatives and the derivatives of the volumetric average. This derivation was based on the 'cellular average'. Later, Marle (1982) and Quintard and Whitaker (1993, 1994) developed a

weighted function version of the spatial averaging theorem. Here, the SPH averaging method is applied to obtain those theorems from the definition presented in Equation (4.4). The details are presented in Appendix A where the volumetric averages of spatial and temporal derivatives are presented in Equations (A.6) and (A.13), respectively.

4.2 Macroscopic governing equations

To derive the macroscopic governing equations, the spatial averaging method presented in Section 4.1 is applied into the microscopic equations (4.1) and (4.2). For details of the mathematical derivation see Appendix B, where the Lagrangian form of the macroscopic equations of mass and momentum are presented in terms of intrinsic averages in Equations (B.12) and (B.43), respectively. These equations are rewritten as the following by representing $G*\gamma$ by ϕ according to Equation (4.22),

$$\frac{D\left\langle \rho \right\rangle^{\alpha}}{Dt}+\frac{1}{\phi}\left\langle \rho \right\rangle^{\alpha}\nabla\cdot\left(\phi\left\langle \mathbf{u} \right\rangle^{\alpha}\right)=0 \tag{4.24}$$

$$\begin{aligned}\frac{D\left\langle \mathbf{u} \right\rangle^{\alpha}}{Dt}=&-\frac{1}{\left\langle \rho \right\rangle^{\alpha}}\nabla\left\langle P \right\rangle^{\alpha}+\mathbf{g}+\frac{\mu}{\phi\left\langle \rho \right\rangle^{\alpha}}\nabla^{2}\left(\phi\left\langle \mathbf{u} \right\rangle^{\alpha}\right)-\frac{\mu}{\phi\left\langle \rho \right\rangle^{\alpha}}\nabla\left\langle \mathbf{u} \right\rangle^{\alpha}\nabla\phi\\&-\frac{1}{\phi\left\langle \rho \right\rangle^{\alpha}}\nabla\cdot\left(\phi\left\langle \tau \right\rangle^{\alpha}\right)+\frac{1}{\phi\left\langle \rho \right\rangle^{\alpha}}\left\{G*\left[\left(-\mathbf{I}\tilde{P}^{\alpha}+\mu\nabla\tilde{\mathbf{u}}^{\alpha}\right)\mathbf{n}_{\alpha\beta}\delta_{\alpha\beta}\right]\right\}\end{aligned} \tag{4.25}$$

where the last two terms on the right-hand side of the momentum equation represent, respectively, the effect of turbulence and frictional effect of the solid skeleton on the intrinsic average flow field. The estimation of these terms will be investigated in Sections 4.2.1 and 4.2.2.

The key assumptions that have been made to arrive at the current form of the macroscopic governing equations are summarised as below.

Assumption #1: Volumetric average of the spatial deviation of a fluid quantity from its intrinsic average is negligible, i.e. $G*\left(\gamma\tilde{\psi}^{\alpha}\right)\approx 0$ (Equation 4.19).

Assumption #2: no-slip boundary condition is applied at the $\alpha-\beta$ interfaces $A_{\alpha\beta}$, i.e. $\mathbf{u}_{\alpha\beta}\cdot\mathbf{n}_{\alpha\beta}=0$.

Assumption #3: the characteristic length scales of density and its intrinsic average, L_{ρ} and $L_{\langle\rho\rangle^{\alpha}}$ respectively, are infinite. This assumption leads to the density being considered as a spatially constant value over the averaging volume.

Furthermore, the constraints by which the validity of the macroscopic equations is satisfied are summarised as follows.

Constraint #1: The support of the weighting function G is much larger than the microscopic characteristic length scale of a quantity ψ, i.e. $r_{\Omega}>>L_{\psi}$ (Equation 4.9). This constraint ensures that the averaging volume is 'large enough' to contain all of the essential geometrical characteristics of the porous medium under consideration.

Constraint #2: The support of the weighting function *G* is much smaller than the macroscopic characteristic length scale, i.e. $r_{\Omega}<<L_{\langle\psi\rangle^{\alpha}}$ (Equation 4.10). This length constraint ensures that the size of averaging volume is negligible compared to the macroscopic flow field and led to a key relationship between the volumetric (superficial) and intrinsic averages of ψ as presented in Equation (4.21). Using this constraint, specifically for velocity and pressure as represented in Equations (B.28) and (B.35), led to removal of higher order derivative terms in Equations (B.33) and (B.34) and finally obtaining Equations (B.36) and (B.37) for the surface integrals in the momentum equation (Quintard and Whitaker 1994).

Constraint #3: The averaging volume Ω (and the weighting function G) should not change with local time. In other words, they should remain unchanged relative to the centroid of the volume over the total (material) time. If this constraint is satisfied, the local time derivative of porosity ($G*\gamma$) will be zero.

It is now possible to determine the turbulent stress and the drag terms (the last two terms in Equation 4.25). The closure developed by Whitaker (1996) will be employed for the surface integral, and an eddy-viscosity model for the turbulent stress.

4.2.1 Drag closure

Different closure models have been introduced in the literature for estimating the effect of solid skeleton on the macroscopic flow field. In the present study, the approximation of Whitaker (1996) is used to estimate the surface integral term (the last term on the right-hand side of Equation 4.25) as follows.

$$\frac{1}{\phi\left\langle\rho\right\rangle^{\alpha}}\left\{G*\left[\left(-\mathbf{I}\tilde{P}^{\alpha}+\mu\nabla\tilde{\mathbf{u}}^{\alpha}\right)\mathbf{n}_{\alpha\beta}\delta_{\alpha\beta}\right]\right\}=-\nu_0\,\mathbf{K}^{-1}\left\langle\mathbf{u}\right\rangle^{\Omega}-\nu_0\,\mathbf{K}^{-1}\mathbf{F}\left\langle\mathbf{u}\right\rangle^{\Omega} \tag{4.26}$$

where $\left\langle\mathbf{u}\right\rangle^{\Omega}$ is the superficial velocity vector (equal to $\phi\left\langle\mathbf{u}\right\rangle^{\alpha}$ according to Equation 4.23); and $\mathbf{K}$, $\mathbf{I}$ and $\mathbf{F}$ are the permeability, unit, and Forchheimer tensors, respectively. The first term on the right-hand side of the equation is known as the Darcy's term which shows the viscous effect and the second one is known as the Forchheimer term which represents the form-drag effect.

A well-known relationship to estimate the drag effects is Ergun's equation which was developed based on laboratory measurements of flow through packed beds (Ergun, 1952). Estimating the permeability and Forchheimer tensors in Whitaker (1996) closure model, respectively, as

$$\mathbf{K}=\frac{{d_s}^2\phi^3}{c_1\left(1-\phi\right)^2}\mathbf{I} \tag{4.27}$$

$$\mathbf{F}=\widehat{F}\left|\left\langle\mathbf{u}\right\rangle^{\alpha}\right|\mathbf{I}\ ,\ \widehat{F}=\frac{c_2\,\phi}{c_1\left(1-\phi\right)}\frac{d_s}{\nu_0} \tag{4.28}$$

will lead to Ergun's equation as

$$\frac{1}{\phi\langle\rho\rangle^{\alpha}}\left\{G*\left[\left(-\mathbf{I}\tilde{P}^{\alpha}+\mu\nabla\tilde{\mathbf{u}}^{\alpha}\right)\mathbf{n}_{\alpha\beta}\delta_{\alpha\beta}\right]\right\}= -c_1\frac{(1-\phi)^2}{\phi^2}\frac{\nu_0}{{d_s}^2}\langle\mathbf{u}\rangle^{\alpha}-c_2\frac{(1-\phi)}{\phi}\frac{1}{d_s}\langle\mathbf{u}\rangle^{\alpha}\left|\langle\mathbf{u}\rangle^{\alpha}\right| \tag{4.29}$$

where d_s is the mean size of solid particles of the porous media; ν_0 is the kinematic viscosity coefficient; and c_1 and c_2 are empirical constants. Ergun (1952) obtained values of 150 and 1.75 for c_1 and c_2, respectively, from his experiments although different values were also later introduced by others (e.g. in Macdonald et al., 1979 and van Gent, 1995).

4.2.2 Turbulence closure

In SPH, the turbulent stress can be estimated by the SPS model which is based on the eddy-viscosity assumption (Gotoh et al., 2001). It means, Equation (B.32) is approximated by Equation (2.14) as

$$\frac{\tau_{ij}}{\langle\rho\rangle^{\alpha}}=-2\nu_t S_{ij}+\frac{2}{3}k_t\delta_{ij} \tag{4.30}$$

where i and j denote coordinate components, τ_{ij} is component of the intrinsic shear stress tensor $\langle\tau\rangle^{\alpha}$, S_{ij} is component of the strain tensor $\langle\mathbf{S}\rangle^{\alpha}$ calculated by Equation (2.15), ν_t is the turbulence eddy-viscosity, k_t is the turbulence kinetic energy calculated by Equation (2.16) and δ_{ij} is the Kronecker delta function. In Equations (2.15) and (2.16), x is component of the position vector and u is component of the intrinsic average of velocity $\langle\mathbf{u}\rangle^{\alpha}$.

To estimate the eddy-viscosity ν_t, the Smagorinsky model (Equation 2.17) is usually applied. In Chapter 3 (Section 3.2.6), it was shown that the Smagorinsky model with standard C_s value (about 0.15) does not reproduce the required momentum balance

in the LES of highly-sheared channel flow cases where the roughness (solid phase) effect is modelled macroscopically. Therefore, the model for estimating ν_t should be chosen carefully based on the specific application.

4.3 Particle approximation of the macroscopic equations

The aim of the present section is to approximate the macroscopic governing equations developed in Section 4.2 (Equations 4.24 and 4.25) based on the SPH particle approximation scheme. The spatial derivative of a fluid quantity in those equations needs to be formulated in terms of the product of that quantity and the derivative of a weighting (kernel) function. This is the basic characteristic of the SPH method in discretising the equations. To bring the macroscopic governing equations (4.24) and (4.25) in the SPH discretised form, firstly, another convolution product is needed to be applied to those equations but using a different weighting function from that used in deriving the macroscopic equations. The convolution products will be later turned into summations using the standard SPH formulations. Although the same function *G* can be used, a different notation will be used here for the weighting (kernel) function in order to distinguish the solution process on the macroscopic field (Equations 4.24 and 4.25) from the determination of porosity $G*\gamma$ on the microscopic field (see Figure 4-4).

4.3.1 SPH-Averaged Macroscopic (SPHAM) governing equations

Volumetric average of an intrinsic average quantity of the macroscopic field like $\langle \psi \rangle^{\alpha}$ is carried out in a similar way to Equation (4.4), but with a distribution function equal to one. This is because there are no fluid-solid interfaces ($\delta_{\alpha\beta} = 0$) in the macroscopic field which contains only one phase over the whole domain. This is shown in Figure 4-2. Considering an averaging volume Υ on the macroscopic field (as shown in the

figure), the volumetric average of $\langle\psi\rangle^{\alpha}$ using a kernel function W with a support of r_{Υ} ($=2h_{\Upsilon}$) on the averaging volume will be written as follows

$$W*\langle\psi\rangle^{\alpha}=\int_{\Upsilon}W\left(\mathbf{r}-\mathbf{r}',h_{\Upsilon}\right)\langle\psi\rangle^{\alpha}\Big|_{\mathbf{r}'}\,d\mathbf{r}' \tag{4.31}$$

where h_{Υ} is the smoothing length of the kernel W. The convolution product of the spatial derivative of $\langle\psi\rangle^{\alpha}$ can be estimated by following the procedure adopted in Appendix A for deriving the averaging theorem of the spatial derivative. However, simply replacing ψ in Equation (A.6) with $\langle\psi\rangle^{\alpha}$ and noting that the distribution function γ is one as mentioned above and the second term on the right-hand side of the equation is zero due to the same reason ($\delta_{\alpha\beta}=0$), it will be possible to show that:

$$W*\left(\nabla\langle\psi\rangle^{\alpha}\right)=\nabla W*\langle\psi\rangle^{\alpha} \tag{4.32}$$

where

$$\nabla W*\langle\psi\rangle^{\alpha}=\int_{\Upsilon}\nabla W\left(\mathbf{r}-\mathbf{r}',h_{\Upsilon}\right)\langle\psi\rangle^{\alpha}\Big|_{\mathbf{r}'}\,d\mathbf{r}' \tag{4.33}$$

In fact, Equation (A.6) is the general form of this equation which represents the standard SPH approximation of a spatial derivative.

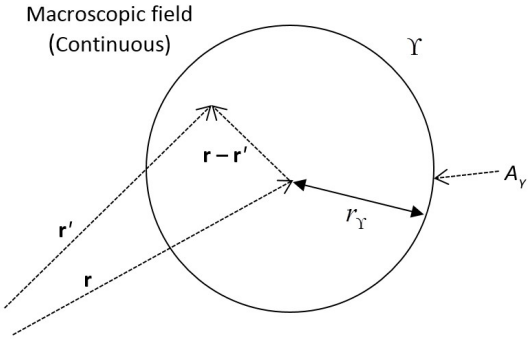

Figure 4-2 Averaging volume Υ on the macroscopic field.

It should be noted that the kernel function W should satisfy the following Delta function property condition as well as the compact, normalisation and symmetry conditions stated in Equations (4.6), (4.7) and (4.8), respectively (Liu and Liu, 2003).

$$\lim_{h_\Upsilon \to 0} W\left(\mathbf{r}-\mathbf{r}', h_\Upsilon\right) = \delta\left(\mathbf{r}-\mathbf{r}'\right) \tag{4.34}$$

Besides, length scale constraints similar to *constraints #2* and *#3* are also required here for approximating the macroscopic field using the kernel function W over the averaging volume Υ, i.e.

Constraint #4: The support of the kernel function W (i.e. r_Υ) should be much smaller than the characteristic length scale of the average flow field, i.e. $r_\Upsilon << L_{\langle\psi\rangle^\alpha}$.

Constraint #5: The averaging volume Υ (and the weighting function W) should not change by the local time. It means they should remain unchanged relative to the centroid of the volume over the total time. This constraint restricts the particles from changing their volumes when they move from one point to another. In other words, since particles are movable, their initial volume (relating to r_Υ or h_Υ) should be set equally over space and should remain unchanged over time. This is the reason that in the standard SPH formulation, using non-isotropic particle spacing, non-uniform computational discretisation, and particle refinement is not possible. This constraint (together with *constraint #4*) are required to satisfy that the convolution product of the material derivative of the macroscopic quantities like $\langle\rho\rangle^\alpha$ and $\langle\mathbf{u}\rangle^\alpha$ are equal to the material derivative of those quantities (see Equation 4.37).

It is noted that a constraint similar to *constraint #1* is not required to be imposed in the averaging process over the macroscopic field since the porous media domain is considered as a single-phase continuum.

In the following, the macroscopic field is averaged by constructing the convolution products of the macroscopic equations of mass and momentum (4.24) and (4.25) using the kernel function W as follows, respectively,

$$W * \left(\frac{D \langle \rho \rangle^{\alpha}}{Dt} \right) + W * \left[\frac{1}{\phi} \langle \rho \rangle^{\alpha} \nabla \cdot \left(\phi \langle \mathbf{u} \rangle^{\alpha} \right) \right] = 0 \tag{4.35}$$

$$\begin{aligned} W * \left(\frac{D \langle \mathbf{u} \rangle^{\alpha}}{Dt} \right) = & -W * \left(\frac{1}{\langle \rho \rangle^{\alpha}} \nabla \langle P \rangle^{\alpha} \right) + W * \mathbf{g} + W * \left[\frac{\mu}{\phi \langle \rho \rangle^{\alpha}} \nabla^2 \left(\phi \langle \mathbf{u} \rangle^{\alpha} \right) \right] \\ & - W * \left(\frac{\mu}{\phi \langle \rho \rangle^{\alpha}} \nabla \langle \mathbf{u} \rangle^{\alpha} \nabla \phi \right) - W * \left[\frac{1}{\phi \langle \rho \rangle^{\alpha}} \nabla \cdot \left(\phi \langle \tau \rangle^{\alpha} \right) \right] \\ & + W * \left\{ \frac{1}{\phi \langle \rho \rangle^{\alpha}} \left\{ G * \left[\left(-\mathbf{I} \tilde{P}^{\alpha} + \mu \nabla \tilde{\mathbf{u}}^{\alpha} \right) \mathbf{n}_{\alpha\beta} \delta_{\alpha\beta} \right] \right\} \right\} \end{aligned} \tag{4.36}$$

If the material derivatives of density and velocity are re-written in terms of the local time derivatives using Equation (B.11), then applying *assumption #3* and *constraints #4* and *#5*, it will be readily shown that

$$W * \left(\frac{D \langle \rho \rangle^{\alpha}}{Dt} \right) \approx \frac{D \langle \rho \rangle^{\alpha}}{Dt} \qquad \text{and} \qquad W * \left(\frac{D \langle \mathbf{u} \rangle^{\alpha}}{Dt} \right) \approx \frac{D \langle \mathbf{u} \rangle^{\alpha}}{Dt} \tag{4.37}$$

The second term on the left-hand side of the macroscopic mass Equation (4.35) is approximated using Equation (4.32) as follows

$$\begin{aligned} W * \left[\frac{1}{\phi} \langle \rho \rangle^{\alpha} \nabla \cdot \left(\phi \langle \mathbf{u} \rangle^{\alpha} \right) \right] &= \frac{1}{\phi} \langle \rho \rangle^{\alpha} \left\{ W * \left[\nabla \cdot \left(\phi \langle \mathbf{u} \rangle^{\alpha} \right) \right] \right\} \\ &= \frac{1}{\phi} \langle \rho \rangle^{\alpha} \left[\nabla W * \left(\phi \langle \mathbf{u} \rangle^{\alpha} \right) \right] \end{aligned} \tag{4.38}$$

It is noted that ϕ is taken out of the convolution product since it is calculated as $G * \gamma$ thereby not being a function of the limits of the integration with W. In addition, $\langle \rho \rangle^{\alpha}$ can also be taken out of the convolution product due to *assumption #3*. Similarly, the first, third, fourth and fifth terms on the right-hand side of Equation (4.36), are approximated as the following

$$-W * \left(\frac{1}{\langle \rho \rangle^{\alpha}} \nabla \langle P \rangle^{\alpha} \right) = -\frac{1}{\langle \rho \rangle^{\alpha}} \left(\nabla W * \langle P \rangle^{\alpha} \right) \tag{4.39}$$

$$W * \left[\frac{\mu}{\phi \langle \rho \rangle^{\alpha}} \nabla^2 \left(\phi \langle \mathbf{u} \rangle^{\alpha} \right) \right] = \frac{\mu}{\phi \langle \rho \rangle^{\alpha}} \left\{ \nabla W * \left[\nabla \left(\phi \langle \mathbf{u} \rangle^{\alpha} \right) \right] \right\} \tag{4.40}$$

$$-W * \left[\frac{\mu}{\phi \langle \rho \rangle^{\alpha}} \nabla \langle \mathbf{u} \rangle^{\alpha} \nabla \phi \right] = -\frac{\mu \nabla \phi}{\phi \langle \rho \rangle^{\alpha}} \left(\nabla W * \langle \mathbf{u} \rangle^{\alpha} \right) \tag{4.41}$$

$$-W * \left[\frac{1}{\phi \langle \rho \rangle^{\alpha}} \nabla \cdot \left(\phi \langle \tau \rangle^{\alpha} \right) \right] = -\frac{1}{\phi \langle \rho \rangle^{\alpha}} \left[\nabla W * \left(\phi \langle \tau \rangle^{\alpha} \right) \right] \tag{4.42}$$

The second and the last terms on the right-hand side of the momentum equation are estimated as follows since $\mathbf{g}$ is constant and the surface integral is independent of the limits of the integration with W because it is evaluated over Ω using the weighting function G .

$$W * \mathbf{g} = \mathbf{g} \left(W * 1 \right) = \mathbf{g} \tag{4.43}$$

$$\begin{aligned} W * & \left\{ \frac{1}{\phi \langle \rho \rangle^{\alpha}} \left\{ G * \left[\left(-\mathbf{I} \tilde{P}^{\alpha} + \mu \nabla \tilde{\mathbf{u}}^{\alpha} \right) \mathbf{n}_{\alpha\beta} \delta_{\alpha\beta} \right] \right\} \right\} \\ & = \frac{1}{\phi \langle \rho \rangle^{\alpha}} \left\{ G * \left[\left(-\mathbf{I} \tilde{P}^{\alpha} + \mu \nabla \tilde{\mathbf{u}}^{\alpha} \right) \mathbf{n}_{\alpha\beta} \delta_{\alpha\beta} \right] \right\} \left(W * 1 \right) \\ & = \frac{1}{\phi \langle \rho \rangle^{\alpha}} \left\{ G * \left[\left(-\mathbf{I} \tilde{P}^{\alpha} + \mu \nabla \tilde{\mathbf{u}}^{\alpha} \right) \mathbf{n}_{\alpha\beta} \delta_{\alpha\beta} \right] \right\} \end{aligned} \tag{4.44}$$

It is noted that $\left(W * 1 \right) = 1$ if one replaces $\langle \psi \rangle^{\alpha}$ with 1 in Equation (4.31) and considers the normalization condition of the kernel function W .

Substituting Equations (4.37) to (4.44) into Equations (4.35) and (4.36) gives the following equations for the SPH-Averaged Macroscopic (SPHAM) equations of mass and momentum, respectively.

$$\frac{D\left\langle \rho \right\rangle^{\alpha}}{Dt} = -\frac{1}{\phi}\left\langle \rho \right\rangle^{\alpha}\left[\nabla W *\left(\phi\left\langle \mathbf{u} \right\rangle^{\alpha}\right)\right] \tag{4.45}$$

$$\begin{aligned}\frac{D\left\langle \mathbf{u} \right\rangle^{\alpha}}{Dt} = &-\frac{1}{\left\langle \rho \right\rangle^{\alpha}}\left(\nabla W *\left\langle P \right\rangle^{\alpha}\right)+\mathbf{g}+\frac{\mu}{\phi\left\langle \rho \right\rangle^{\alpha}}\left\{\nabla W *\left[\nabla\left(\phi\left\langle \mathbf{u} \right\rangle^{\alpha}\right)\right]\right\} \\ &-\frac{\mu\nabla\phi}{\phi\left\langle \rho \right\rangle^{\alpha}}\left(\nabla W *\left\langle \mathbf{u} \right\rangle^{\alpha}\right)-\frac{1}{\phi\left\langle \rho \right\rangle^{\alpha}}\left[\nabla W *\left(\phi\left\langle \tau \right\rangle^{\alpha}\right)\right] \\ &+\frac{1}{\phi\left\langle \rho \right\rangle^{\alpha}}\left\{G *\left[\left(-\mathbf{I}\tilde{P}^{\alpha}+\mu\nabla\tilde{\mathbf{u}}^{\alpha}\right)\mathbf{n}_{\alpha\beta}\delta_{\alpha\beta}\right]\right\}\end{aligned} \tag{4.46}$$

where $\phi = G * \gamma$. Besides, $\left\langle \tau \right\rangle^{\alpha}$ and the surface integral in the last term on the right-hand side of the momentum equation are estimated by the closure models presented in Sections 4.2.2 and 4.2.1, respectively.

To solve the developed SPHAM equations by the programming codes, it is required to bring those equations in the discretised form, i.e. expressing the convolution products (averages) in terms of summations over a discretised computational domain.

4.3.2 Discretised form of the SPHAM equations

By expressing Equations (4.31) and (4.33) in the following discretised form, the SPH convolution product of an intrinsic quantity $\left\langle \psi \right\rangle^{\alpha}$ and its spatial derivative at the position of a generic particle a are formulated in terms of the values of the intrinsic quantity at the position of neighbouring particles b.

$$\left(W *\left\langle \psi \right\rangle^{\alpha}\right)_a \approx \sum_b W\left(\mathbf{r}_a - \mathbf{r}_b, h_{\Upsilon}\right)\left\langle \psi \right\rangle_b^{\alpha}\Delta V_b \tag{4.47}$$

$$\left(\nabla W *\left\langle \psi \right\rangle^{\alpha}\right)_a \approx \sum_b \nabla W\left(\mathbf{r}_a - \mathbf{r}_b, h_{\Upsilon}\right)\left\langle \psi \right\rangle_b^{\alpha}\Delta V_b \tag{4.48}$$

where ΔV_b denotes the volume of neighbouring particle b. The particle volume of a generic particle like a is computed as

$$\Delta V_a = \frac{m_a}{\rho_a^{app}} \tag{4.49}$$

Where m_a and ρ_a^{app} are the particle's mass and apparent density, respectively. Apparent density is the volume occupied by the particle, not the density of the fluid. Therefore, it is equivalent to the particle volumetric density which is approximated according to Equation (4.23) as

$$\rho_a^{app} = \langle \rho \rangle_a^{\Omega} = \phi_a \langle \rho \rangle_a^{\alpha} \tag{4.50}$$

in which ϕ_a is the porosity at the position of the particle. Therefore

$$\Delta V_a = \frac{m_a}{\phi_a \langle \rho \rangle_a^{\alpha}} \tag{4.51}$$

According to this definition and knowing that the intrinsic average of density remains nearly unchanged due to incompressibility of flow (*assumption #3*), when a fluid particle moves into an area with lower porosity, its volume increases (and vice versa) to satisfy the conservation of fluid mass. This process is depicted in Figure 4-3.

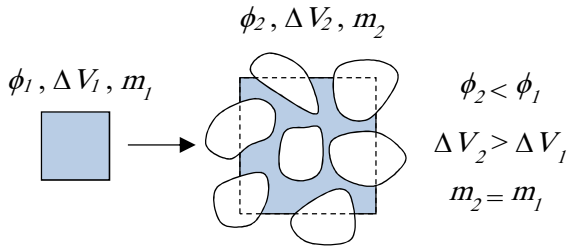

Figure 4-3 Particle volume change due to change of porosity. φ, ΔV and m are porosity, particle volume, and fluid mass confined in the volume, respectively.

If Equation (4.51) is used for estimating the volume of neighbouring particles ΔV_b in Equations (4.47) and (4.48), those convolution products will be then represented as follows.

$$\left(W * \langle \psi \rangle^{\alpha}\right)_a \approx \sum_b \frac{m_b}{\phi_b \langle \rho \rangle_b^{\alpha}} W\left(\mathbf{r}_a - \mathbf{r}_b, h_{\Upsilon}\right) \langle \psi \rangle_b^{\alpha} \tag{4.52}$$

$$\left(\nabla W * \langle \psi \rangle^{\alpha}\right)_a \approx \sum_b \frac{m_b}{\phi_b \langle \rho \rangle_b^{\alpha}} \nabla W\left(\mathbf{r}_a - \mathbf{r}_b, h_{\Upsilon}\right) \langle \psi \rangle_b^{\alpha} \tag{4.53}$$

These equations acknowledge that the solution of the governing equations at a particle's location is performed by averaging over those neighbouring particles which are located in a distance less than $r_{\Upsilon} (= 2h_{\Upsilon})$ from the central particle using the kernel function W (see Figure 4-4 b). The support of the kernel function (r_{Υ}) should be chosen to be small enough to satisfy *constraint #4* and should not change during time to satisfy *constraint #5*.

To estimate the porosity at the position of particles, as seen from Equation (4.22), the weighting function G is used to spatially average the distribution function γ (which has prescribed values) over the microscopic field. Since the solid phase (porous skeleton) is fixed, the porosity distribution can be described on an Eulerian domain. Hence, a background mesh consisting of fixed grid points is defined where the information of the microscopic field (i.e. the location of fluid and solid phases) is held (see Figure 4-4 a). The distribution function is determined at each grid point using Equation (4.3) and then the porosity at particle a is approximated by the following equation which is the discretised form of Equation (4.22).

$$\phi_a = \left(G * \gamma\right)_a \approx \sum_c G\left(\mathbf{r}_a - \mathbf{r}_c, h_{\Omega}\right) \gamma_c \Delta V_c \tag{4.54}$$

This equation shows that the porosity at the position of a SPH particle is computed by averaging the values of the distribution function of grid points located in a distance less than r_{Ω} ($2h_{\Omega}$) from the particle using the weighting function G (Figure 4-4 a). In this equation, γ_c denotes the value of the distribution function at the grid point c which is equal to one or zero, if the grid point locates in the fluid or solid phases,

respectively (Equation 4.3, Figure 4-4 a). ΔV_c is the volume of the mesh element associates with the grid point c which is equal to l_c^2 and l_c^3 in 2D and 3D respectively, if one considers a regular mesh of grid points with spacing l_c (see Figure 4-4 a). The grid spacing should be chosen to be small enough so as to resolve the fluid-solid interfaces in the porous media adequately; and the smoothing length h_Ω of the weighting function G should be chosen to be large enough to satisfy *constraint #1*.

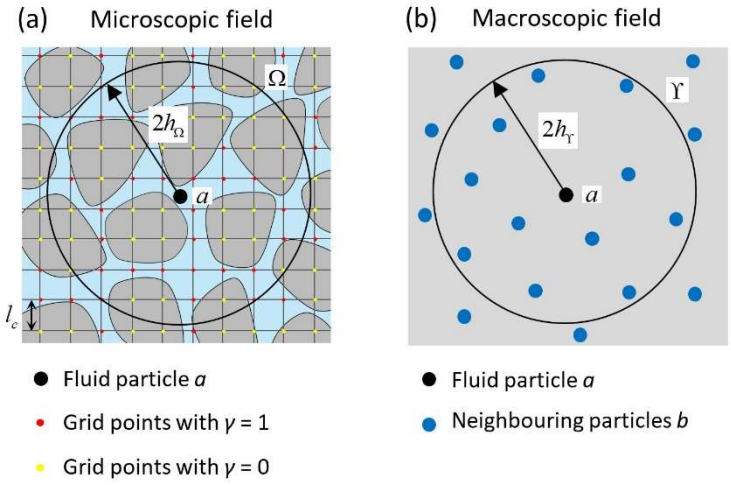

Figure 4-4 A schematic 2D representation of the microscopic and macroscopic fields, a) Computing porosity at the position of a particle over the microscopic field using the weighting function *G*. b) Solution of the governing equations at the position of a particle using the kernel function *W* over the macroscopic field.

For approximating the time derivative of an intrinsic quantity, the following finite difference scheme is used.

$$\frac{D\langle\psi\rangle_a^\alpha}{Dt} \approx \frac{\langle\psi\rangle_a^\alpha\Big|^{(t+\Delta t)} - \langle\psi\rangle_a^\alpha\Big|^{(t)}}{\Delta t} \tag{4.55}$$

where t and Δt denote computational time and its increment.

Now using Equations (4.52) to (4.55), it is possible to discretise the SPHAM equations (4.45) and (4.46) so that they can be solved at the position of a set of discrete moving elements (particles). The detailed procedure is presented in Appendix C where the

discretised version of the SPHAM equations of mass and momentum are written in Equations (C.5) and (C.15), respectively. After manipulation, these equations are written as the following,

$$\frac{\rho_a\Big|^{(t+\Delta t)} - \rho_b\Big|^{(t)}}{Dt} = \sum_b \frac{m_b}{\phi_a \phi_b} \left(\phi \mathbf{u}\right)_{ab} \nabla_d W_{ab} \tag{4.56}$$

$$\begin{aligned} \frac{\mathbf{u}_a\Big|^{(t+\Delta t)} - \mathbf{u}_b\Big|^{(t)}}{\Delta t} = & -\sum_b \left\{ \frac{m_b}{\phi_b} \nabla_d W_{ab} \frac{P_a + P_b}{\rho_a \rho_b} \right\} + \mathbf{g} \\ & + \sum_b \left\{ \frac{\mu m_b}{\phi_a \phi_b} \frac{\mathbf{r}_{ab} \cdot \nabla_d W_{ab}}{\left|\mathbf{r}_{ab}\right|^2 + \eta^2} \frac{2\left(\phi \mathbf{u}\right)_{ab} + \phi_{ab} \mathbf{u}_{ab}}{\rho_a \rho_b} \right\} \\ & - \sum_b \left\{ \frac{m_b}{\phi_a \phi_b} \nabla_d W_{ab} \cdot \frac{\phi_a \boldsymbol{\tau}_a + \phi_b \boldsymbol{\tau}_b}{\rho_a \rho_b} \right\} - \mathbf{A}_a \end{aligned} \tag{4.57}$$

where

$$\begin{aligned} & \rho_a = \left\langle \rho \right\rangle_a^\alpha \;\; , \;\; \rho_b = \left\langle \rho \right\rangle_b^\alpha \\ & P_a = \left\langle P \right\rangle_a^\alpha \;\; , \;\; P_b = \left\langle P \right\rangle_b^\alpha \\ & \mathbf{u}_a = \left\langle \mathbf{u} \right\rangle_a^\alpha \;\; , \;\; \mathbf{u}_b = \left\langle \mathbf{u} \right\rangle_b^\alpha \\ & \boldsymbol{\tau}_a = \left\langle \tau \right\rangle_a^\alpha \;\; , \;\; \boldsymbol{\tau}_b = \left\langle \tau \right\rangle_b^\alpha \\ & \mathbf{u}_{ab} = \left\langle \mathbf{u} \right\rangle_a^\alpha - \left\langle \mathbf{u} \right\rangle_b^\alpha \\ & \phi_{ab} = \phi_a - \phi_b \\ & \left(\phi \mathbf{u}\right)_{ab} = \phi_a \left\langle \mathbf{u} \right\rangle_a^\alpha - \phi_b \left\langle \mathbf{u} \right\rangle_b^\alpha \\ & \mathbf{r}_{ab} = \mathbf{r}_a - \mathbf{r}_b \\ & \nabla_d W_{ab} = \nabla W \left(\mathbf{r}_a - \mathbf{r}_b, h_\Upsilon\right) \end{aligned} \tag{4.58}$$

and $\mathbf{A}_a$ represents the surface integral terms in Equation (4.46). It incorporates the effect of porous solid skeleton on the fluid particle and can be approximated by the closure model introduced in Section 4.2.1. Moreover, the porosity at the position of particles is calculated by Equation (4.54) over the background mesh.

All derivative terms in the discretised SPHAM equations of mass and momentum are presented in a symmetric form. The divergence in the mass equation vanishes for a uniform macroscopic velocity distribution and the derivatives in the momentum equation conserve the linear momentum so that in the absence of external forces, the total linear momentum of the continuum is exactly preserved. However, the momentum equation may not conserve the angular momentum. According to Khayyer et al. (2008), the angular moment between a pair of particles will vanish only if the internal stress tensor is isotropic. Therefore, the pressure gradient term preserves the angular momentum while the viscosity and turbulent stress terms do not. To resolve this issue, the correction of Khayyer et al. (2008) can be applied into the kernel gradients thereby enforcing preservation of angular momentum for viscous internal forces. Khayyer et al. (2008) stated that in SPH simulation, preservation of angular momentum is necessary for the cases with violent free surface deformations such as breaking of water waves. Although those large surface deformations are not usually observed in water flows in porous media, correcting kernel gradients as carried out by Khayyer et al. (2008) can enhance the computational efficiency.

In the WCSPH method, the equation of state (3.11) is employed to compute the pressure of a particle explicitly from the change in its density, where ρ_0 is the reference intrinsic density of the particle, and c_0 is the speed of sound.

Figure 4-5 illustrates a time advancement algorithm for the model if one adopts a two-step predictor-corrector scheme for time implementation (see Section 3.1.3). In this flow chart, $\rho^{(t)}$, $u^{(t)}$ and $r^{(t)}$ denote density, component of intrinsic velocity vector, and component of particle position, respectively, at time t; $\rho^{(t+\Delta t/2)}$, $u^{(t+\Delta t/2)}$ and $r^{(t+\Delta t/2)}$ denote those quantities at mid-time $t+\Delta t/2$; and $\rho^{(t+\Delta t)}$, $u^{(t+\Delta t)}$ and $r^{(t+\Delta t)}$ show them at time $t+\Delta t$. Besides, $D_{mass}^{(t)}$ and $D_{mass}^{(t+\Delta t/2)}$ denote the right-hand side of mass equation (4.56) at times t and $t+\Delta t/2$, while $D_{moment}^{(t)}$ and $D_{moment}^{(t+\Delta t/2)}$ show the right-hand side of momentum equation (4.57) at those time intervals, respectively.

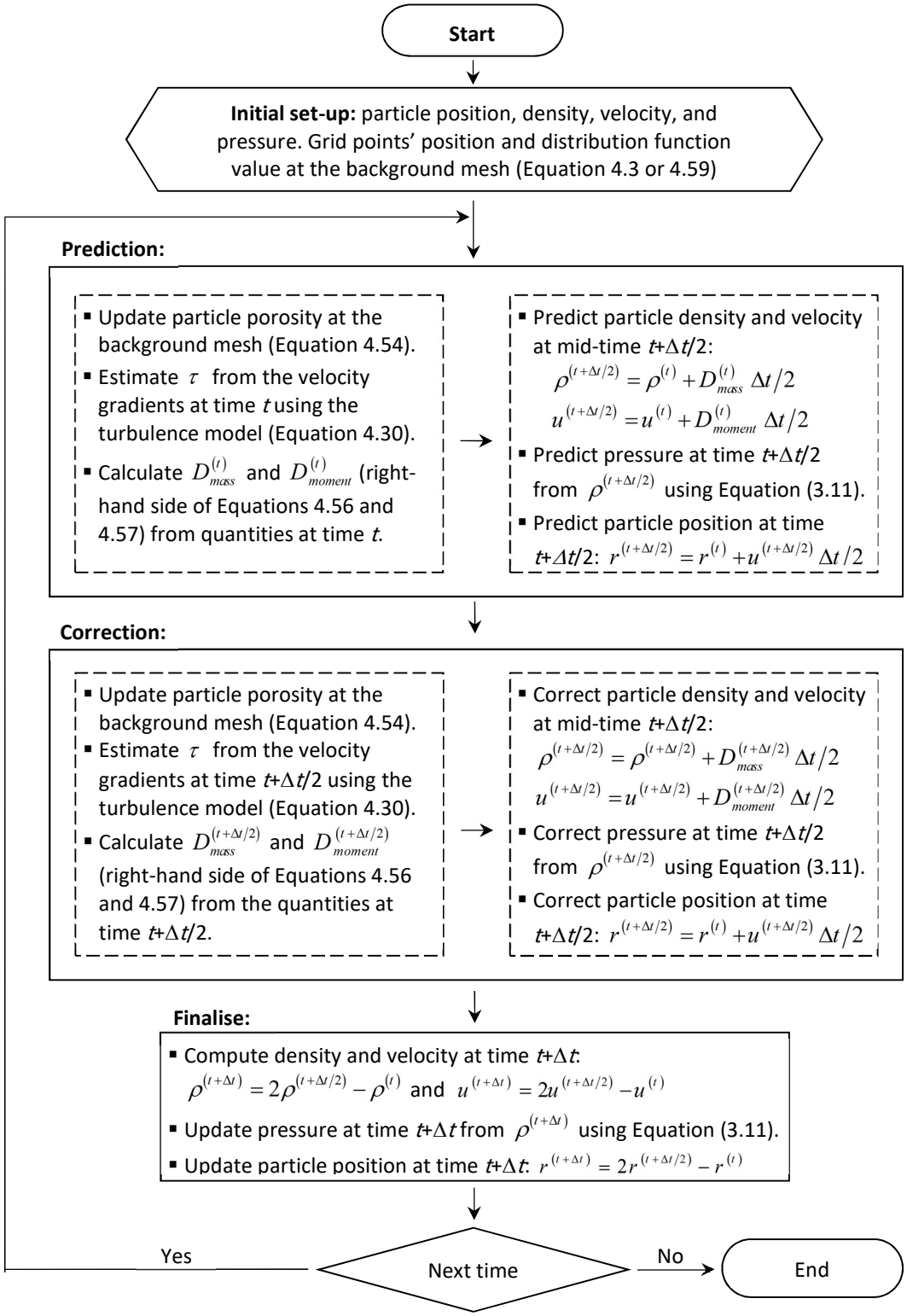

Figure 4-5 Time advancement algorithm.

4.4 Determination of porosity and treating interfacial boundaries in practical situations

The system governed by Equations (4.56) and (4.57) is defined as a unified framework, i.e. the equations are solved at a single computational domain including the porous and free flow regions. The change in the system from one region to another is addressed by the change in the porosity. A fixed background mesh is used which contains the information of the distribution function at each grid point (Figure 4-4 a). The mesh resolution should be high enough to resolve the fluid-solid interfaces adequately. To determine the porosity at the position of a particle, the distribution function is averaged over the background mesh using the weighting function G by Equation (4.54). This function holds the *constraints #1, #2* and *#3*. In view of that the averaging at the microscopic field should provide constant values for $G*\gamma$ (i.e. the averaging volume should contain all the essential geometrical characteristics) in the porous region, *constraint #1* may be expressed in the form of $r_\Omega >> L_d$ where L_d is a characteristic length of the solid matrix. In fact, it is assumed that L_ψ is in the order of L_d (Figure 4-6, left). Quintard and Whitaker (1993) pointed out that this constraint can be considered as $r_\Omega \approx L_d$ for an ordered porous media, i.e. a media 'composed of spherical, micro porous particles'.

Quintard and Whitaker (1994) noted that their analysis to derive the Stokes equation is of questionable validity since the constraints they used, similar to *constraints #1* and *#2*, may not be satisfied in the region near an impermeable solid. This issue could be even more important at the interfacial boundary with a water flow over which the average field may have large variations in properties, i.e. when the interfacial boundary layer is highly sheared. In such a condition, $L_{\langle\psi\rangle^\alpha}$ is not too much larger than L_d at the interface so that satisfying *constraints #1* and *#2*, i.e. $L_d << r_\Omega << L_{\langle\psi\rangle^\alpha}$,

seems to be not straightforward. Figure 4-6 shows an example of a highly sheared interfacial boundary between a porous medium (region 1) and a free (clear water) flow (region 3) where an average flow quantity $\langle \psi \rangle^{\alpha}$ changes sharply over a relatively thin layer (region 2).

In practical applications, there is often no definitive information about the fluid-solid interfaces so that the determination a priori of the distribution function for Equation (4.3) is not always feasible. Moreover, applying Equation (4.54) for computing porosity needs a 3D representation of the distribution function γ. In the following text, two situations are discussed when it is needed to modify some definitions in order to be able to apply the model to practical applications containing highly sheared turbulent flows over a porous boundary in 2D.

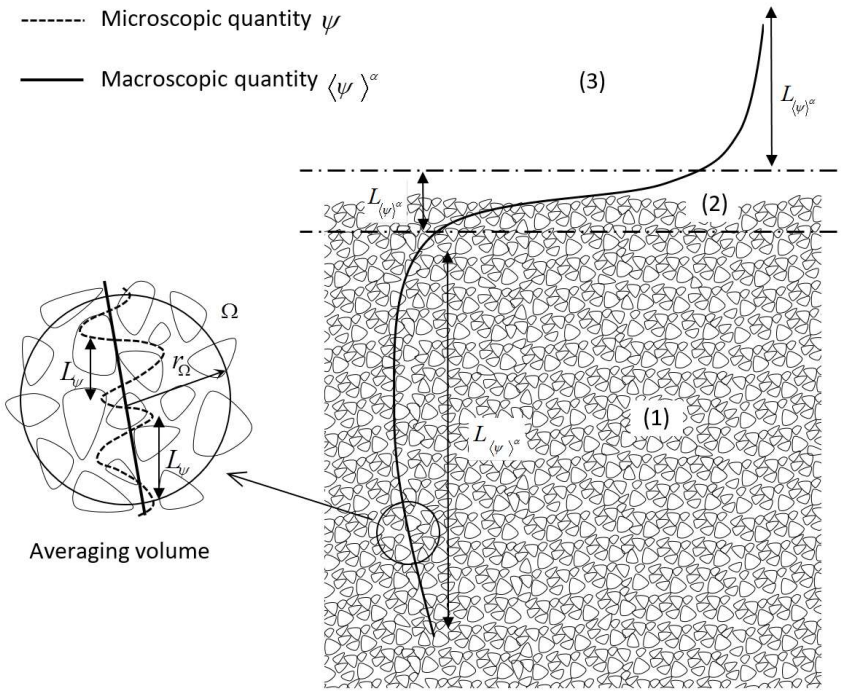

Figure 4-6 A schematic view of distribution of an arbitrary average flow quantity. (1), (2), and (3) denote porous media, interface layer, and free flow regions respectively.

4.4.1 Situation #1

In practical cases, the geometrical arrangement of the solid material is often unknown. Instead, a single value is usually introduced for porosity which is in fact representative of the mean porosity of the whole media. This value is obtained in the laboratory as the volume of fluid a medium contains divided by the total volume of the medium. Hence, to be able to apply the present model in 2D simulation of practical cases where the exact value of the distribution function γ is not available, the definition of this function needs to be modified. Here, Equation (4.3) is redefined as the following,

$$\gamma = \begin{cases} 1.0 & \text{in the free flow (clear water) region} \\ \phi_0 & \text{in the porous region} \end{cases} \tag{4.59}$$

where ϕ_0 is the mean value of porosity for the media. By this modification, it has been assumed that the media is homogeneous and continuous. In this case, *constraint #1* is satisfied instinctively since using any size of r_Ω will provide constant values for $G * \gamma$ within the porous region. Nonetheless, at the interfacial boundary, r_Ω needs to be specified so as to reproduce the physical transition of the average flow field from the porous region to the sheared flow. Therefore, in the present situation, both *constraints #1* and *#2* can be represented as $r_\Omega \approx L_{d,i}$ where $L_{d,i}$ is a characteristic length of the solid matrix at the interfacial boundary (region 2 in Figure 4-6), such as the mean size of solid particles near the boundary. Hence, the constraints associated with the weighting function G (for averaging over the background mesh) as well as the constraints associate with W (*constraints #5* and *#6* of r_Υ) may be summarised as the following if one considers the present situation.

(a) $r_\Omega \approx L_{d,i}$,

(b) r_Ω and *G* should not change with time,

(c) $r_\Upsilon << L_{\langle \mathbf{u} \rangle^\alpha}$, (4.60)

(d) r_Υ and W should be set equally over space and should remain unchanged over time.

It is noted that for point (d) of this constraint, r_Υ and W should not only remain unchanged over time, but also be set equally over space, while according to point (b), r_Ω and G only need to be unchanged with time. This is because r_Υ associates with fluid particles which are movable, while r_Ω associates with the background mesh which is fixed. It is also noted that point (c) (*constraint #4*) is written only in terms of average velocity field, because this constraint is instinctively satisfied for other flow quantities such as density and pressure due to the incompressibility of flow. In other words, in the case of interaction of an incompressible sheared flow with a porous medium, velocity is the only flow quantity which may have large variations over the interfacial boundary and need careful considerations with regard to *constraint #4*. Since in SPH, the support of weighting function has a certain relation with the particle spacing (smoothing length is usually taken as 1.2 times the particle spacing), a sufficient computational resolution will therefore satisfy the requirement $r_\Upsilon << L_{\langle \mathbf{u} \rangle^\alpha}$.

If one employs the present treatment, a boundary which separates the free flow (clear water) and porous regions should be defined so that Equation (4.59) can be used for determination of γ . This is not easy particularly when the surface of the porous media is rough, namely when the size of solid particles on the surface is relatively large compared to the characteristic dimension of the free flow (for example flow depth). Figure 4-7 illustrates the determination of the interface of an arbitrary porous medium with a free flow. The two regions are separated by a line (namely a separating line in 2D or a separating surface in 3D). The question is that how to determine the

location of the separating line/surface in a numerical simulation. One may consider the crest of solid particles at the interface as the separating line/surface. It seems a fair approximation when the surface is smooth, i.e. the roughness at the surface is relatively small compared to the flow characteristic length. However, one may consider the so called 'zero-plane displacement' level for the interfacial separating line, when the surface is rough. Zero-plane displacement is discussed in detail by Nikora et al. (2002). Figure 4-7 (c) shows the distribution of γ based on the separating line, while Figure 4-7 (d) presents the distribution of the porosity obtained by Equation (4.54) which guarantees a smooth change of porosity at the interfacial boundary from the porous media to the free flow. The curvature of the porosity profile at the interface depends on the type of the weighting function G as well as its support size r_Ω which is determined based on Equation (4.60).

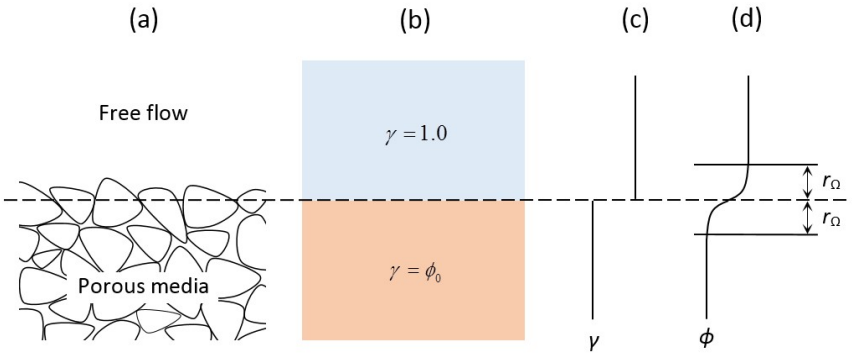

Figure 4-7 Determination of distribution function and porosity by the separating line/surface.

4.4.2 Situation #2

Sometimes a spatial distribution of porosity is available so that it can be used directly in the model without the need of averaging γ on a background mesh. For instance, the porosity can be measured in a laboratory flume at different vertical strips as the proportion of the volume of fluid contained in the strip to the total volume of the strip. In this case, a smooth transitional interface layer may be observed from the

porous media to the free flow, particularly when the surface roughness is quite large. In the cases in which the measured values of porosity at the interface are not available, it may still be possible to define a certain profile for interfacial porosity based on the size, shape and geometry of the solid particles. In other words, when the knowledge about the condition of solid material at the interface is available, the porosity could be approximated directly without the need of using a background mesh and solving Equation (4.54). An example is illustrated in Figure 4-8 where the porosity has the values of ϕ_0 and 1 in the porous and free flow regions, respectively, as well as a transition between those values at the interface boundary which is related to the physical properties of the solid particles. In this situation, the only constraints to be satisfied are

$$\begin{aligned} &\text{(a) } r_\Upsilon << L_{\langle \mathbf{u} \rangle^\alpha}, \\ &\text{(b) } r_\Upsilon \text{ and } W \text{ should be set equally over space and} \\ &\quad \text{should remain unchanged over time.} \end{aligned} \tag{4.61}$$

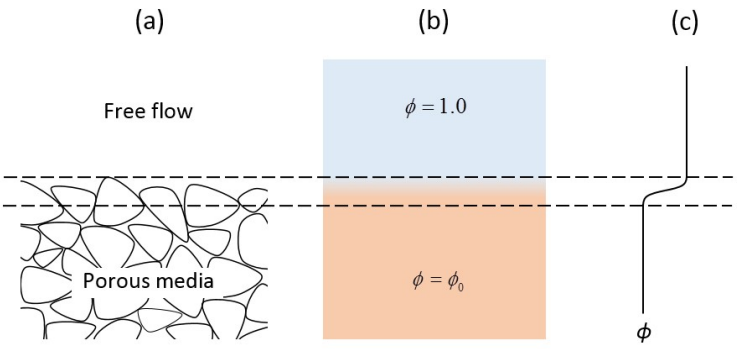

Figure 4-8 Determination of porosity at a transitional interface layer.

4.5 Summary

In this chapter, firstly, a spatial averaging method was introduced following Quintard and Whitaker (1993, 1994), then it was applied to the microscopic equations of mass

and momentum using relevant convolution products to derive the macroscopic governing equations of fluid flow through fixed porous media in terms of intrinsic averages of flow quantities. The assumptions made to arrive at the present form of the equations as well as the constraints required for validity of the equations were highlighted. The drag effect of the porous solid skeleton and the effect of turbulence on the average flow field were incorporated into the momentum equation as two stress terms. Then, another convolution product was applied to the developed macroscopic equations but using a different weighting function in order to distinguish between the determination of porosity at the microscopic field and the calculation of flow quantities at the macroscopic field. The equations were then discretised in a symmetric form using the standard SPH formulation, where the effect of fluid particle volume change (due to porosity change) was incorporated. Finally, two practical situations of 2D flow interaction with porous media were introduced and then, the determination of porosity as well as modification of the length constraint was investigated.

Now, the desirable macroscopic equations for SPH, the closure models, and the relevant numerical treatments are available; and the limitations and constraints are clear. In the next chapter, a model will be constructed based on the present mathematical developments in order to simulate several engineering applications.

Chapter 5 Modelling Flow Interaction with Porous Media at a Macroscopic Scale: II) Applications

The aim of the present chapter is to test the model developed in the previous chapter by simulating some general applications of flow interaction with porous media. A 2D model will be developed based on the SPHAM equations of mass (4.45) and momentum (4.46) which are presented in the discretised form in Equations (4.56) and (4.57), respectively. The algorithm presented in Figure 4-5 will be applied for time implementation. Three test cases will be simulated, and the results will be compared to the experimental data in order to verify the accuracy of the developed model. The test cases are i) dam break wave through porous dams; ii) solitary wave interaction with a porous structure; and ii) solitary wave run-up on smooth, rough, and porous breakwaters. These case studies are selected to test the capacity of the model in dealing with flow and wave interactions with porous structures of different types. Existing experimental data is available for these three cases in the literature. The first case is considered as a bench-mark test which has been employed in many studies to test the numerical models. In contrast to the first one, in the experimental study of the second case, there is available data of velocity distributions around a porous structure which provides the opportunity to test the model capacity in estimating the velocity field. The third case study provides data of water surface elevation for wave

interaction with three different breakwater slopes, i.e. smooth, rough, and porous beds. Therefore, the capacity of the model in identifying the effect of different bed conditions can be examined. In addition, this data set has not been employed yet in similar numerical studies so that there is no existing knowledge on the choice of numerical parameters.

Firstly, the computational specifications of the present 2D model including boundary conditions, initial set-up of particles and background mesh will be presented in Section 5.1, and then the model applications will be carried out in Sections 5.2, 5.3 and 5.4. In Section 5.5, the effect of computational resolution on the result and the satisfaction of required length constraints will be investigated. Finally, a summery will be provided in Section 5.6.

5.1 Computational specifications

Two types of boundary conditions to be considered in the present study are free surface and wall boundaries. In the WCSPH method, free surface is tracked with no special treatment. For the wall boundaries, several layers of dummy particles are placed beyond the boundary line to fill the truncated kernel area in the vicinity of the boundary. These dummy particles are fixed through the simulation and their velocity is set to zero. The momentum equations are not solved at these particles, while their density changes are computed through the conservation of mass (Equation 4.56) and then their pressure is computed by Equation (3.11) so that enough pressure gradient force is reproduced to prevent the fluid particles from penetrating the wall boundaries.

The particle volume is defined by Equation (4.51) in which $\phi\langle\rho\rangle^{\alpha}$ denotes the particle's apparent density. Since particle's mass and intrinsic density are nearly constant, the volume of a particle may change depending on its porosity as its position

changes (Figure 4-3). If the particle volume at a position with porosity ϕ_1 is ΔV_1, its volume at a position with porosity ϕ_2 will be $\phi_1 \Delta V_1 / \phi_2$. Therefore, if the initial particle spacing at the free flow region (with porosity 1.0) is set to l_0, then the initial spacing of a generic particle with porosity ϕ_a should be set according to the following relationship.

$$l_a = \frac{l_0}{\sqrt[N]{\phi_a}} \tag{5.1}$$

where N is the number of dimensions which is 2 in the present model.

In the present applications, at the initial time, particle intrinsic velocity is set to zero; particle intrinsic pressure has a hydrostatic distribution with a zero value at water surfaces; and initial intrinsic density is computed by Equation (3.11) based on the initial intrinsic pressure.

The situation #1 presented in Section 4.4.1 is adopted here since the model is 2D and the exact location of the fluid-solid interfaces is not available. Therefore Equation (4.59) is employed to determine the distribution function γ of the grid points. According to the treatment adopted here, porosity at the position of particles in the pure fluid and pure porous regions (fully white and fully grey areas respectively, in Figure 5-1 a) is set to constant values of 1.0 and ϕ_0, and a background mesh with regular square elements is defined as to cover only the required area at the interface where the porosity changes, instead of using a mesh for the whole computational domain. Therefore, Equation (4.54) is not used to calculate the porosity of particles which are located in the pure fluid and pure porous regions. Only the porosity of those particles which are in the transition zone (hatched area in Figure 5-1 a) is calculated by averaging γ at the background mesh which is extended to $2r_\Omega$ far from the separating line in both directions, as depicted in Figure 5-1 (a).

In the present simulations, the separating line is considered to be $0.5d_s$ far from the crest of the first row of solid particles at the interface towards the media (d_s is the

mean diameter of the particles). As an example, Figure 5-1 (b) depicts an arbitrary porous medium with spherical particles where the separating line is set at the middle of the first row of particles. Following the length constraint (4.60) (a), the diameter of the averaging volume Ω is set equal to d_s, i.e. $r_\Omega = 0.5d_s$ and $h_\Omega = 0.25d_s$. In fact, it is assumed that the thickness of the layer at the interface over which the porosity changes from ϕ_0 to 1 is equal to the mean diameter of solid particles (see Figure 5-1 a, the hatched area). The mesh spacing l_c is taken as $h_\Omega / 1.2$ so that enough grid points lie in the averaging volume Ω for porosity calculation.

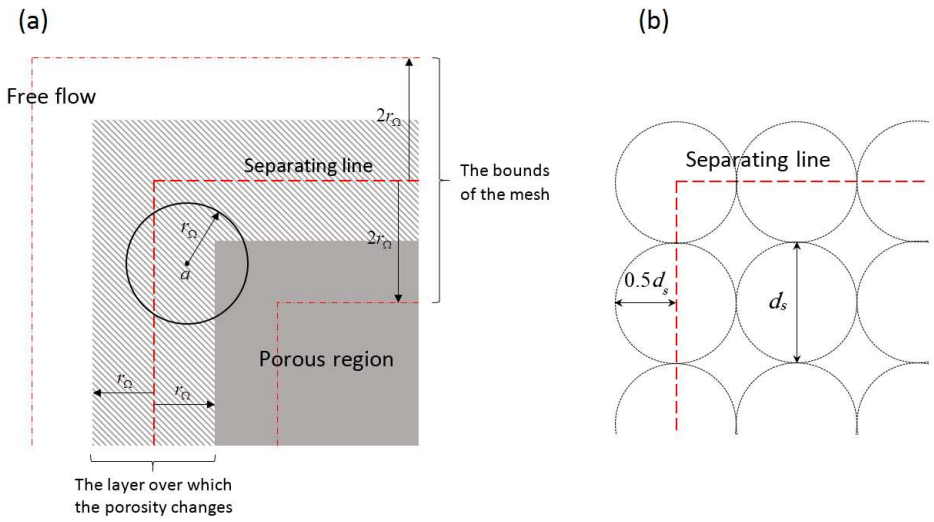

Figure 5-1 Computation of porosity in the present simulations: (a) The porous, free flow and transition zones marked by fully grey, fully white and hatched areas, respectively, with the bounds of the background mesh (dash-dotted lines); (b) separating line with a distance of 0.5d_s from the crest of solid particles.

Other computational specifications in the present simulations of all three test cases are as the following. Three layers of fixed dummy particles are placed at the wall boundaries. The number of layers depends on the support of the kernel function r_Υ ($= 2h_\Upsilon$). Since in the present study h_Υ is set to $1.2\,l_0$, r_Υ is equal to $2.4\,l_0$. Therefore, three layers of dummy particles are used at impermeable wall boundaries. The

reference intrinsic density ρ_0 is 1000 kg/m^3 (water density) and the speed of sound c_0 is set according to the following equation in order to restrict the compressibility to be less than 1%.

$$c_0 = 10\sqrt{9.81 H_0} \tag{5.2}$$

where H_0 is the initial water depth. The dynamic and kinematic viscosity coefficients, μ and ν_0 are 10^{-3} kg/(m.s) and 10^{-6} m^2/s, respectively. The computational time step Δt is chosen according to the CFL condition (Equation 3.15). A Shepard density filter is applied at every 30 computational time steps in order to minimize the pressure noise. The cubic Spline kernel function of Monaghan and Lattanzio (1985) is for both G and W as

$$G\left(\mathbf{r}-\mathbf{r}', h_\Omega\right) = \lambda_\Omega \times \begin{cases} 2/3 - {q_\Omega}^2 + {q_\Omega}^3/2 & 0 \le q_\Omega < 1 \\ \left(2-q_\Omega\right)^3/6 & 1 \le q_\Omega < 2 \\ 0 & 2 \le q_\Omega \end{cases} \tag{5.3}$$

$$W\left(\mathbf{r}-\mathbf{r}', h_\Upsilon\right) = \lambda_\Upsilon \times \begin{cases} 2/3 - {q_\Upsilon}^2 + {q_\Upsilon}^3/2 & 0 \le q_\Upsilon < 1 \\ \left(2-q_\Upsilon\right)^3/6 & 1 \le q_\Upsilon < 2 \\ 0 & 2 \le q_\Upsilon \end{cases} \tag{5.4}$$

where $q_\Omega = \left|\mathbf{r}-\mathbf{r}'\right|/h_\Omega$ and $q_\Upsilon = \left|\mathbf{r}-\mathbf{r}'\right|/h_\Upsilon$. Besides, λ_Ω and λ_Υ are equal to $15/7\pi {h_\Omega}^2$ and $15/7\pi {h_\Upsilon}^2$ in 2D. The function in the above equations satisfies the required conditions mentioned in Equations (4.5), (4.6), (4.7), (4.8) and (4.34).

Regarding the effect of turbulence, the SPS model (Section 4.2.2, Equation 4.30) is applied to estimate the turbulent shear stress. In order to estimate the eddy-viscosity ν_t, the Smagorinsky model with C_s =0.15 is applied. In Chapter 3, Section 3.2.6, it was shown that the Smagorinsky model with C_s =0.15 is unable to reproduce the correct amount of shear stress for highly-sheared free surface channel flows over rough bed boundaries and therefore a mixing-length model was proposed to estimate the eddy-viscosity. In the present simulations, the wall surfaces are considerably less rough

than those simulated in Chapter 3, and there are also no established relationships similar to Nezu and Rodi (1986) formula nor existing knowledge on the distribution of the mixing-length to estimate the eddy-viscosity. Therefore, the Standard Smagorinsky model will be applied here although some errors are expected in the results.

The flow conditions in the present case studies are different from the flow condition studied in Chapter 3. Firstly, they are unsteady and non-uniform, so that the velocity gradients in both streamwise and depthwise directions are comparable. The wall surfaces are smooth except at the interface boundaries between free flow and porous regions. In contrast to the case study in Chapter 3, the size of roughness elements compared to the water characteristic length scale (such as the water depth) is much lower. Moreover, it is expected that the potential error in the turbulent shear stress will only have minor effects on the water surface elevation particularly in the first test case, i.e. dam break wave through porous dams. However, some errors are expected in the simulation of the second test case where a solitary wave passes a porous structure with streamwise velocity of about 0.1 to 0.5 m/s above the structure. Unfortunately, the data of fluid shear stress is not available for this case, particularly at the interfacial boundaries, to check the accuracy of the turbulence model. However, this issue will be investigated deeply in Chapter 6 where the developed model will be applied for a highly-sheared turbulent free surface channel flow over porous armour layers where detailed experimental data of velocities and shear stresses is available.

Regarding the drag effect of porous media on the flow, Ergun's equation is employed, i.e. $\mathbf{A}_a$ in Equation (4.57) is approximated by Equation (4.29) as the following.

$$\mathbf{A}_a = -c_1 \frac{\left(1-\phi_a\right)^2}{\phi_a{}^2} \frac{\nu_0}{d_s{}^2} \mathbf{u}_a - c_2 \frac{\left(1-\phi_a\right)}{\phi_a} \frac{1}{d_s} \mathbf{u}_a \left|\mathbf{u}_a\right| \tag{5.5}$$

where ϕ_a and $\mathbf{u}_a$ are, respectively, porosity and intrinsic velocity at the position of particle a, and c_1 and c_2 are the empirical coefficients which were originally proposed to be 150 and 1.75, respectively, by Ergun (1952). Slightly different values have also been proposed for these two coefficients based on different experimental studies (e.g. in Macdonald et al., 1979) Nonetheless, it is still difficult to determine these coefficients in the numerical simulations since the characteristics of the porous media under consideration is usually unknown and the knowledge about these coefficients is poor. Hence, usually different values have been used in different simulations often through numerical calibrations. But, in the present study, these values are considered to be predefined rather than being adjusted. For this purpose, Ergun's constants (i.e. c_1=150 and c_2=1.75) will be used for all the present applications based on the fact that these values have been obtained from measurements of various flow conditions (a wide range of flow Reynolds Numbers) through packed beds with various particle sizes (Allen et al., 2013). The idea behind the choice of these constants for all the present simulations is that it is reasonable to tolerate the expected error, if it is within an acceptable range, rather than constructing the model based on arbitrary numerical adjustments.

5.2 Test case I: dam break wave through porous dams

The developed model is employed to simulate 2D dam break flow through porous dams. The numerical results of free surface profiles are compared to the experimental data from Liu et al. (1999) where two different porous dams were studied, one constructed with crushed rocks and another with glass beads. The description of the experimental model is as the following. The water tank was 89.2 cm long, 44 cm wide, and 58 cm high. The porous dam was 29 cm long, 44 cm wide, and 37 cm high. It was located at the centre of the tank and was built once by crushed rocks with mean diameter of 1.59 cm (mean porosity $\phi_0 = 0.49$) and in the next test with glass beads

of a diameter of 0.3 cm (mean porosity $\phi_0 = 0.39$), and a gate was placed 2 cm away from the front side of the dam. At the beginning of each experiment, the gate was opened manually within 0.1 s. Figure 5-2 illustrates a schematic 2D view of the physical model which is considered as the computational domain in the present simulations. In their experiments, Liu et al. (1999) used 3 different initial water depths H_0, about 35, 25 and 15 cm, for each material. They presented water surface profiles for the case of crushed rocks with H_0 = 25 cm, and for the case of glass beads with H_0 = 15 cm. These two cases are simulated here using the developed SPH model.

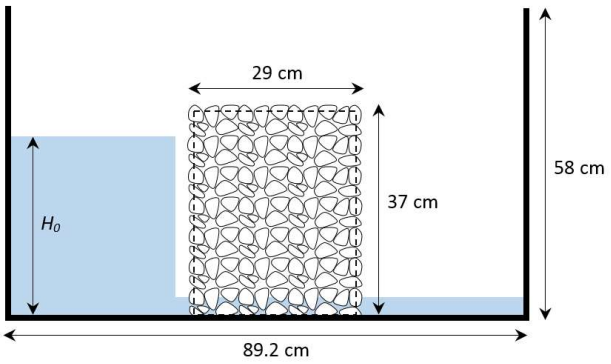

Figure 5-2 A schematic 2D view of Liu et al. (1999) physical model (dam break wave through porous dams) with the separating line in the model shown by the dashed line.

In the clear water region, initial particle spacing (l_0) is set to 3 mm, while in the porous structure, it is initially set according to Equation (5.1). The smoothing length h_Υ for all particles is set to $1.2l_0$. The situation #1 (Section 4.4.1) is considered while the clear water and porous regions are separated by the separating line shown in Figure 5-2 (dashed line). The drag coefficients c_1 and c_2 are set to 150 and 1.75, respectively. Figure 5-3 presents the model result for the case of crushed rocks in comparison with the experimental water surface profiles from Liu et al. (1999) at different times. Table 5-1 presents the Root Mean Square Error (RMSE) at those times which represent the

deviation of the numerical water surface profiles from the experimental ones calculated as the following

$$\mathrm{RMSE} = \sqrt{\frac{1}{n}\sum_{k=1}^{n}\left(A_k - B_k\right)^2} \tag{5.6}$$

where A and B denote the experimental and numerical quantities (water surface elevation here), n is the number of points at which the numerical and experimental quantities are compared and k is the numerator of the points. A reasonable match is observed between the numerical and experimental profiles except at t = 0.2 s.

Figure 5-4 shows the snapshot associated with time 1.0 s where the difference between particle spacing in clear water and porous regions is more clearly observed. This change in the particle spacing takes place due to the conservation of fluid mass which was determined by Equation (4.51) and represented in Figure 4-3.

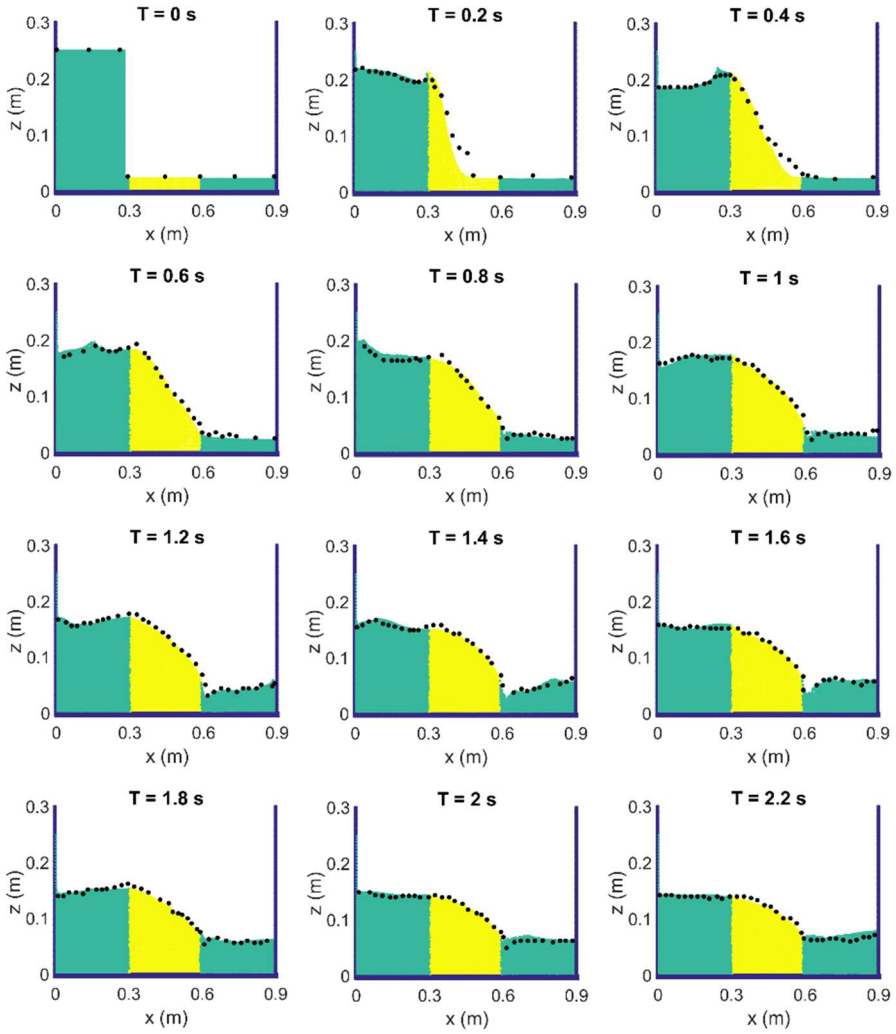

Figure 5-3 Snapshots of dam break flow through crushed rocks at different times. Blue, green, and yellow particles show the wall, free flow, and porous regions respectively, while black circles present the experimental water surface profiles of Liu et al. (1999).

Table 5-1 RMSE of the estimated water surface elevation with respect to the experimental data in dam break flow through crushed rocks.

t (s)	0.2	0.4	0.6	0.8	1	1.2
RMSE (m)	0.0157	0.0085	0.0066	0.0064	0.0063	0.0066
t (s)	1.4	1.6	1.8	2	2.2	
RMSE (m)	0.0062	0.0051	0.0043	0.0061	0.0068	

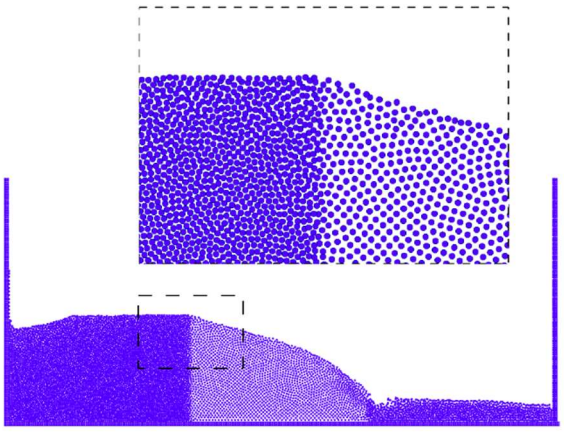

Figure 5-4 Particle configuration/spacing at t = 1.0 s for the case of crushed rocks.

In order to examine the conservation of volume at the porous dam interface, the particle volume is calculated as the particle mass (which is initially-specified and fixed) divided by the computed fluid density at two fixed positions on the interface line (as shown in Figure 5-5). Figure 5-6 presents the time histories of the computed particle volume at those points for the case of crushed rock porous material. The strange distribution at the beginning of the simulation is probably due to two issues: 1) the kernel area around the points are initially empty and after the collapse of the water column, they start to become fully occupied by particles; and 2) the strong collapse of the water column at the beginning produces a wave by which particles move fast into the porous region, their porosity decreases (and therefore their calculated volume increases), but it takes some time for the particle spacing between them to be adjusted. This causes a strong fluctuation in the calculated volume at the first 0.1 - 0.2 s. After that, the particle volume becomes constant and it is also nearly equal at both p_1 and p_2 locations. This denotes the conservation of volume at the interface boundary from the free flow to the porous region. It is noted that the small noise in the time histories is due to the fact that the WCSPH formulation inherently develops noise in density.

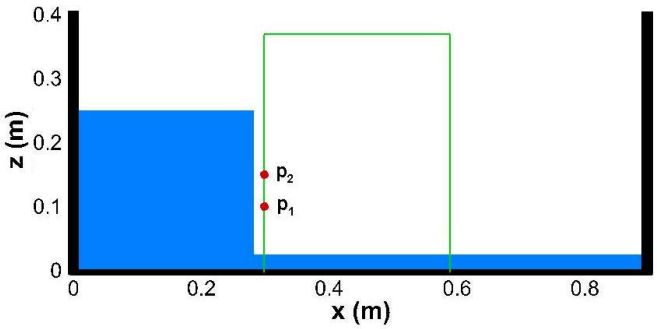

Figure 5-5 The points (p_1 and p_2) at which time histories of fluid density is calculated. Horizontal position of p_1 and p_2 is at x = 0.3 m and their vertical positions are at z = 0.1 m and 0.15 m, respectively. The green line shows the boundary of the porous dam.

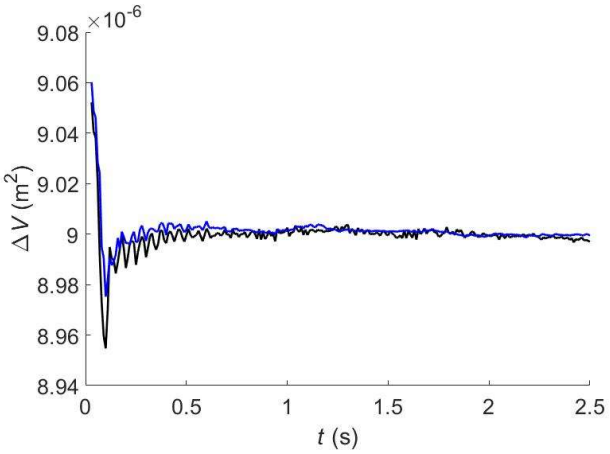

Figure 5-6 Time histories of fluid density calculated at two fixed points p_1 (upper) and p_2 (lower) for the case of crushed rocks. The location of points is shown in the previous figure.

To check the smoothness of the computed pressure around the porous structure, the pressure distribution at different times is presented in Figures 5-7 and 5-8. As can be seen, computed pressure is almost continuous over the interface as well as inside the porous structure. However, due to the unavailability of experimental pressure data, it is not possible to validate the compted pressure field.

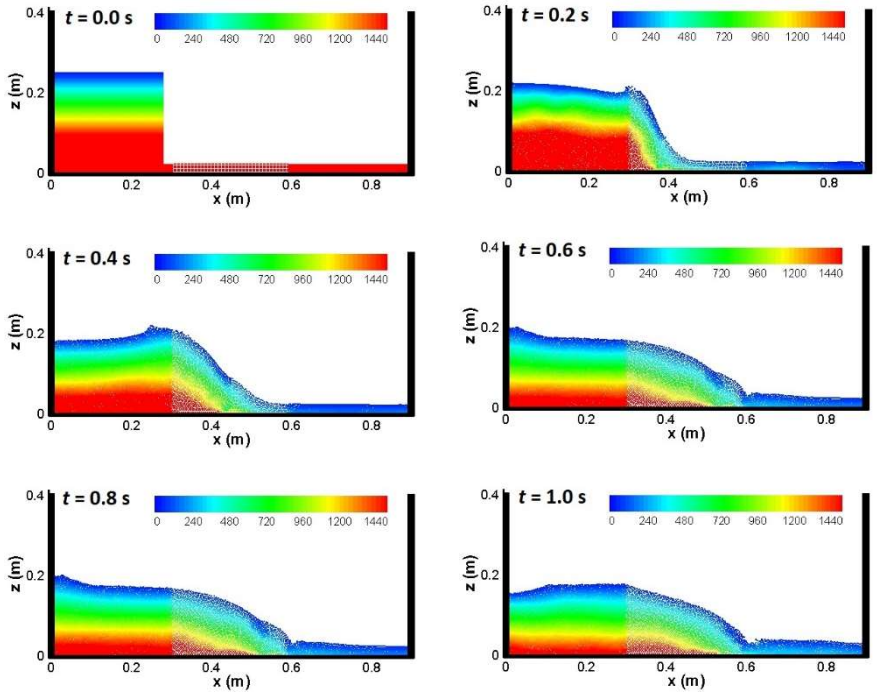

Figure 5-7 Pressure distribution at times *t* = 0 to 1 s for the case of crushed rocks.

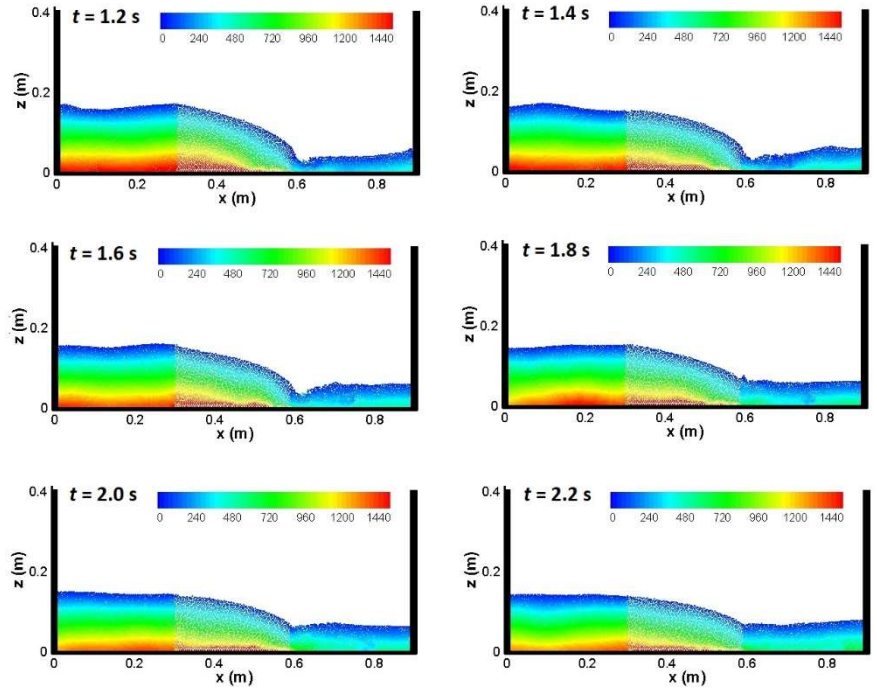

Figure 5-8 Pressure distribution at times *t* = 1.2 to 2.2 s for the case of crushed rocks.

Dam break flow through the porous dam with glass beads is also simulated with the same parameters defined for the case of crushed rocks. Figure 5-9 shows the result in comparison with the experimental free surface profiles of Liu et al. (1999) and Table 5-2 presents the RMSE values for those profiles. In this case, the initial water depth H_0 is about 15 cm and the mean porosity of the dam ϕ_0 is 0.39. The same drag constants ($c_1 = 150$, $c_2 = 1.75$) are used for this case. Bearing in mind that the water surface elevation in the present case is lower than the case of crushed rocks, the RMSE values in Table 5-2 show that the agreement between numerical and experimental profiles in the present case is not as good as that in the case of crushed rocks.

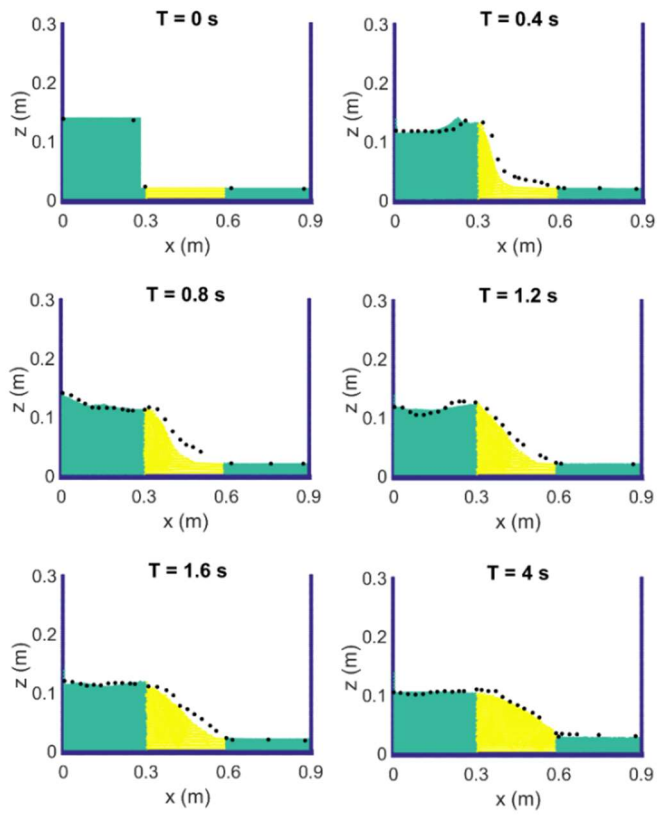

Figure 5-9 Snapshots of dam break flow through glass beads at different times. Blue, green, and yellow particles show the wall, free flow, and porous regions respectively, while black circles present the experimental water surface profiles of Liu et al. (1999).

Table 5-2 RMSE of the estimated water surface elevation with respect to the experimental data in dam break flow through glass beads.

t (s)	0.4	0.8	1.2	1.6	4
RMSE (m)	0.0115	0.0116	0.0085	0.008	0.004

In addition to their physical model, Liu et al (1999) also solved an Eulerian form of the spatially averaged N-S equations to simulate the water wave through the porous dams of crushed rocks and glass beads. They applied the Ergun's equation similar to the present drag terms in their model, but with different values for the constants c_1 and c_2. Following van Gent (1995), they used $c_1 = 1000$ and $c_2 = 1.1$ and obtained good agreement with the experimental data for the case of crushed rocks but a poor result for the test with glass beads. Then they decreased c_1 to 200 and achieved a better agreement for the water surface profiles. They argued the reason for using a smaller value for c_1 was that the size of glass beads was outside of the test range of van Gent (1995) where the viscous effect had been negligible due to high flow Re number. They also noted that in the case of glass beads, the Re Number was low, thus the water surface in the porous dam was retained on the flume wall in some regions due to surface tension and capillary effects. This led to an overestimation of water surface profile in some areas inside the porous dam.

Akbari and Namin (2013) investigated the sensitivity of the estimated water surface profile to the linear and non-linear drag constants (c_1 and c_2, respectively), in their simulations of the present cases of dam break flows through porous dams. According to their study, the case of crushed rocks is sensitive to the form-drag (non-linear) term due to high Re Number of flow, while the case of glass beads is sensitive to the viscous (linear) term as flow Re Number is low in this case. They achieved fair agreement between numerical and experimental water surface profiles by employing the same values for c_1 and c_2 as Liu et al. (1999) had used. Later, Akbari (2014) modified the ISPH model and employed the analytical equations of Du Plessis (1994) to predict the

drag coefficients. Those equations give values of 212 and 1.83 for the case of crushed rocks and values of 203 and 1.93 for the case of glass beads, which are nearly close to the values originally proposed by Ergun (150 and 1.75, respectively). Ren et al. (2016) also used Du Plessis's equations to determine the drag constants in their WCSPH model.

Figure 5-10 provides a comparison between the present model result of water surface profile at time t = 1.2 s for the case of crushed rocks with the above-mentioned SPH studies and the experiment of Liu et al. (1999). As can be seen, the present model as well as the model of Ren et al. (2016) provide better estimations compared to the studies of Akbari and Namin (2013) and Akbari (2014). This improvement is probably related to the treatment of the interfacial boundaries. In Akbari and Namin (2013) and Akbari (2014), the thickness of the interfacial transitional layer over which the porosity is variable was set to $4d_s$ (where d_s is the solid grain diameter), while in the present model as well as Ren et al. (2016), porosity changes over a layer with the thickness of d_s. The choice of the size of averaging volume Ω for calculation of porosity in the present simulations was based on constraint (a) in Equation (4.60). Moreover, the comparison of Ren et al. (2016) and present model in Figure 5-10 reveals that in spite of using different values for the drag coefficients, the estimated water surface profiles lie closely to each other. This can be also seen by comparing Akbari and Namin (2013) and Akbari (2014) results. In fact, a slight change in the drag coefficient does not considerably affect the result of water surface elevations, while the treatment of the interfacial boundary has a greater effect.

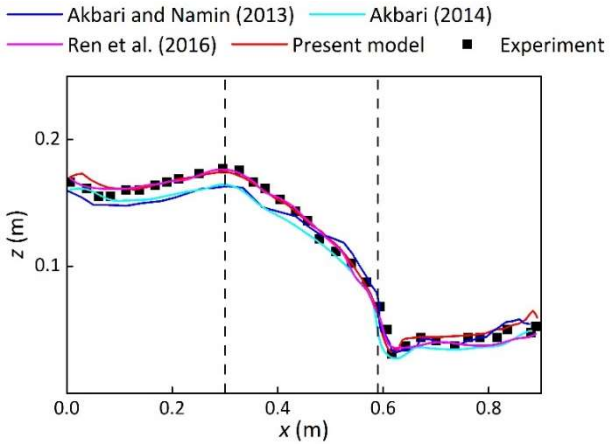

Figure 5-10 Comparison of the present model result of water surface profile at *t* = 1.2 s with other SPH studies and the experiment of Liu et al. (1999). Dashed lines show the sides of the porous dam.

Del Jesus et al. (2012) defined pore-based Reynolds Number as

$$\mathrm{Re}_p = \frac{\rho u^s d_s}{\mu \phi_0} \tag{5.7}$$

where u^s is component of volumetric velocity; and reported the values of $\mathrm{Re}_p = 325$ and $\mathrm{Re}_p = 9.6$ for the cases of crushed rocks and glass beads, respectively. Besides, Allen et al. (2013) defined Ergun Reynolds Number, Re_{ERG} as

$$\mathrm{Re}_{ERG} = \frac{\rho u^s d_s}{\mu\left(1-\phi_0\right)} \tag{5.8}$$

Allen et al. (2013) stated that Ergun (1952) did not explicitly declare the range of Re Number over which his equation is valid, but Re_{ERG} of the data from which the Ergun's constants were originally measured or the data with which the equation was compared to, is in the range of $1 < \mathrm{Re}_{ERG} < 2400$. Considering the values of Re_p reported by Del Jesus et al. (2012) for the crushed rocks and glass beads experiments, Re_{ERG} of these cases are about 312 and 6.15, respectively, which are within the range.

The mismatch in the result of glass beads case could also be due to the probable overestimation of the free surface profiles in the experiments (as also noted by Liu et

al. 1999). To check this issue, a calculation of water volume conservation has been carried out here. The initial water surface profile at *t* = 0.0 s (which is equal for both experiments and simulations) is plotted in Figure 5-11 (a) and the experimental and numerical profiles at *t* = 0.8 s are plotted in Figure 5-11 (b). The domain is divided into three regions: (1) left free flow, (2) middle porous, and (3) right free flow regions. Then, at each region, the area under each profile is calculated and multiplied by the width of the channel to find the volumes under the profiles associated with each region (Vol_1, Vol_2 and Vol_3). In the free flow regions, Vol_1 and Vol_3 denote the water volume in those regions while in the porous region, Vol_2 multiplied by ϕ_0 represents the water volume in that region. Therefore, the summation of Vol_1, $Vol_2 \times \phi_0$ and Vol_3 associated with each profile represents the water volume under that profile. Through this computation, the water volumes under the initial water surface profile (Figure 5-11 a) and under the numerical and experimental profiles at *t* = 0.8 s (Figure 5-11 b) are obtained as 0.0212, 0.0214 and 0.0227 m^3, respectively. According to these values, the water volume is nearly conserved in the numerical model, while a considerable increase is observed in the experimental water volume from *t* = 0.0 s to *t* = 0.8 s, which is not physical. Although the computed values are not exact, they roughly imply the overestimation of water surface profiles in the measurements.

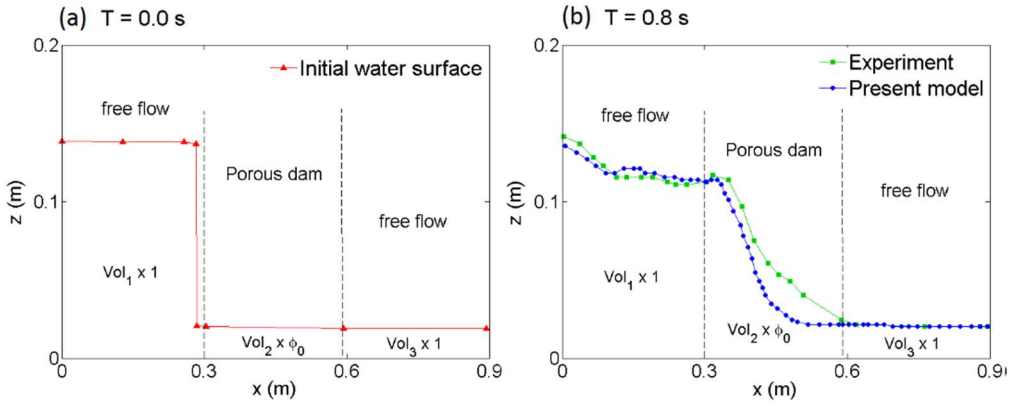

Figure 5-11 Comparison of water volumes under water surface profiles at t = 0.0 and 0.8 s.

5.3 Test case II: wave interaction with a porous structure

The model was tested with the experimental data of Liu et al. (1999) for the case of dam break wave through porous dams. However, the data provides only water surface profiles. A set of data which provides detailed velocity profiles is needed to further investigate the accuracy of the developed model. Wu and Hsiao (2013) studied propagation of solitary waves over a submerged porous structure experimentally and numerically. They measured horizontal and vertical velocity profiles around the structure at different times which makes the data useful for the present study. Hence, this case is simulated here, and the data is used for comparison. This data was also used by Gui et al. (2015) to test the result of their SPH model.

The experiments were carried out in a 25 m long, 0.5 m wide and 0.6 m deep wave tank with glass wall and glass bottom. Figure 5-12 (a) depicts a schematic view of the Wu and Hsiao (2013) flume set-up. A digital servo-controlled piston-type wavemaker is placed at one end of the flume to generate solitary waves based on Goring (1978) method, while a slope was located at the other end of the flume to absorb the waves. The wave tank was filled with water at a constant depth H_0 = 10.6 cm and Solitary waves with three different heights were generated in the experiments. But only the result for the wave height of $H_w = 0.45H_0$ was presented. A porous structure composed of spherical glass beads with diameter d_s = 1.5 cm and porosity ϕ_0 = 0.52 was placed at the middle of the flume. The length and height of the structure are 13 and 6.5 cm respectively. The origin of the coordinate system (x = 0, z = 0) considered at the intersection of the front side of the structure and the flume bottom as shown in Figure 5-12 (a). The time history of the water surface profiles was measured at x = -1.8 m and x = 1.8 m by two capacitance-type wave gauges. Reference time t = 0.0 s was considered when the crest of the wave arrives at the wave gauge 1 (x = -1.8 m). Horizontal and vertical velocity profiles were measured around the structure at different horizontal locations x = -0.04, 0.0, 0.04, 0.08, 0.12, 0.16 and 0.20 m at different times t = 1.45, 1.65, 1.85, 2.05 and 2.25 s using a PIV system. Since the porous

structure covers the whole width of the flume, this case can be simulated in 2D in a macroscopic scale.

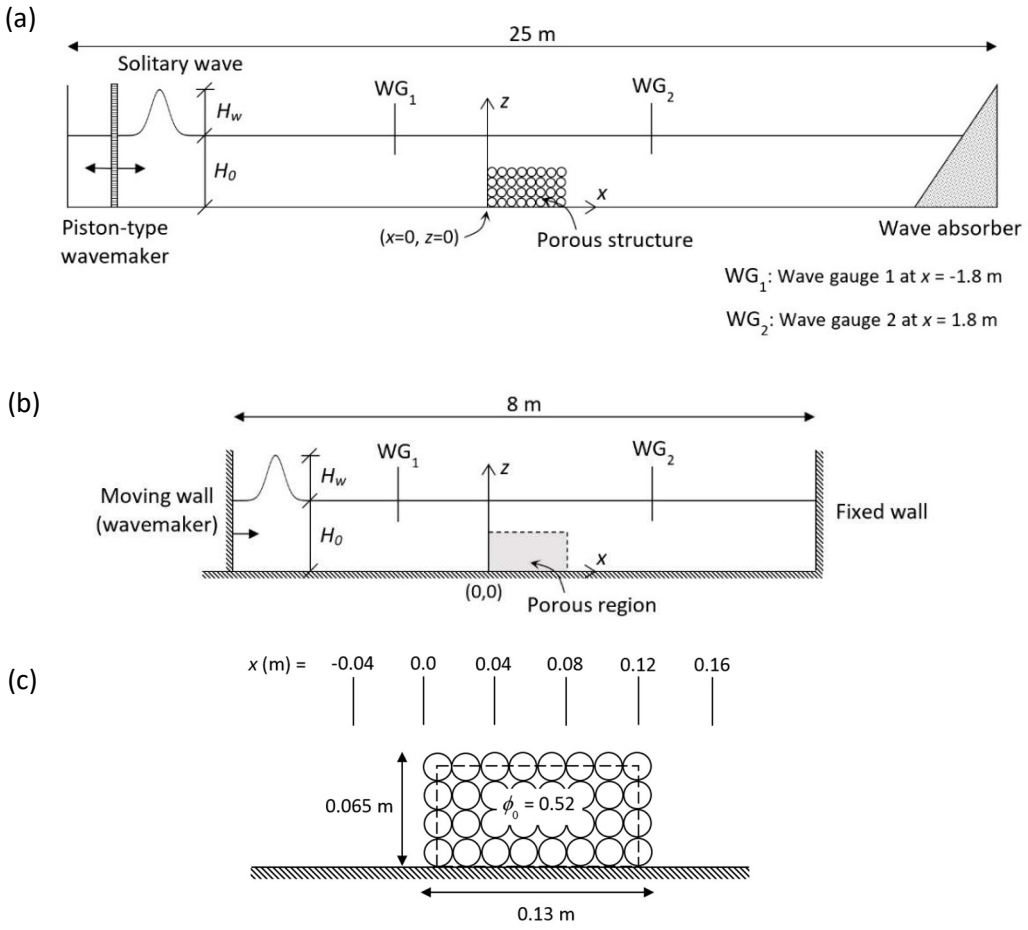

Figure 5-12 Experimental and numerical set-up for solitary wave interaction with a porous structure: (a) experimental flume of Wu and Hsiao 2013, (b) 2D computational domain of the present model, and (c) porous structure with the separating line and the velocity profiles locations.

In the present model, a computational domain is chosen with the following characteristics. Initial particle spacing in the free flow region (l_0) is set to 3 mm, while in the porous dam it is initially set according to Equation (5.1). The smoothing length h_Υ is set to $1.2l_0$. Following Gui et al. (2015), a numerical wave tank is constructed with 8 m length instead of simulating the 25 m long experimental wave tank due to

computational cost restriction. The front side of the porous structure is assumed to be in the middle of the channel at x = 0.0 m that is 4 m far from the left and right-side walls where a moving wall representing a piston-type wavemaker and a fixed wall are placed, respectively (see Figure 5-12 b). According to the data, the still water depth is set to H_0 = 10.6 cm. Using this set-up for the computational domain, Gui et al. (2015) found out a solitary wave with height 4.77 cm should be generated at the wavemaker location (x = -4 m) to have a numerical wave height matched with the measured one at the location of the reference wave gauge WG_1 (x = -1.8 m). Three layers of dummy particles are placed at the bottom, left and right walls to represent solid wall boundaries as described in Section 5.1. The dummy particles at the bottom and right walls are fixed, while the particles representing a piston-type wavemaker at the left wall move as to produce a solitary wave with height 4.77 cm. The displacements of these particles are determined based on Goring (1978) wavemaker theory. The simplified version of this theory which expresses the motion of piston wavemaker is used as the following.

$$X_p(t) = \frac{1}{2} S_G \tanh\left[7.6\left(\frac{t}{T_p} - 0.5\right)\right] \tag{5.9}$$

where X_p denotes the displacement of the piston, t is time, T_p is the duration of piston motion, and S_G is the total stroke of the piston which is calculated as follows (Goring, 1978).

$$S_G = 4\sqrt{\frac{H_w H_0}{3}} \tag{5.10}$$

Gui et al. (2015) applied a damping zone at the right wall in order to absorb the effect of wave reflection. However, in the present study no numerical wave absorber is used since the flow in the vicinity of the porous structure is studied at times *t* = 1.45 to 2.25 s when the wave crest is within a short distance from the structure. No reflection effect was observed from the right wall to the wave during this time due to long distance between the wave and the wall. Figure 5-12 (c) shows the porous structure

as well as the locations where the numerical velocity profiles are considered to be compared to the experimental data. Besides, situation #1 introduced in Section 4.4.1 is applied by separating the free flow and porous regions using the separating line shown in Figure 5-12 (b) and Figure 5-12 (c) by dashed lines. The values of 150 and 1.75 are taken for the drag coefficients c_1 and c_2, respectively.

Figures 5-13 and 5-14 present contours of horizontal and vertical velocity around the structure at different times from *t* = 1.45 to 2.25 s. Note that *t* = 0.0 s is when the crest of the wave arrives at wave gauge 1 (WG_1). According to these figures, when the wave arrives at the front side of the structure, the flow feels the impediment caused by the structure and separates at the frontal edge of the structure. Consequently, the flow in the lower part of the channel weakens and the particle velocity direction changes towards the area above the structure. A major part of the particles passes from that area until the wave reaches the lee side of the structure. Then particle velocity direction changes downward so that a vortex is created at the trailing edge of the structure. The vortex becomes stronger while the wave is travelling over the lee side until it loses strength after some time. These processes during the transition of flow from the weather side to the lee side can also be seen in Figure 5-15 where the model results of velocity vectors around the structure at different times from *t* = 1.45 to 2.25 s are compared to the experimental data. This figure reveals the accuracy of the model in predicting the direction and magnitude of velocity when the wave is passing the structure, though some discrepancies are seen at the vortex behind the structure.

It is noted that in the presented results, the SPH velocities are averaged over a grid with spacing of 1 mm for contour plots and 5 mm for vector plots using the kernel function presented in Equation (5.3). To identify the water surface profile at this grid, divergence of particle position is calculated at each grid point as the following.

$$\left(\nabla\cdot\mathbf{r}\right)_m = -\sum_b \frac{m_b}{\phi_b \left\langle\rho\right\rangle_b^{\alpha}} \left(\mathbf{r}_m - \mathbf{r}_b\right)\cdot\nabla W\left(\mathbf{r}_m - \mathbf{r}_b, h\right) \tag{5.11}$$

where m and b denote the averaging grid point and neighbouring particles, respectively. The calculated value will be 2, 1 and 0 when the averaging (kernel) area of the grid point is full, half-full and empty of particles, respectively. Therefore, it is assumed that the grid points with $\left(\nabla\cdot\mathbf{r}\right)_m$ higher than 1.0 are located below the water surface so that they are considered as fluid points and are presented in the contours.

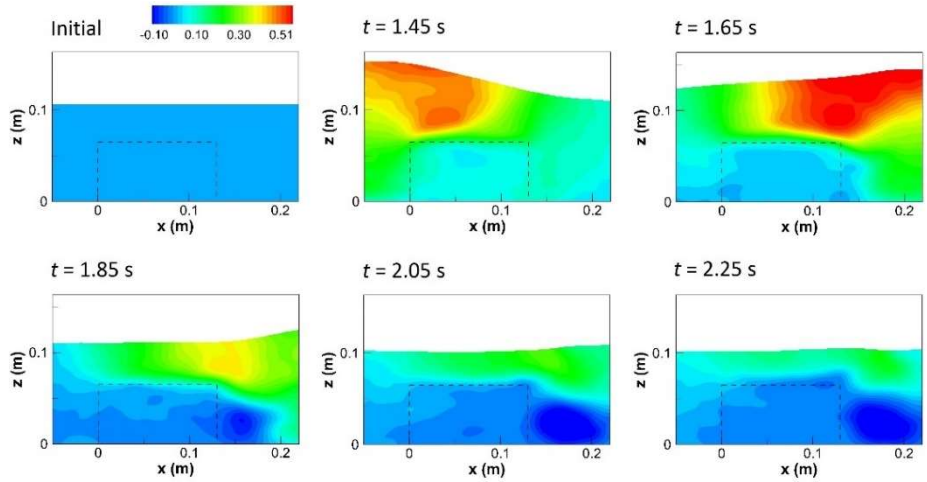

Figure 5-13 Horizontal velocity contours at different times around the structure. Dashed line shows the boundary of the structure (separating line).

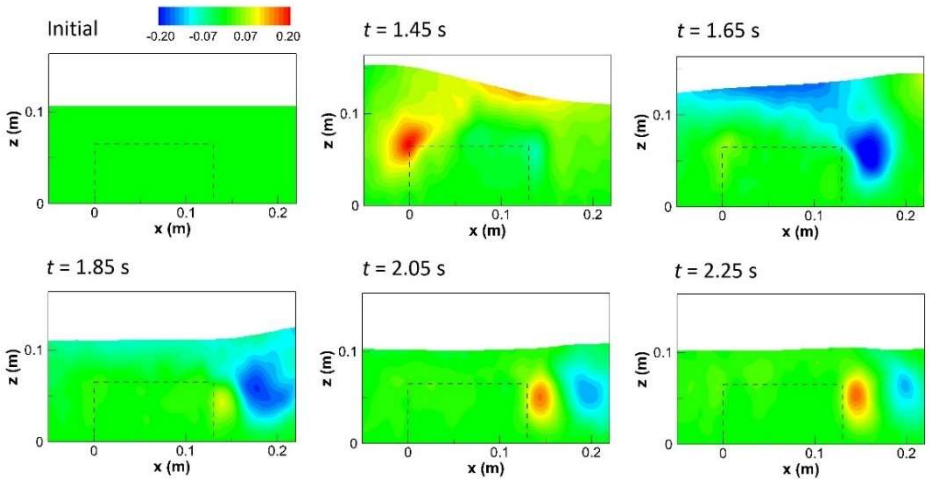

Figure 5-14 Vertical velocity contours at different times around the structure. Dashed line shows the boundary of the structure (separating line).

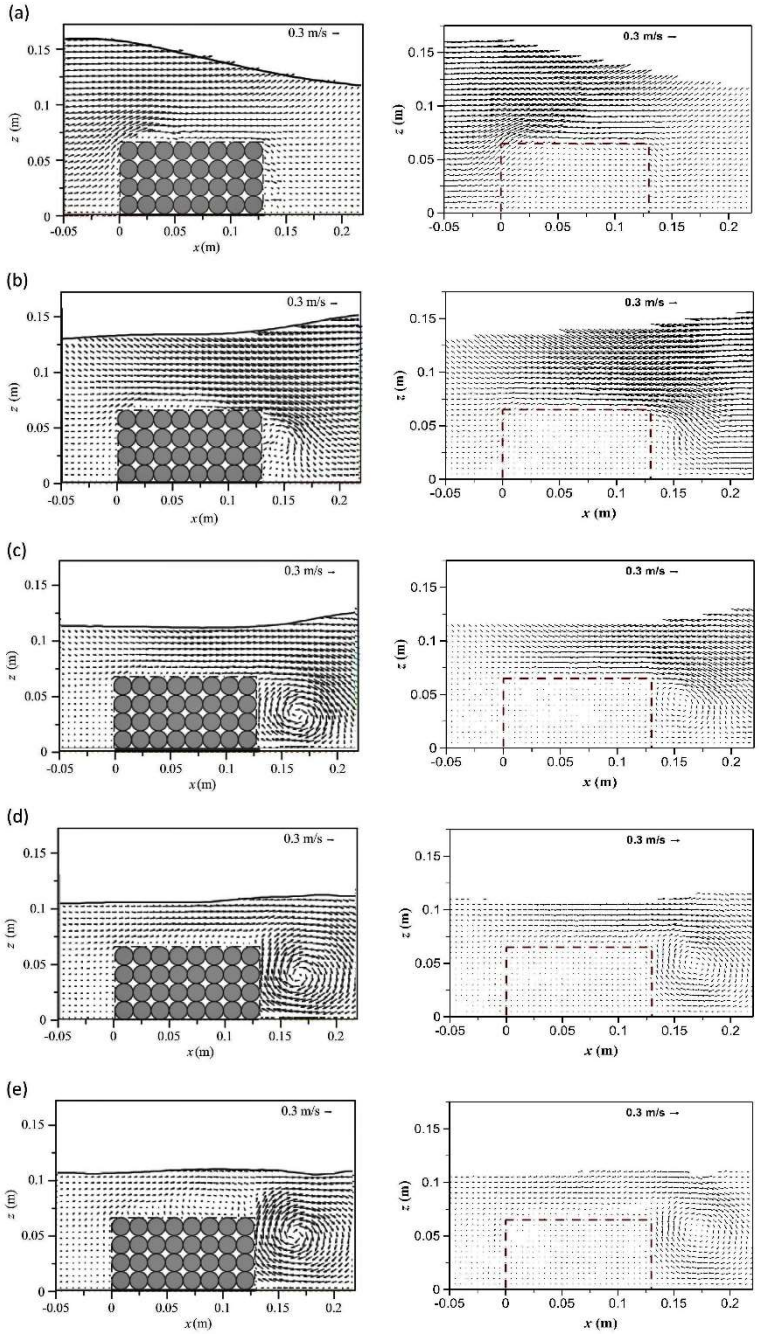

Figure 5-15 Comparison of velocity vectors between the present model (right) and experimental data of Wu and Hsiao (2013) (left) at different times around the structure: a) *t* = 1.45 s, b) *t* = 1.65 s, c) *t* = 1.85 s, d) *t* = 2.05 s, e) *t* = 2.25 s

To further investigate the model results, horizontal and vertical velocity profiles at several sections around the structure (x = -0.04, 0.0, 0.04, 0.08, -0.12 and 0.016 m)

are presented in comparison with the experimental profiles. Figures 5-16 to 5-25 present the horizontal and vertical velocity profiles at those sections at times 1.45, 1.65, 1.85, 2.05 and 2.25 s. Note that x = 0.0 m is at the front side of the structure and t = 0.0 s is when the wave crest is at the wave gauge 1 (x = -1.8 m). Tables 5-3 and 5-4 present RMSE values of, respectively, horizontal and vertical velocity profiles with respect to the experimental data. The RMSE values are calculated using Equation (5.6). As observed, fair agreement is seen between numerical and experimental profiles of both horizontal and vertical velocities at all times and all sections except at x = 0.16 m which is associated with the vortex behind the structure.

Wu and Hsiao (2013) and Gui et al. (2015) also simulated the present case using numerical methods based on RANS equations and the ISPH method, respectively, and observed discrepancies in the results of velocity at the vortex area, although they used different closure models and coefficients for the drag effects. It is believed that the mismatch in the numerical profiles and the experimental data at the vortex area could be due to dimensional and geometrical differences. It may also be related to the fact that those models as well as the present model solve the averaged equations at a macroscopic domain, while in the experiments the flow takes place at a microscopic scale through the porous structure. The structure is composed of regularly-spaced spheres with uniform size as depicted in Figure 5-12 (c). Therefore, the flow at sphere faces is inconsiderable and water can exit the structure at the lee side only from the horizontal gaps between layers of spheres, while in the present model (as well as the models of Wu and Hsiao, 2013 and Gui et al., 2015), water flow through the whole section of the structure mostly uniformly. This can be seen in Figure 5-15 especially parts (a) and (b) where the experimental velocity at the lee side of the structure is higher at some points and smaller at other points, while the numerical velocity vectors at the same location are uniformly distributed. This can be more clearly seen in Figure 5-26 where the experimental and numerical velocity profiles are presented at t = 1.45 s and x= 0.14 m which is just 1 cm far from the lee side of the structure.

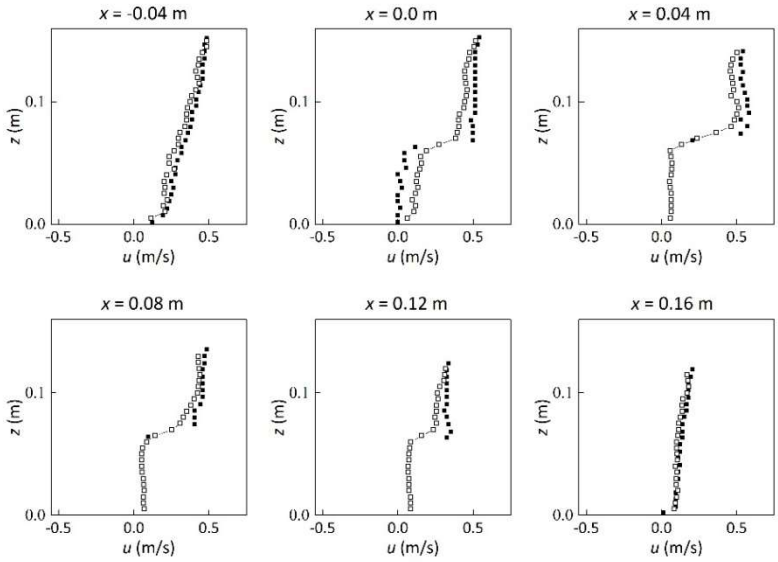

Figure 5-16 Numerical results of horizontal velocity profiles in comparison with the experimental profiles at time *t* = 1.45 s at *x* = -0.04, 0.0, 0.04, 0.08, 0.12 and 0.16 m (squares and lines denote numerical result and bold squares denote experimental data).

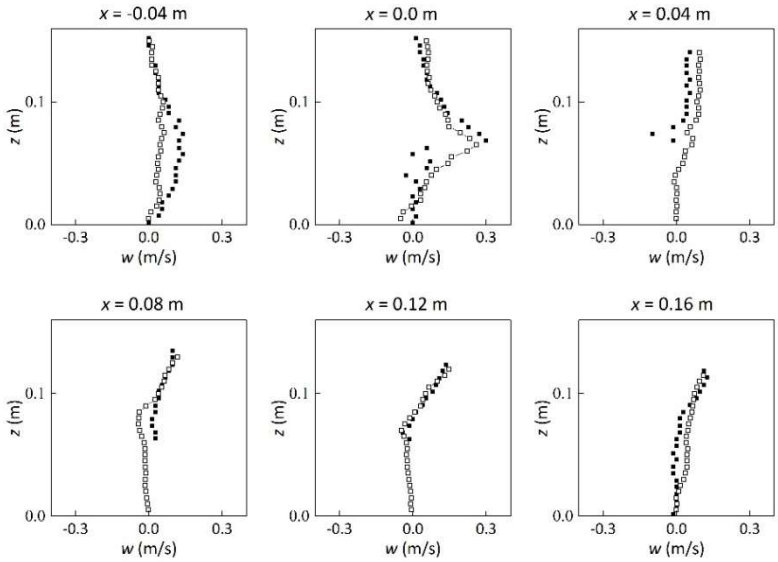

Figure 5-17 Numerical results of vertical velocity profiles in comparison with the experimental profiles at time *t* = 1.45 s at *x* = -0.04, 0.0, 0.04, 0.08, 0.12 and 0.16 m (squares and lines denote numerical result and bold squares denote experimental data).

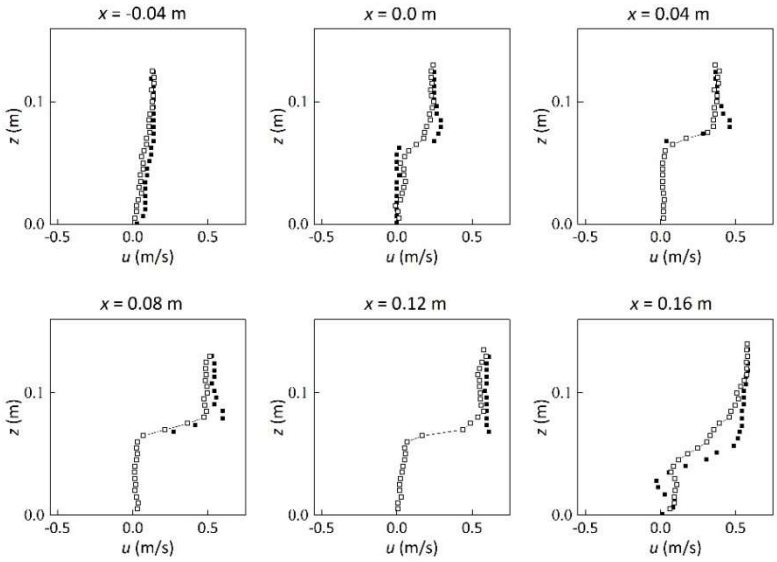

Figure 5-18 Numerical results of horizontal velocity profiles in comparison with the experimental profiles at time *t* = 1.65 s at *x* = -0.04, 0.0, 0.04, 0.08, 0.12 and 0.16 m (squares and lines denote numerical result and bold squares denote experimental data).

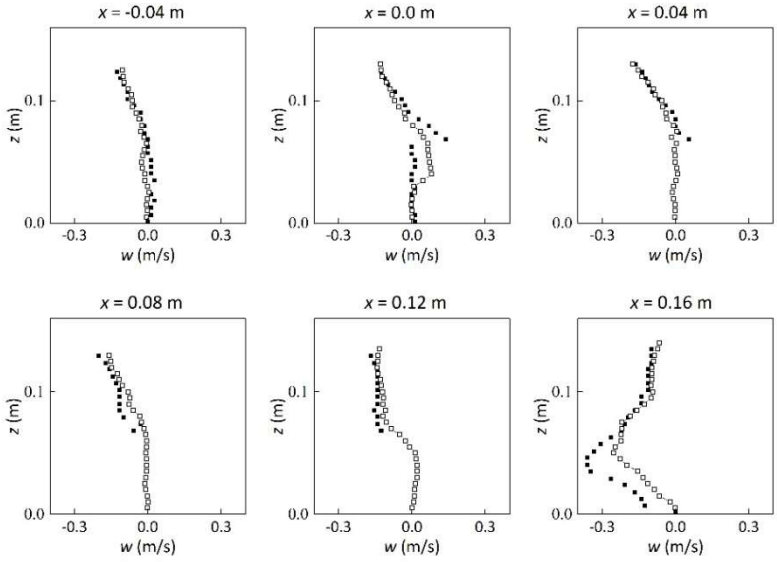

Figure 5-19 Numerical results of vertical velocity profiles in comparison with the experimental profiles at time *t* = 1.65 s at *x* = -0.04, 0.0, 0.04, 0.08, 0.12 and 0.16 m (squares and lines denote numerical result and bold squares denote experimental data).

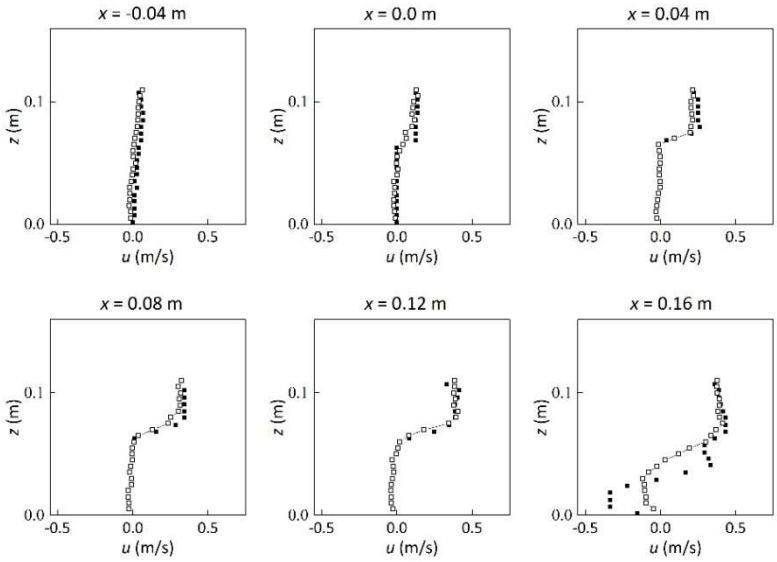

Figure 5-20 Numerical results of horizontal velocity profiles in comparison with the experimental profiles at time *t* = 1.85 s at *x* = -0.04, 0.0, 0.04, 0.08, 0.12 and 0.16 m (squares and lines denote numerical result and bold squares denote experimental data).

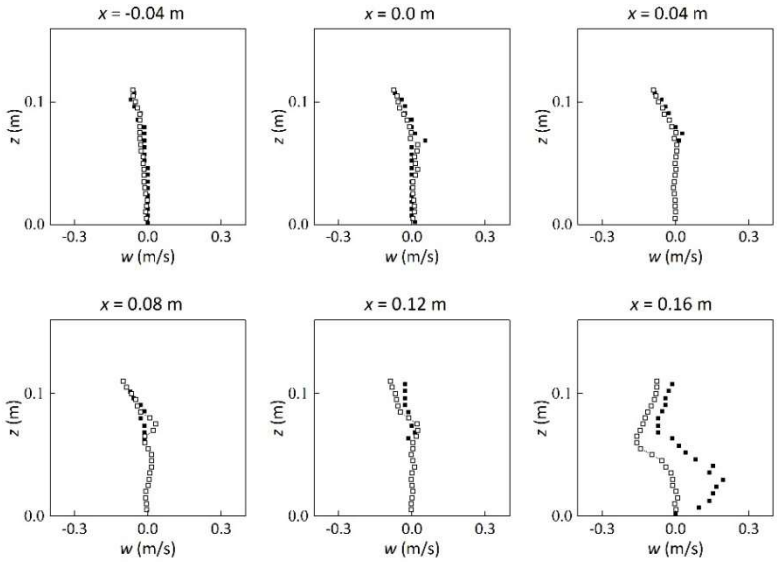

Figure 5-21 Numerical results of vertical velocity profiles in comparison with the experimental profiles at time *t* = 1.85 s at *x* = -0.04, 0.0, 0.04, 0.08, 0.12 and 0.16 m (squares and lines denote numerical result and bold squares denote experimental data).

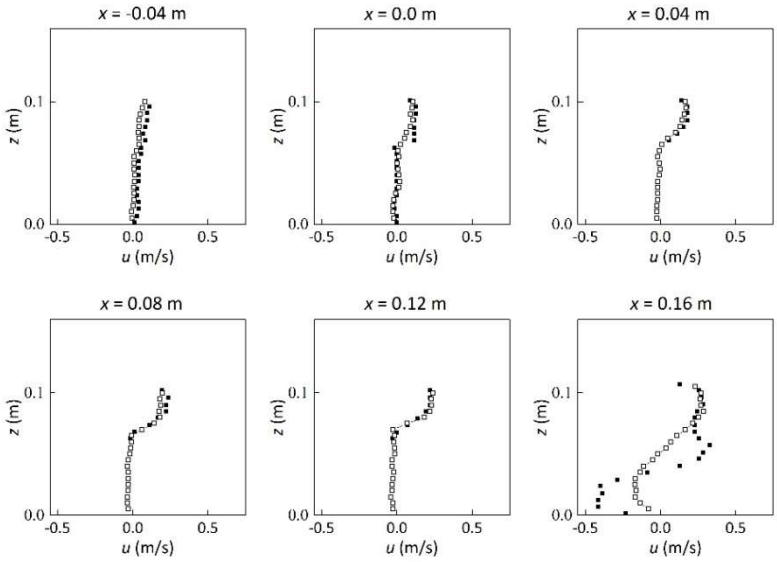

Figure 5-22 Numerical results of horizontal velocity profiles in comparison with the experimental profiles at time *t* = 2.05 s at *x* = -0.04, 0.0, 0.04, 0.08, 0.12 and 0.16 m (squares and lines denote numerical result and bold squares denote experimental data).

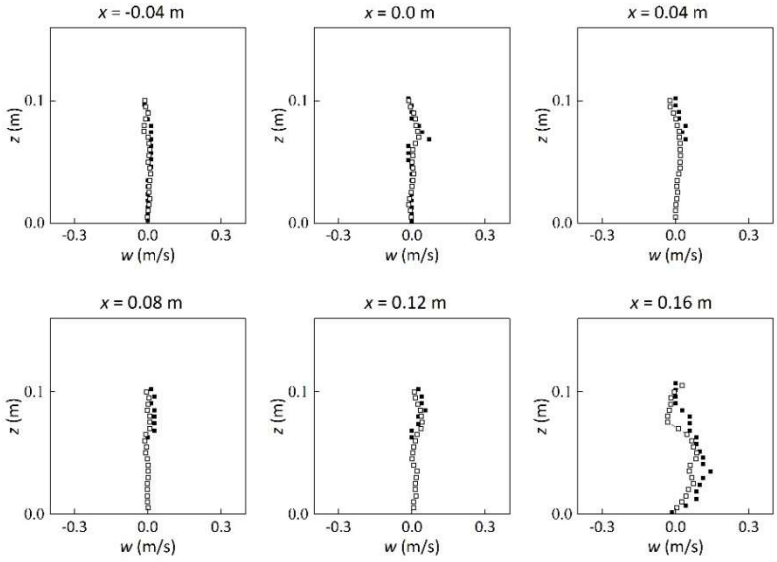

Figure 5-23 Numerical results of vertical velocity profiles in comparison with the experimental profiles at time *t* = 2.05 s at *x* = -0.04, 0.0, 0.04, 0.08, 0.12 and 0.16 m (squares and lines denote numerical result and bold squares denote experimental data).

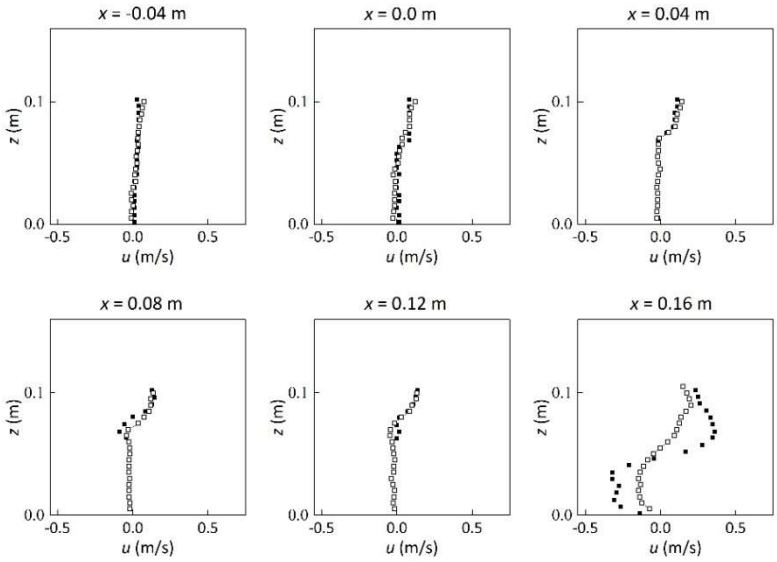

Figure 5-24 Numerical results of horizontal velocity profiles in comparison with the experimental profiles at time *t* = 2.25 s at *x* = -0.04, 0.0, 0.04, 0.08, 0.12 and 0.16 m (squares and lines denote numerical result and bold squares denote experimental data).

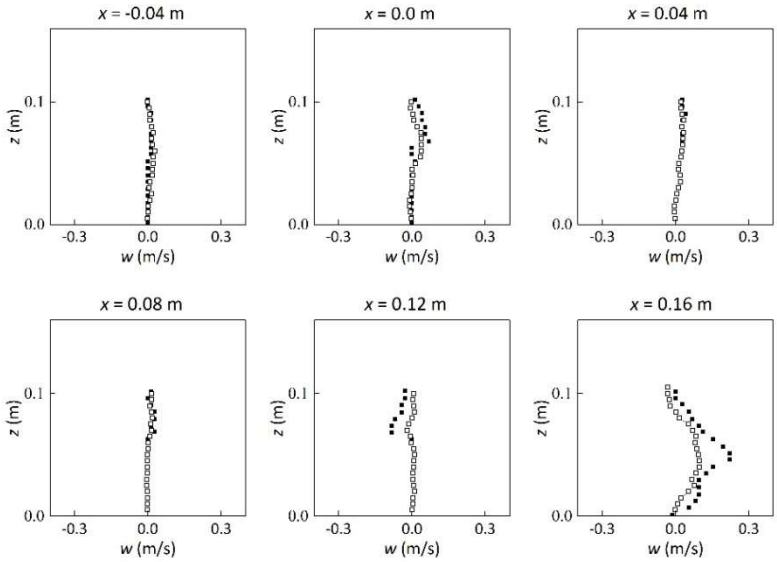

Figure 5-25 Numerical results of vertical velocity profiles in comparison with the experimental profiles at time *t* = 2.25 s at *x* = -0.04, 0.0, 0.04, 0.08, 0.12 and 0.16 m (squares and lines denote numerical result and bold squares denote experimental data).

Table 5-3 RMSE (m/s) of the estimated horizontal velocity u (m/s) profiles with respect to the data.

Section / Time	*x* = -0.04 m	*x* = 0.0 m	*x* = 0.04 m	*x* = 0.08 m	*x* = 0.12 m	*x* = 0.16 m
t = 1.45 s	0.0382	0.0921	0.087	0.0536	0.088	0.0208
t = 1.65 s	0.0353	0.0515	0.0579	0.0918	0.105	0.1035
t = 1.85 s	0.0305	0.0299	0.0434	0.0631	0.0549	0.1578
t = 2.05 s	0.036	0.0291	0.0308	0.0268	0.0209	0.1802
t = 2.25 s	0.0182	0.0247	0.02	0.044	0.027	0.1737

Table 5-4 RMSE (m/s) of the estimated vertical velocity w (m/s) profiles with respect to the data.

Section / Time	*x* = -0.04 m	*x* = 0.0 m	*x* = 0.04 m	*x* = 0.08 m	*x* = 0.12 m	*x* = 0.16 m
t = 1.45 s	0.0504	0.0663	0.0639	0.0356	0.0155	0.0319
t = 1.65 s	0.0207	0.043	0.0221	0.0402	0.029	0.0812
t = 1.85 s	0.0116	0.018	0.0168	0.0262	0.0324	0.1289
t = 2.05 s	0.0105	0.0158	0.0231	0.0201	0.0207	0.0437
t = 2.25 s	0.0106	0.0228	0.0074	0.0115	0.0503	0.0669

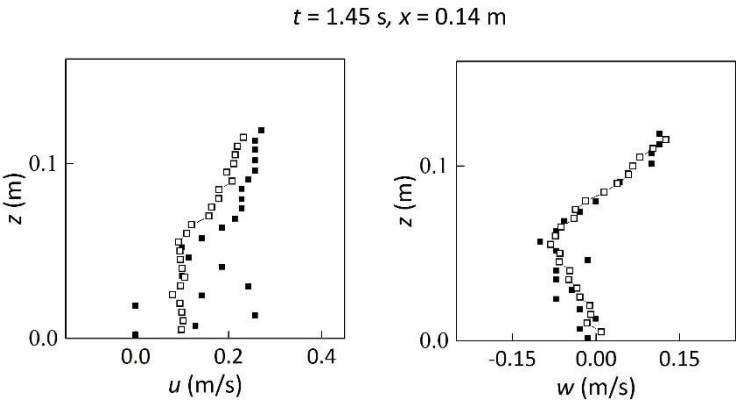

Figure 5-26 Numerical results of horizontal (left) and vertical (right) velocity profiles in comparison with the experimental profiles at time *t* = 1.45 s and *x* = 0.14 m. (squares and lines denote numerical result and bold squares denote experimental data).

Wu and Hsiao (2013) noted that the flow in the present case is considered as a fully-turbulent flow since the pore-based Re Number calculated by Equation (5.7) is larger than 1000. Therefore, the effect of viscous drag which is addressed by coefficient c_1 is negligible while c_2 plays an important role in the representation of solid matrix effect on the flow. Wu and Hsiao used Ergun's Equation (4.29) for the drag closure in the momentum equation but with different coefficients c_1 and c_2 from the present study. They tested their model using three sets of coefficients $c_1 = 200$ and $c_2 = 1.1$, $c_1 = 1000$ and $c_2 = 1.1$, and $c_1 = 724.57$ and $c_2 = 8.15$, referring to Liu et al. (1999), van Gent (1995), and Lara et al. (2011), respectively. The first two sets of coefficients provided similar results of velocity and water surface elevation while the third one led to a slightly different results. This was because the first two sets of coefficients are different only in c_1 which is not important in the present problem due to high pore-based Re Number of flow while in the third set of coefficients a higher c_2 has been chosen which has significant influence due to the same reason. Finally, they suggested $c_2 = 1.1$ (van Gent, 1995 and Liu et al., 1999) as the optimal value.

In their ISPH simulations of the present case, Gui et al. (2015) used completely different relationships for the permeability and Forchheimer tensors in the drag closure model presented in Equation (4.26). Figure 5-27 compares the streamwise velocity profiles estimated by the present model in comparison with the results of Gui et al. (2015) and the experiments of Wu and Hsiao (2013) at different times and sections. Three upper subplots show the profiles associated with time *t* = 1.45 s, when the wave is travelling above sections x = -0.04, 0.0 and 0.04 m. Three middle subplots presents the results associated with time *t* = 1.65 s when the wave is above sections x = 0.08, 0.12, and 0.16 m. Finally, three lower subplots associate with section x = 0.16 m (vortex region) at times *t* = 1.85, 2.05, and 2.25 s when the wave has already passed the structure. The figure shows that the present model provides better estimation of

velocity distribution above the structure while the wave is travelling over the structure. However, after the wave has passed the structure (when the vortex is generated at the lee side), both models perform similarly, particularly after t = 2.05 s. Although the vortex is generated in the same location as in the experiments, both models are unable to reproduce the correct magnitude of velocity in the vortex zone. Inside the porous structure, both models provide similar velocity profiles, although different drag closure models have been used. However, at the interface boundary between the porous structure and free flow region above it, the slope of velocity profiles is estimated closer to the experimental data by the present model. This effect also produces better velocity distribution above the structure by the present model. Gui et al. (2015) used a transitional layer at the interface with a thickness of 4 times particle spacing and averaged the SPH-estimated pressure over this layer to smooth out flow quantities at the interface. But, in the present model, the thickness of the interface layer over which porosity changes from ϕ_0 to 1.0, is chosen based on the characteristic length of the solid skeleton at the interface (to satisfy constraint 4.60 a) rather than being related to the computational resolution. It is also notable that Gui et al. (2015) ignored the effect of particle volume change (Equation 4.51 and Figure 4-3) in the continuity equation.

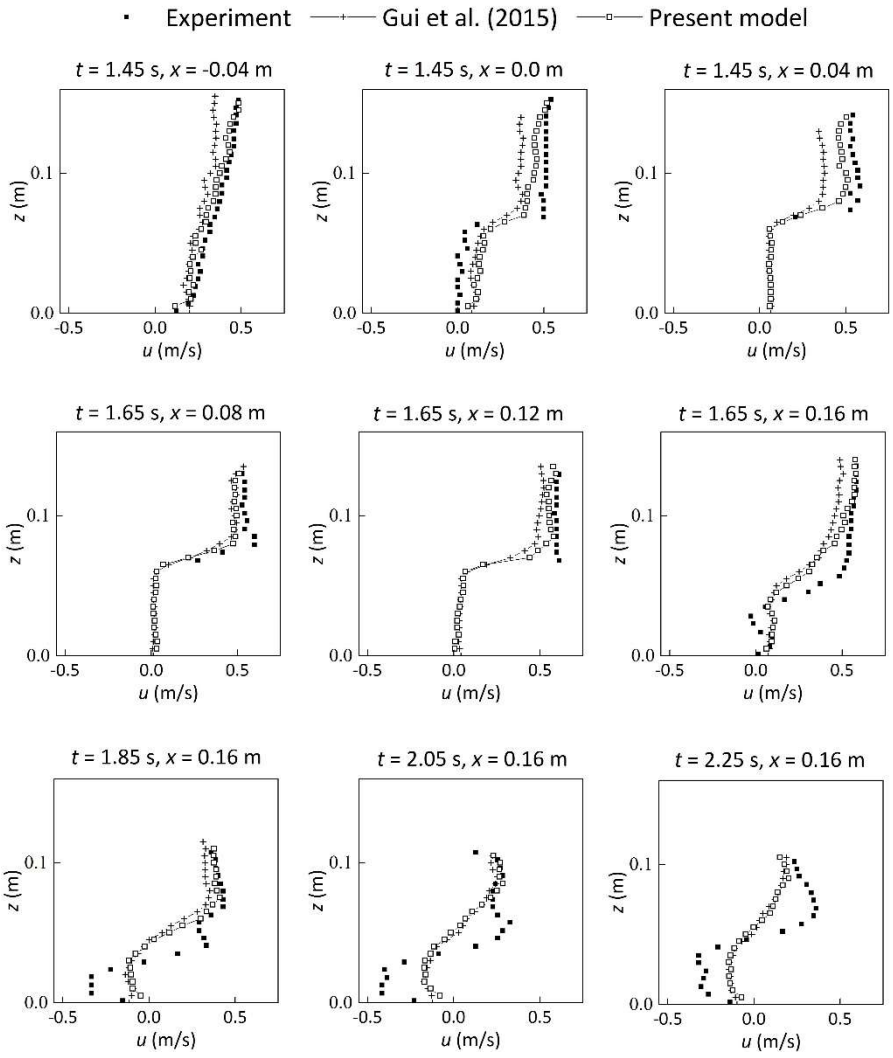

Figure 5-27 Streamwise velocity profiles estimated by the present model in comparison with the results of Gui et al. (2015) and experiments of Wu and Hsiao (2013) at different sections and different times.

5.4 Test case III: wave run-up on smooth, rough, and porous breakwaters

In Sections 5.2 and 5.3, two cases of dam break wave through porous dam and solitary wave interaction with a porous structure were solved using the developed SPH model. It was shown that Ergun's constants $c_1 = 150$ and $c_2 = 1.75$ yields satisfactory results

in both simulations. Here the model will be applied with the same drag coefficients into another case which is a solitary wave run-up and run-down on a breakwater slope based on the experiments of Jensen et al. (2015). There are two issues about this case which motivated to simulate it by the proposed model. One is that it has not been simulated by similar numerical models so that no knowledge is available on the choice of computational parameters, particularly the drag coefficients. It will be find out whether the application of Ergun's constants (150 and 1.75) could lead to satisfactory results. The other issue is that the experimental data is available for three different breakwater slopes: smooth (rigid), rough, and porous. This will be helpful in observing the effect of porosity on the flow field and investigating the model capacity with regard to this issue. In the following, some details of the experiments of Jensen et al. (2015) as well as the numerical model set-up are presented.

The experiments were carried out in a 25 m long, 0.6 m wide and 0.8 m deep flume. Still water depth (H_0) was fixed to 0.4 m and a solitary wave with height of H_w = 0.14 m was generated at all experiments. A piston-type wavemaker was placed at one end of the flume and a breakwater with front and rear slopes of 1:1.5 was constructed with its toe being located 13.55 m from the wavemaker. See Figure 5-28 (a) for a schematic view of the experimental set-up. For the case of smooth (rigid) surface, the breakwater slope was made out of a plastic PVC plate with a width of 0.6 m corresponded to the flume width. For the case of rough surface, the plate was covered by an armour layer of plastic spherical particles with diameter d_s = 38 mm. For the case of a porous breakwater, the same type and size of spheres were used to construct the breakwater core and the plastic PVC plate was replaced by a 2 mm thick perforated plate. Values of 0.40 and 0.41 were reported for porosity of the core material and void-to-plate ratio (porosity) of the perforated plate, respectively. To measure water surface elevation, two wave gauges were set up, one at offshore and another at the toe of the breakwater which the latter was considered as the reference gauge (WG_o and WG_t, respectively, in Figure 5-28 a). For velocity measurements, a LDA system was employed. The velocity was measured at two sections above the

breakwater slope at several points. The measurement sections and their distances to the toe are shown in Figure 5-28 (c). The results of water surface elevation at WG_1 and velocity profiles at section I (at 2 and 19 mm above the slope for the smooth case, and at 2 and 57 mm above the bed for the rough and porous cases) are reported in Jensen et al. (2015).

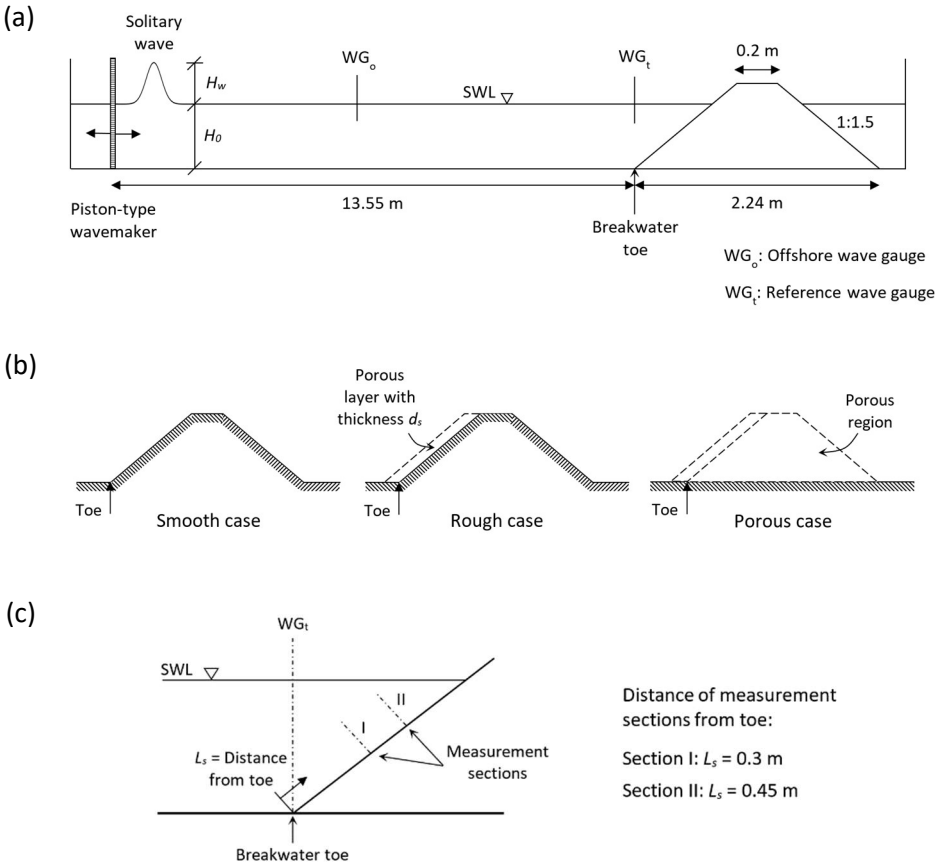

Figure 5-28 Experimental and numerical set-up for solitary wave run-up on a breakwater with smooth, rough and porous slope: (a) experimental flume of Jensen et al., 2015, (b) configuration of breakwater boundaries for smooth, rough and porous cases (hatched areas show the solid wall boundaries), and (c) measurement sections in the experimental and numerical models.

The 2D SPH model developed in the present study is employed to simulate all three cases of solitary wave run-up on smooth, rough and porous breakwater slopes and

the data provided by Jensen et al. (2015) is used for result comparison. The drag coefficients c_1 and c_2 are set to the same values as in the two previous test cases. Initial particle spacing in the free flow region l_0 is 10 mm and smoothing length h_Υ is set to $1.2l_0$. Three layers of fixed dummy particles are placed at the wall boundaries which are depicted by hatched areas in Figure 5-28 (b). At the wavemaker location, a moving wall with three layers of particles is placed while their displacement is determined by Equation (5.9). For the case of smooth slope, as there is no porous region in the domain, the porosity of fluid particles are set to one and no background mesh was employed. For the case of rough surface, as seen in Figure 5-28 (b), the armour layer is simulated as a porous layer with porosity of 0.4 and a thickness equal to the plastic spheres diameter (38 mm). For the porous case, the armour layer as well as the breakwater core are considered as a porous region with porosity of 0.4 (Figure 5-28 b). In the simulations of rough and porous cases, the situation #1 introduced in Section 4.4.1 is applied so that a background mesh is employed for calculation of porosity.

Figures 5-29, 5-30 and 5-31 represent water surface elevation at the breakwater toe and slope parallel velocity at 19 mm above the slope for the smooth case and 57 mm above the slope for rough and porous cases, respectively, in comparison with the experiments. *t* = 0 is considered when the wave crest arrives at the reference gauge (breakwater toe). Table 5-5 presents RMSE values calculated by Equation (5.6) for the water surface elevation as well as velocity profiles with respect to the experimental data. As seen from the figures and the table, the model results are more accurate for smooth, porous, and rough beds, respectively.

The velocities plotted in the figures are obtained by averaging SPH-estimated velocities at each time between *t* = -2 and 4 s at 57 mm (19 mm for the smooth case) above the slope using the cubic Spline function (5.3). Besides, to obtain the water surface elevation at each time, a line of fixed points is placed vertically at the toe location (dash-dotted line in Figure 5-28 c) with a spacing of $0.1l_0$ and divergence of

SPH particle position is calculated at each point using Equation (5.11). Then the point with closest value to 1 is considered as the free surface point and its elevation is considered as the water surface elevation at that time. It is noted that value of the divergence of particle position calculated by Equation (5.11) is 2 when the kernel area of the averaging point is full of neighbouring particles and it is zero when the kernel area is empty. Only slope-parallel velocities at 57 mm (19 mm for the smooth case) above the slope are presented here, although the velocity at 2 mm from the slope is also provided by Jensen et al. (2015). The reason is that the particle spacing l_0 is set to 10 mm in the present simulations so that the resolution is not enough to capture velocity at 2 mm above the slope. By using l_0 = 10 mm, about 57000 particles are used to simulate the case, while using l_0 = 2 mm would need about 1.5 million particles which is not feasible in the framework of the present study.

According to Figures 5-29, 5-30 and 5-31, the velocity is predicted well during the run-up and run-down processes. However, after the run-down (during the second run-up) some discrepancies are observed in the results of water surface elevation and velocity. It seems the velocity variations are restricted during the secondary run-up. A reason could be that the computational resolution is not enough to capture those post-run-up fluctuations. Besides, the agreement between the predicted and measured velocity profiles in the case of rough surface is poorer than the smooth and porous cases (Table 5-5). It reveals that considering a single roughness layer (spheres) as a porous layer in the model may lead to a mismatch when the computational resolution is not sufficient. This issue needs more investigation and is considered as a future study.

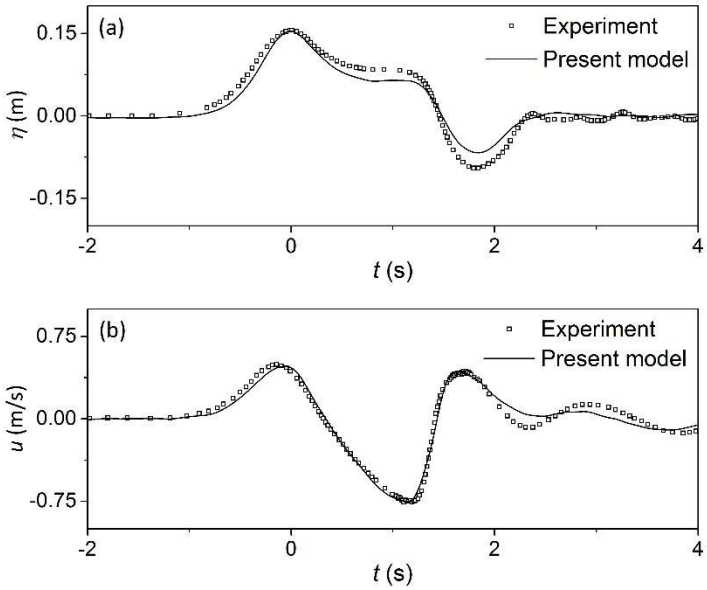

Figure 5-29 Wave run-up and run-down on the smooth slope: (a) water surface elevation at the toe, and (b) slope parallel velocity at 19 mm above the surface, between *t* = -2 and 4 s.

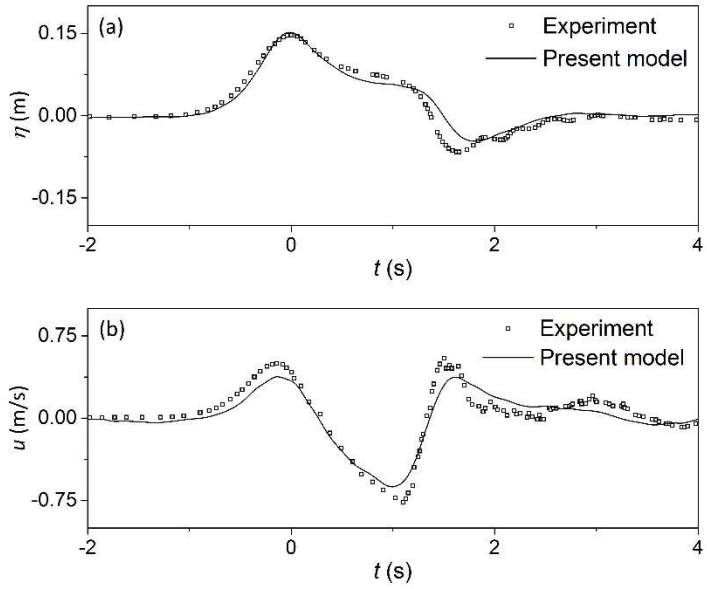

Figure 5-30 Wave run-up and run-down on the rough slope: (a) water surface elevation at the toe, and (b) slope parallel velocity at 57 mm above the surface, between *t* = -2 and 4 s.

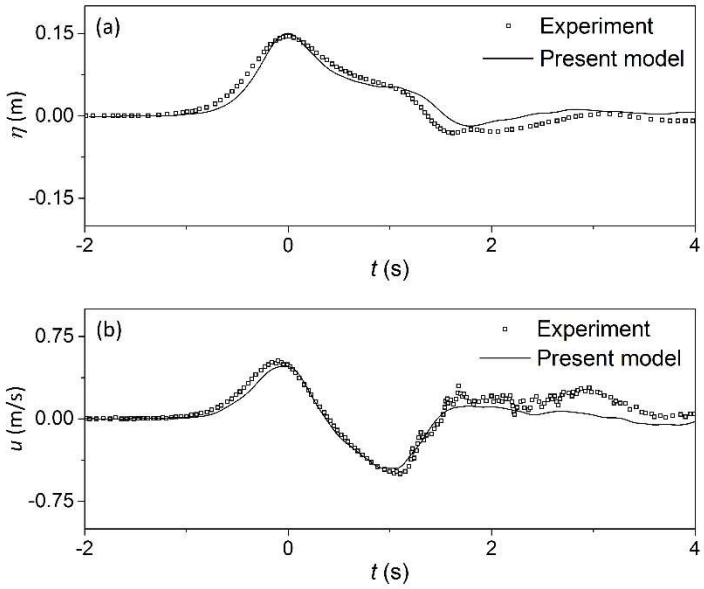

Figure 5-31 Wave run-up and run-down on the porous breakwater: (a) water surface elevation at the toe, and (b) slope parallel velocity at 57 mm above the surface, between *t* = -2 and 4 s.

Table 5-5 RMSE of the estimated water surface elevation η_w and horizontal velocity *u* profiles with respect to the experimental data.

	Smooth surface	Rough surface	Porous surface
RMSE of η_w (m)	0.0142	0.0161	0.0145
RMSE of *u* (m/s)	0.063	0.1059	0.0889

To investigate the effect of porosity on the run-up and run-down, the numerical results of water surface elevation and velocity profiles for three cases of smooth, rough and porous breakwater are represented together in Figure 5-32. According to this figure, water surface elevation in the rough and porous cases is only a few millimetres less than the smooth case when the wave is running up on the slope, while this difference gets significantly higher during run-down and secondary run-up. Besides, the figure shows that the variation of parallel-slope velocity is higher on the smooth slope while it decreases when the slope is rough. The variation becomes even

less in the case of porous breakwater as the secondary run-up cannot be observed clearly over the porous slope. It is due to the penetration of water into the structure so that a significant part of the momentum in the slope-parallel direction is removed.

Looking at Figures 5-29, 5-30 and 5-31, one may notice that in the case of smooth slope the experimental velocity was little influenced by fluctuations except at a short time during the run-down process (the bottom of the profile in Figure 5-29 b), while in the cases of rough and porous slopes, velocity fluctuations are clearly seen during the run-down and secondary run-up processes. Jensen et al. (2015) noted that these fluctuations are mainly due to the presence of solid particles. However, such fluctuations are not seen in the model results of velocity. A reason is insufficient computational resolution. But the more important one is that in the present model the flow is simulated at a macroscopic scale, i.e. the porous material is not simulated as solid boundaries. Therefore, the dispersion of flow due to the existence of solid spheres is not taken into account.

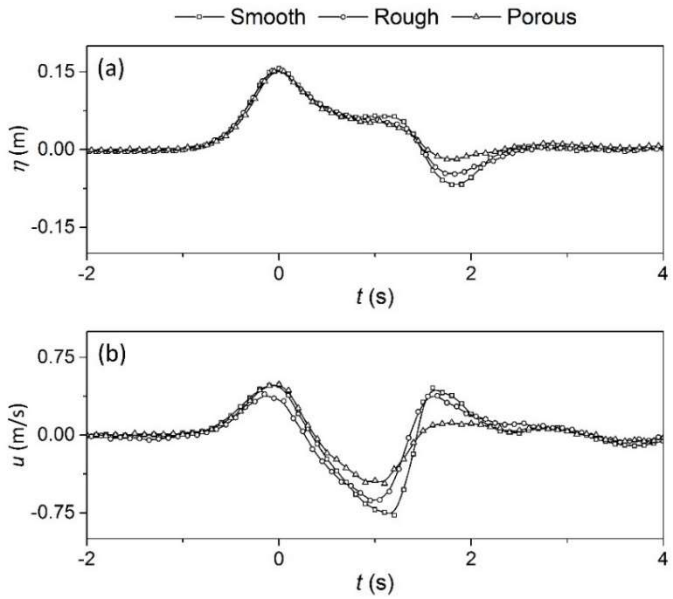

Figure 5-32 Comparison between numerical result of (a) water surface elevation at the toe, and (b) slope parallel velocity at 57 mm (19 mm for the smooth case) above the surface, for all three smooth, rough and porous cases. The lines show the spline fitting to the data symbols.

5.5 Computational resolution effect on the interface layer

In Section 4.2, the required constraints for G and r_Ω; and in Section 4.3, the constraints associated with W and r_Υ were discussed. Later in Section 4.4.1, it was noted that in the practical situation #1 (which was the case in all application tests in the present chapter), the *constraint #1* will be instinctively satisfied within the porous region and the required constraints will be those represented in Equation (4.60). In the present simulations, following Equation (4.60), r_Ω was set equal to the mean diameter of solid particles at the interface and was kept unchanged over time. Besides, r_Υ was set equally over space for all particles and kept unchanged over time. However, the satisfaction of *constraint #4* (or point c of Equation 4.60, $r_\Upsilon << L_{\langle \mathbf{u} \rangle^\alpha}$) might be uncertain in some simulations. According to this constraint, the kernel support size r_Υ should be much smaller than the characteristic length scale of the average flow field. Since in SPH, r_Υ is related to the particle spacing ($h_\Upsilon = 1.2 l_0$ as a common practice), l_0 should be chosen as to satisfy *constraint #4*. To investigate this issue, the simulations of test cases I and II are repeated with using different particle spacing.

Figure 5-33 presents a comparison between water surface profiles of test case I (dam break wave through crushed rocks) at time *t* = 1.2 s with using different particle spacing. No considerable difference is seen between the profiles. This is because of the following issues: i) flow Re Number is relatively low; and ii) interfacial boundary between porous and free flow regions is not 'sharp', i.e. a significant change does not take place in average flow quantities when transferring from free flow to porous structure and vice versa. Therefore, *constraint #4* is already nearly satisfied with using the applied computational resolutions.

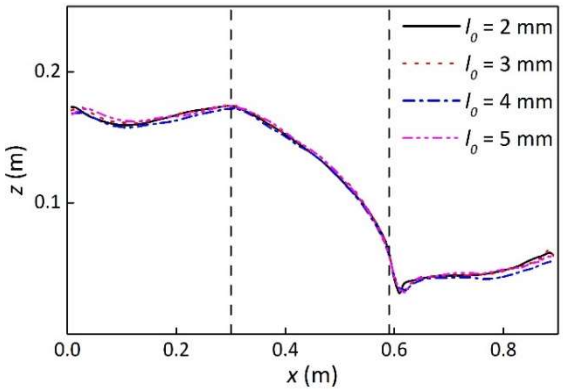

Figure 5-33 Water surface profiles of test case I (dam break flow through crushed-rocks porous dam) at time *t* = 1.2 s, with using different computational resolution (particle spacing l_0).

However, the situation for the test case II may be different. Looking at the experimental data of Wu and Hsiao (2013) which were presented in Figures 5-16 to 5-25, and assuming that velocity in the porous region is much smaller than above the structure, the horizontal velocity shows a significant change over a thin layer at the interface. This can be seen more clearly at times *t* = 1.45 s and 1.65 s when the wave is travelling above the structure. For instance, at *t* = 1.45 s and x = 0.0 m, the measured horizontal velocity increases from about 0.04 to 0.5 over about 10 mm at the interface. Another example can be given at *t* = 1.65 s and x = 0.12 m, where the experimental horizontal velocity has a value of 0.61 m/s only about 2.5 mm above the structure boundary (spheres crest). To resolve such a thin boundary and thereby satisfying *constraint #4*, the kernel support size should be chosen much smaller than the interface layer thickness. In other words, the particle spacing should be chosen as to satisfy *constraint #4*, particularly for velocity, i.e. $r_\Upsilon << L_{\langle \mathbf{u} \rangle^\alpha}$ (Equation 4.60 c).

To investigate this issue, the simulation of test case II is repeated by using different initial particle spacing l_0 of 3, 4, 5 and 6 mm. Figures 5-34 and 5-35 show the result in comparison with the experimental data. In Figure 5-34, the horizontal and vertical velocity profiles at two different sections x = 0.0 and 0.04 m at *t* = 1.45 s when the wave is travelling above those two sections are presented. Similarly, Figure 5-35 represents the velocity profiles at two sections x = 0.08 and 0.12 m at *t* = 1.65 s when

the wave is passing the end of the structure. As can be seen, both horizontal and vertical velocity profiles inside the porous region as well as above it are similar for different computational resolutions. However, at the interface, a small difference can be observed in the slope of the profiles. This can be seen more clearly from Figure 5-36 where the horizontal velocity profiles at t = 1.65 s and x = 0.12 m and vertical velocity profiles at t = 1.45 s and x = 0.0 m are plotted at a different scale. As particle spacing is set to a smaller value (the resolution gets higher), the slope of velocity profile gets closer to the experimental one, though it is still far from a perfect match. This is because by using smaller particle spacing the satisfaction of *constraint #4* at the interface is approached. Although this constraint may not be fully satisfied at such cases with 'sharp' interfacial boundaries, the error is not significant, which means the model can reproduce satisfactory results for the applications simulated here.

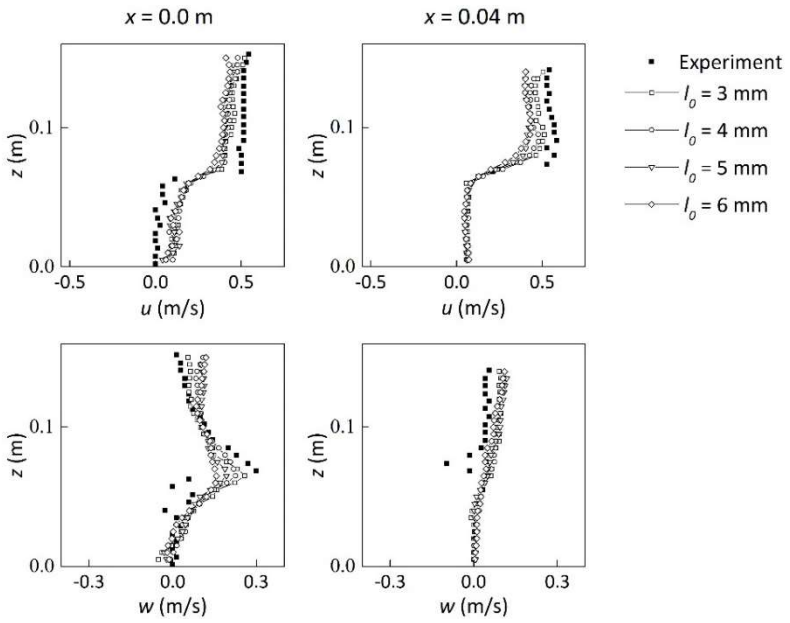

Figure 5-34 Numerical horizontal (two top figures) and vertical (two bottom figures) velocity profiles with different particle spacing l_0 in comparison with the experimental data at t = 1.45 s at two sections x = 0.0 and 0.04 m.

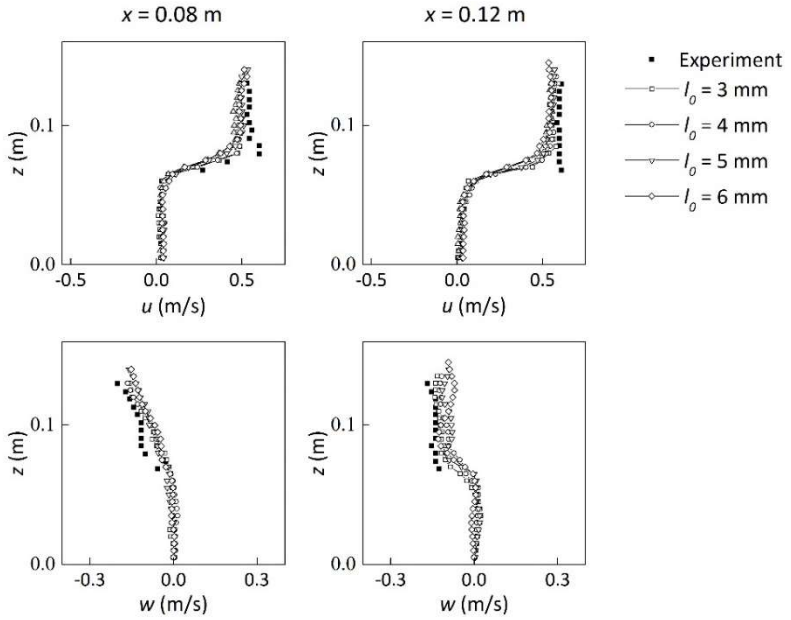

Figure 5-35 Numerical horizontal (two top figures) and vertical (two bottom figures) velocity profiles with different particle spacing l_0 in comparison with the experimental data at *t* = 1.65 s at two sections *x* = 0.08 and 0.12 m.

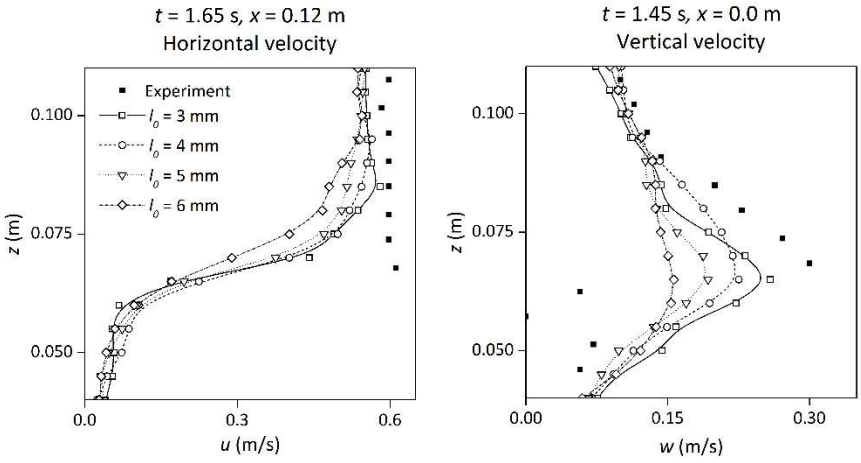

Figure 5-36 Numerical horizontal velocity at *t* = 1.65 s and *x* = 0.12 m (left) and vertical velocity at *t* = 1.45 s and *x* = 0.0 m (right) with using different particle spacing l_0 in comparison with the experimental data.

5.6 Summary

Three test cases of flow interaction with porous structures were simulated by the developed model. The treatment of interfacial boundary was carried out carefully in order to address the mathematical requirements introduced in Chapter 4. The first case is a benchmark test which has been applied in many numerical studies in order to validate the models in predicting water surface elevation; the second case was selected to test the accuracy of the model in predicting velocity field; and case III was employed as a new test case which has not been simulated in other numerical studies. In all the cases, the situation #1 introduced in Section 4.4.1 was employed for numerical treatments. Besides, Ergun's constants (c_1= 150 and c_2 = 1.75) were employed for drag coefficients. Although the characteristics of different porous structures are not the same, it was shown that using these constants provides satisfactory results of water surface elevation in the first and third applications as well as acceptable velocity distributions around the porous structures in the second and third cases. This is attributed to the fact that all the present cases are in the range of the data Ergun used to derive his equation. In fact, the aim of using same constants was to avoid test-specific numerical adjustments. The comparison between the present model with the existing SPH models in estimating water surface elevation for the case of dam break wave through crushed rocks revealed how the interfacial boundary is treated has a greater effect on the results than a slight change in the drag coefficient.

The effect of computational resolution was investigated in order to check the validity of the equations at the interfacial boundaries with regard to the length constraints introduced in Chapter 4. Using different particle spacing did not affect the results of water surface elevation in the first test case, while it had a considerable effect in the streamwise velocity distributions in the second case. The latter is attributed to the length *constraint #4* for velocity, i.e. the size of averaging volume (computational

discretisation) should be small enough to capture the variations in the average velocity field at the interface boundary.

The SPS model was applied with the Smagorinsky approach to estimate the eddy-viscosity. As shown in Chapter 3, this model was not sufficient in predicting turbulent shear stress in open channel flows over rough surfaces. Here also the results are expected to be affected by this issue, probably near the porous interfaces where the roughness may be considerable, particularly for the test case II where velocity changes rapidly over the interface boundary. However, due to the unavailability of detailed turbulence data, it was not possible to investigate the accuracy of the turbulence closure model in the present applications. The investigation of this issue will be carried out deeply in the next chapter as highly-sheared turbulent free surface channel flow over natural porous beds will be studied where detailed experimental data of velocity and turbulent shear stress are available.

Chapter 6 Modelling Turbulent Open Channel Flow Over and Within Natural Porous Beds with High Gradient Interfacial Boundaries

Turbulent free surface channel flows over porous gravel beds are simulated in this chapter using the model developed in Chapter 4. Appropriate modifications are introduced into the drag and turbulence modelling. For turbulence, a three-layer mixing-length model is proposed based on the experimental data and the Nezu and Rodi (1986) formula. Besides, the challenge in reproducing a steady and uniform flow condition within a reasonable distance is tackled by introducing a new porous inflow boundary technique and an outflow imaginary wall. The model is constructed to simulate an existing set of experimental data of turbulent open channel flows over porous gravel bed armour layers. Twelve test cases with 2 different gravel bed configurations and various flow conditions are simulated by the model and results are compared to the experimental data. The effects of computational resolution on the results of velocity and shear stress as well as the validity of the proposed turbulence model are all investigated.

6.1 The case study

The case study is the simulation of turbulent free surface channel flows over and within porous beds with high gradient interfacial boundaries. A set of existing

experimental data (from Technical University of Braunschweig) of different flow discharges over an armour layer with 2 different surface roughness is employed to validate the model results of velocity and shear stress. A brief description of the experimental study is presented in the following. For more details see Aberle (2006), Aberle (2007), and Aberle et al. (2008).

The experiments were carried out in the laboratory of the Leichtweiss-Institute for Hydraulic Engineering, Technical University of Braunschweig, in a tilting flume with a constant slope of about 0.0027. The length, width and height of the flume were 20 m, 0.90 m and 0.60 m, respectively. A mixture of coarse gravel sediments (0.63 to 0.64 mm) was placed in the bottom of the flume. The test section was located 9 m downstream of the flume inlet where the width of the channel was decreased in order to reduce the effects side walls. A flow with discharge Q_{armour} = 120 l/s was firstly run into the flume, mobilising the sediment and then maintained flow until the bed surface reached stable condition, i.e. the sediments became stable. For this bed, then, several measuring discharges less than the armouring discharge (Q_{armour} = 120 l/s) were run into the flume and flow velocity was measured using a 3D Laser Doppler Anemometer (LDA) system at 24 vertical profiles distributed randomly in the test section. In all experiments conducted with measuring discharges less than the reference armouring discharge, the bed material was immobile, and the flow was steady and uniform. Figure 6-1 depicts a schematic side view of the flume including porous armour layer, free flow (clear water), and interface (roughness) layer.

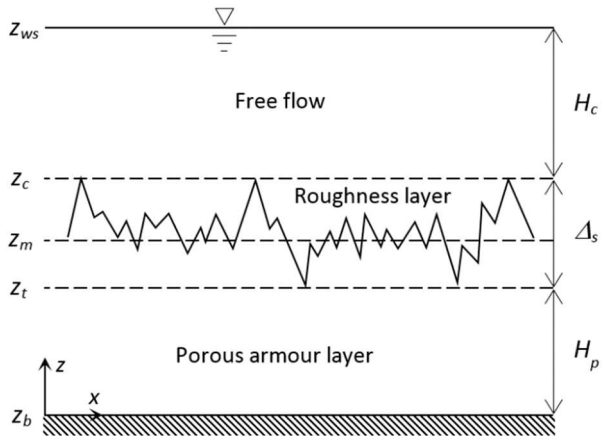

Figure 6-1 Schematic 2D view of the experimental condition of the bed. z_b is the level of bottom wall of the flume; z_t and z_c show trough and crest of the roughness layer; z_m is z_t plus the equivalent height of roughness (i.e., the volume of melted roughness materials per unit bottom area) and z_{ws} is the water surface level.

The experiment was repeated for a discharge higher than the first armouring discharge, i.e. for Q_{armour} = 180 l/s, so that the armour layer was destroyed and then a new one developed. Accordingly, z_t , z_m and z_c levels changed, although the change in the bed material below z_t was supposed to be very small. For the new bed, also several measuring discharges less than 180 l/s were run into the flume and 3D velocities were measured at the same 24 locations for each discharge. The experiments were repeated for another 2 armouring discharges (Q_{armour} = 220 and 250 l/s) so that 2 other beds were developed. For each one, several measuring discharges less than the forming armouring discharge were examined, and measurements were accordingly carried out. All measuring flows were in the steady and uniform condition. Table 6-1 presents a list of experiments. As seen in the table, the experiments with armouring discharge Q_{armour} = 250 l/s were repeated since the armour layer was accidently destroyed in the upstream in one of the experiments.

Table 6-1 Armouring experiments.

Q_{armour} (l/s)	Bed slope	d_{50} (mm)
120	0.0027	11.1
180	0.0026	13.6
220	0.0026	18.4
250a	0.0028	19.5
250b	0.0028	19.6

The location of the 24 velocity profiles are shown with white circles in Figure 6-2 where the scan of bed topography (obtained by a laser displacement meter) is depicted for three different armouring discharges of 120, 220 and 250 l/s. Besides, Figure 6-3 shows the procedure of velocity measurements with the LDA system for the cases with shallower and deeper depths, where respectively, a tank set-up (left) and an aerodynamic housing system (right) were employed. The applied system allowed measurement of the velocity within the roughness layer (the layer between z_t and z_c in Figure 6-1). For each experiment, the double-averaged velocity and Reynolds Stress profiles were provided by spatial averaging of time-averaged profiles on planes parallel to the average bed level over the 24 measuring locations. Within the roughness layer, all 24 measuring points were not available at some planes due to the existence of solid material. Therefore, the averaging was carried out from the levels with at least 5 available points. Some preliminary results of the hydraulic measurements can be found in Aberle and Koll (2004), Aberle (2006) and Nikora et al. (2007).

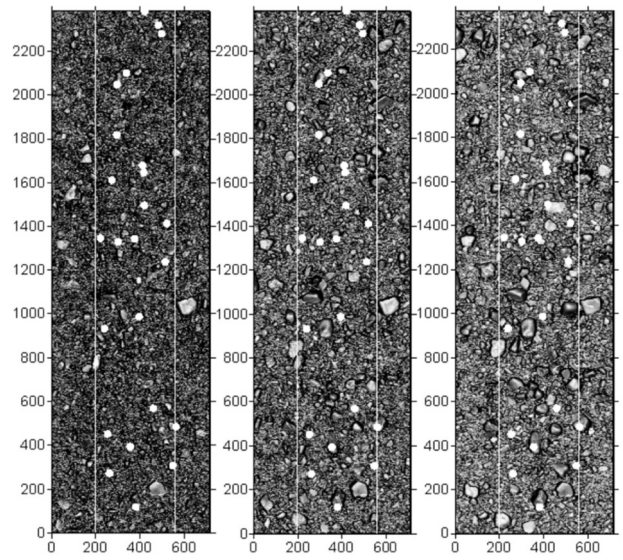

Figure 6-2 Armour layer topography after armouring discharges of 120, 220, and 250 l/s (from left to right). Lines indicate the test section and points indicate the location of velocity profiles in the xy-plane. (Aberle, 2006)

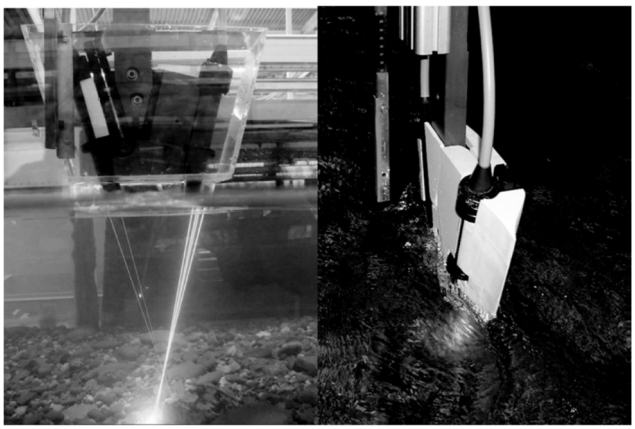

Figure 6-3 Tank setup for LDA-measurements (left) and measurement situation using submerged probes with aerodynamic housing (right). (Aberle, 2006)

Table 6-2 The twelve test cases.

Bed ID (armouring discharge)	z_t (mm)	z_c (mm)	Δ_s (mm)	Measuring discharges (l/s)	z_{ws} (mm)	H_c (mm)	Test case ID
B1 (Q_{armour} = 180 l/s)	36.6	87.6	51	60	184	96	B1-Q60
				90	217	129	B1-Q90
				120	248	160	B1-Q120
				150	271	184	B1-Q150
				180	296	208	B1-Q180
B2 (Q_{armour} = 250 l/s)	-5.5	71.5	77	60	166	95	B2-Q60
				90	200	128	B2-Q90
				120	230	159	B2-Q120
				150	256	185	B2-Q150
				180	279	207	B2-Q180
				220	306	235	B2-Q220
				250	330	258	B2-Q250

In the present study, the experiments of armouring discharges Q_{armour} = 180 l/s and 250b l/s (shown in Table 6-1) are selected to be simulated. In these two sets of experiments, respectively, 5 and 7 measuring discharges are tested. Therefore, there are two different porous beds, each tested with several flow conditions, to be simulated in the present study. Table 6-2 represents some details of the bed and flow conditions at these test cases. It is noted that the values of vertical levels (z_t , z_c , and z_{ws}) are measured from an arbitrary reference.

6.2 Numerical modelling scheme

The SPHAM equations of mass and momentum (Equations 4.45 and 4.46) are considered as the governing equations for the present simulations. The discretised form of these equations is presented in Equations (4.56) and (4.57), where the last two terms in the momentum equation represent the effects of turbulence and bed drag. Determination of these two terms will be discussed in Sections 6.2.2 and 6.2.3.

The equation of state (Equation 3.11) is used to link the equations of mass and momentum for calculation of pressure from the temporal change in the fluid density. However, this change is restricted to be less than 1% by choosing an appropriate value for the speed of sound (WCSPH scheme). The predictor-corrector method presented in Section 4.3.2 and Figure 4-5 is employed for time implementation. Besides, a Shepard density filter is applied at every 30 time steps to reduce the pressure error due to the density variations, and a link-list method is used for particle searching in order to enhance the efficiency of the model in terms of computational time.

6.2.1 Determination of porosity

For determination of porosity and the interfacial boundary layer, the situation #2 (Section 4.4.2) is considered here, i.e. the distribution of porosity ϕ is assumed to be known rather than being calculated by Equation (4.54). In other words, no background mesh is employed. The reason is that in addition to that the model is 2D, the porous bed in the experimental study is highly heterogeneous with no information on the geometry and characteristics of the solid matrix. Besides, the porosity distribution is not known for all cases. Therefore, a method is required to determine the distribution of porosity over the total depth to be applied into the model.

In the experiments, the porosity has been measured only for the bed under Q_{armour} = 220 l/s by filling water stepwise into the laboratory flume. It has been observed that the solid matrix at the interface had significant changes under different armouring discharges while it remained unchanged below the roughness trough. Therefore, it is assumed that the mean porosity below the roughness trough z_t in the case of Q_{armour} = 220 l/s (i.e. ϕ_0 = 0.22) is applicable for other cases too. Accordingly, in the present study, a constant distribution of porosity with the value of ϕ_0 = 0.22 is considered for below z_t while the distribution of porosity over the roughness layer (from z_t to z_c) needs to be defined for each bed condition (B1 and B2 in Table 6-2). The simplest definition could be a linear profile over the roughness layer from roughness trough z_t

with the value of ϕ_0 to the roughness crest z_c with a value of 1.0 as clear water porosity. However, it is noted that z_t and z_c are absolute lower and higher levels of the roughness layer where the density of solid material may have a lower change near these levels compared to its variation within the centre of the roughness layer. Therefore, it is assumed that variation of porosity occurs in a layer (namely porosity interface layer) with a thickness less than Δ_s as depicted in Figure 6-4. As the knowledge on the distribution of solid phase density in the roughness layer is not available, the thickness of porosity interface layer is assumed to be half of Δ_s with a centre at z_m. Porosity variation over this layer is assumed to be linear. According to this definition, distribution of porosity over the total depth is presented as the red solid line in Figure 6-4. In order to have a smooth change of porosity from the linear profile to the constant values at the lower and upper bounds of the porosity interface layer (red dash-dotted lines), cubic Spline function (Equation 5.4) with supports of, respectively, r_t and r_c is employed to smooth out the profile.

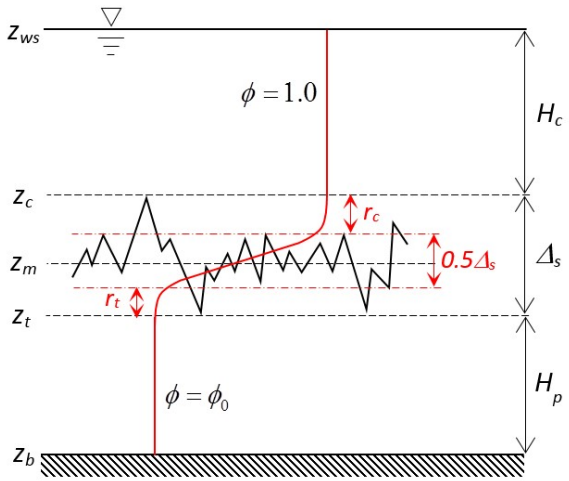

Figure 6-4 Distribution of porosity over the total depth including porous bed, roughness layer and free flow regions. The layer bounded by dash-dotted lines is the porosity interface layer over which the porosity changes linearly from ϕ_0 to 1.0.

6.2.2 Determination of drag effect

The last term added to the momentum Equation (4.57), $\mathbf{A}_a$, is the discrete (modelled) form of the surface integral term in the SPHAM equation of momentum (4.46). This term represents the viscous and form-drag effects of solid skeleton on the macroscopic flow field and has been estimated using various drag closure models in the literature. In the simulation of test cases in Chapter 5, comparison of the results of water surface and velocity profiles with the experimental data showed that the application of Ergun's closure equation with its original coefficients, i.e. $c_1 = 150$ and $c_2 = 1.75$ provides good accuracy for flow through porous media in different engineering applications. Ergun's equation has been obtained from measuring various flow conditions in packed beds. In the present study, the armour layer below the roughness trough level z_t is assumed to be packed so that the Ergun's equation (presented in Equation 4.29) is applied for estimating the viscous and form-drag effects within the bed from z_b to z_t as follows.

$$\mathbf{A}_a = -c_1 \frac{(1-\phi_a)^2}{\phi_a{}^2} \frac{\nu_0}{d_s{}^2} \mathbf{u}_a - c_2 \frac{(1-\phi_a)}{\phi_a} \frac{1}{d_s} \mathbf{u}_a |\mathbf{u}_a| \qquad : \qquad z \le z_t \tag{6.1}$$

Where $\mathbf{A}_a$ is the drag effect on a generic particle a; ϕ_a is fluid porosity at particle position, ν_0 is kinematic viscosity coefficient, c_1 and c_2 are viscous and form-drag coefficients, and d_s is bed mean particle size which is assumed to be equivalent to d_{50} in the present study.

Observing the experimental data such as bed topography scans shown in Figures 6-2 and 6-5, one may notice that the bed is not packed within the roughness layer, but with considerable spacing between solid particles. In fact, within this layer, the drag force from solid material to the flow is rather from the interaction between flow and single (or few) particles so that the application of Ergun's equation may be inaccurate. For this reason, the drag force model introduced in Section 3.1.1.1 (Equations 3.3 and

3.4) is applied here with some modifications for the estimation of drag-induced shear stress term ($\mathbf{A}_a$) within the roughness layer.

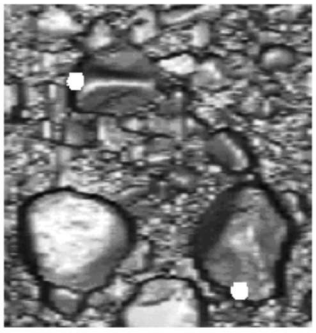

Figure 6-5 Two measurement locations (white points) and surrounding topography in one of the experiments.

As discussed in 3.1.4.2, the cross-sectional area A_d in Equation (3.4) and the bed-parallel planar area A_τ in Equation (3.3) are equivalent to the fluid particle size l_0 and the product of $d_s l_0$, respectively. Moreover, the shape function W_d can be replaced by $(1-\phi)$ which represents density distribution of solid phase within the roughness layer. By applying these replacements into Equations (3.3) and (3.4), the form-induced shear stress term $\mathbf{A}_a$ within the roughness layer is formulated as

$$\mathbf{A}_a = -C_d\left(1-\phi_a\right)\frac{1}{d_s}\mathbf{u}_a\left|\mathbf{u}_a\right| \qquad : \qquad z_t < z \le z_c \tag{6.2}$$

where C_d is the drag coefficient which is taken to be around 0.9 according to the study of Schmeeckle et al. (2007). In that study, C_d was found to be 0.76, 1.36, and 0.91 for spheres, cubes, and natural particles, respectively.

By using Equation (6.2), the effect of viscous drag is neglected within the roughness layer. Based on the fact that 'viscous effect is dominant when flow Re Number is low while form-induced drag is dominant when flow Re Number is high', this equation is

valid in the present simulations. By comparing Equations (6.1) and (6.2), Equation (6.2) is equivalent to (6.1) if one replaces c_1 and c_1 with zero and $C_d\phi_a$, respectively. Therefore, the drag-induced shear term is formulated as the following to be applied over the whole domain including armour layer, roughness layer, and clear water regions.

$$\begin{aligned}\mathbf{A}_a = &-C_1\frac{(1-\phi_a)^2}{\phi_a{}^2}\frac{\nu_0}{d_s{}^2}\mathbf{u}_a \\ &-C_2\frac{(1-\phi_a)}{\phi_a}\frac{1}{d_s}\mathbf{u}_a|\mathbf{u}_a| \quad : \quad \begin{cases} C_1 = c_1,\ C_2 = c_2 & \text{if} \quad z \le z_t \\ C_1 = 0.0,\ C_2 = C_d\phi_a & \text{if} \quad z > z_t \end{cases}\end{aligned} \tag{6.3}$$

where ϕ_a is estimated using the procedure introduced in Section 6.2.1. Obviously, $\mathbf{A}_a$ is zero in the clear water where porosity is equal to 1.0. The calculated drag term will have a smooth distribution near the bounds of the roughness layer (z_t and z_c) as it is related to the porosity and velocity which have smooth transition over the interface.

6.2.3 Determination of the effect of turbulence

A major source of turbulence in free surface flows is from interaction with the bed boundary. The geometry of the bed surface causes a disturbance in the flow near the boundary which transfers through the depth in the form of turbulence. Therefore, in order to resolve turbulence in a numerical model, one needs to simulate the bed microscopically. In this case, a part of turbulence is resolved by the computational discretisation while the unresolved part is modelled by an appropriate model such as SPS. This issue was presented in Chapter 3 (Equation 3.5) as the basic idea of LES.

As also discussed in Chapter 3 (Sections 3.1.1.2 and 3.2.6), due to the macroscopic modelling of the roughness layer/porous bed in the present study, physical dispersion which is a result of flow obstruction by solid particles is disregarded. Therefore, the part of turbulent stress resolved by particle motion is only from deviations in the average macroscopic field rather than the microscopic flow. Besides, the modelled shear stress estimated by the SPS model with the Smagorinsky constant (about 0.15)

was shown to be significantly underestimated due to the same reason and/or the inaccurate estimation of velocity-pressure interactions (as addressed by Mayrhofer et al., 2015). Based on this fact, it was assumed that the total shear stress should be modelled in the case of macroscopic simulation of a rough bed (Equation 3.6) and therefore the mixing-length model was proposed to be used for the estimation of eddy-viscosity in the SPS model rather than using the standard Smagorinsky formulation. This procedure is adopted in the present simulations too, since the flow condition is similar to the case studied in Chapter 3, i.e. flow is uniform, and bed is rough which is represented macroscopically.

The main advantage of the mixing-length model is that it is computationally simple, while the main drawback of this approach is that the spatial distribution of mixing-length should be known. For open channel flows, usually established formulas such as Nezu and Rodi (1986) are available to estimate the mixing-length. But those formulas are basically derived from measurements of turbulent flow over flat beds. In the present test cases, the bed is porous and the surface is rough with a relatively thick roughness layer so that the slope of the mixing-length profile could be different from $\kappa = 0.41$.

Thanks to the availability of the detailed velocity and Reynolds Stress data to some distance below and above the roughness crest z_c in the present experiments, it is feasible to check whether Nezu and Rodi (1986) formula is valid for the present cases. According to Equations (2.4) and (2.5), if Reynolds Stress and slope of streamwise velocity profile are available, then assuming that $\partial u/\partial z$ is significantly higher than the velocity gradients in other directions, the mixing-length can be estimated simply using the following equation.

$$l_m = \sqrt{\frac{\tau_{\exp}}{\rho\left(\partial u/\partial z\right)^2}} \tag{6.4}$$

where $\tau_{\exp} = \rho\overline{u'w'}$ is the Reynolds Stress derived from the experimental velocity data where u' and w' are the fluctuations of the horizontal (x) and vertical (z) components of the experimental velocity and the overbar denotes the temporal averaging operator. The coordinate components x and z are shown in Figure 6-1.

Here, firstly, a cubic Spline interpolation is used to fit smooth profiles to the experimental velocity and Reynolds Stress profiles and then the velocity gradient $\partial u/\partial z$ is calculated from the continuous velocity profile. Then, using the continuous Reynolds Stress and velocity gradient profiles, the mixing-length distribution is estimated by Equation (6.4). The result is shown in Figures 6-6 to 6-9 for all the 12 test cases. Note that the measurements have been carried out only to some distance above the roughness layer since velocity data near water surface has not been collected.

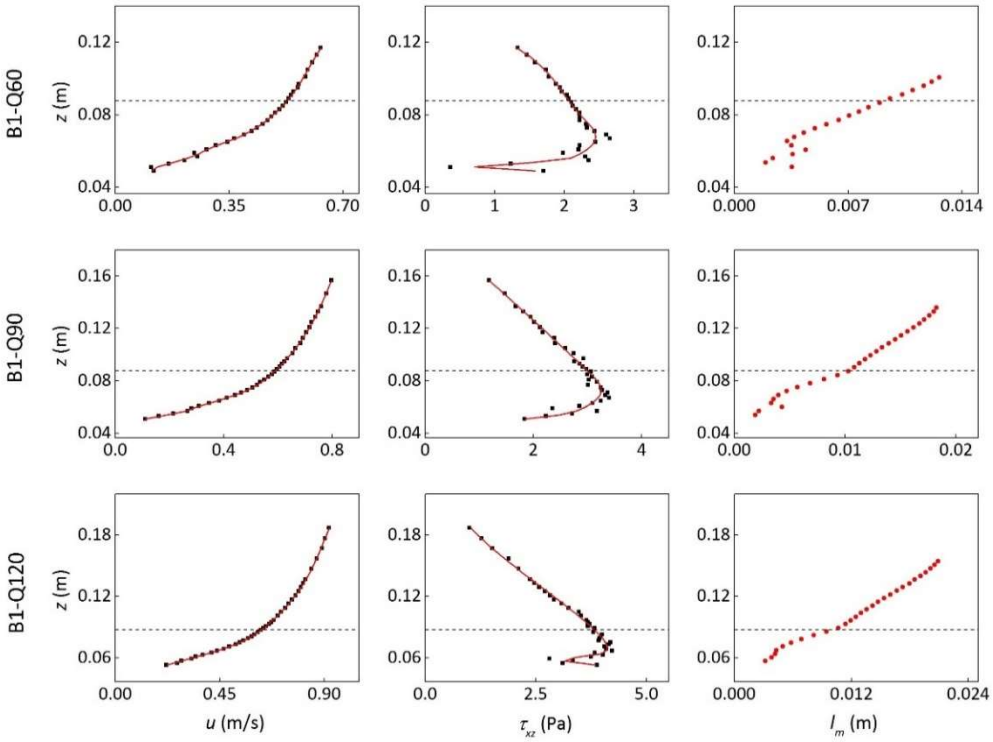

Figure 6-6 Profiles of experimental streamwise velocity, Reynolds Stress, and mixing-length for the test cases B1-Q60, B1-Q90 and B1-Q120. Black squares: experimental profiles; red solid lines: Spline fittings; red circles: calculated mixing-length; dashed line: roughness crest.

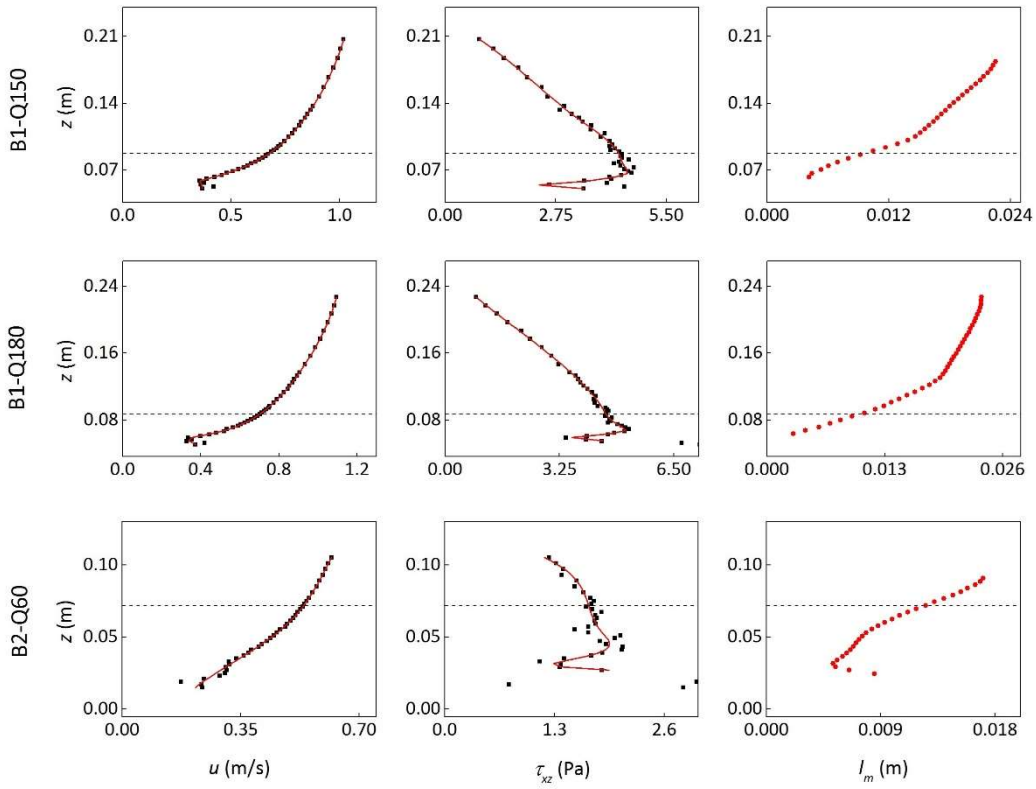

Figure 6-7 Profiles of experimental streamwise velocity, Reynolds Stress, and mixing-length for the test cases B1-Q150, B1-Q180 and B2-Q60. Black squares: Experimental profiles; Red solid lines: Spline fittings; Red circles: calculated mixing-length; dashed line: roughness crest.

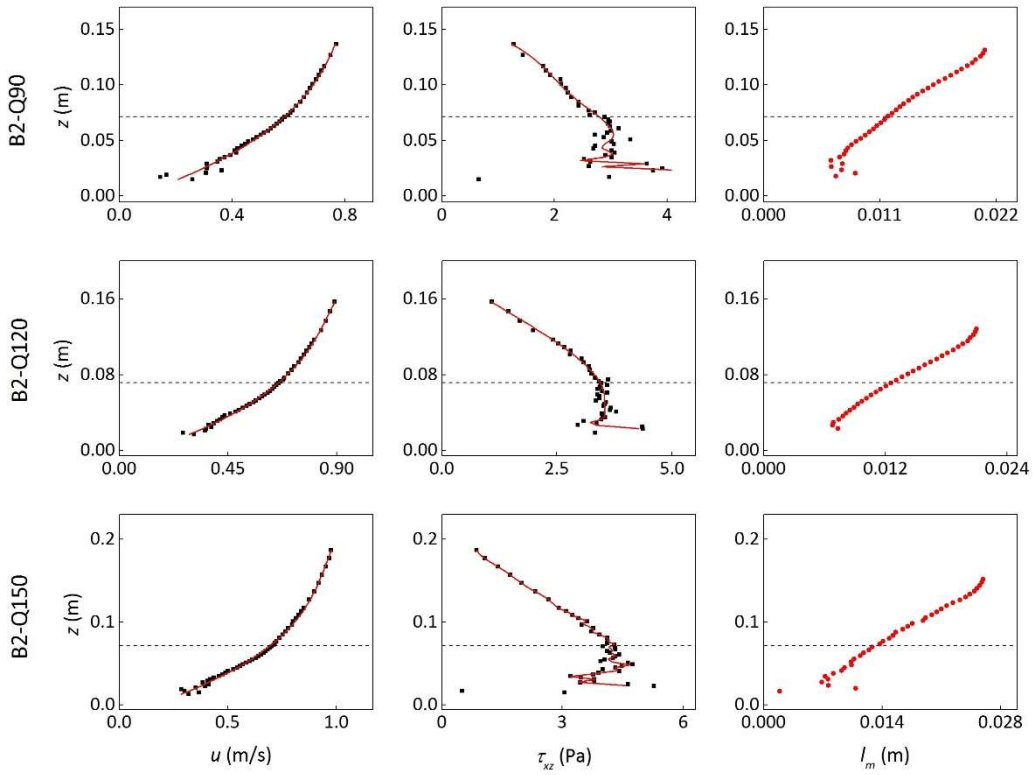

Figure 6-8 Profiles of experimental streamwise velocity, Reynolds Stress, and mixing-length for the test cases B2-Q90, B2-Q120 and B2-Q150. Black squares: Experimental profiles; Red solid lines: Spline fittings; Red circles: calculated mixing-length; dashed line: roughness crest.

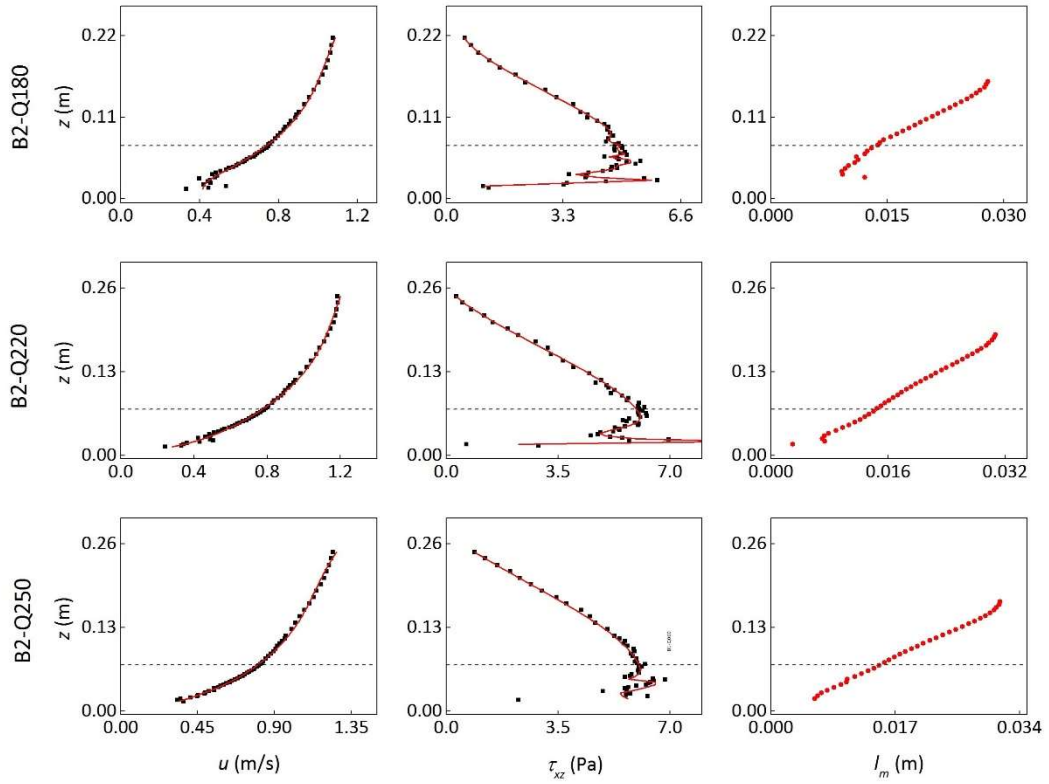

Figure 6-9 Profiles of experimental streamwise velocity, Reynolds Stress, and mixing-length for the test cases B2-Q180, B2-Q220 and B2-Q250. Black squares: Experimental profiles; Red solid lines: Spline fittings; Red circles: calculated mixing-length; dashed line: roughness crest.

Now it is possible to compare the obtained mixing-length profiles with Nezu and Rodi (1986) formula. It can be seen from Figures 6-6 to 6-9 that in most cases, the mixing-length distribution within and above the roughness layer seems linear but with different slopes below and above z_c. Since Nezu and Rodi (1986) have derived their formula by measurements above flat beds, it is assumed that the upper part of the profiles above z_c could be comparable to that formula. In order to define a general relationship for the present mixing-length distribution to be applied in the present simulations, the following procedure is adopted.

Considering the crest of roughness layer (dashed line in the figures) as the reference level of Nezu and Rodi (1986) formula, Equation (3.8) is rewritten as follows

$$l_m = l_{mc} + \kappa_f \left(z - z_c\right)\sqrt{1 - \frac{\left(z - z_c\right)}{H_c}} \tag{6.5}$$

where l_{mc} is the value of the mixing-length at the roughness crest and H_c is the distance from z_c to z_{ws} as depicted in Figure 6-1. This relationship is applied to fit a profile to the experimental mixing-length profiles (Figures 6-6 to 6-9, right) by fixing l_{mc} to the experimental value at z_c and adjusting κ_f which determines the slope of the profile at z_c. The value of $\kappa_f = 0.22$ is found to provide good agreement between experimental profiles and Equation (6.5) for all the 12 test cases (see Figure 6-10).

Determination of mixing-length distribution within the roughness layer and below the roughness trough z_t is not straightforward since the data is available only to some distance below the roughness crest, but not within the bed. Although the velocity and Reynolds Stress data within the roughness layer have large perturbations in some cases (Figures 6-6 to 6-9), it is fair to assume that mixing-length is linear at the upper part of this layer. The data is not available in the lower part, but it is assumed that l_m has a linear distribution over the whole layer between z_t and z_c. Hence, the following relationship is used to fit profiles to the experimental l_m distributions within the roughness layer for all the 12 cases.

$$l_m = l_{mc} + \kappa_r \left(z - z_c\right) \tag{6.6}$$

where κ_r is the slope of the profile. The values of $\kappa_r =$ 0.27 and 0.15 provide good match between the experimental profiles and Equation (6.6) for beds B1 (Q_{armour} = 180 l/s) and B2 (Q_{armour} = 250 l/s), respectively (see Figure 6-10). Using these values, the linear profiles become zero at some levels about 10 mm above z_t and about 0 to 20 mm below z_t for the test cases associated with the beds B1 and B2, respectively.

It is noted that the mixing-length is not physically zero within the bed, although flow turbulence may be negligible in that region. The fact that Equation (6.6) goes to zero at some level above the bed B1 (for example see Figure 6-11) demonstrates that the distribution of mixing-length cannot be linear in the lower part of the roughness layer. It has probably a nonlinear distribution with a smooth connection to a small value within the bed. However, by applying Equation (6.6), the distribution of the mixing-length is assumed to be linear over the whole roughness layer. In fact, the assumption is that the mixing-length profile is fixed with a small value (l_{mb}) at a certain level close to the roughness trough ($z_t + \Delta z_0$) below which it has a constant distribution with l_{mb}. Hence, the following equation is applied to estimate the mixing-length distribution in the depth-wise direction from z_b to z_{ws} in the present simulations (see Figure 6-11).

$$\begin{aligned} l_m &= l_{mb} && : \quad z \le z_0 \\ l_m &= l_{mb} + \kappa_r \left(z - z_0\right) && : \quad z_0 < z \le z_c \\ l_m &= l_{mb} + \kappa_r \left(z_c - z_0\right) + \kappa_f \left(z - z_c\right)\sqrt{1-\left(z - z_c\right)/H_c} && : \quad z_c < z \end{aligned} \tag{6.7}$$

where $z_0 = z_t + \Delta z_0$. To apply this equation in the numerical model, Δz_0, l_{mb}, κ_r and κ_f need to be determined. Considering a constant value of l_{mb} = 2 mm within the bed, Δz_0 will be about 18 to 23 mm and -10 to 10 mm for beds B1 and B2, respectively. Besides, according to the data, κ_r is taken to be 0.27 and 0.15 for beds B1 and B2, respectively, while κ_f is equal to 0.22 for all cases. Table 6-3 summarises the values applied in the present simulations.

Table 6-3 Mixing-length parameters (Equation 6.7) adopted in the present simulations.

Bed	Test cases	l_{mb}	Δz_0	κ_r	κ_f
B1	B1-Q60, B1-Q90, B1-Q120, B1-Q150, B1-Q180	2 mm	20 mm	0.27	0.22
B2	B2-Q60, B2-Q90, B2-Q120, B2-Q150, B2-Q180, B2-Q220, B2-Q250	2 mm	0.0	0.15	0.22

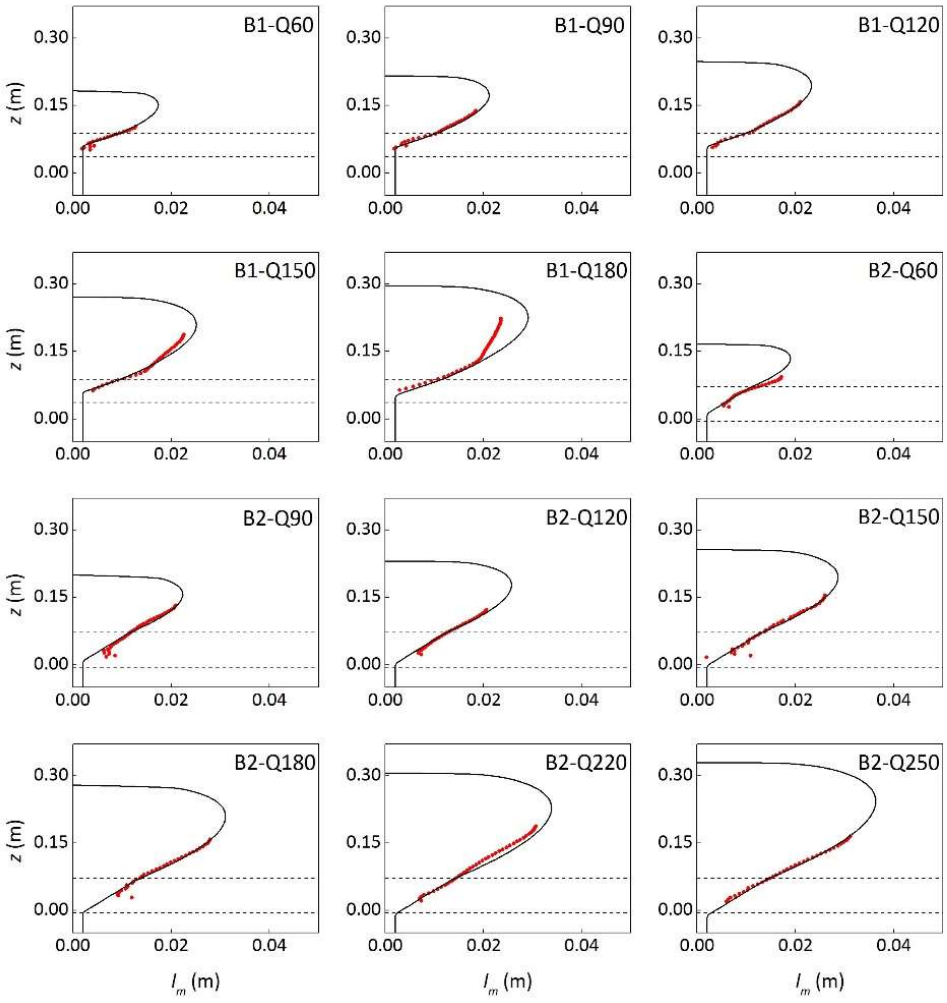

Figure 6-10 Mixing-length profiles for all the 12 test cases. Red circles: experimental profiles; Solid lines: numerical profiles; and dashed lines: bounds of the roughness layer (z_t and z_c).

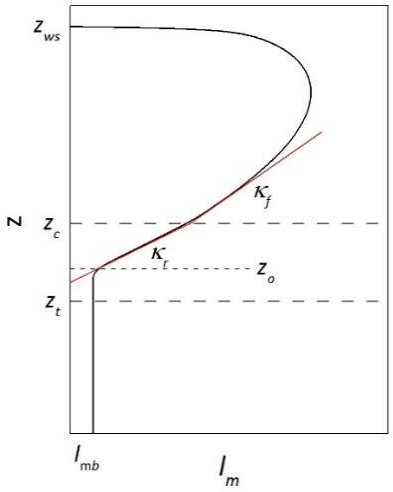

Figure 6-11 Typical mixing-length distribution adopted in the present study.

6.2.4 Computational domain and boundary conditions

The computational domain is set up based on the physical model introduced in Section 6.1. Those flow conditions can be simulated in 2D since the flow change in the lateral direction (normal to the flume sidewalls) is negligible compared to the streamwise and depthwise changes. Although flow near the bed surface is 3D, since the average flow field is studied in a macroscopic framework, the 2D simulation is considered to be reasonable.

The same setup of the physical model with the same flume length (20 m) is not possible to be applied here due to limited computational time and costs, thus a shorter domain is considered, and appropriate boundary conditions are defined. A rectangular is defined as the computational domain including porous armour layer, roughness layer and free flow regions as depicted in Figure 6-1, but macroscopically. The governing equations (4.56) and (4.57) are solved in a unified framework while the difference between the regions is characterised by the change in the porosity as well as the drag coefficients as defined in Equation (6.3). Three boundary conditions for inlet, outlet, and bottom rigid wall need to be defined while the free surface boundary is tracked without any special treatment.

6.2.4.1 Bottom rigid wall boundary

At level z_b (Figure 6-1) a rigid wall is defined by placing several layers of fixed dummy particles as the topmost layer lies at z_b. These particles are used in order to fill the truncated kernel area of the fluid particles located in the vicinity of the boundary. Thus the number of layers depends on the kernel support size. Their velocity is set to zero, while their density and pressure are updated in every time step according to the continuity equation (4.56) and equation of state (3.11), respectively. These dummy particles prevent fluid particles from penetrating into the wall as they contribute in the computation of pressure gradient term (first term on the right-hand side of Equation 4.57) of the fluid particles located in the vicinity of the wall.

6.2.4.2 Inflow boundary

The approach adopted here for modelling inflow boundary is similar to the one introduced in Chapter 3 for flow over impermeable boundaries in terms of that the distribution of velocity is unknown at the inlet. Similar to Section 3.1.4.1, several layers of dummy particles are set in the inflow region (see Figures 3-2 and 3-3 a) in order to address the truncated support area of fluid particles. The governing equations are not solved at these particles but their properties such as pressure and velocity are determined based on desirable hydraulic conditions. The inflow particles move according to their velocity and become fluid particles when passing the inflow boundary line, while a new inflow particle with the same properties is generated at the same elevation but in the beginning of the inflow region, i.e. at the inlet threshold (see Figure 3-3 a).

In the simulation of test cases in Chapter 3, an averaging method was introduced to determine the velocity of inflow particles. According to that method, the velocity of fluid particles was averaged in the vicinity of inflow boundary line using a SPH kernel function and set accordingly as the velocity of inflow particles (see Figure 3-3 b). This method is not applicable for the present simulations due to the existence of

permeable bed. The reason is that the flow condition within the porous layer which has a considerable depth is very different from the high Re Number flow above the bed. Moreover, the averaging process would disturb flow transfer at the bed interface where the change in the velocity is significant. Generally speaking, the application of the inflow averaging technique introduced in Chapter 3 for the present case has shown to produce unstable solutions due the existence of a permeable boundary.

In the present work, instead, an inflow boundary with a constant velocity distribution is defined at the inlet which provides the desirable (experimental) discharge into the computational domain. Since the porosity distribution is not constant over depth (Figure 6-4), it is expected that velocity and particle spacing are also variable. Therefore, a transition zone is required from the inflow boundary to an area with the desirable porosity profile shown in Figure 6-4. In order to shorten the length of the transition zone, a porous inflow region with certain depth (H_t^{in}) and porosity (ϕ_0^{in}) is introduced rather than using a clear water inflow with $\phi = 1.0$. The constant inflow velocity is determined according to the desired flow discharge (measuring discharge for each test case in Table 6-2) by the following equation.

$$U_0^{in} = \frac{q_0^{in}}{\phi_0^{in} H_t^{in}} \tag{6.8}$$

where H_t^{in} is equal to $z_{ws}^{in} - z_b$ as depicted in Figure 6-12 and q_0^{in} is the discharge per unit width which is equal to Q/B_w where Q is the measuring volume discharge presented in Table 6-2 and B_w is the flume width at the measuring section. Besides, the pressure of inflow particles is considered to be hydrostatic. In this way, the inflow region acts as a porous medium where water flows into the domain with a constant rate. It is noted that Equation (6.8) defines U_0^{in} as the inflow intrinsic velocity since the governing equations have been developed in terms of intrinsic quantities.

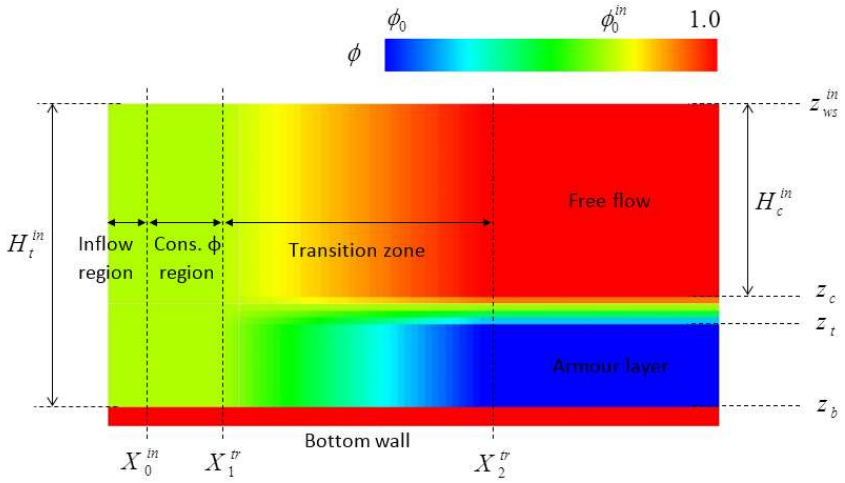

Figure 6-12 Inflow boundary setup.

Figure 6-12 presents inflow setup at the initial time step and the change of porosity from inflow boundary to the specific fluid domain with required porosity profile (Figure 6-4). As can be seen, porosity within the inflow region and to some distance away from the inflow boundary is set to a constant value between ϕ_0 and 1. After that, it starts decreasing gradually (linearly here) from X_1^{tr} to X_2^{tr} and reaches to the required value beyond X_2^{tr} (which is equal to ϕ_0, 1.0, and some value between these two, respectively in the porous bed, free flow region and roughness layer). Usually a porosity between ϕ_0 and 1.0 is chosen for the porous inflow region ϕ_0^{in} and therefore a depth higher than the desirable one (experimental depth) is set at the inlet in order to have a stable solution, i.e. $z_{ws}^{in} > z_{ws}$.

Since the porosity changes in both x and z directions due to the porous inflow boundary, the drag term $\mathbf{A}_a$ is rewritten as the following.

$$\mathbf{A}_a = -C_1 \frac{(1-\phi_a)^2}{\phi_a^2} \frac{\nu}{d_s^2} \mathbf{u}_a - C_2 \frac{(1-\phi_a)}{\phi_a} \frac{1}{d_s} \mathbf{u}_a |\mathbf{u}_a|$$
$$: \begin{cases} C_1 = 0.0,\ C_2 = C_d \phi_a & : \text{ within the roughness layer and } x > X_2^{tr} \\ C_1 = c_1,\ C_2 = c_2 & : \text{ elsewhere} \end{cases} \tag{6.9}$$

It is expected that flow depth decreases gradually over the transition zone to a certain depth beyond X_2^{tr}. The final depth depends on various factors such as bed roughness, bed slope, and turbulence effects. If all these factors are modelled correctly, the flow momentum should be balanced after some distance. However, since the computational length is limited ($8H_t^{in}$ in the present simulations), an open outflow boundary could not satisfy the required uniform flow condition within the domain. Hence, the following section is devoted to defining an appropriate outflow boundary technique for the present application.

6.2.4.3 Outflow boundary

Since the domain is truncated at the outlet boundary, the balance in the momentum equation is disturbed so that the water column collapses (i.e. open boundary) if no special treatment is used. Due to the reason mentioned in the previous section, the outflow boundary technique developed in Chapter 3 for flow over impermeable boundary is not applicable here.

If momentum balance at the outlet is disturbed, uniform flow condition cannot be satisfied within a short distance from the outlet boundary. On the other hand, if one uses several layers of dummy particles beyond the outlet boundary to recover the truncated kernel area, there is still problem in defining flow quantities at those particles due to the lack of knowledge on the distribution of those quantities. Hence, a simple outflow boundary technique is proposed here by introducing a pressure force in the opposite direction of flow thereby reproducing a constant depth which leads to uniform flow condition within the domain. For this purpose, an imaginary wall is placed at the outlet which provides only pressure gradient on fluid particles as described in the following.

Several layers of fixed imaginary particles are set beyond the outlet line (X_o in Figure 6-13 b) in order to create an imaginary wall with a certain height (H_{ow}) and a certain

distribution of pressure. The wall extends from z_b to $z_b + H_{ow}$ and a hydrostatic pressure distribution is considered at the imaginary particles in the present simulations. These particles contribute only in the calculation of pressure gradient at fluid particles. Therefore, the following term is added to the momentum equation (4.57) of a certain fluid particle a when it is located within a distance shorter than $2h_{\Upsilon}$ ($h_{\Upsilon} =$ smoothing length) from the outlet boundary line (see Figure 6-13 b).

$$\mathbf{O}_a = -\sum_o \left\{ \frac{1}{\rho_a} \Delta V_o \nabla_a W_{ao} \left(P_a + P_o \right) \right\} \tag{6.10}$$

where a and o denote fluid and neighbouring imaginary particles, respectively; and ΔV_o is the volume of imaginary particle. In this way, the imaginary wall reproduces a pressure force on the fluid particles located in the vicinity of the outlet boundary. However, since the imaginary particles are fixed while fluid particles are moving, they will not allow fluid particles to move through the outlet boundary so that continuity is not preserved. To resolve this, in the calculation of extra pressure gradient term $\mathbf{O}_a$ of a certain fluid particle, the volume of its neighbouring imaginary particles ΔV_o starts to decrease from when the fluid particle locates at $X_o - 2h_{\Upsilon}$ until it reaches the outlet boundary line X_o where ΔV_o becomes zero. Then, fluid particle is removed at the same time, i.e. when it arrives at X_0. Decrease in ΔV_o is performed using a relaxing factor which is considered to be linear in the present simulations, so that Equation (6.10) is rewritten in the following form. This process allows fluid particles to move smoothly through the imaginary wall so that mass conservation is preserved.

$$\mathbf{O}_a = -\sum_o \left\{ \frac{1}{\rho_a} F_o \Delta V_o \nabla_a W_{ao} \left(P_a + P_o \right) \right\} \tag{6.11}$$

F_o is the relaxing factor defined as the following linear form in the present study.

$$F_o = \frac{X_o - x_a}{2h_{\Upsilon}} \tag{6.12}$$

in which x_a is the horizontal position of the approaching fluid particle.

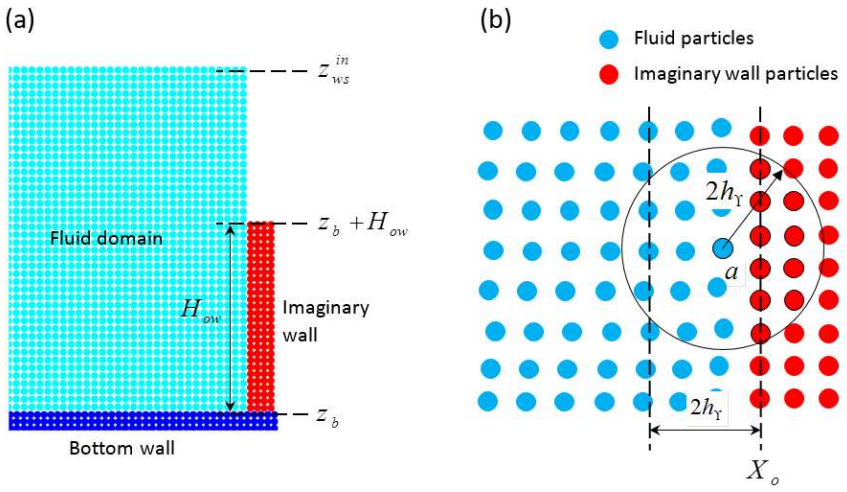

Figure 6-13 Outflow boundary treatment. (a) Initial set-up of the outflow boundary with an imaginary wall; (b) interaction between fluid and imaginary particles.

By using the proposed imaginary wall technique, only the pressure gradient force is applied on the fluid particles near the outlet boundary, while the effects of other terms such as viscosity and turbulent terms are disregarded. The reason for using only the pressure effect is that its distribution in a uniform flow condition is known if one assumes that it is nearly hydrostatic, while the distribution of velocity is unknown particularly in the case of existence of a permeable boundary with a rough surface.

Considering a hydrostatic pressure distribution, neglecting the effect of other terms such as viscosity, and using a linear relaxing factor for mass elimination at the outlet boundary, means the outflow boundary treatment is unable to guarantee an adequate balance in the flow momentum at the outlet. Therefore, the height of imaginary wall H_{ow} is considered to be adjustable in order to be able to get the depth constant within the domain thereby providing the required balance in the momentum. In other words, for each test case, different values of H_{ow} are applied until the water surface (computed by the procedure introduced in Section 5.3 and Equation 5.11) becomes parallel to the bed line. In addition, the depth-averaged streamwise velocity is compared at several sections with certain distances from the outlet boundary; and if the difference is less than a threshold, flow is considered as

uniform. Otherwise, H_{ow} is increased/decreased and simulation is repeated until achieving the constant depth and depth-averaged velocity.

6.3 Results and discussion

The 12 test cases introduced in Table 6-2 are simulated following the numerical treatments introduced in Sections 6.2.1 to 6.2.4. Firstly, some computational specifications applied in the present simulations are mentioned briefly and then the results are presented and compared to the experimental data.

A rectangular computational domain is adopted with initial height and length of H_t^{in} and $8H_t^{in}$. The domain is discretised using particles with clear water particle spacing l_0 of 5 mm, i.e. the particle spacing associated with porosity of 1.0 is set to 5 mm. Besides, some simulations will be repeated with different particle sizes to check the effect of resolution on the results. Initial particle spacing is set using Equation (5.1) based on ϕ_0 = 0.22 within the armour and roughness layers ($z < z_c$ and $x > X_2^{tr}$) and $\phi_0 = \phi_0^{in}$ elsewhere. It is expected that spacing between particles will be corrected based on porosity defined in Figure 6-12 after few time steps. The vertical levels z_t, z_m, z_c and z_{ws} are set from Table 6-2 for each test case. The cubic Spline function presented in Equation (5.4) is employed and the smoothing length is chosen to be 1.2 l_0. The speed of sound c_0 is set to 10 times the maximum velocity in each simulation according to the discussion presented in Section 3.2.1 on the choice of c_0. To determine the time step size, the CFL condition (3.15) is adopted with the coefficient of 0.125. Furthermore, the Shepherd density filter is applied at every 30 time steps.

At the inflow boundary, ϕ_{in} is set to 0.75 and H_t^{in} is set to $H_p + 1.5\left(z_{ws} - z_t\right)$ (see Figure 6-1 for H_p, z_{ws} and z_t). Accordingly, the inflow velocity is set to the value estimated by Equation (6.8) and the inflow pressure distribution is assumed to be hydrostatic. The number of layers of the inflow dummy particles is set to 3. X_1^{tr} and

X_2^{tr} are set to $X_{in}+H_c$ and $X_{in}+4H_c$, respectively. At the outflow boundary, 3 layers of imaginary particles are placed beyond the outlet boundary line ($x=X_o$) to construct the imaginary wall. The spacing between those particles is set to the clear water particle spacing l_0 so that ΔV_o is equal to l_0^2 and their porosity is 1.0. As discussed in Section 6.2.4.3, the simulation of each test case is repeated with different values of H_{ow}, until achieving constant flow depth. Besides, the porosity of bottom wall dummy particles is set to 1.0 so that their spacing is set to l_0.

6.3.1 Flow steadiness and uniformity

Figures 6-14 and 6-16 show snapshots of instantaneous particle position and streamwise velocity at different times from initial time step to *t* = 30 s for the test cases B1-Q60 and B1-Q90, respectively, and Figures 6-15 and 6-17 present the distribution of porosity for these two test cases. As expected, during first 8.0 seconds, flow depth decreases gradually from the inflow boundary (X_0^{in}) to the end of the transition zone (X_2^{tr}) after which the porosity becomes constant in the bed and clear water regions. Then flow develops in the constant depth region until about *t* = 20 s when flow becomes steady. For each case, to achieve constant depth from X_2^{tr} to X_o, different values of the outlet imaginary wall height H_{ow} are applied and the uniformity of the flow is checked. The optimum H_{ow} for all test cases were found to be in the range of 90 to 100 % of the experimental total depth ($z_{ws}-z_b$).

A measuring zone is chosen from $X_1^s=X_0^{in}+4.5H_t^{in}$ to $X_3^s=X_0^{in}+6.5H_t^{in}$ with a mid-section of $X_2^s=X_0^{in}+5.5H_t^{in}$ (Figure 6-18). As the length of the domain L is $8H_t^{in}$, the distance between the end of the measuring section X_3^s to the outlet boundary line X_o is about $1.5H_t^{in}$. To post-process the simulation results, a fixed grid

is defined over the measuring zone with grid spacing equal to 5 mm where particle quantities are averaged at grid points using the cubic Spline kernel function (5.4).

To check steadiness of flow, water surface elevation and streamwise velocity profile at $x = X_2^s$ are compared at different time steps. When the changes in the water depth and depth-averaged streamwise velocity become less than 1%, flow is considered to be steady. To calculate water surface elevation, the divergence of particle position is calculated at grid points using Equation (5.11) and the level at which the divergence value is about 1.0 is considered to be the numerical water surface level. Figure 6-19 presents the velocity profiles of two test cases B1-Q60 and B1-Q90 at section $x = X_2^s$ at different times. As can be seen, the differences between the velocity profiles are small. After about *t* = 20 s, the difference falls below 1% for all the test cases.

In order to check uniformity of the flow, streamwise velocity profiles at sections X_1^s, X_2^s and X_3^s are averaged over time and the time-averaged profiles are compared as when the difference between the depth-averaged value is less than 2%, flow is considered to be uniform over the measuring zone. The time averaging is performed over a period of 10 s during the steady state, i.e. from *t* = 35 s to 45 s. Figure 6-20 shows the time-averaged streamwise velocity contours for test cases B1-Q60 and B1-Q90 and Figure 6-21 presents the time-averaged velocity profiles at sections X_1^s, X_2^s and X_3^s for those test cases. The difference between these profiles is less than 1% for case B1-Q60 and about 1.5% for case B1-Q90. For most the test cases, the difference is below 2%, while in few of them it exceeds 2% slightly. The main part of the difference attributes to the top of velocity profiles (near the water surface) where velocity seems not fully uniform in some cases. The reason is probably related to the outflow boundary where the balance in the momentum is disrupted and only pressure gradient force is used to get a constant flow depth.

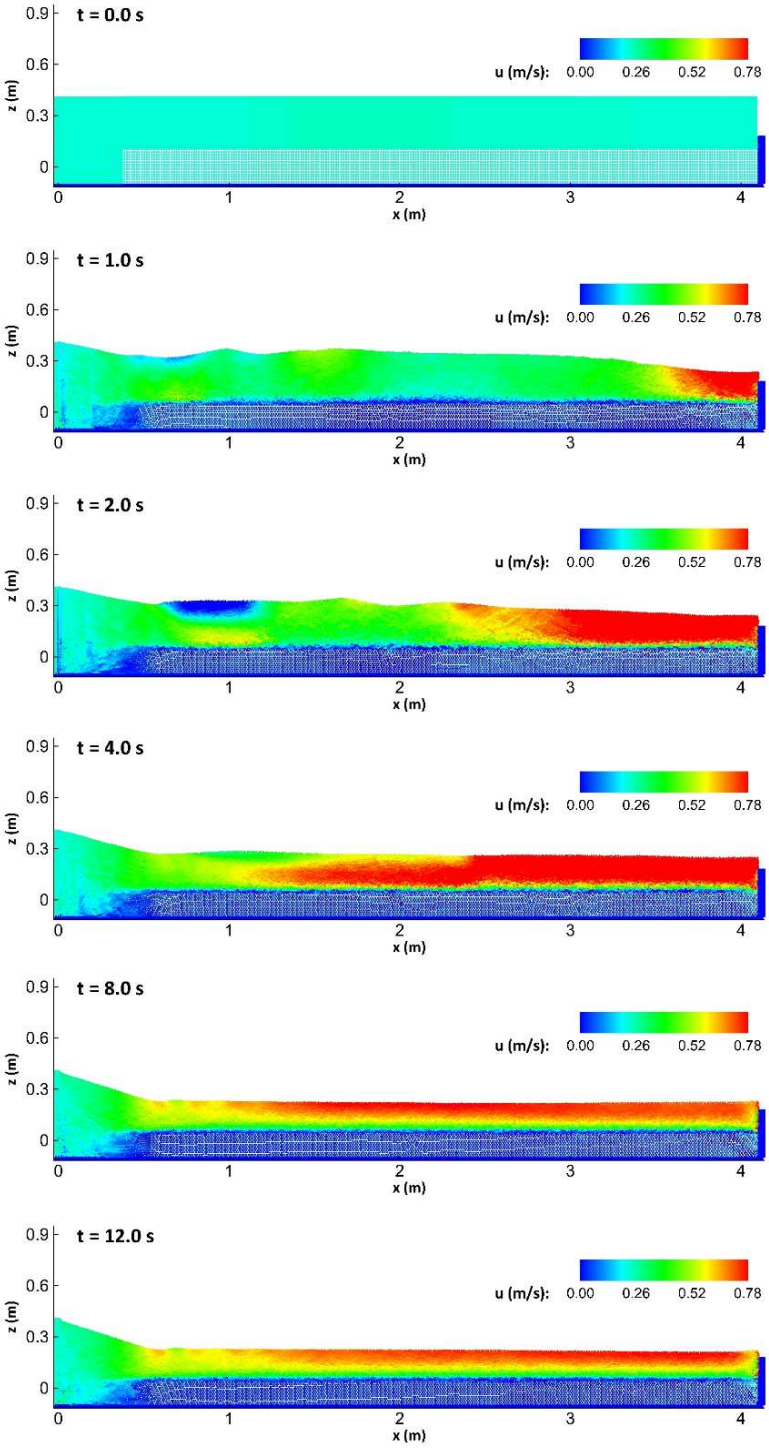

Figure 6-14 Development of flow in test case B1-Q60. Snapshots of particle position and velocity at different times from *t* = 0 to 30 s (continued on the following page).

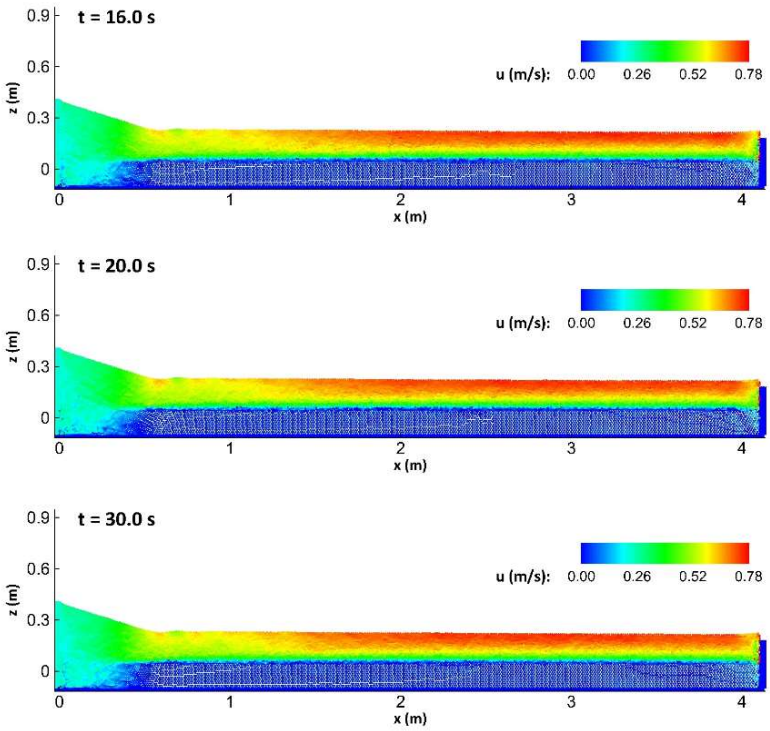

Figure 6-14 (continued from the previous page) Development of flow in test case B1-Q60. Snapshots of particle position and velocity at different times from *t* = 0 to 30 s.

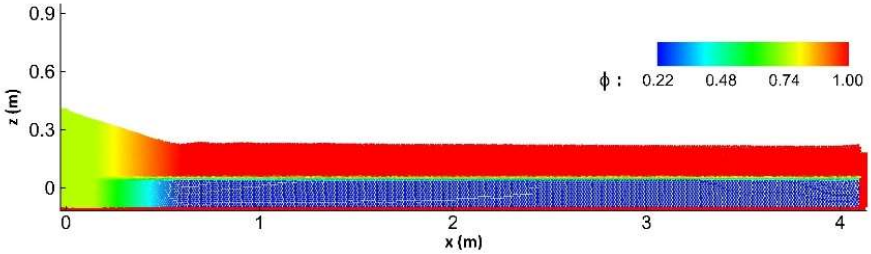

Figure 6-15 Porosity distribution in test case B1-Q60 (*t* = 30 s).

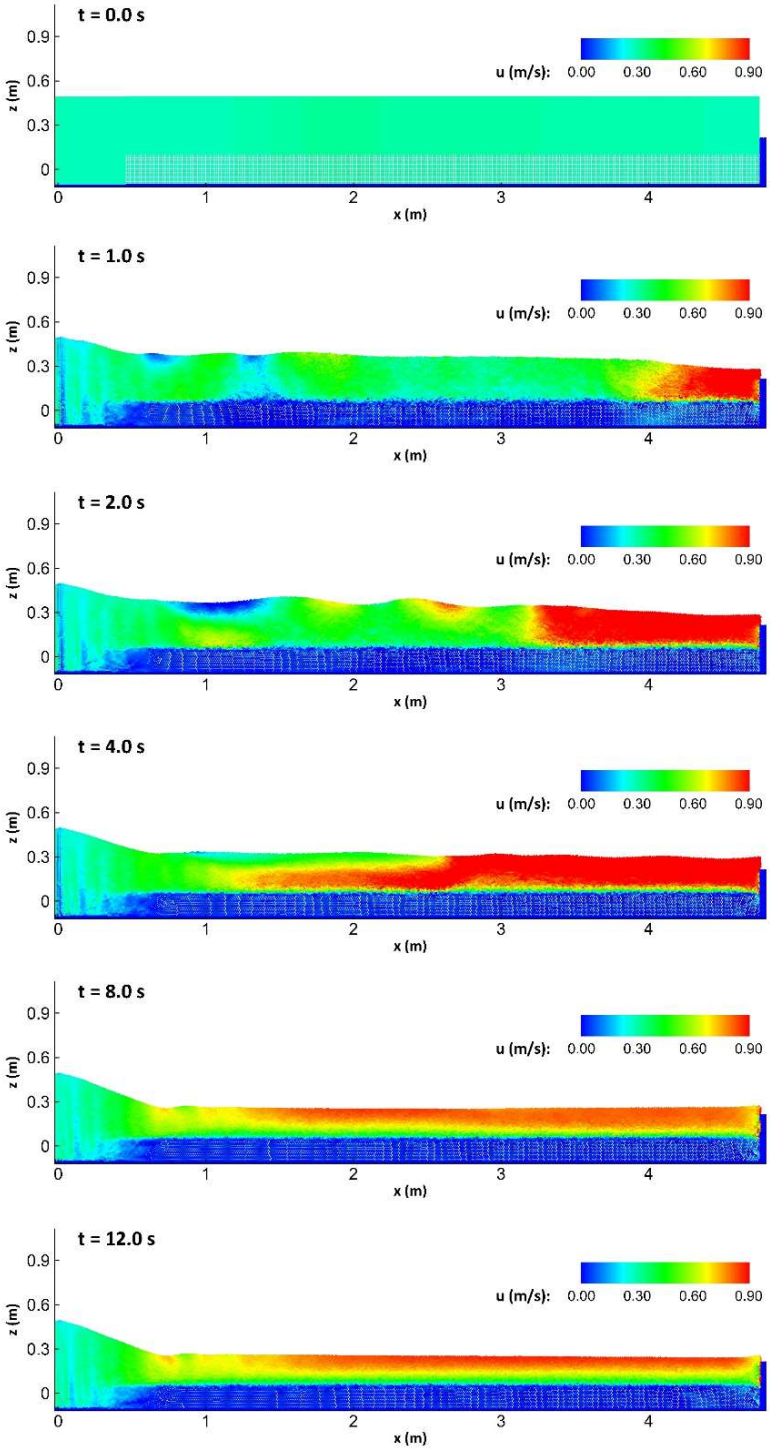

Figure 6-16 Development of flow in test case B1-Q90. Snapshots of particle position and velocity at different times from *t* = 0 to 30 s (continued on the following page).

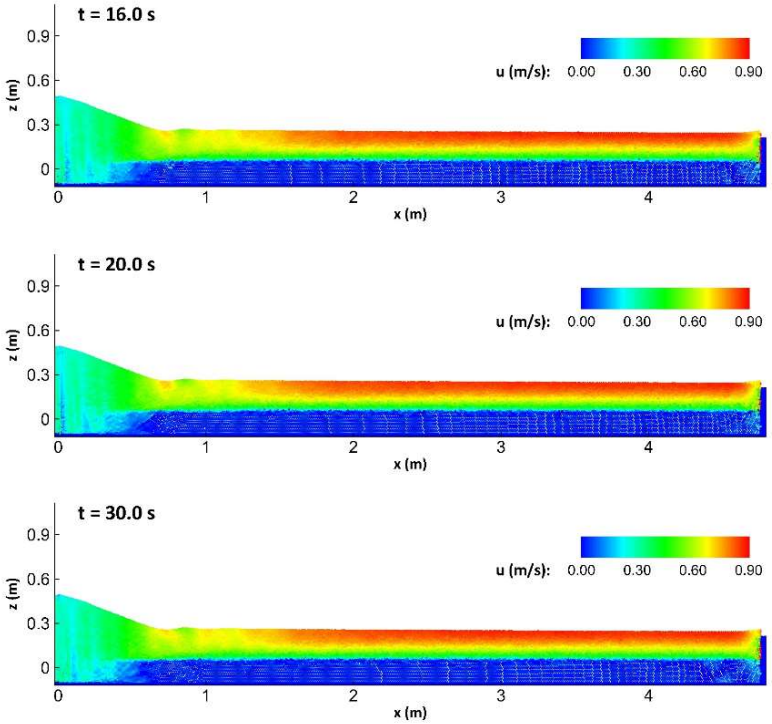

Figure 6-16 (continued from the previous page) Development of flow in test case B1-Q90. Snapshots of particle position and velocity at different times from *t* = 0 to 30 s.

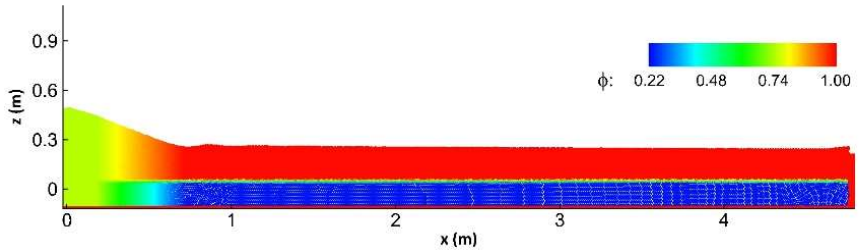

Figure 6-17 Porosity distribution in test case B1-Q90 (*t* = 30 s).

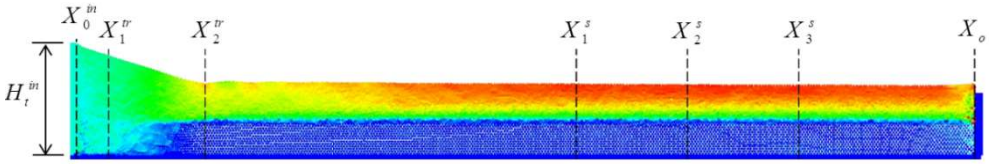

Figure 6-18 Inflow, outflow and measuring zones. X_0^{in} is the inflow boundary line; X_1^{tr} and X_2^{tr} are the bounds of the transition zone; X_1^s to X_3^s represents the measuring zone while X_2^s is the mid-section of this zone; and X_o is the outlet boundary line.

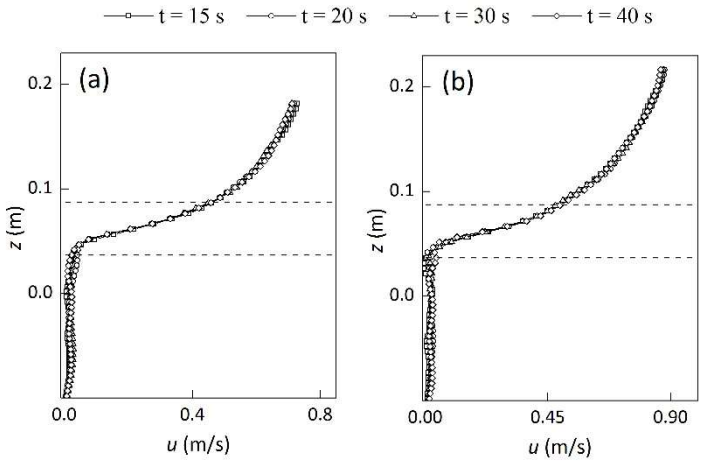

Figure 6-19 Flow steadiness for test cases (a) B1-Q60 and (b) B1-Q90. Profiles present streamwise velocity distribution at section X_2^s at different times. Dashed lines represent the bounds of the roughness layer (i.e. z_t and z_c).

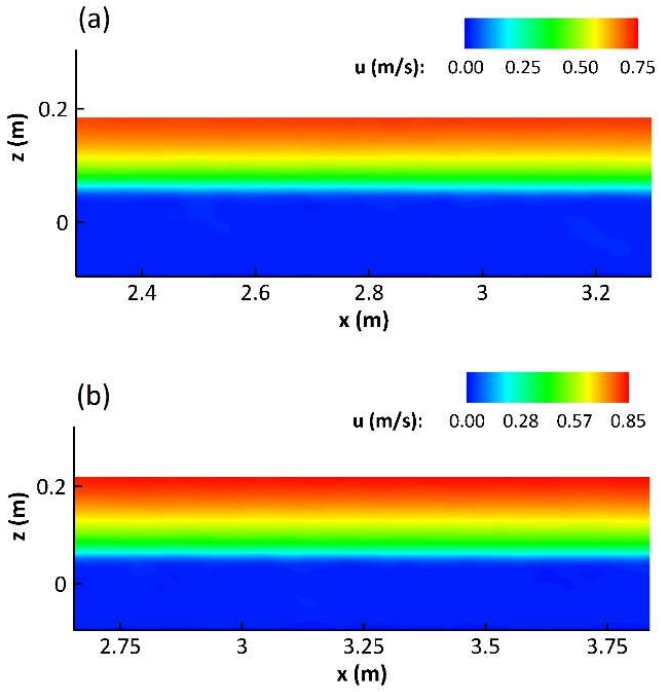

Figure 6-20 Streamwise velocity contours for test cases (a) B1-Q60 and (b) B1-Q90 over the measuring zone (X_1^s to X_3^s) averaged over a time period of 10 s (*t* = 35 s to 45 s).

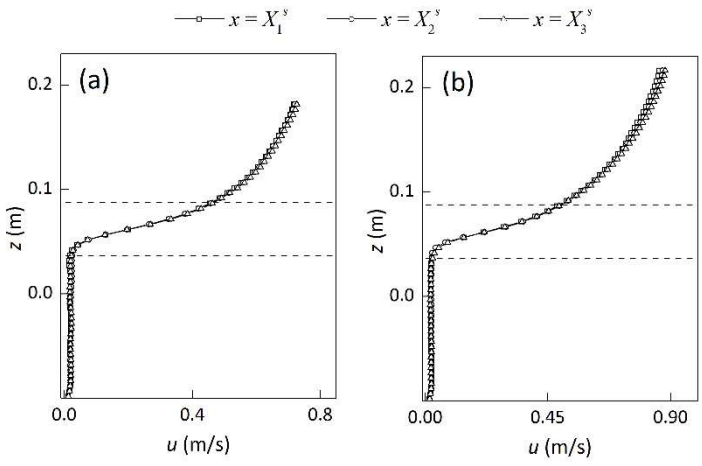

Figure 6-21 Flow uniformity for test cases (a) B1-Q60 and (b) B1-Q90. Profiles present streamwise velocity distribution at sections X_1^s, X_2^s and X_3^s averaged over a time period of 10 s. Dashed lines represent the bounds of the roughness layer (i.e. z_t and z_c).

6.3.2 Velocity and shear stress results

In this section, the results of streamwise velocity and turbulent shear stress are presented for all the 12 test cases. SPH-estimated velocity, its gradient, and shear stress are averaged over a time period of 10 s from *t* = 35 s to 45 s at the mid-section X_2^s of the measuring zone and compared to the experimental profiles in Figures 6-20 to 6-33. The presented results are from simulations with l_0 = 5 mm.

In all cases, streamwise velocity is underestimated by the model. In the test cases of bed B1 (Q_{armour} = 180 l/s), the underestimation appears as a vertical shift in the average velocity profiles compared to the experimental ones. This could be because the roughness effect at the bed is overestimated by the model due to the use of relatively large particle spacing l_0 (low computational resolution). In other words, the length constraint (4.61) (a), i.e. $r_\Upsilon << L_{\langle \mathbf{u} \rangle^\alpha}$, is probably not satisfied near the interface layer using l_0 = 5 mm.

Due to the shift in the velocity profile, its gradient $\partial u/\partial z$ is overestimated over the depth. As a result, the MSPH-ML shear stress profiles are also overestimated, especially above the roughness layer in the test cases of bed B1. According to Equation (6.4), shear stress is related to the squares of velocity gradient and mixing-length. Therefore, a small overestimation in the velocity gradient may cause significant overestimation in the turbulent shear stress particularly above the roughness crest where the mixing-length has a larger magnitude according to Nezu and Rodi (1986) formula (Figure 6-11). Furthermore, for each bed condition (B1 and B2), the reference level z_0 of the mixing-length formula (Equation 6.7) is assumed to be fixed under various flow conditions, while it has a small range for different test cases. Generally speaking, the mixing-length distribution estimated by Equation (6.7) does not match perfectly with the experimental mixing-length profiles. As a result, some errors might be produced in the estimation of turbulent shear stress.

In the test cases of bed B2 (Q_{armour} = 250 l/s), the underestimation of velocity is not constant through the depth, but it is higher around the roughness layer and lower near the water surface. Velocity underestimation in these cases also may be related to the fact that constraint (4.61) (a) is not fully satisfied due to the use insufficient computational resolution near the bed.

In order to check the effect of computational resolution, simulation of test cases B1-Q60, B1-Q90, B2-Q60 and B2-Q90 is repeated using different values of initial particle spacing l_0. The result is presented in Figure 6-34 where velocity, its gradient and shear stress profiles are plotted with using l_0 = 3, 5 and 7 mm in comparison with the experimental data. According to the figure, as smaller particle spacing (higher resolution) is applied, the numerical profiles get closer to the experimental data. In other words, using higher resolution in the numerical model leads to a more accurate estimation of velocity gradient since constraint (4.61) (a) is closer to satisfaction particularly near the interfacial boundary. Although using l_0 = 3 mm provides significant improvement in the result of the test cases associated with bed B1, the result of the test cases of bed B2 do not show such an improvement with l_0 = 3 mm (Figure 6-34). According to Figures 6-27 to 6-33, within the roughness layer, velocity and its gradient profiles of the test cases of bed B2 are a poorer match with the experimental data compared to the test cases of bed B1 (Figures 6-22 to 6-26). It could be due to the fact that the solid skeleton below the roughness layer of bed B2 might be different from that in bed B1, while in the present simulations it was assumed that both beds have similar condition below z_t with a constant porosity of 0.22. As the armouring discharge for bed B2 (Q_{armour} = 250 l/s) was considerably higher than that for bed B1 (Q_{armour} = 180 l/s) in the experiments, it is expected that flow affects a deeper area below z_t under Q_{armour} = 250 l/s so that the porosity below z_t of bed B2 could be slightly higher. It is evidenced by higher d_{50} of bed B2 (Table 6-1) which means smaller grains were probably washed out under Q_{armour} = 250 l/s so that

porosity might have increased below z_t. If this assumption is true, applying a higher porosity below z_t in the model will decrease the amount of drag shear stress terms in the momentum equation so that a more appropriate velocity distribution would be achieved near the bed. However, since the knowledge about the solid skeleton is poor, no further investigation is performed on this issue in the present study.

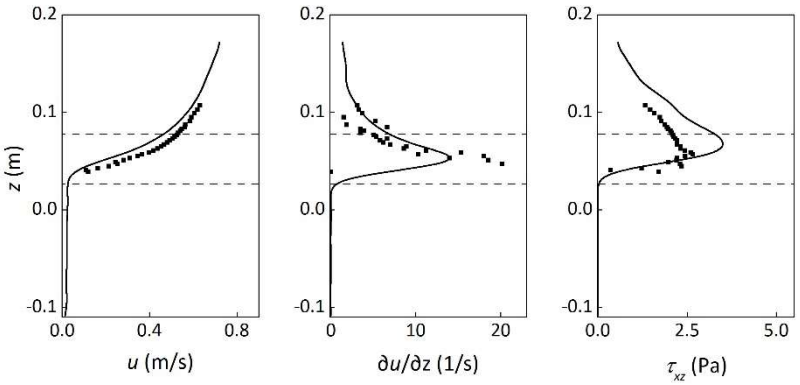

Figure 6-22 Numerical results (solid lines) of streamwise velocity (left), its gradient (middle), and turbulent shear stress (right) in comparison with the experimental data (dark symbols) for test case B1-Q60. Dashed lines show the bounds of the roughness layer (z_t and z_c).

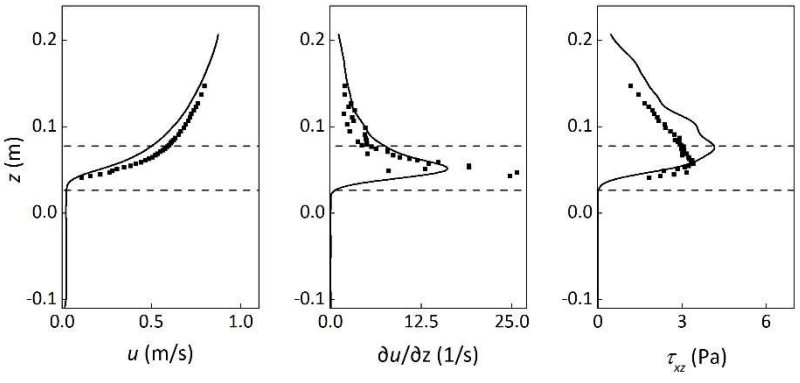

Figure 6-23 Numerical results (solid lines) of streamwise velocity (left), its gradient (middle), and turbulent shear stress (right) in comparison with the experimental data (dark symbols) for test case B1-Q90. Dashed lines show the bounds of the roughness layer (z_t and z_c).

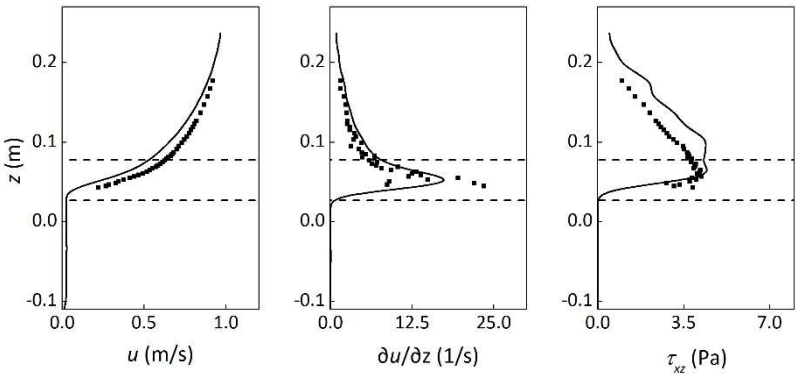

Figure 6-24 Numerical results (solid lines) of streamwise velocity (left), its gradient (middle), and turbulent shear stress (right) in comparison with the experimental data (dark symbols) for test case B1-Q120. Dashed lines show the bounds of the roughness layer (z_t and z_c).

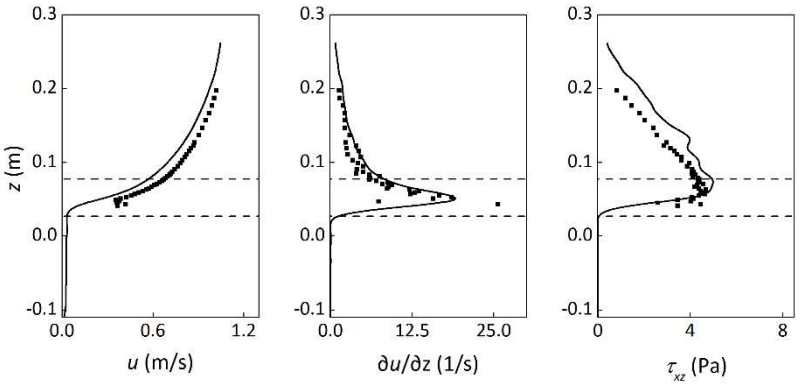

Figure 6-25 Numerical results (solid lines) of streamwise velocity (left), its gradient (middle), and turbulent shear stress (right) in comparison with the experimental data (dark symbols) for test case B1-Q150. Dashed lines show the bounds of the roughness layer (z_t and z_c).

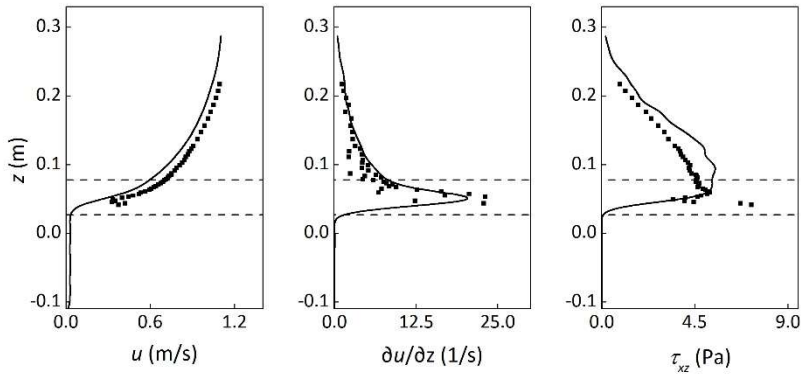

Figure 6-26 Numerical results (solid lines) of streamwise velocity (left), its gradient (middle), and turbulent shear stress (right) in comparison with the experimental data (dark symbols) for test case B1-Q180. Dashed lines show the bounds of the roughness layer (z_t and z_c).

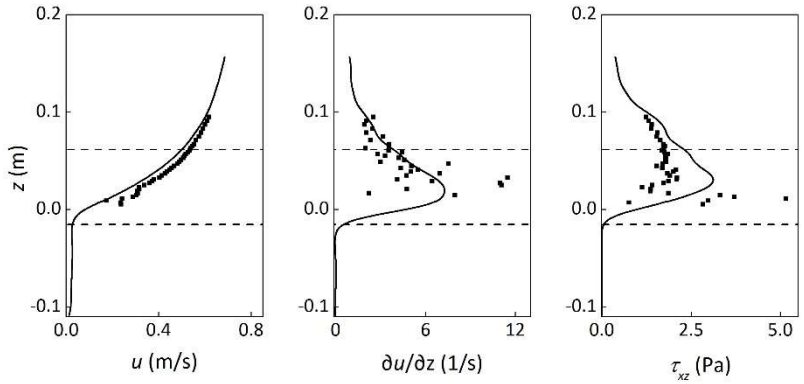

Figure 6-27 Numerical results (solid lines) of streamwise velocity (left), its gradient (middle), and turbulent shear stress (right) in comparison with the experimental data (dark symbols) for test case B2-Q60. Dashed lines show the bounds of the roughness layer (z_t and z_c).

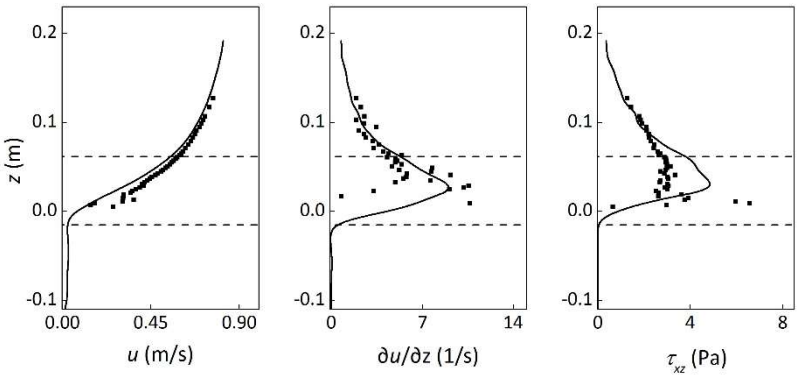

Figure 6-28 Numerical results (solid lines) of streamwise velocity (left), its gradient (middle), and turbulent shear stress (right) in comparison with the experimental data (dark symbols) for test case B2-Q90. Dashed lines show the bounds of the roughness layer (z_t and z_c).

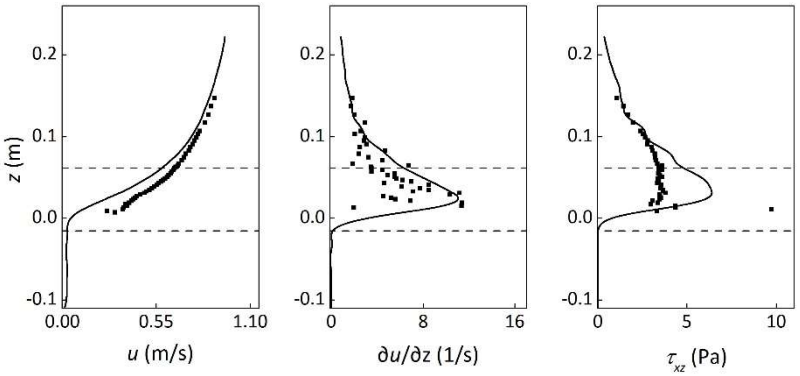

Figure 6-29 Numerical results (solid lines) of streamwise velocity (left), its gradient (middle), and turbulent shear stress (right) in comparison with the experimental data (dark symbols) for test case B2-Q120. Dashed lines show the bounds of the roughness layer (z_t and z_c).

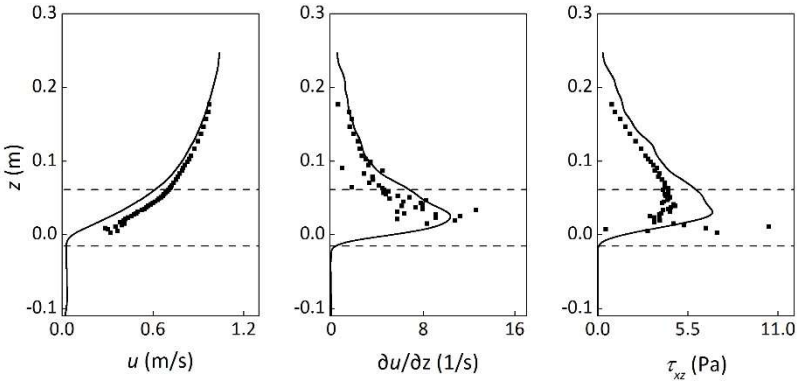

Figure 6-30 Numerical results (solid lines) of streamwise velocity (left), its gradient (middle), and turbulent shear stress (right) in comparison with the experimental data (dark symbols) for test case B2-Q150. Dashed lines show the bounds of the roughness layer (z_t and z_c).

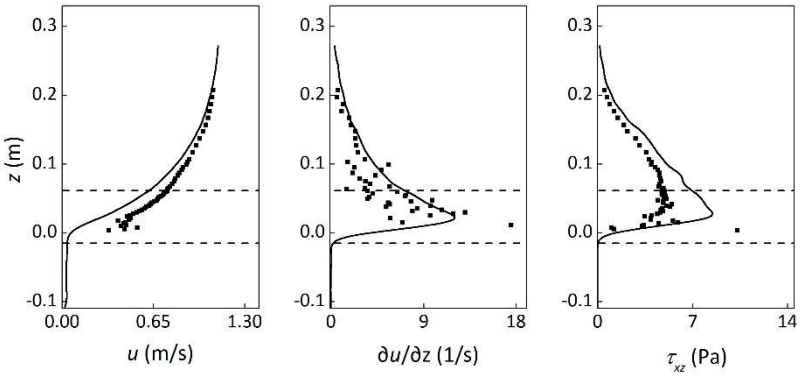

Figure 6-31 Numerical results (solid lines) of streamwise velocity (left), its gradient (middle), and turbulent shear stress (right) in comparison with the experimental data (dark symbols) for test case B2-Q180. Dashed lines show the bounds of the roughness layer (z_t and z_c).

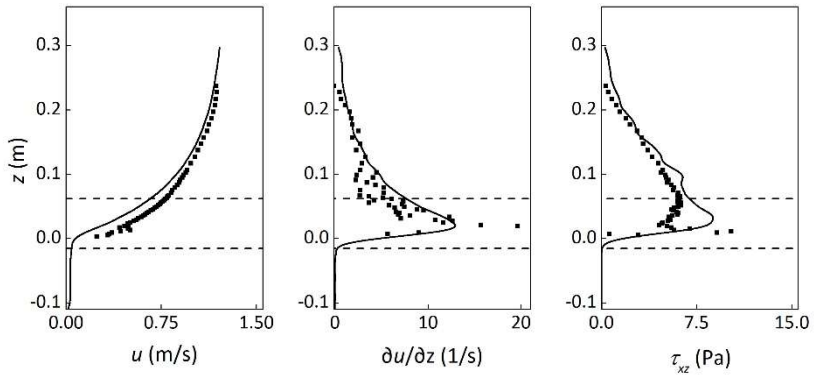

Figure 6-32 Numerical results (solid lines) of streamwise velocity (left), its gradient (middle), and turbulent shear stress (right) in comparison with the experimental data (dark symbols) for test case B2-Q220. Dashed lines show the bounds of the roughness layer (z_t and z_c).

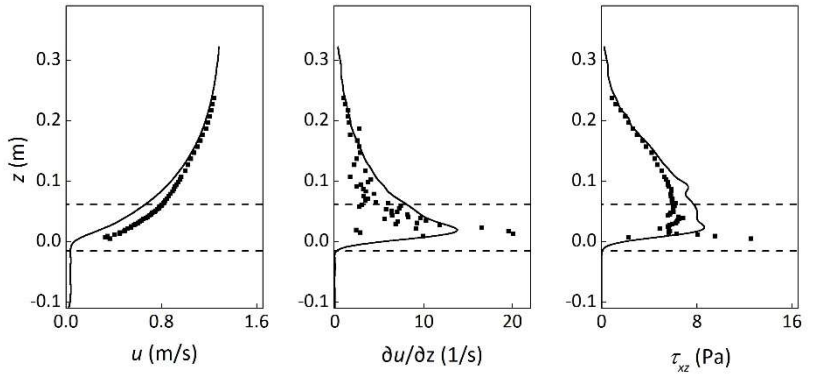

Figure 6-33 Numerical results (solid lines) of streamwise velocity (left), its gradient (middle), and turbulent shear stress (right) in comparison with the experimental data (dark symbols) for test case B2-Q250. Dashed lines show the bounds of the roughness layer (z_t and z_c).

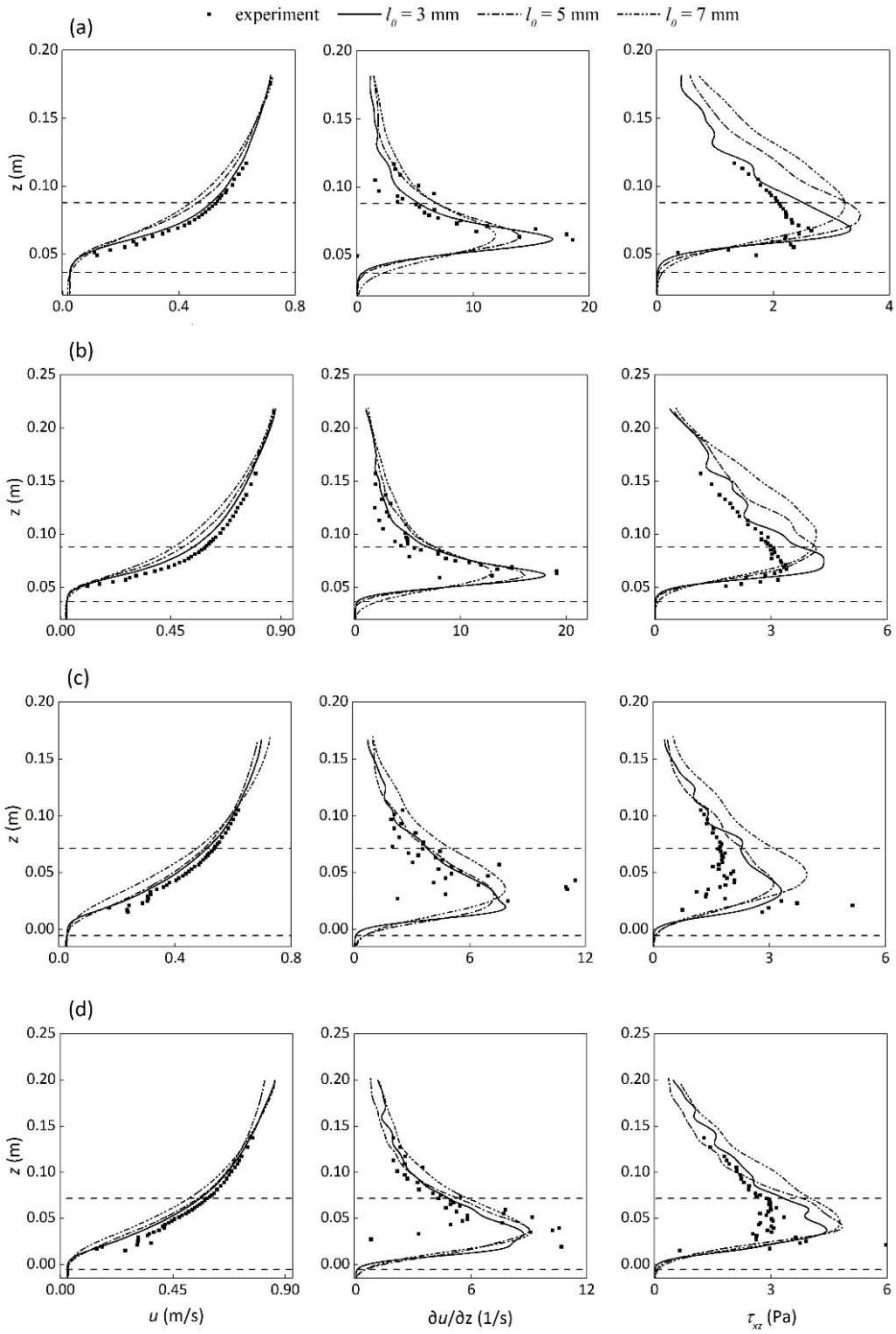

Figure 6-34 Using different particle spacing for test cases (a) B1-Q60, (b) B1-Q90, (c) B2-Q60, and (d) B2-Q90. Dashed lines show the bounds of the roughness layer (z_t and z_c).

6.3.3 Validity of the turbulence model

The turbulent shear stress profiles presented in Section 6.3.2 were in fact the modelled shear stress ($\boldsymbol{\tau}_t$) estimated by the proposed MSPH-ML model. As discussed in Section 6.2.3, the effect of flow disturbance near the bed (which is a result of dispersion due to the existence of solid boundaries) on the average flow field is disregarded because of macroscopic modelling of the bed. Therefore, the turbulent stresses resolved by particle motion (computational discretisation) as well as the part modelled by the SPS-Smagorinsky model were expected to be small. Hence, the MSPH-ML model proposed in Chapter 3 was applied for the present simulations.

In this section, the simulations of test cases B1-Q60 and B1-Q90 are repeated by using the SPS-Smagorinsky model with C_s = 0.15 in order to be compared with the results of the present MSPH-ML model. The part of turbulent stress resolved by particle motion ($\boldsymbol{\tau}_r$) is also presented for comparison. Figures 6-35 and 6-37 present resolved and modelled shear stress, together with the estimated velocity, by using the SPS-Smagorinsky model for test cases B1-Q60 and B1-Q90, respectively. Besides, Figures 6-36 and 6-38 present those quantities for these two test cases respectively, when the MSPH-ML model is employed. For both cases of using MSPH-ML and SPS-Smagorinsky models, $\boldsymbol{\tau}_r$ which is resolved by the computational discretisation is quite small compared to the experimental data. In the case of using SPS-Smagorinsky model (Figures 6-35 and 6-37), the modelled part ($\boldsymbol{\tau}_{SPS}$) is also significantly lower than the experimental value, so that the total shear stress ($\boldsymbol{\tau}_t$) which is the summation of $\boldsymbol{\tau}_r$ and $\boldsymbol{\tau}_{SPS}$ (red solid lines) is highly underestimated. As a result, the estimated velocity profile does not match with the experimental profile since the exchange of momentum over the depth has not been adequately reproduced. In contrast, the application of the MSPH-ML model provides a much better match between numerical and experimental profiles (Figures 6-36 and 6-38). The figures show that the resolved part of turbulent stress ($\boldsymbol{\tau}_r$) is too small so that the total shear stress ($\boldsymbol{\tau}_t$) is almost

equal to the modelled part ($\boldsymbol{\tau}_l$). It confirms the approximation made in the present study (Equation 3.6) that the total turbulent stress should be modelled in the case of macroscopic modelling of the bed.

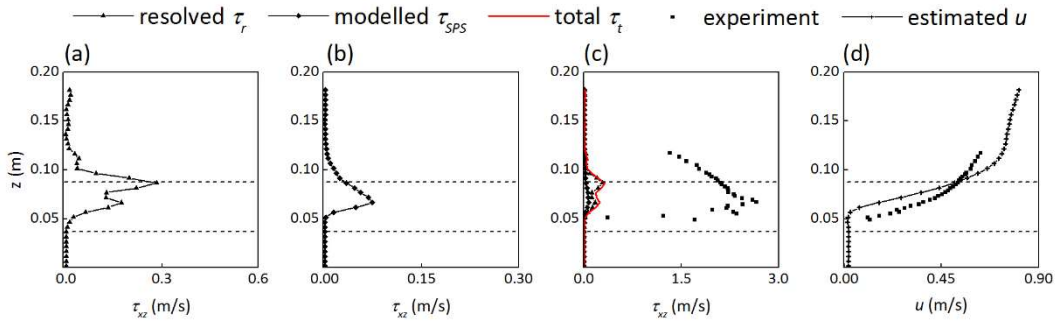

Figure 6-35 Results of the SPS-Smagorinsky model with C_s = 0.15 in estimating shear stress and velocity for test case B1-Q60. (a) Resolved shear stress; (b) modelled shear stress; (c) resolved, modelled and total shear stress; and (d) predicted velocity profile. Dashed lines show the bounds of the roughness layer (z_t and z_c).

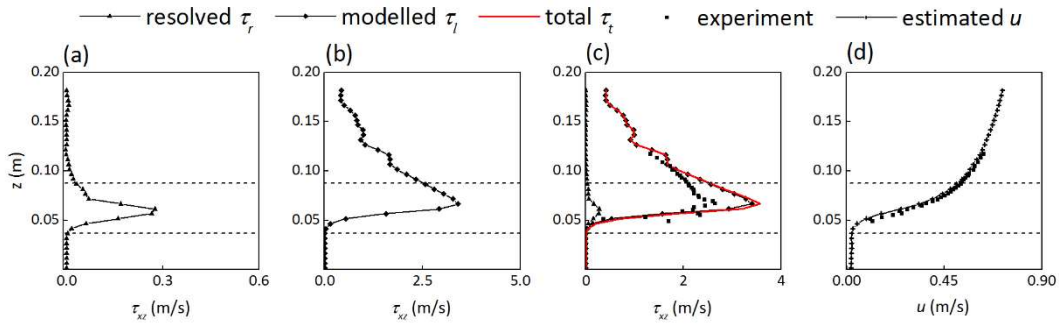

Figure 6-36 Results of the MSPH-ML model in estimating shear stress and velocity for test case B1-Q60. (a) Resolved shear stress; (b) modelled shear stress; (c) resolved, modelled and total shear stress; and (d) predicted velocity profile. Dashed lines show the bounds of the roughness layer (z_t and z_c).

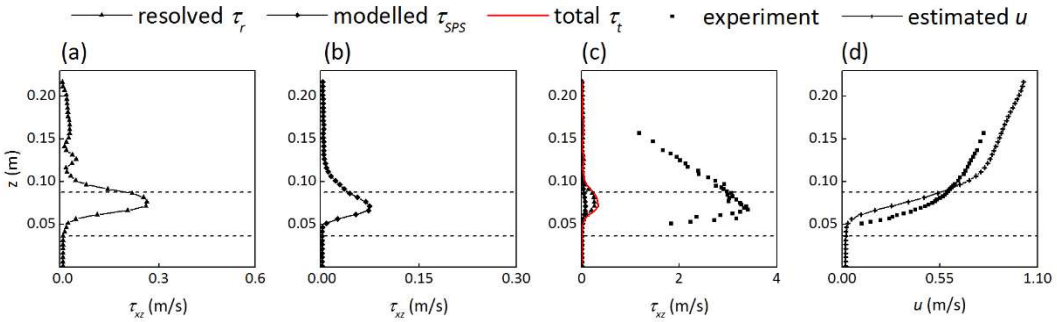

Figure 6-37 Results of the SPS-Smagorinsky model with C_s = 0.15 in estimating shear stress and velocity for test case B1-Q90. (a) Resolved shear stress; (b) modelled shear stress; (c) resolved, modelled and total shear stress; and (d) predicted velocity profile. Dashed lines show the bounds of the roughness layer (z_t and z_c).

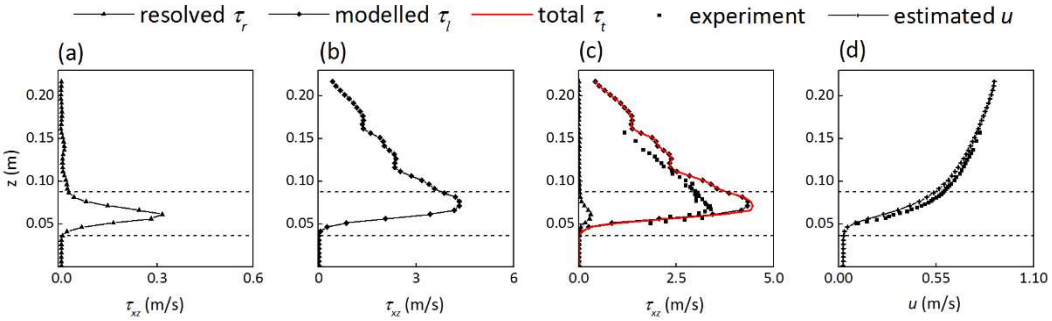

Figure 6-38 Results of the MSPH-ML model in estimating shear stress and velocity for test case B1-Q90. (a) Resolved shear stress; (b) modelled shear stress; (c) resolved, modelled and total shear stress; and (d) predicted velocity profile. Dashed lines show the bounds of the roughness layer (z_t and z_c).

This issue was also investigated in Chapter 3, Section 3.2.6, where turbulent flows over rough impermeable boundaries were studied. The result presented in that section as well as the current result show that the present MSPH-ML model is capable of recovering the effect of missing part of turbulent stress which comes from neglecting flow dispersion and/or the deficiency of the SPH method in estimating velocity-pressure interactions (as addressed by Mayrhofer et al., 2015). In other words, the effect of turbulence on the average macroscopic flow field is addressed adequately by the present MSPH-ML model.

Although the proposed MSPH-ML model is effective in reproducing the required balance in the flow momentum, it has some limitations such as that the distribution of mixing-length should be known. For some cases, such as steady uniform open channel flows, there are established formulas or at least some useful knowledge about the behaviour of flow velocity gradients so that defining the mixing-length should not be too difficult. However, in some more complex cases such as unsteady and/or non-uniform flows, determination of eddy-viscosity based on the mixing-length model is not easy, so that this limits the applicability of the model for such cases.

6.4 Summary

The 2D macroscopic model developed in Chapter 4 for flow interaction with porous media was shown to be applicable to turbulent open channel flows over and within natural porous beds if appropriate modifications are introduced into the drag and turbulence closure models. Twelve test cases of turbulent flow with different discharges over 2 different porous armour layers were simulated and the results of velocity and shear stress profiles were compared to the experimental data. Ergun's equation with its original drag coefficients were employed for the effect of solid skeleton within the armour layer while the drag effects within the roughness layer were incorporated by a modified version of the drag force model developed in Chapter 3 for flow over impermeable rough boundaries. Turbulence was modelled by the MSPH-ML model proposed in Chapter 3 with a three-layer mixing-length profile which was formulated by fitting Nezu and Rodi (1986) formula to the present experimental data. Besides, a porous inflow boundary as well as an imaginary outlet wall were introduced to obtain uniform flow conditions within the computational domain.

Using different particle spacing l_0 = 3, 5 and 7 mm in the simulation of 4 test cases revealed that as higher resolution is applied, the numerical results get closer to the experimental data. This issue was attributed to the satisfaction of the length constraint (4.61) (a) when a higher resolution is used. However, using l_0 = 3 mm did not provide significant improvements for the test cases associated with bed B2. It was probably because the drag and turbulence effects just below the roughness layer has not been represented correctly in the model due to the lack of knowledge on the spatial characteristics of the armour layer below z_t.

In spite of limitations of the applied drag and turbulence models with regard to definition of drag coefficients and mixing-length distribution, the present model has shown appreciable potential for simulating different cases ranging from coastal applications (in Chapter 5) to the turbulent channel flows over natural gravel beds in the present chapter.

Chapter 7 Key Findings and Conclusions

Free surface turbulent flow was studied due to its importance for water engineers. The aim of the thesis was investigating turbulent free surface flows over/within rough impermeable and permeable beds using the SPH method with a focus on the turbulence modelling and the treatment of the bed boundary. The ultimate goal was providing a simple and appropriate mathematical representation of the complicated processes occur at the bed so that flow quantities in this region can be estimated accurately. The objectives were developing SPH models for turbulent flows over rough impermeable and porous beds in a macroscopic scale, simulating relevant 2D problems, and validating the models by using existing sets of experimental data.

In Chapter 2, a detailed review was carried out on the background of the problem and the existing particle models for open channel flows and flow interaction with porous structures. Then, the required improvements were highlighted. In Chapter 3, the WCSPH method was used to develop a 2D model for simulating 12 test cases of steady uniform turbulent open channel flows over a layer of fixed spherical particles with a relatively high roughness. In Chapter 4, the average macroscopic governing equations were developed based on the SPH formulation and the required computational treatments were investigated focusing on the treatment of the interfacial boundary between porous media and an adjacent free flow (clear water). In Chapter 5, the model was applied to simulate 3 test cases of flow/wave interactions with porous structures and the results were compared to the existing experimental data as well as some other SPH studies. Finally, in Chapter 6, the model was applied to simulate 12

test cases of steady uniform turbulent open channel flows over natural sediment porous armour layers with 2 different bed configurations, and the model results were compared to a set of experimental data.

The conclusions and some key findings are as the following.

- In most of the existing SPH models developed for open channel flows, the effect of bed boundary has been taken into account usually based on numerical adjustments and neglecting the characteristics of the bed. Through the literature review on the treatment of rough boundaries, it was found that the drag force model is capable of representing the effect of rough bed if it is applied together with an adequate turbulence model to transfer this effect to the water column. Therefore, a drag force model was adopted in Chapter 3 for simulating turbulent open channel flows over sloping rough boundaries with using a macroscopic roughness layer near the bed with a variable thickness which depends on the flow condition. Through calibrating the thickness of the roughness layer, the model provided good results of velocity and shear stress for all the 12 test cases.
- It was found that, both momentum reduction at the bed as well as transferring its effect to the upper layers of flow are necessary to be adequately estimated in order to obtain well simulated velocity profiles. In other words, the treatment of both the rough bed boundary and the effect of the turbulence play an important role in producing the desirable balance in the flow momentum. In Chapter 3, it was found that the SPS-Smagorinsky model which is often used with SPH for turbulence modelling is not capable of reproducing this balance, when a C_s of about 0.15 is used. The reason was attributed to the macroscopic modelling of the roughness layer as well as the deficiency of the SPH method in estimation of velocity-pressure interactions (as addressed by Mayrhofer et al., 2015). Besides, the resolved part of turbulent shear stress was also found to be highly underestimated due to the same reasons. Therefore, it was assumed that the total turbulent shear stress should be modelled for the problems such as those studied

in Chapter 3. Hence, the mixing-length model which is usually used in RANS modelling was employed to estimate the eddy-viscosity in the proposed MSPH-ML model. The results of shear stress and velocity profiles showed the accuracy of the proposed turbulence model; and the comparison between the results of the MSPH-ML model (with Nezu and Nakagawa 1986 formula) and the SPS-Smagorinsky model (with C_s = 0.15) confirmed the validity of the assumption that the total shear stress should be modelled in the cases studied in Chapter 3.

- The macroscopic bed boundary treatment proposed in Chapter 3 had some limitations such as that the effect of solid/fluid volume (porosity) within the roughness layer was neglected in the conservation of mass. It was assumed that this effect should be small since the height of the roughness layer (porous area) was small compared to the depth of flow. However, it is necessary to take the effect of porosity into account in the governing equations when the thickness of the (porous) bed is significant.

- In addition to the above-mentioned limitation of the model, the following points motivated the author to investigate the governing equations of flow through porous media in detail, particularly with focusing on the treatment of the interfacial boundary between porous media and an adjacent free (clear water) flow: i) in most of the existing SPH models developed for flow interaction with porous media, the interface boundary layer has been simulated often based on numerical calibrations rather than rigorous mathematical justifications; and no investigation has been performed on the behaviour of flow quantities at the interfacial boundary; ii) The turbulence effect has been disregarded, or included by the SPS model with no further validation; and iii) Most of the existing SPH studies are in the area of coastal engineering (wave interaction with porous structures), mostly providing the results of water surface elevation, while there have been no applications in turbulent open channel flows over/within porous beds, especially for the situation of high velocity gradients at the interface, which

is of interest in the present study. Therefore, Chapter 4 was devoted to the development of the SPH form of the macroscopic governing equations with an insight into the validity and accuracy of them when dealing with an interfacial boundary in practical civil engineering applications. The most important constraints were found to be that: i) the support of the weighting function applied for porosity calculation should be chosen based on the characteristic length of solid material at the interface; ii) the computational resolution should be fine enough near the interface boundaries to adequately capture the variations in the macroscopic velocity; and iii) the size of the averaging volume (smoothing length) applied for the solution of the governing equations should be set equally over space and should remain unchanged over time.

- The model developed in Chapter 4 was completed in Chapter 5 and applied to simulate 3 test cases of flow interactions with porous structures with different characteristics in 2D. The results revealed that: i) using Ergun's equation with its original coefficients for estimation of drag effects of solid skeleton on the average flow field provides satisfactory results for different engineering applications as long as the flow and porous media conditions are in the range of those employed by Ergun to derive his equation; ii) the accuracy of the model predictions depends on the accuracy of the interface boundary treatment. In the simulation of dam break flow through porous dams (test case I), it was observed that the way that the interfacial boundary is treated is more important than introducing a slight change in the drag coefficient; iii) the satisfaction of the required length constraint $r_{\Upsilon} << L_{\langle \mathbf{u} \rangle^{\alpha}}$ is more important when flow Re Number is higher and/or the interfacial boundary is sharper. In Section 5.5, it was shown that employing higher resolution does not have a considerable effect on the results of water surface elevation in the case of dam break flow through porous dams, while it significantly affects the results of velocity distribution near a porous structure when a wave is travelling over it (test case III).

- In Chapter 6, the model developed in Chapter 4 was applied for simulating turbulent flows over and within natural porous armour layers with 2 bed configurations and different flow conditions. It was concluded that if the drag effects and porosity distribution are accurately defined, the model is capable of providing good results for such a practical case with high velocity gradients at the interface boundary. The following points were observed from the simulations: i) again, the proposed MSPH-ML model showed higher efficiency in reproducing the momentum balance compared to the SPS-Smagorinsky model with C_s = 0.15 in simulating the present cases; ii) a limitation with the MSPH-ML model is that the distribution of the mixing-length should be known while the model results of turbulent shear stress is very sensitive to it; iii) the lack of knowledge on the distribution of porosity in a natural bed (particularly near the interface) would result in non-accurate predictions of flow velocity; and iv) satisfaction of length constraint (4.61) (a), i.e. $r_\Upsilon << L_{\langle \mathbf{u} \rangle^\alpha}$, through the application of higher computational resolution improves the results especially the slope of velocity profiles near the interfacial boundary.
- Defining inflow/outflow boundaries in open channel cases to get uniform conditions is difficult. In the simulation of the test cases in both Chapter 3 and Chapter 6, it was required to reproduce steady uniform flow conditions. Several layers of dummy particles were set at the inflow and outflow regions to recover the truncated area of the kernel function of those fluid particles near the boundary lines, while their properties were set based on the desirable hydraulic conditions. In Chapter 3 an averaging technique was introduced to determine the velocity of inflow particles based on the velocity of inner-fluid particles. This method was not applicable in the simulation of turbulent flow over permeable boundaries, so that a porous inflow and an outflow imaginary wall were introduced accordingly to generate steady uniform flow conditions. Both techniques were constructed based on the fact that the distribution of flow

quantities at the inlet and outlet boundaries is unknown, with the difference that in the method proposed in Chapter 6, flow discharge was fixed to the experimental discharge. These techniques provided the required flow conditions within the computational domains with good accuracies.

In conclusion, the models developed in the present study demonstrated the capability of the SPH method in dealing with turbulent channel flows over rough impermeable and permeable boundaries. If the extra terms in the momentum equation which represent the effects of bed drag and flow turbulence are adequately determined, and the SPH averaging process near the bed boundary is performed consistent with the physical properties of the bed, the model has the potential to provide accurate distribution of flow quantities over the whole water column. The accuracy in the results depend on the accuracy of the parameters in the closure terms such as the drag coefficients and the mixing-length. The mixing-length model is limited when the distribution of the mixing-length is not available. However, it performs more efficient than the SPS-Smagorinsky model for those cases studied here. On the other hand, unlike some other RANS models, it has only one empirical coefficient which makes it easier to be applied.

Nevertheless, the application of other turbulence closures with SPH should be tested to check their capability in tackling the turbulence problem in the macroscopic simulation of turbulent open channel flows over rough and porous beds. The ideal way is to deeply investigate the problem of the SPH and SPS methods in dealing with highly-sheared channel cases and providing a model which can incorporate the effect of the missing part of turbulence more rigorously. These issues are considered as future study.

References

Aberle, J., 2006. Spatially averaged near-bed flow field over rough armor layers, River Flow 2006, Two Volume Set. Taylor & Francis.

Aberle, J., 2007. Measurements of armour layer roughness geometry function and porosity. Acta Geophysica 55, 23-32.

Aberle, J., Koll, K., 2004. Double-averaged flow field over static armor layers, River Flow 2004. CRC Press, pp. 225-233.

Aberle, J., Koll, K., Dittrich, A., 2008. Form induced stresses over rough gravel-beds. Acta Geophysica 56, 584-600.

Akbari, H., 2014. Modified moving particle method for modeling wave interaction with multi layered porous structures. Coastal Engineering 89, 1-19.

Akbari, H., Namin, M.M., 2013. Moving particle method for modeling wave interaction with porous structures. Coastal Engineering 74, 59-73.

Allen, K.G., von Backström, T.W., Kröger, D.G., 2013. Packed bed pressure drop dependence on particle shape, size distribution, packing arrangement and roughness. Powder Technology 246, 590-600.

Aristodemo, F., Marrone, S., Federico, I., 2015. SPH modeling of plane jets into water bodies through an inflow/outflow algorithm. Ocean Engineering 105, 160-175.

Beavers, G.S., Joseph, D.D., 1967. Boundary conditions at a naturally permeable wall. Journal of Fluid Mechanics 30, 197-207.

Bonet, J., Lok, T.S.L., 1999. Variational and momentum preservation aspects of Smooth Particle Hydrodynamic formulations. Computer Methods in Applied Mechanics and Engineering 180, 97-115.

Breugem, W.P., Boersma, B.J., 2005. Direct numerical simulations of turbulent flow over a permeable wall using a direct and a continuum approach. Physics of Fluids 17, 025103.

Brinkman, H.C., 1949. On the permeability of media consisting of closely packed porous particles. Flow, Turbulence and Combustion 1, 81.

Busse, A., Sandham, N.D., 2012. Parametric forcing approach to rough-wall turbulent channel flow. Journal of Fluid Mechanics 712, 169-202.

Carney, S.K., Bledsoe, B.P., Gessler, D., 2006. Representing the bed roughness of coarse-grained streams in computational fluid dynamics. Earth Surface Processes and Landforms 31, 736-749.

Charles, K.S., Ralph, H.C., 1972. Wave Transmission through Permeable Breakwaters, Proceedings of the 13th International Conference on Coastal Engineering ASCE, Vancouver, British Columbia, Canada, pp. 1827–1846.

Chern, M., Syamsuri, S., 2013. Effect of corrugated bed on hydraulic jump characteristic using SPH method. Journal of Hydraulic Engineering ASCE 139, 221–232.

Christoph, G.H., Pletcher, R.H., 1983. Prediction of rough-wall skin friction and heat transfer. AIAA Journal 21, 509-515.

Clauser, F.H., 1954. Turbulent Boundary Layers in Adverse Pressure Gradients. Journal of the Aeronautical Sciences 21, 91-108.

Coleman, N.L., 1981. Velocity profiles with suspended sediment. Journal of Hydraulic Research 19, 211.

Coles, D., 1956. The law of the wake in the turbulent boundary layer. Journal of Fluid Mechanics 1, 191.

Cui, J., Patel, V.C., Lin, C.-L., 2003. Prediction of Turbulent Flow Over Rough Surfaces Using a Force Field in Large Eddy Simulation. Journal of Fluids Engineering 125, 2-9.

De Padova, D., Mossa, M., Sibilla, S., Torti, E., 2013. 3D SPH modelling of hydraulic jump in a very large channel. Journal of Hydraulic Research 51, 158-173.

Deardorff, J.W., 1970. A numerical study of three-dimensional turbulent channel flow at large Reynolds numbers. Journal of Fluid Mechanics 41, 453-480.

Del Jesus, M., Lara, J.L., Losada, I.J., 2012. Three-dimensional interaction of waves and porous coastal structures: Part I: Numerical model formulation. Coastal Engineering 64, 57-72.

Deresiewicz, H., Skalak, R., 1963. On uniqueness in dynamic poroelasticity. Bulletin of the Seismological Society of America 53, 783.

Du Plessis, J.P., 1994. Analytical quantification of coefficients in the Ergun equation for fluid friction in a packed bed. Transport in Porous Media 16, 189-207.

Ergun, S., 1952. Fluid flow through packed columns. Chemical Engineering Progress 48, 89-94.

Federico, I., Marrone, S., Colagrossi, A., Aristodemo, F., Antuono, M., 2012. Simulating 2D open-channel flows through an SPH model. European Journal of Mechanics - B/Fluids 34, 35-46.

Forchheimer, P.H., 1901. Wasserbeuregung durch boden. Zeit. Ver. Deutsch. Ingenieur 45, 1782–1788.

Fu, L., Jin, Y.-C., 2013. A mesh-free method boundary condition technique in open channel flow simulation. Journal of Hydraulic Research 51, 174-185.

Germano, M., Piomelli, U., Moin, P., Cabot, W.H., 1991. A dynamic subgrid-scale eddy viscosity model. Physics of Fluids A: Fluid Dynamics 3, 1760-1765.

Gingold, R.A., Monaghan, J.J., 1977. Smoothed particle hydrodynamics: theory and application to non-spherical stars. Monthly Notices of the Royal Astronomical Society 181, 375-389.

Goring, D.G., 1978 Tsunamis—The Propagation of Long Waves onto a Shelf, California Institute of Technology, Pasadena, California.

Gotoh, H., Sakai, T., 1999. Lagrangian simulation of breaking waves using particle method. Coastal Engineering Journal 41, 303-326.

Gotoh, H., Shibahara, T., Sakai, T., 2001. Sub-particle-scale turbulence model for the MPS method - Lagrangian flow model for hydraulic engineering. Advanced Methods for Computational Fluid Dynamics 9-4, 339-347.

Granville, P.S., 1985. Mixing-length formulations for turbulent boundary layers over arbitrary rough surfaces. Journal of Ship Research 29, 223–233.

Granville, P.S., 1988. Eddy viscosities and mixing lengths for turbulent boundary layers on flat plates, smooth or rough. Journal of Ship Research 32, 229–237.

Gray, W.G., 1975. A derivation of the equations for multi-phase transport. Chemical Engineering Science 30, 229-233.

Gray, W.G., Lee, P.C.Y., 1977. On the theorems for local volume averaging of multiphase systems. International Journal of Multiphase Flow 3, 333-340.

Gui, Q., Dong, P., Shao, S., Chen, Y., 2015. Incompressible SPH simulation of wave interaction with porous structure. Ocean Engineering 110, Part A, 126-139.

Hahn, S., Je, J., Choi, H., 2002. Direct numerical simulation of turbulent channel flow with permeable walls. Journal of Fluid Mechanics 450, 259-285.

Hsu, C.C., Wu, F.S., Lee, W.J., 1998. Flow at 90 degrees equal-width open-channel junction. Journal of Hydraulic Engineering, ASCE 124, 186-191.

Huang, C.-J., Chang, H.-H., Hwung, H.-H., 2003. Structural permeability effects on the interaction of a solitary wave and a submerged breakwater. Coastal Engineering 49, 1-24.

Huang, C.-J., Shen, M.-L., Chang, H.-H., 2008. Propagation of a solitary wave over rigid porous beds. Ocean Engineering 35, 1194-1202.

Jensen, B., Christensen, E.D., Sumer, B.M., Vistisen, M., 2015. Flow and Turbulence at Rubble-Mound Breakwater Armor Layers under Solitary Wave. Journal of Waterway, Port, Coastal, and Ocean Engineering 141.

Khayyer, A., Gotoh, H., Shao, S.D., 2008. Corrected Incompressible SPH method for accurate water-surface tracking in breaking waves. Coastal Engineering 55, 236-250.

Krogstad, P.A., 1989. A calculation method for turbulent boundary layers on rough surfaces, 10th Australasian Fluid Mechanics Conference, Melbourne, Australia.

Krogstad, P.A., 1991. Modification of the van Driest damping function to include the effects of surface roughness. AIAA Journal 29, 888-894.

Lara, J.L., Losada, I.J., Maza, M., Guanche, R., 2011. Breaking solitary wave evolution over a porous underwater step. Coastal Engineering 58, 837-850.

Liu, P.L.-F., Lin, P., Chang, K.A., Sakakiyama, T., 1999. Numerical modeling of wave interaction with porous structures. Journal of Waterway, Port, Coastal, and Ocean Engineering, ASCE 125, 322–330.

López, D., Marivela, R., Garrote, L., 2010. Smoothed particle hydrodynamics model applied to hydraulic structures: a hydraulic jump test case. Journal of Hydraulic Research 48, 142-158.

Lucy, L.B., 1977. A numerical approach to the testing of the fission hypothesis. Astronomical Journal 82, 1013-1024.

Macdonald, I.F., El-Sayed, M.S., Mow, K., Dullien, F.A.L., 1979. Flow through Porous Media – the Ergun Equation Revisited. Industrial & Engineering Chemistry Fundamentals 18, 199-208.

Marle, C.M., 1982. On macroscopic equations governing multiphase flow with diffusion and chemical reactions in porous media. International Journal of Engineering Science 20, 643-662.

Mayrhofer, A., Laurence, D., Rogers, B.D., Violeau, D., 2015. DNS and LES of 3-D wall-bounded turbulence using Smoothed Particle Hydrodynamics. Computers & Fluids 115, 86-97.

Mayrhofer, A., Rogers, B.D., Violeau, D., Ferrand, M., 2013. Investigation of wall bounded flows using SPH and the unified semi-analytical wall boundary conditions. Computer Physics Communications 184, 2515–2527.

Michel, R., Quemard, C., Durant, R., 1969. Hypotheses on the mixing length and application to the calculation of the turbulent boundary layers. , Proceedings of Computation of Turbulent Boundary Layers. AFORS-IFP-Stanford Conference, Stanford.

Miyake, Y., Tsujimoto, K., Agata, Y., 1999. A DNS of a turbulent flow in a rough-wall channel using roughness elements model. JSME International Journal 43, 233-242.

Monaghan, J.J., 1989. On the problem of penetration in particle methods. Journal of Computational Physics 82, 1-15.

Monaghan, J.J., 2005. Smoothed particle hydrodynamics. Reports on Progress in Physics 68, 1703.

Monaghan, J.J., 2011. A turbulence model for Smoothed Particle Hydrodynamics, European Journal of Mechanics - B/Fluids 30, 360-370.

Monaghan, J.J., 2017. SPH-ϵ simulation of 2D turbulence driven by a moving cylinder. European Journal of Mechanics - B/Fluids 65, 486-493.

Monaghan, J.J., Lattanzio, J.C., 1985. A refined particle method for astrophysical problems. Astronomy & Astrophysics 149, 135-143.

Nezu, I., Nakagawa, H., 1993. Turbulence in Open Channel Flows. Taylor & Francis.

Nezu, I., Rodi, W., 1986. Open-channel Flow Measurements with a Laser Doppler Anemometer. Journal of Hydraulic Engineering 112, 335-355.

Nicholas, A.P., 2001. Computational fluid dynamics modelling of boundary roughness in gravel-bed rivers: an investigation of the effects of random variability in bed elevation. Earth Surface Processes and Landforms 26, 345-362.

Nicholas, A.P., 2005. Roughness Parameterization in CFD Modelling of Gravel-Bed Rivers, Computational Fluid Dynamics. John Wiley & Sons, Ltd, pp. 329-355.

Nicholas, A.P., Sambrook Smith, G.H., 1999. Numerical simulation of three-dimensional flow hydraulics in a braided channel. Hydrological Processes 13, 913-929.

Nichols, A., 2013. Free surface dynamics in shallow turbulent flows, School of Engineering. University of Bradford, UK.

Nikora, V., Goring, D., McEwan, I., Griffiths, G., 2001. Spatially Averaged Open-Channel Flow over Rough Bed. Journal of Hydraulic Engineering 127, 123-133.

Nikora, V., Koll, K., McEwan, I., McLean, S., Dittrich, A., 2004. Velocity Distribution in the Roughness Layer of Rough-Bed Flows. Journal of Hydraulic Engineering 130, 1036-1042.

Nikora, V., Koll, K., McLean, S., Dittrich, A., Aberle, J., 2002. Zero-plane displacement for rough-bed open-channels flows, International conference on fluvial hydraulics, River flow, Louvain-la-Neuve, Belgium, pp. 83-92.

Nikora, V., McLean, S., Coleman, S., Pokrajac, D., McEwan, I., Campbell, L., Aberle, J., Clunie, D., Koll, K., 2007. Double-Averaging Concept for Rough-Bed Open-Channel and Overland Flows: Applications. Journal of Hydraulic Engineering 133, 884-895.

Nikuradse, J., 1933. Laws of flow in rough pipes. VDI Forschungsheft 361 English translation: NACA TM 1292, 1950.

Ochoa-Tapia, J.A., Whitaker, S., 1995. Momentum transfer at the boundary between a porous medium and a homogeneous fluid—I. Theoretical development. International Journal of Heat and Mass Transfer 38, 2635-2646.

Pahar, G., Dhar, A., 2016. Modeling free-surface flow in porous media with modified incompressible SPH, Engineering Analysis with Boundary Elements 68, 75-85.

Pahar, G., Dhar, A., 2017a. Numerical modelling of free-surface flow-porous media interaction using divergence-free Moving Particle Semi-Implicit method. Transport in Porous Media 118, 157–175.

Pahar, G., Dhar, A., 2017b. On modification of pressure gradient operator in integrated ISPH for multifluid and porous media flow with free-surface. Engineering Analysis with Boundary Elements 80, 38–48.

Patel, V.C., 1998. Perspective: Flow at High Reynolds Number and Over Rough Surfaces—Achilles Heel of CFD. Journal of Fluids Engineering 120, 434-444.

Perry, A.E., Schofield, W.H., Joubert, P.N., 2006. Rough wall turbulent boundary layers. Journal of Fluid Mechanics 37, 383-413.

Philip, L.F.L., Pengzhi, L., Kuang-An, C., Tsutomu, S., 1999. Numerical Modeling of Wave Interaction with Porous Structures. Journal of Waterway, Port, Coastal, and Ocean Engineering 125, 322-330.

Piomelli, U., Zang, T.A., 1991. Large-eddy simulation of transitional channel flow. Computer Physics Communications 65, 224-230.

Quintard, M., Whitaker, S., 1993. Transport Processes in Ordered and Disordered Porous Media: Volume-Averaged Equations, Closure Problems, and Comparison with Experiment. Chemical Engineering Science 48, 2537-2564.

Quintard, M., Whitaker, S., 1994. Transport in ordered and disordered porous media II: Generalized volume averaging. Transport in Porous Media 14, 179-206.

Rameshwaran, P., Naden, P.S., Lawless, M., 2011. Flow modelling in gravel-bed rivers: rethinking the bottom boundary condition. Earth Surface Processes and Landforms 36, 1350-1366.

Ren, B., Wen, H., Dong, P., Wang, Y., 2014. Numerical simulation of wave interaction with porous structures using an improved smoothed particle hydrodynamic method. Coastal Engineering 88, 88-100.

Ren, B., Wen, H., Dong, P., Wang, Y., 2016. Improved SPH simulation of wave motions and turbulent flows through porous media. Coastal Engineering 107, 14-27.

Rogallo, R.S., Moin, P., 1984. Numerical Simulation of Turbulent Flows. Annual Review of Fluid Mechanics 16, 99-137.

Rotta, J.C., 1962. Turbulent boundary layers in incompressible flow. Progress in Aerospace Sciences 2, 1-95.

Sagaut, P., 2001. Large Eddy Simulation for Incompressible Flows. Springer, Berlin/Heidelberg.

Sahebari, A., Jin, Y.-C., Shakibaeinia, A., 2011. Flow over sills by the MPS mesh-free particle method. Journal of Hydraulic Research 49, 649-656.

Sakakiyama, T., Kajima, R., 1992. Numerical simulation of nonlinear wave interacting with permeable breakwaters, Proceedings of 23rd International Conference on Coastal. Engineering, ASCE, pp. 1517–1530.

Sam, S., Ming-Jyh, C., 2013. Effect of Corrugated Bed on Hydraulic Jump Characteristic Using SPH Method. Journal of Hydraulic Engineering 139, 221-232.

Schmeeckle, M.W., Nelson, J.M., Shreve, R.L., 2007. Forces on stationary particles in near-bed turbulent flows. Journal of Geophysical Research: Earth Surface 112, F02003, doi:10.1029/2006JF000536.

Shakibaeinia, A., Jin, Y.-C., 2011. MPS-Based Mesh-Free Particle Method for Modeling Open-Channel Flows. Journal of Hydraulic Engineering 137, 1375-1384.

Shao, S., 2010. Incompressible SPH flow model for wave interactions with porous media. Coastal Engineering 57, 304-316.

Sivykh, G., 1984. Turbulent Viscosity for the Analysis of an Incompressible Boundary Layer on a Rough Surface. Journal of Applied Mechanical and Technical Physics 25, 226–232.

Slattery, J.C., 1967. Flow of viscoelastic fluids through porous media. AIChE Journal 13, 1066-1071.

Smagorinsky, J., 1963. General circulation experiments with the primitive equations. Monthly Weather Review 91, 99-164.

Tan, S.K., Cheng, N.-S., Xie, Y., Shao, S., 2015. Incompressible SPH simulation of open channel flow over smooth bed. Journal of Hydro-environment Research 9, 340-353.

Taylor, R.P., Coleman, H.W., Hodge, B.K., 1985. Prediction of Turbulent Rough-Wall Skin Friction Using a Discrete Element Approach. Journal of Fluids Engineering 107, 251-257.

Vafai, K., Tien, C.L., 1981. Boundary and inertia effects on flow and heat transfer in porous media. International Journal of Heat and Mass Transfer 24, 195-203.

Van Driest, E.R., 1956. On Turbulent Flow Near a Wall. Journal of the Aeronautical Sciences 23, 1007-1011.

Van Gent, M.R.A., 1995. Wave interaction with permeable coastal structures, Delft University of Technology, Delft, The Netherlands.

Violeau, D., Issa, R., 2007. Numerical modelling of complex turbulent free-surface flows with the SPH method: an overview. International Journal for Numerical Methods in Fluids 53, 277-304.

Violeau, D., Piccon, S., Chabard, J.P., 2002. Two attempts of turbulence modelling in smoothed particle hydrodynamics, Proceedings of the 8th Symposium on Flow Modelling and Turbulence Measurements. Advances in Fluid Modelling and Turbulence Measurements. World Scientific, Singapore, pp. 339–346.

Whitaker, S., 1969. Advances in theory of fluid motion in porous media. Industrial and Engineering Chemistry 61, 14-28.

Whitaker, S., 1996. The Forchheimer equation: A theoretical development. Transport in Porous Media 25, 27-61.

Wiberg, P.L., Smith, J.D., 1991. Velocity distribution and bed roughness in high-gradient streams. Water Resources Research 27, 825-838.

Wu, Y.-T., Hsiao, S.-C., 2013. Propagation of solitary waves over a submerged permeable breakwater. Coastal Engineering 81, 1-18.

Zeng, C., Li, C.W., 2012. Modeling flows over gravel beds by a drag force method and a modified S–A turbulence closure. Advances in Water Resources 46, 84-95.

Appendix A The spatial averaging theorem in porous media

In this appendix, two important theorems associated with the convolution product of spatial and temporal derivatives are introduced. These theorems provide the key relationships to derive the macroscopic governing equations of flow through porous media.

A.1 Spatial derivative

The basic idea in formulating the spatial derivative of a quantity in SPH is that the derivative is described in terms of the product of the quantity and the derivative of the weighting function, i.e. the derivative operator transfers from the quantity to the weighting function. The spatial derivative of ψ is formulated by substituting $\nabla\psi$ with ψ in Equation (4.4) as follows

$$\left\langle \nabla\psi \right\rangle^{\Omega} = \int_{\Omega} G\left(\mathbf{r}-\mathbf{r}',h_{\Omega}\right)\gamma\left(\mathbf{r}'\right)\nabla\psi\left(\mathbf{r}'\right)\,d\mathbf{r}' \tag{A.1}$$

The integrand can be expressed as

$$\begin{aligned} G\left(\mathbf{r}-\mathbf{r}',h_{\Omega}\right)\gamma\left(\mathbf{r}'\right)\nabla\psi\left(\mathbf{r}'\right) &= \nabla\left[G\left(\mathbf{r}-\mathbf{r}',h_{\Omega}\right)\gamma\left(\mathbf{r}'\right)\psi\left(\mathbf{r}'\right)\right] \\ &-\left[-1\times\nabla G\left(\mathbf{r}-\mathbf{r}',h_{\Omega}\right)\gamma\left(\mathbf{r}'\right)\psi\left(\mathbf{r}'\right)\right]-G\left(\mathbf{r}-\mathbf{r}',h_{\Omega}\right)\nabla\gamma\left(\mathbf{r}'\right)\psi\left(\mathbf{r}'\right) \end{aligned} \tag{A.2}$$

Since the differentiation is carried out with respect to $\mathbf{r}'$, the derivative of the kernel function in the last term on the right-hand side of the equation is multiplied by -1

according to the symmetry condition (Equation 4.8). Substituting Equation (A.2) into (A.1) gives the following relationship.

$$\begin{aligned}\left\langle \nabla \psi \right\rangle^{\Omega} = & \int_{\Omega} \nabla \left[G\left(\mathbf{r}-\mathbf{r}', h_{\Omega}\right) \gamma\left(\mathbf{r}'\right) \psi\left(\mathbf{r}'\right) \right] d\mathbf{r}' \\ & + \int_{\Omega} \nabla G\left(\mathbf{r}-\mathbf{r}', h_{\Omega}\right) \gamma\left(\mathbf{r}'\right) \psi\left(\mathbf{r}'\right) d\mathbf{r}' - \int_{\Omega} G\left(\mathbf{r}-\mathbf{r}', h_{\Omega}\right) \nabla \gamma\left(\mathbf{r}'\right) \psi\left(\mathbf{r}'\right) d\mathbf{r}'\end{aligned} \tag{A.3}$$

Grey and Lee (1977) showed that

$$\nabla \gamma = -\mathbf{n}_{\alpha\beta} \delta_{\alpha\beta} \tag{A.4}$$

Where $\mathbf{n}_{\alpha\beta}$ is the unit normal vector pointing from the α-phase to the β-phase (Figure 4-1) and $\delta_{\alpha\beta}$ is the Dirac distribution associated with the α-β interfaces. By substituting Equation (A.4) into Equation (A.3), and applying the divergence theorem to the first term on the right-hand side of Equation (A.3),

$$\begin{aligned}\left\langle \nabla \psi \right\rangle^{\Omega} = & \int_{\Omega} G\left(\mathbf{r}-\mathbf{r}', h_{\Omega}\right) \gamma\left(\mathbf{r}'\right) \psi\left(\mathbf{r}'\right) \mathbf{n}_{\Omega}\left(\mathbf{r}'\right) \delta_{\Omega}\left(\mathbf{r}'\right) d\mathbf{r}' \\ & + \int_{\Omega} \nabla G\left(\mathbf{r}-\mathbf{r}', h_{\Omega}\right) \gamma\left(\mathbf{r}'\right) \psi\left(\mathbf{r}'\right) d\mathbf{r}' \\ & + \int_{\Omega} G\left(\mathbf{r}-\mathbf{r}', h_{\Omega}\right) \psi\left(\mathbf{r}'\right) \mathbf{n}_{\alpha\beta}\left(\mathbf{r}'\right) \delta_{\alpha\beta}\left(\mathbf{r}'\right) d\mathbf{r}'\end{aligned} \tag{A.5}$$

where the first integral associates with the surface of the averaging volume A_{Ω}, and the last one associates with the α-β interfaces $A_{\alpha\beta}$ (Figure 4-1). $\mathbf{n}_{\Omega}$ and δ_{Ω} are the unit normal vector and the Dirac distribution associated with A_{Ω} (Figure 4-1). According to the compact condition (Equation 4.6), the value of the weighting function on the A_{Ω} surface is zero. Therefore, the first term on the right-hand side of Equation (A.5) is zero so that this equation is obtained in the following form (shown by the convolution product) which is the spatial averaging theorem associated with the spatial derivative.

$$G * \left(\gamma \nabla \psi\right) = \nabla G * \left(\gamma \psi\right) + G * \left(\psi \mathbf{n}_{\alpha\beta} \delta_{\alpha\beta}\right) \tag{A.6}$$

If the weighting function is differentiable and its derivative is integrable, it is possible to show that

$$\nabla G * (\gamma\psi) = \nabla\left[G * (\gamma\psi)\right] \tag{A.7}$$

which can be substituted into (A.6) to obtain the following relationship.

$$G * (\gamma\nabla\psi) = \nabla\left[G * (\gamma\psi)\right] + G * \left(\psi \mathbf{n}_{\alpha\beta}\delta_{\alpha\beta}\right) \tag{A.8}$$

This equation represents the weighted function version of the classical (Slattery's) spatial averaging theorem which was also presented by Marle (1982) and Quintard and Whitaker (1993, 1994).

A.2 Temporal derivative

The volumetric average of the temporal derivative is obtained by substituting $\partial\psi/\partial t$ into Equation (4.4) as follows.

$$\left\langle \frac{\partial\psi}{\partial t} \right\rangle^{\Omega} = \int_{\Omega} G(\mathbf{r}-\mathbf{r}', h_{\Omega})\,\gamma(\mathbf{r}')\frac{\partial\psi(\mathbf{r}')}{\partial t}\,d\mathbf{r}' \tag{A.9}$$

Applying a similar definition used in Equation (A.2) leads to

$$\begin{aligned}\left\langle \frac{\partial\psi}{\partial t} \right\rangle^{\Omega} = &\int_{\Omega} \frac{\partial}{\partial t}\left[G(\mathbf{r}-\mathbf{r}', h_{\Omega})\,\gamma(\mathbf{r}')\psi(\mathbf{r}')\right] d\mathbf{r}' \\ &+ \int_{\Omega} \frac{\partial G(\mathbf{r}-\mathbf{r}', h_{\Omega})}{\partial t}\gamma(\mathbf{r}')\psi(\mathbf{r}')\,d\mathbf{r}' - \int_{\Omega} G(\mathbf{r}-\mathbf{r}', h_{\Omega})\frac{\partial\gamma(\mathbf{r}')}{\partial t}\psi(\mathbf{r}')\,d\mathbf{r}'\end{aligned} \tag{A.10}$$

If the local time derivative is not a function of the limits of the integration, the second term on the right-hand side of the equation will be zero. The requirement is that the averaging volume Ω as well as the weighting function G do not change with the local time. In other words, they should remain unchanged relative to the centroid of the volume over the total time (*constraint #3*). Imposing this constraint, the second term on the right-hand side of the equation will be omitted. For the third term, the

following relationship (Grey and Lee 1977) for the temporal derivative of the distribution function is applied

$$\frac{\partial \gamma}{\partial t} = -\mathbf{u}_{\alpha\beta} \nabla \gamma \tag{A.11}$$

in which $\mathbf{u}_{\alpha\beta}$ is the velocity at the $\alpha - \beta$ interface and $\nabla\gamma$ is defined by Equation (A.4). Therefore,

$$\begin{aligned} \left\langle \frac{\partial \psi}{\partial t} \right\rangle^{\Omega} = & \frac{\partial}{\partial t} \int_{\Omega} G\left(\mathbf{r} - \mathbf{r}', h_{\Omega}\right) \gamma\left(\mathbf{r}'\right) \psi\left(\mathbf{r}'\right) d\mathbf{r}' \\ & - \int_{\Omega} G\left(\mathbf{r} - \mathbf{r}', h_{\Omega}\right) \psi\left(\mathbf{r}'\right) \mathbf{u}_{\alpha\beta} \cdot \mathbf{n}_{\alpha\beta} \, d\mathbf{r}' \end{aligned} \tag{A.12}$$

It is noted that the time derivative operator can be separated from the integrand and instead multiplied by the integral since it is not a function of the limits of the integration (*constraint #3*).

Using the convolution product, the above equations is represented as

$$G * \left(\gamma \frac{\partial \psi}{\partial t} \right) = \frac{\partial}{\partial t} \left[G * \left(\gamma \psi \right) \right] - G * \left(\psi \mathbf{u}_{\alpha\beta} \cdot \mathbf{n}_{\alpha\beta} \delta_{\alpha\beta} \right) \tag{A.13}$$

where in the present study, the surface integral (the last term on the right-hand side) is zero according to the no-slip boundary condition at the $\alpha - \beta$ interface (*assumption #2*). Therefore, the particle volumetric average of the temporal derivative reads as follows.

$$G * \left(\gamma \frac{\partial \psi}{\partial t} \right) = \frac{\partial}{\partial t} \left[G * \left(\gamma \psi \right) \right] \tag{A.14}$$

The relationships presented in Equations (A.6) and (A.13) are the two key theorems for deriving the macroscopic equations.

Appendix B Spatially averaged (macroscopic) equations of mass and momentum for flow through porous media

Making use of the convolution product with the weighting function G, the Lagrangian spatially averaged equations of mass and momentum will be derived in terms of intrinsic averages of flow properties based on the theorems developed in Appendix A.

B.1 Conservation of mass

The convolution products of the microscopic conservation equation of mass (4.1) is represented as follows

$$\underbrace{G*\left(\gamma\frac{\partial\rho}{\partial t}\right)}_{I}+\underbrace{G*\left[\gamma\nabla\cdot\left(\rho\mathbf{u}\right)\right]}_{II}=0 \tag{B.1}$$

Applying Equation (A.14) into the first term on the left-hand side of the equation (I), and then making use of Equation (4.21) for density yields

$$I=\frac{\partial}{\partial t}\left[\left(G*\gamma\right)\left\langle\rho\right\rangle^{\alpha}\right]=\left(G*\gamma\right)\frac{\partial\left\langle\rho\right\rangle^{\alpha}}{\partial t}+\frac{\partial\left(G*\gamma\right)}{\partial t}\left\langle\rho\right\rangle^{\alpha} \tag{B.2}$$

It is possible to show that the second term on the right-hand side of the above equation which represents the time derivative of the porosity is zero. According to *constraint #3*, the time derivative operator can move into the integrand, hence

$$\frac{\partial\left(G*\gamma\right)}{\partial t}=\int_{\Omega}\frac{\partial G\left(\mathbf{r}-\mathbf{r}',h_{\Omega}\right)}{\partial t}\gamma\left(\mathbf{r}'\right)d\mathbf{r}'+\int_{\Omega}G\left(\mathbf{r}-\mathbf{r}',h_{\Omega}\right)\frac{\partial\gamma\left(\mathbf{r}'\right)}{\partial t}d\mathbf{r}' \tag{B.3}$$

in which the first term on the right-hand side is zero since the local time derivative of the weighting function is zero due to *constraint #3*. Using Equations (A.11) and (A.4); and applying the no-slip boundary condition at the $\alpha-\beta$ interfaces, i.e. $\mathbf{u}_{\alpha\beta}\cdot\mathbf{n}_{\alpha\beta}=0$ (*assumption #2*), the second term on the right-hand side will be zero too. Hence

$$\frac{\partial\left(G*\gamma\right)}{\partial t}=0 \tag{B.4}$$

Therefore, Equation (B.2) comes into

$$I=\left(G*\gamma\right)\frac{\partial\left\langle\rho\right\rangle^{\alpha}}{\partial t} \tag{B.5}$$

For the second term II of the mass Equation (B.1), the theorem presented in Equation (A.8) is employed as

$$II=\nabla\left[G*\left(\gamma\rho\mathbf{u}\right)\right]+G*\left(\rho\mathbf{u}\cdot\mathbf{n}_{\alpha\beta}\delta_{\alpha\beta}\right) \tag{B.6}$$

Applying the no-slip condition at the $\alpha-\beta$ boundary, the second term on the right-hand side becomes zero, so that

$$II=\nabla\cdot\left[G*\left(\gamma\rho\mathbf{u}\right)\right] \tag{B.7}$$

If one applies the decomposition presented in Equation (4.11) for density, and applies the Taylor series expansion (Equation 4.13) for the intrinsic average of density at $\mathbf{r}'$, then by assuming that the characteristic length scale of density and its intrinsic average, L_{ρ} and $L_{\langle\rho\rangle^{\alpha}}$ respectively, are infinite (*assumption #3*) due to the incompressibility of flow, it will be readily shown that

$$G*\left(\gamma\rho\mathbf{u}\right)=\left\langle\rho\right\rangle^{\alpha}\left[G*\left(\gamma\mathbf{u}\right)\right] \tag{B.8}$$

Substituting this into Equation (B.7) and using Equation (4.21) to express $G*(\gamma\mathbf{u})$, and making some rearrangements leads to

$$II = (G*\gamma)\langle\mathbf{u}\rangle^{\alpha}\nabla\langle\rho\rangle^{\alpha} + \langle\rho\rangle^{\alpha}\nabla\cdot\left[(G*\gamma)\langle\mathbf{u}\rangle^{\alpha}\right] \tag{B.9}$$

Now, substituting Equations (B.5) and (B.9) into Equation (B.1) gives the averaged equation of mass as the following.

$$(G*\gamma)\frac{\partial\langle\rho\rangle^{\alpha}}{\partial t} + (G*\gamma)\langle\mathbf{u}\rangle^{\alpha}\nabla\langle\rho\rangle^{\alpha} + \langle\rho\rangle^{\alpha}\nabla\cdot\left[(G*\gamma)\langle\mathbf{u}\rangle^{\alpha}\right] = 0 \tag{B.10}$$

Considers the relationship between the local time and material derivatives, ($\partial/\partial t$ and D/Dt respectively), as

$$\frac{D}{Dt} = \frac{\partial}{\partial t} + \langle\mathbf{u}\rangle^{\alpha}\cdot\nabla \tag{B.11}$$

and substitute it into (B.10), the Lagrangian form of the macroscopic equation of mass will be obtained as the following.

$$(G*\gamma)\frac{D\langle\rho\rangle^{\alpha}}{Dt} + \langle\rho\rangle^{\alpha}\nabla\cdot\left[(G*\gamma)\langle\mathbf{u}\rangle^{\alpha}\right] = 0 \tag{B.12}$$

This equation is in the local transport form since it is written in terms of intrinsic averages of flow quantities.

B.2 Conservation of momentum

The convolution products of the microscopic conservation equation of momentum (4.2) is represented as follows.

$$\underbrace{G*\left[\gamma\frac{\partial(\rho\mathbf{u})}{\partial t}\right]}_{L_I} + \underbrace{G*\left[\gamma\nabla\cdot(\rho\mathbf{u}\mathbf{u})\right]}_{L_{II}} = \underbrace{-G*(\gamma\nabla P)}_{R_I} + \underbrace{G*(\gamma\rho\mathbf{g})}_{R_{II}} + \underbrace{G*(\gamma\mu\nabla^2\mathbf{u})}_{R_{III}} \tag{B.13}$$

In the following, each term on both left-hand side (LHS) and right-hand side (RHS) of the equation will be derived in terms of convolution product of intrinsic averages.

Using Equation (A.14) as well as the expression in Equation (B.8), the first term on the LHS (L_I) is approximated as

$$L_I = \frac{\partial}{\partial t}\left\{\langle\rho\rangle^{\alpha}\left[G*(\gamma\mathbf{u})\right]\right\} \tag{B.14}$$

Now applying Equation (4.21) for $G*(\gamma\mathbf{u})$ and considering Equation (B.4), one may obtain the following relationship for term L_I .

$$L_I = (G*\gamma)\langle\mathbf{u}\rangle^{\alpha}\frac{\partial\langle\rho\rangle^{\alpha}}{\partial t} + (G*\gamma)\langle\rho\rangle^{\alpha}\frac{\partial\langle\mathbf{u}\rangle^{\alpha}}{\partial t} \tag{B.15}$$

The nonlinear convective term (L_{II} in Equation B.13) is expressed as follows by applying Equation (A.8) and the no-slip condition at the $\alpha-\beta$ interface (*assumption #2*).

$$L_{II} = \nabla\cdot\left[G*(\gamma\rho\mathbf{u}\mathbf{u})\right] \tag{B.16}$$

Separating the velocity components and expressing this nonlinear term in terms of product of velocity averages will lead to the closure problem of turbulence which will be described in Section B.3.

To form the RHS of the momentum equation (B.13), the convolution products of pressure gradient, gravity force and viscosity, i.e. R_I , R_{II} and R_{III} , respectively, need to be evaluated. By applying Equation (A.8), and using Equation (4.21) for pressure, R_I will be presented as follows.

$$R_I = -\nabla\left[(G*\gamma)\langle P\rangle^{\alpha}\right] - G*\left(P\mathbf{n}_{\alpha\beta}\delta_{\alpha\beta}\right) \tag{B.17}$$

Noting that the gravitational acceleration $\mathbf{g}$ is constant, and considering Equation (4.21) for density, R_{II} is presented as

$$R_{II} = \left(G * \gamma\right)\left\langle \rho \right\rangle^{\alpha} \mathbf{g} \tag{B.18}$$

According to equation (A.8), R_{III} is written as the following.

$$R_{III} = \nabla\left[G * \left(\gamma\mu\nabla\mathbf{u}\right)\right] + G * \left(\mu\nabla\mathbf{u}\cdot\mathbf{n}_{\alpha\beta}\delta_{\alpha\beta}\right) \tag{B.19}$$

Again applying Equation (A.8) to $G*\left(\gamma\mu\nabla\mathbf{u}\right)$, considering the no-slip condition at the $\alpha-\beta$ interface, noting that μ is constant, and using Equation (4.21) for velocity, gives

$$G*\left(\gamma\mu\nabla\mathbf{u}\right) = \mu\nabla\left[\left(G*\gamma\right)\left\langle\mathbf{u}\right\rangle^{\alpha}\right] \tag{B.20}$$

which leads to the following relationship for R_{III}.

$$R_{III} = \mu\nabla^2\left[\left(G*\gamma\right)\left\langle\mathbf{u}\right\rangle^{\alpha}\right] + G*\left(\mu\nabla\mathbf{u}\cdot\mathbf{n}_{\alpha\beta}\delta_{\alpha\beta}\right) \tag{B.21}$$

Substituting Equations (B.15), (B.16), (B.17), (B.18) and (B.21) into Equation (B.13) leads to the following representation for the averaged equation of momentum.

$$\begin{aligned}\left(G*\gamma\right)\left\langle\mathbf{u}\right\rangle^{\alpha}\frac{\partial\left\langle\rho\right\rangle^{\alpha}}{\partial t} + \left(G*\gamma\right)\left\langle\rho\right\rangle^{\alpha}\frac{\partial\left\langle\mathbf{u}\right\rangle^{\alpha}}{\partial t} + \nabla\cdot\left[G*\left(\gamma\rho\mathbf{u}\mathbf{u}\right)\right] = \\ -\nabla\left[\left(G*\gamma\right)\left\langle P\right\rangle^{\alpha}\right] + \left(G*\gamma\right)\left\langle\rho\right\rangle^{\alpha}\mathbf{g} + \mu\nabla^2\left[\left(G*\gamma\right)\left\langle\mathbf{u}\right\rangle^{\alpha}\right] \\ -G*\left(P\mathbf{n}_{\alpha\beta}\delta_{\alpha\beta}\right) + G*\left(\mu\nabla\mathbf{u}\cdot\mathbf{n}_{\alpha\beta}\delta_{\alpha\beta}\right)\end{aligned} \tag{B.22}$$

This equation is written in a non-local transport form since some of the convolution products contain point values of fluid properties $\mathbf{u}$ and P (the third term on the left-hand side and the last two terms on the right-hand side). Hence, a method needs to be adopted to replace the point values with the averages in order to close the equations.

B.3 Closure of the momentum equation

In this section, the convolution products in Equation (B.22) will be written in terms of intrinsic averages of fluid properties to provide local transport form of the momentum equation which can be approximated later by the SPH approximation scheme (Section 4.3). By expressing the convolution products in terms of average values, the turbulent stress and drag terms will appear as result of the nonlinear convective term (B.16) and the surface integral terms in (B.17) and (B.21), respectively. One should note that the term $G*\gamma$ (which represents the porosity associated with the averaging volume Ω) does not make the equation non-local although γ is appoint value. This is because the distribution function γ is not an unknown in the solution procedure as it is not a fluid property but is an input to the equations.

To deal with the nonlinear convective term on the left-hand side of the momentum equation (B.22), firstly the following expression is employed for the product of velocities

$$\mathbf{uu} = \mathbf{uu} - \langle \mathbf{u} \rangle^{\alpha} \langle \mathbf{u} \rangle^{\alpha} + \langle \mathbf{u} \rangle^{\alpha} \langle \mathbf{u} \rangle^{\alpha} \tag{B.23}$$

This is the basic idea which leads to the LES of flow. Substituting the above equation into the convective term yields

$$\nabla \cdot \left[G * \left(\gamma \rho \mathbf{uu} \right) \right] = \nabla \cdot \left[G * \left(\gamma \rho \langle \mathbf{u} \rangle^{\alpha} \langle \mathbf{u} \rangle^{\alpha} \right) \right] + \nabla \cdot \left[G * \left(\gamma \tau \right) \right] \tag{B.24}$$

where

$$\tau = \rho \mathbf{uu} - \rho \langle \mathbf{u} \rangle^{\alpha} \langle \mathbf{u} \rangle^{\alpha} \tag{B.25}$$

The term $G*(\gamma\tau)$ represents the effect of deviations in the average velocity field. It is noted that the intrinsic averages of velocity in the convolution product inside the first derivative term on the right-hand side of Equation (B.24) are evaluated at

position $\mathbf{r}'$. If the Taylor series expansion is written for one of the intrinsic velocity components and note that $\rho \approx \langle\rho\rangle^{\alpha}\big|_{\mathbf{r}} \approx \langle\rho\rangle^{\alpha}\big|_{\mathbf{r}'}$ (*assumption #3*), then

$$\begin{aligned} G*\left(\gamma\rho\langle\mathbf{u}\rangle^{\alpha}\langle\mathbf{u}\rangle^{\alpha}\right) &= \int_{\Omega} G\left(\mathbf{r}-\mathbf{r}',h_{\Omega}\right)\gamma\left(\mathbf{r}'\right)\langle\rho\rangle^{\alpha}\big|_{\mathbf{r}}\langle\mathbf{u}\rangle^{\alpha}\big|_{\mathbf{r}}\langle\mathbf{u}\rangle^{\alpha}\big|_{\mathbf{r}'}d\mathbf{r}' \\ &+\int_{\Omega} G\left(\mathbf{r}-\mathbf{r}',h_{\Omega}\right)\gamma\left(\mathbf{r}'\right)\langle\rho\rangle^{\alpha}\big|_{\mathbf{r}}\left(\mathbf{r}'-\mathbf{r}\right)\nabla\langle\mathbf{u}\rangle^{\alpha}\big|_{\mathbf{r}}\langle\mathbf{u}\rangle^{\alpha}\big|_{\mathbf{r}'}d\mathbf{r}' \\ &+\frac{1}{2}\int_{\Omega} G\left(\mathbf{r}-\mathbf{r}',h_{\Omega}\right)\gamma\left(\mathbf{r}'\right)\langle\rho\rangle^{\alpha}\big|_{\mathbf{r}}\left(\mathbf{r}'-\mathbf{r}\right)^{2}\nabla^{2}\langle\mathbf{u}\rangle^{\alpha}\big|_{\mathbf{r}}\langle\mathbf{u}\rangle^{\alpha}\big|_{\mathbf{r}'}d\mathbf{r}' \\ &+\cdots \end{aligned} \tag{B.26}$$

Since the averages associated with the centroid of the volume $\mathbf{r}$ can be taken out of the integral,

$$\begin{aligned} G*\left(\gamma\rho\langle\mathbf{u}\rangle^{\alpha}\langle\mathbf{u}\rangle^{\alpha}\right) &= \langle\rho\rangle^{\alpha}\langle\mathbf{u}\rangle^{\alpha}\int_{\Omega} G\left(\mathbf{r}-\mathbf{r}',h_{\Omega}\right)\gamma\left(\mathbf{r}'\right)\langle\mathbf{u}\rangle^{\alpha}\big|_{\mathbf{r}'}d\mathbf{r}' \\ &+\langle\rho\rangle^{\alpha}\nabla\langle\mathbf{u}\rangle^{\alpha}\int_{\Omega} G\left(\mathbf{r}-\mathbf{r}',h_{\Omega}\right)\gamma\left(\mathbf{r}'\right)\left(\mathbf{r}'-\mathbf{r}\right)\langle\mathbf{u}\rangle^{\alpha}\big|_{\mathbf{r}'}d\mathbf{r}' \\ &+\frac{1}{2}\langle\rho\rangle^{\alpha}\nabla^{2}\langle\mathbf{u}\rangle^{\alpha}\int_{\Omega} G\left(\mathbf{r}-\mathbf{r}',h_{\Omega}\right)\gamma\left(\mathbf{r}'\right)\left(\mathbf{r}'-\mathbf{r}\right)^{2}\langle\mathbf{u}\rangle^{\alpha}\big|_{\mathbf{r}'}d\mathbf{r}' \\ &+\cdots \end{aligned} \tag{B.27}$$

If the *constraint #2* (4.10) is valid for velocity, i.e. if

$$r_{\Omega} << L_{\langle\mathbf{u}\rangle^{\alpha}} \tag{B.28}$$

then it will be possible to show that

$$\begin{cases} \langle\rho\rangle^{\alpha}\langle\mathbf{u}\rangle^{\alpha}\int\limits_{\Omega} G\left(\mathbf{r}-\mathbf{r}',h_{\Omega}\right)\gamma\left(\mathbf{r}'\right)\langle\mathbf{u}\rangle^{\alpha}\Big|_{\mathbf{r}'}\,d\mathbf{r}' \\ \qquad = \mathrm{O}\left(\langle\rho\rangle^{\alpha}\langle\mathbf{u}\rangle^{\alpha}\langle\mathbf{u}\rangle^{\alpha}\right) \propto \langle\rho\rangle^{\alpha}\langle\mathbf{u}\rangle^{\alpha}\langle\mathbf{u}\rangle^{\alpha} \\ \langle\rho\rangle^{\alpha}\nabla\langle\mathbf{u}\rangle^{\alpha}\int\limits_{\Omega} G\left(\mathbf{r}-\mathbf{r}',h_{\Omega}\right)\gamma\left(\mathbf{r}'\right)\left(\mathbf{r}'-\mathbf{r}\right)\langle\mathbf{u}\rangle^{\alpha}\Big|_{\mathbf{r}'}\,d\mathbf{r}' \\ \qquad = \mathrm{O}\left(\dfrac{r_{\Omega}}{L_{\langle\mathbf{u}\rangle^{\alpha}}}\langle\rho\rangle^{\alpha}\langle\mathbf{u}\rangle^{\alpha}\langle\mathbf{u}\rangle^{\alpha}\right) << \langle\rho\rangle^{\alpha}\langle\mathbf{u}\rangle^{\alpha}\langle\mathbf{u}\rangle^{\alpha} \\ \dfrac{1}{2}\langle\rho\rangle^{\alpha}\nabla^{2}\langle\mathbf{u}\rangle^{\alpha}\int\limits_{\Omega} G\left(\mathbf{r}-\mathbf{r}',h_{\Omega}\right)\gamma\left(\mathbf{r}'\right)\left(\mathbf{r}'-\mathbf{r}\right)^{2}\langle\mathbf{u}\rangle^{\alpha}\Big|_{\mathbf{r}'}\,d\mathbf{r}' \\ \qquad = \mathrm{O}\left[\dfrac{1}{2}\left(\dfrac{r_{\Omega}}{L_{\langle\mathbf{u}\rangle^{\alpha}}}\right)^{2}\langle\rho\rangle^{\alpha}\langle\mathbf{u}\rangle^{\alpha}\langle\mathbf{u}\rangle^{\alpha}\right] << \langle\rho\rangle^{\alpha}\langle\mathbf{u}\rangle^{\alpha}\langle\mathbf{u}\rangle^{\alpha} \\ \quad \vdots \end{cases} \tag{B.29}$$

The above equation demonstrates that second and higher terms in Equation (B.27) are negligible compared to the first term. Therefore, that equation can be represented as

$$G*\left(\gamma\rho\langle\mathbf{u}\rangle^{\alpha}\langle\mathbf{u}\rangle^{\alpha}\right) = \langle\rho\rangle^{\alpha}\langle\mathbf{u}\rangle^{\alpha}\left[G*\left(\gamma\langle\mathbf{u}\rangle^{\alpha}\right)\right] \tag{B.30}$$

Substituting this into Equation (B.24), applying Equation (4.21) for $G*\left(\gamma\langle\mathbf{u}\rangle^{\alpha}\right)$ as well as $G*\left(\gamma\tau\right)$, and making some manipulation yields

$$\begin{aligned} \nabla\cdot\left[G*\left(\gamma\rho\mathbf{u}\mathbf{u}\right)\right] &= \left(G*\gamma\right)\langle\rho\rangle^{\alpha}\langle\mathbf{u}\rangle^{\alpha}\cdot\nabla\langle\mathbf{u}\rangle^{\alpha} + \left(G*\gamma\right)\langle\mathbf{u}\rangle^{\alpha}\langle\mathbf{u}\rangle^{\alpha}\nabla\langle\rho\rangle^{\alpha} \\ &+ \langle\rho\rangle^{\alpha}\langle\mathbf{u}\rangle^{\alpha}\cdot\nabla\left[\left(G*\gamma\right)\langle\mathbf{u}\rangle^{\alpha}\right] + \nabla\cdot\left[\left(G*\gamma\right)\langle\tau\rangle^{\alpha}\right] \end{aligned} \tag{B.31}$$

where following Equation (B.25), and *assumption #3*, it is possible to show that

$$\frac{\langle\tau\rangle^{\alpha}}{\langle\rho\rangle^{\alpha}} = \langle\mathbf{u}\mathbf{u}\rangle^{\alpha} - \left\langle\langle\mathbf{u}\rangle^{\alpha}\langle\mathbf{u}\rangle^{\alpha}\right\rangle^{\alpha} \tag{B.32}$$

$\langle \tau \rangle^{\alpha}$ is the SPS stress tensor which arises due to the spatial filtering of the nonlinear convective term and represents the effect of turbulence on the average flow field. It is equivalent to the classical SGS stress tensor in grid-based methods. The phrase SPS is often used as the particle version of the SGS in particle methods (e.g. MPS and SPH). This term should be modelled by an appropriate closure model since it contains point values of velocity. The SPS stress tensor is expressed with the sign of intrinsic average $\langle\ \rangle^{\alpha}$ as it will be formulated in terms of intrinsic flow quantities in the present study (Section 4.2.2).

The surface integrals (the last two terms in Equation B.22) also need to be represented in terms of intrinsic averages of velocity and pressure. Quintard and Whitaker (1994) employed Taylor series expansions (Equation 4.13) for velocity and pressure, developed some useful geometrical theorems, and showed that

$$\begin{aligned} -G*\left(P\mathbf{n}_{\alpha\beta}\delta_{\alpha\beta}\right) &= \langle P\rangle^{\alpha}\nabla\left(G*\gamma\right) \\ &+\nabla\langle P\rangle^{\alpha}\nabla\left\{G*\left[\gamma\left(\mathbf{r}'-\mathbf{r}\right)\right]\right\} \\ &+\frac{1}{2}\nabla^{2}\langle P\rangle^{\alpha}\nabla\left\{G*\left[\gamma\left(\mathbf{r}'-\mathbf{r}\right)^{2}\right]\right\} \\ &+\cdots \\ &-G*\left(\tilde{P}^{\alpha}\mathbf{n}_{\alpha\beta}\delta_{\alpha\beta}\right) \end{aligned} \tag{B.33}$$

and

$$\begin{aligned} G*\left(\mu\nabla\mathbf{u}\cdot\mathbf{n}_{\alpha\beta}\delta_{\alpha\beta}\right) &= -\mu\nabla\langle\mathbf{u}\rangle^{\alpha}\nabla\left(G*\gamma\right) \\ &-\mu\nabla^{2}\langle\mathbf{u}\rangle^{\alpha}\nabla\left\{G*\left[\gamma\left(\mathbf{r}'-\mathbf{r}\right)\right]\right\} \\ &-\frac{1}{2}\mu\nabla^{3}\langle\mathbf{u}\rangle^{\alpha}\nabla\left\{G*\left[\gamma\left(\mathbf{r}'-\mathbf{r}\right)^{2}\right]\right\} \\ &-\cdots \\ &+G*\left(\mu\nabla\tilde{\mathbf{u}}^{\alpha}\cdot\mathbf{n}_{\alpha\beta}\delta_{\alpha\beta}\right) \end{aligned} \tag{B.34}$$

In addition to the *constraint #2* for velocity (i.e. Equation B.28), they applied that constraint to the pressure too as

$$r_{\Omega} << L_{\langle P\rangle^{\alpha}} \tag{B.35}$$

and concluded that the pressure derivatives of order one and higher in Equation (B.33) and the pressure derivatives of order two and higher in Equation (B.34) are negligible so that

$$-G*\left(P\mathbf{n}_{\alpha\beta}\delta_{\alpha\beta}\right)=\langle P\rangle^{\alpha}\nabla\left(G*\gamma\right)-G*\left(\tilde{P}^{\alpha}\mathbf{n}_{\alpha\beta}\delta_{\alpha\beta}\right) \tag{B.36}$$

and

$$G*\left(\mu\nabla\mathbf{u}\cdot\mathbf{n}_{\alpha\beta}\delta_{\alpha\beta}\right)=-\mu\nabla\langle\mathbf{u}\rangle^{\alpha}\nabla\left(G*\gamma\right)+G*\left(\mu\nabla\tilde{\mathbf{u}}^{\alpha}\cdot\mathbf{n}_{\alpha\beta}\delta_{\alpha\beta}\right) \tag{B.37}$$

Now by substituting Equations (B.31), (B.36) and (B.37) into Equation (B.22), after manipulation, the following relationships are obtained, respectively, for the left- and right-hand sides of the averaged equation of momentum.

$$\begin{aligned}LHS=&\left(G*\gamma\right)\langle\rho\rangle^{\alpha}\frac{\partial\langle\mathbf{u}\rangle^{\alpha}}{\partial t}+\left(G*\gamma\right)\langle\mathbf{u}\rangle^{\alpha}\frac{\partial\langle\rho\rangle^{\alpha}}{\partial t}\\&+\left(G*\gamma\right)\langle\rho\rangle^{\alpha}\langle\mathbf{u}\rangle^{\alpha}\cdot\nabla\langle\mathbf{u}\rangle^{\alpha}+\left(G*\gamma\right)\langle\mathbf{u}\rangle^{\alpha}\langle\mathbf{u}\rangle^{\alpha}\nabla\langle\rho\rangle^{\alpha}\\&+\langle\rho\rangle^{\alpha}\langle\mathbf{u}\rangle^{\alpha}\cdot\nabla\left[\left(G*\gamma\right)\langle\mathbf{u}\rangle^{\alpha}\right]+\nabla\cdot\left[\left(G*\gamma\right)\langle\tau\rangle^{\alpha}\right]\end{aligned} \tag{B.38}$$

$$\begin{aligned}RHS=&-\nabla\left[\left(G*\gamma\right)\langle P\rangle^{\alpha}\right]+\mu\nabla^{2}\left[\left(G*\gamma\right)\langle\mathbf{u}\rangle^{\alpha}\right]+\left(G*\gamma\right)\langle\rho\rangle^{\alpha}\mathbf{g}\\&+\langle P\rangle^{\alpha}\nabla\left(G*\gamma\right)-\mu\nabla\langle\mathbf{u}\rangle^{\alpha}\nabla\left(G*\gamma\right)-G*\left[\left(\mathbf{I}\tilde{P}^{\alpha}+\mu\nabla\tilde{\mathbf{u}}^{\alpha}\right)\mathbf{n}_{\alpha\beta}\delta_{\alpha\beta}\right]\end{aligned} \tag{B.39}$$

where $\mathbf{I}$ represents the unit tensor. Equation (B.38) can be rewritten in the following form

$$\begin{aligned}LHS=&\left(G*\gamma\right)\langle\rho\rangle^{\alpha}\left(\frac{\partial\langle\mathbf{u}\rangle^{\alpha}}{\partial t}+\langle\mathbf{u}\rangle^{\alpha}\cdot\nabla\langle\mathbf{u}\rangle^{\alpha}\right)\\&+\langle\mathbf{u}\rangle^{\alpha}\left\{\left(G*\gamma\right)\frac{\partial\langle\rho\rangle^{\alpha}}{\partial t}+\left(G*\gamma\right)\langle\mathbf{u}\rangle^{\alpha}\nabla\langle\rho\rangle^{\alpha}+\langle\rho\rangle^{\alpha}\nabla\cdot\left[\left(G*\gamma\right)\langle\mathbf{u}\rangle^{\alpha}\right]\right\}\\&+\nabla\cdot\left[\left(G*\gamma\right)\langle\tau\rangle^{\alpha}\right]\end{aligned} \tag{B.40}$$

where the expression inside the parentheses in the first term is equivalent to the material derivative of $\langle \mathbf{u} \rangle^{\alpha}$ according to Equation (B.11), and the expression inside the braces in the second term is zero according to continuity equation (B.10). Therefore,

$$LHS = (G * \gamma)\langle \rho \rangle^{\alpha} \frac{D \langle \mathbf{u} \rangle^{\alpha}}{Dt} + \nabla \cdot \left[(G * \gamma)\langle \tau \rangle^{\alpha} \right] \tag{B.41}$$

Besides, Equation (B.39) can be expressed as follows after combining the first and fourth terms.

$$\begin{aligned} RHS = &-(G * \gamma)\nabla \langle P \rangle^{\alpha} + (G * \gamma)\langle \rho \rangle^{\alpha} \mathbf{g} + \mu \nabla^2 \left[(G * \gamma)\langle \mathbf{u} \rangle^{\alpha} \right] \\ &-\mu \nabla \langle \mathbf{u} \rangle^{\alpha} \nabla (G * \gamma) - G * \left[\left(\mathbf{I} \tilde{P}^{\alpha} + \mu \nabla \tilde{\mathbf{u}}^{\alpha} \right) \mathbf{n}_{\alpha\beta} \delta_{\alpha\beta} \right] \end{aligned} \tag{B.42}$$

Finally, according to the two above equations, the Lagrangian form of the averaged (macroscopic) equation of momentum is written in terms of intrinsic averages as the following

$$\begin{aligned} (G * \gamma)\langle \rho \rangle^{\alpha} \frac{D \langle \mathbf{u} \rangle^{\alpha}}{Dt} = &-(G * \gamma)\nabla \langle P \rangle^{\alpha} + (G * \gamma)\langle \rho \rangle^{\alpha} \mathbf{g} \\ &+\mu \nabla^2 \left[(G * \gamma)\langle \mathbf{u} \rangle^{\alpha} \right] - \mu \nabla \langle \mathbf{u} \rangle^{\alpha} \nabla (G * \gamma) \\ &-\nabla \cdot \left[(G * \gamma)\langle \tau \rangle^{\alpha} \right] + G * \left[\left(-\mathbf{I} \tilde{P}^{\alpha} + \mu \nabla \tilde{\mathbf{u}}^{\alpha} \right) \mathbf{n}_{\alpha\beta} \delta_{\alpha\beta} \right] \end{aligned} \tag{B.43}$$

Appendix C Discretisation of the SPHAM equations for flow through porous media

The aim of this appendix is to discretise the SPHAM governing equations developed in Section 4.3.1 (Equations 4.45 and 4.46) based on the SPH formulation (Equations 4.52 to 4.55). The SPHAM equations are approximated at the position of a generic particle a with neighbouring particles b using the kernel function W.

C.1 Conservation of mass

The time derivative on the left-hand side and the spatial derivative on the right-hand side of the SPHAM equation of mass (4.45), are discretised using Equations (4.55) and (4.53), respectively, as follows.

$$\frac{D\left\langle \rho \right\rangle_a^\alpha}{Dt} = \frac{\left\langle \rho \right\rangle_a^\alpha \Big|^{(t+\Delta t)} - \left\langle \rho \right\rangle_a^\alpha \Big|^{(t)}}{\Delta t} \tag{C.1}$$

$$-\frac{1}{\phi_a}\left\langle \rho \right\rangle_a^\alpha \left[\nabla W * \left(\phi \left\langle \mathbf{u} \right\rangle^\alpha \right) \right]_a = -\frac{\left\langle \rho \right\rangle_a^\alpha}{\phi_a} \sum_b \frac{m_b}{\phi_b \left\langle \rho \right\rangle_b^\alpha} \nabla W \left(\mathbf{r}_a - \mathbf{r}_b, h_\Upsilon \right) \phi_b \left\langle \mathbf{u} \right\rangle_b^\alpha \tag{C.2}$$

In the present form of Equation (C.2), the divergence does not vanish for a uniform distribution of macroscopic velocity $\phi \left\langle \mathbf{u} \right\rangle^\alpha$. Providing a symmetric form for this term will resolve the problem (Bonet and Lok 1999). Replacing $\left\langle \psi \right\rangle^\alpha$ with 1.0 in equation (4.53) yields

$$\nabla W \ *1 \approx \sum_b \frac{m_b}{\phi_b \langle \rho \rangle_b^\alpha} \nabla W \ (\mathbf{r}_a - \mathbf{r}_b, h_\Upsilon) \approx 0 \tag{C.3}$$

which is equal to zero according to the symmetry condition of the kernel function or the fact that derivative of a scalar is zero. This term can be multiplied by $\langle \rho \rangle_a^\alpha \langle \mathbf{u} \rangle_a^\alpha$ and then added to the right-hand side of Equation (C.2) to obtain the following symmetric form

$$-\frac{1}{\phi_a} \langle \rho \rangle_a^\alpha \left[\nabla W \ * \left(\phi \langle \mathbf{u} \rangle^\alpha \right) \right]_a = -\sum_b \frac{m_b}{\phi_a \phi_b} \frac{\langle \rho \rangle_a^\alpha}{\langle \rho \rangle_b^\alpha} \nabla_a W_{ab} \cdot \left(\phi_b \langle \mathbf{u} \rangle_b^\alpha - \phi_a \langle \mathbf{u} \rangle_a^\alpha \right) \tag{C.4}$$

where $\nabla_a W_{ab}$ denotes $\nabla W(\mathbf{r}_a - \mathbf{r}_b, h_\Upsilon)$. This equation vanishes identically for a constant macroscopic velocity (according to Bonet and Lok 1999).

Substituting Equations (C.1) and (C.4) into Equation (4.45), and assuming that $\langle \rho \rangle_a^\alpha \approx \langle \rho \rangle_b^\alpha$ due to *assumption #3*, the discretised version of the SPHAM equation of mass is presented as follows.

$$\frac{\langle \rho \rangle_a^\alpha \Big|^{(t+\Delta t)} - \langle \rho \rangle_a^\alpha \Big|^{(t)}}{\Delta t} = -\sum_b \frac{m_b}{\phi_a \phi_b} \nabla_a W_{ab} \cdot \left(\phi_b \langle \mathbf{u} \rangle_b^\alpha - \phi_a \langle \mathbf{u} \rangle_a^\alpha \right) \tag{C.5}$$

C.2 Conservation of momentum

Similar to Equation (C.1), the temporal derivative in the momentum equation (4.46) is approximated as the following.

$$\frac{D \langle \mathbf{u} \rangle_a^\alpha}{Dt} = \frac{\langle \mathbf{u} \rangle_a^\alpha \Big|^{(t+\Delta t)} - \langle \mathbf{u} \rangle_a^\alpha \Big|^{(t)}}{\Delta t} \tag{C.6}$$

Using Equation (4.53), the first term on the right-hand side of Equation (4.46) is written as

$$-\frac{1}{\langle\rho\rangle_a^\alpha}\left(\nabla W * \langle P\rangle^\alpha\right)_a = -\frac{1}{\langle\rho\rangle_a^\alpha}\sum_b \frac{m_b}{\phi_b \langle\rho\rangle_b^\alpha}\nabla_a W_{ab}\langle P\rangle_b^\alpha \tag{C.7}$$

This form does not preserve the linear momentum since the resultant of the internal pressure forces on a certain particle is not zero. For the condition of preservation of linear momentum in a particle simulation see Bonet and Lok (1999) and Khayyer et al. (2008). To have the linear momentum being preserved, it is required to bring the above equation in a pairwise symmetric form. Therefore, the summation in Equation (C.3) is multiplied by $-\langle P\rangle_a^\alpha / \langle\rho\rangle_a^\alpha$ and added to Equation (C.7) to arrive at the following form for the pressure gradient term which preserves the linear momentum.

$$-\frac{1}{\langle\rho\rangle_a^\alpha}\left(\nabla W * \langle P\rangle^\alpha\right)_a = -\sum_b \frac{m_b}{\phi_b}\nabla_a W_{ab}\frac{\langle P\rangle_a^\alpha + \langle P\rangle_b^\alpha}{\langle\rho\rangle_a^\alpha \langle\rho\rangle_b^\alpha} \tag{C.8}$$

Similarly, the third term on the right-hand side of momentum equation (4.46) is approximated as follows.

$$\frac{\mu}{\phi_a \langle\rho\rangle_a^\alpha}\left\{\nabla W * \left[\nabla\left(\phi\langle\mathbf{u}\rangle^\alpha\right)\right]\right\}_a = \sum_b \frac{\mu m_b}{\phi_a\phi_b}\nabla_a W_{ab}\frac{\nabla\left(\phi\langle\mathbf{u}\rangle^\alpha\right)_a + \nabla\left(\phi\langle\mathbf{u}\rangle^\alpha\right)_b}{\langle\rho\rangle_a^\alpha \langle\rho\rangle_b^\alpha} \tag{C.9}$$

A finite difference approximation is employed here for the velocity gradient terms as

$$\begin{aligned}\nabla\left(\phi\langle\mathbf{u}\rangle^\alpha\right)_a &= \left(\phi_a\langle\mathbf{u}\rangle_a^\alpha - \phi_b\langle\mathbf{u}\rangle_b^\alpha\right)\frac{\mathbf{r}_a - \mathbf{r}_b}{|\mathbf{r}_a - \mathbf{r}_b|^2}\\ \nabla\left(\phi\langle\mathbf{u}\rangle^\alpha\right)_b &= \left(\phi_b\langle\mathbf{u}\rangle_b^\alpha - \phi_a\langle\mathbf{u}\rangle_a^\alpha\right)\frac{\mathbf{r}_b - \mathbf{r}_a}{|\mathbf{r}_b - \mathbf{r}_a|^2}\end{aligned} \tag{C.10}$$

One should easily find that $\nabla\left(\phi\langle\mathbf{u}\rangle^\alpha\right)_a = \nabla\left(\phi\langle\mathbf{u}\rangle^\alpha\right)_b$. Thus, the following equation is obtained for the viscosity term.

$$\frac{\mu}{\phi_a \langle\rho\rangle_a^\alpha}\left\{\nabla W * \left[\nabla\left(\phi\langle\mathbf{u}\rangle^\alpha\right)\right]\right\}_a = \sum_b \frac{2\mu m_b}{\phi_a\phi_b}\frac{\mathbf{r}_{ab}\cdot\nabla_a W_{ab}}{|\mathbf{r}_{ab}|^2 + \eta^2}\frac{\phi_a\langle\mathbf{u}\rangle_a^\alpha - \phi_b\langle\mathbf{u}\rangle_b^\alpha}{\langle\rho\rangle_a^\alpha \langle\rho\rangle_b^\alpha} \tag{C.11}$$

where $\mathbf{r}_{ab} = \mathbf{r}_a - \mathbf{r}_b$ and η is a small number (usually taken as $0.1h_\Upsilon$) used to prevent singularity.

Equation (4.53) is applied to discretise the fourth term on the right-hand side of momentum equation (4.46). The result is then added to the product of Equation (C.3) and $\mu(\nabla\phi)_a \langle\mathbf{u}\rangle_a^\alpha / \phi_a \langle\rho\rangle_a^\alpha$ to arrive at the following relationship.

$$-\frac{\mu(\nabla\phi)_a}{\phi_a \langle\rho\rangle_a^\alpha}\left(\nabla W * \langle\mathbf{u}\rangle^\alpha\right)_a = -\sum_b \frac{\mu m_b (\nabla\phi)_a}{\phi_a\phi_b} \nabla_d W_{ab} \cdot \frac{\langle\mathbf{u}\rangle_b^\alpha - \langle\mathbf{u}\rangle_a^\alpha}{\langle\rho\rangle_a^\alpha \langle\rho\rangle_b^\alpha} \qquad \text{(C.12)}$$

Then if a finite difference approximation similar to Equation (C.10) is employed for the gradient of porosity $(\nabla\phi)_a$, the following form will be obtained.

$$-\frac{\mu(\nabla\phi)_a}{\phi_a \langle\rho\rangle_a^\alpha}\left(\nabla W * \langle\mathbf{u}\rangle^\alpha\right)_a = -\sum_b \frac{\mu m_b}{\phi_a\phi_b} \frac{\mathbf{r}_{ab}\cdot\nabla_a W_{ab}}{|\mathbf{r}_{ab}|^2 + \eta^2} \frac{(\phi_a - \phi_b)\left(\langle\mathbf{u}\rangle_b^\alpha - \langle\mathbf{u}\rangle_a^\alpha\right)}{\langle\rho\rangle_a^\alpha \langle\rho\rangle_b^\alpha} \qquad \text{(C.13)}$$

The fifth term (turbulent shear stress term) is simply discretised similar to Equation (C.8), by replacing $\langle P \rangle^\alpha$ with $\phi\langle\tau\rangle^\alpha$ as follows.

$$-\frac{1}{\phi_a \langle\rho\rangle_a^\alpha}\left[\nabla W * \left(\phi\langle\tau\rangle^\alpha\right)\right]_a = -\sum_b \frac{m_b}{\phi_a\phi_b} \nabla_a W_{ab} \cdot \frac{\phi_a \langle\tau\rangle_a^\alpha + \phi_b \langle\tau\rangle_b^\alpha}{\langle\rho\rangle_a^\alpha \langle\rho\rangle_b^\alpha} \qquad \text{(C.14)}$$

in which the shear stress tensor $\langle\tau\rangle^\alpha$ is estimated using the eddy-viscosity model introduced in Section 4.2.2. Finally, the last term on the right-hand side of momentum equation (4.46), i.e. the surface integral is added to the equation as an external force $\mathbf{A}_a$ on the particle. $\mathbf{A}_a$ is estimated by the drag closure model introduced in Section 4.2.1.

Now the discretised version of the SPHAM momentum equation can be written as the following, by substituting Equations (C.6), (C.8), (C.11), (C.13), (C.14) into Equation (4.46) and replacing the surface integral term with $\mathbf{A}_a$.

$$\frac{\left\langle \mathbf{u} \right\rangle_a^\alpha \Big|^{(t+\Delta t)} - \left\langle \mathbf{u} \right\rangle_a^\alpha \Big|^{(t)}}{\Delta t} = -\sum_b \frac{m_b}{\phi_b} \nabla_a W_{ab} \frac{\left\langle P \right\rangle_a^\alpha + \left\langle P \right\rangle_b^\alpha}{\left\langle \rho \right\rangle_a^\alpha \left\langle \rho \right\rangle_b^\alpha} + \mathbf{g}$$
$$+ \sum_b \frac{2\mu m_b}{\phi_a \phi_b} \frac{\nabla_a W_{ab} \cdot \mathbf{r}_{ab}}{\left|\mathbf{r}_{ab}\right|^2 + \eta^2} \frac{\phi_a \left\langle \mathbf{u} \right\rangle_a^\alpha - \phi_b \left\langle \mathbf{u} \right\rangle_b^\alpha}{\left\langle \rho \right\rangle_a^\alpha \left\langle \rho \right\rangle_b^\alpha}$$
$$- \sum_b \frac{\mu m_b}{\phi_a \phi_b} \frac{\nabla_a W_{ab} \cdot \mathbf{r}_{ab}}{\left|\mathbf{r}_{ab}\right|^2 + \eta^2} \frac{\left(\phi_a - \phi_b\right)\left(\left\langle \mathbf{u} \right\rangle_b^\alpha - \left\langle \mathbf{u} \right\rangle_a^\alpha\right)}{\left\langle \rho \right\rangle_a^\alpha \left\langle \rho \right\rangle_b^\alpha} \qquad \text{(C.15)}$$
$$- \sum_b \frac{m_b}{\phi_a \phi_b} \nabla_a W_{ab} \cdot \frac{\phi_a \left\langle \tau_t \right\rangle_a^\alpha + \phi_b \left\langle \tau_t \right\rangle_b^\alpha}{\left\langle \rho \right\rangle_a^\alpha \left\langle \rho \right\rangle_b^\alpha} + \mathbf{A}_a$$